ORGANIC CHEMIRESISTIVE AND ORGANIC FIELD EFFECT TRANSISTOR GAS SENSORS

By

Ashwini Kumar
(ENGG 01201104014)
Bhabha Atomic Research Centre Mumbai

A thesis submitted to the
Board of Studies in Engineering Sciences
in partial fulfillment of requirements
for the Degree of

DOCTOR OF PHILOSOPHY
of
HOMI BHABHA NATIONAL INSTITUTE

October 2016

Homi Bhabha National Institute

Recommendations of the Viva Voce Committee

As members of the Viva Voce Committee, we certify that we have read the dissertation prepared by Mr. **ASHWINI KUMAR** entitled **"ORGANIC CHEMIRESISTIVE AND ORGANIC FIELD EFFECT TRANSISTOR GAS SENSORS"** and recommend that it may be accepted as fulfilling the thesis requirement for the award of Degree of Doctor of Philosophy.

Chairman – Prof. A. P. Tiwari **Date:** 27/1/17

Guide / Convener – Prof. D.K. Aswal **Date:** 27/1/17

Co-guide – Prof. Kallol Roy Kallol Roy **Date:**

Examiner - Prof. M .Senthil Kumar M Senthil **Date:** 27/01/2017

Member 1– Prof. A. K. Bhattacharjee AKBhattacharjee **Date:** 27/01/2017

Member 2 – Prof. Saibal Basu **Date:** 27/1/17

Member 3 – Prof. N. K. Sahoo **Date:** 30.1.17

Member 4 – Prof. V. H. Patankar V.H.Patankar **Date:** 27/01/17

Member 5 – Prof. D.C. Kar **Date:**

Final approval and acceptance of this thesis is contingent upon the candidate's submission of the final copies of the thesis to HBNI.

I/We hereby certify that I/we have read this thesis prepared under my/our direction and recommend that it may be accepted as fulfilling the thesis requirement.

Date:

Kallol Roy

27/1/17

Place: Mumbai **Prof. Kallol Roy** **Prof. D. K. Aswal**

Co-guide **Guide**

STATEMENT BY AUTHOR

This dissertation has been submitted in partial fulfillment of requirements for an advanced degree at Homi Bhabha National Institute (HBNI) and is deposited in the Library to be made available to borrowers under rules of the HBNI.

Brief quotations from this dissertation are allowable without special permission, provided that accurate acknowledgement of source is made. Requests for permission for extended quotation from or reproduction of this manuscript in whole or in part may be granted by the Competent Authority of HBNI when in his or her judgment the proposed use of the material is in the interests of scholarship. In all other instances, however, permission must be obtained from the author.

Ashwini Kumar

DECLARATION

I, hereby declare that the investigation presented in the thesis has been carried out by me. The work is original and has not been submitted earlier as a whole or in part for a degree / diploma at this or any other Institution / University.

Ashwini Kumar

List of Publications arising from the thesis

Journal

1. "Flexible cobalt-phthalocyanine thin films with high charge carrier mobility", A. Singh, A. Kumar, **Ashwini Kumar,** S. Samanta, A. K. Debnath, P. Jha, R. Prasad, Z. Salmi, S. Nowak, M. M. Chehimi, D. K. Aswal, S. K.Gupta, *Applied Physics Letters*, **2012**, *101*, 222102-5.

2. "Bending stress induced improved chemiresistive gas sensing characteristics of flexible cobalt-phthalocyanine thin films", A. Singh, **Ashwini Kumar,** A. Kumar, S. Samanta, N. Joshi, V. Balouria, A. K. Debnath, R. Prasad, Z. Salmi, M. M. Chehimi, D. K. Aswal, S. K. Gupta, *Applied Physics Letters,* **2013,** *103*, 132107-4.

3. "Room temperature detection of H_2S by flexible gold–cobalt phthalocyanine heterojunction thin films", **Ashwini Kumar**, N. Joshi, S. Samanta, A. Singh, A. K. Debnath, A. K. Chauhan, M. Roy, R. Prasad, K. Roy, M. M. Chehimi, D. K. Aswal, S. K. Gupta, *Sensors and Actuators B: Chemical*, **2015,** *206*, 653-662.

4. "Fast Response and High Sensitivity of ZnO Nanowires - Cobalt Phthalocyanine Heterojunction based H_2S Sensor", **Ashwini Kumar,** S. Samanta, A. Singh, M. Roy, S. Singh, S. Basu, M. M. Chehimi, K. Roy, N. Ramgir, A. K. Debnath, D. K. Aswal, S. K. Gupta, M. Navneethan, Y. Hayakawa, *ACS Applied Materials & Interfaces*, **2015,** *7,* 17713-17724.

Conferences

1. "Electron accumulation/depletion at F_{16}CoPc/Znq_3 heterojunction: Kelvin probe and charge transport study", **Ashwini Kumar**, R. Prasad, A. Kumar, S. Samanta, A. Singh, A. K. Debnath, D. K. Aswal, S. K. Gupta, *AIP Conference Proceedings*, **2013**, *1512*,770-771.

2. "Flexible Au-CoPc heterojunction film for H_2S detection", **Ashwini Kumar**, S. Samanta, Ajay Singh, A. K. Debnath, R. Prasad, Kallol Roy, M. M. Chehimi, D. K. Aswal, S. K. Gupta, *Organic Devices : The Future Ahead*, March 3-6, **2014**, BARC Mumbai.

3. "Cobalt Phthalocyanine / ZnO Nanowire Heterojunction Film For H_2S Sensor", **Ashwini Kumar**, Ajay Singh, Soumen Samanta, Mainak Roy, R. Prasad, A. K. Debnath, D. K. Aswal, *AIP Conference Proceedings*, **2015**, *1665*, 050193-3.

4. Poly [N-9′ heptadecanyl-2, 7-carbazole-alt-5, 5-(4′7′-di-2-thienyl 2′, 1′, 3′ benzothiadiazole)] based Chemical Field Effect Transistor for selective detection of NO_2", **Ashwini Kumar**, P. Jha, S. Samanta, A. Singh, A. K. Debnath, K. Roy, D. K. Aswal, *15th European Conference on Molecular Electronics*, September 1-5, **2015**, University of Strasbourg, Strasbourg, France.

5. "Studies on different Configurations of Cobalt Phthalocyanine based Flexible Organic Field Effect Transistor", **Ashwini Kumar**, P. Jha, S. Samanta, A. Singh. A .K. Debnath, D. K. Aswal, S. K. Gupta, *AIP Conference Proceedings*, **2016**, *1731*, 110001-3

Other Publications (not included in thesis)

1. "Photo-induced synthesis of polypyrrole-silver nanocomposite films on N-(3-trimethoxysilylpropyl)pyrrole-modified biaxially oriented polyethylene terephthalate flexible substrates", Ajay Singh, Zakaria Salmi, Nirav Joshi, Purushottam Jha, **Ashwini Kumar**, Hélène Lecoq, Stephanie Lau, Mohamed M. Chehimi, Dinesh K. Aswal and Shiv K. Gupta, *RSC Advances*, **2013,** *3*, 5506-5523.

2. "One step synthesis of highly ordered free standing flexible polypyrrole-silver nanocomposite films at air–water interface by photopolymerization", Ajay Singh, Zakaria Salmi, Purushottam Jha, Nirav Joshi, **Ashwini Kumar**, Philippe Decorse, Hélène Lecoq, Stephanie Lau-Truong, Dinesh K. Aswal, Shiv K. Gupta and Mohamed M. Chehimi, *RSC Advances*, **2013**,*3*, 13329-13336.

3. "Interface mediated semiconducting to metallic like transition in ultrathin Bi2Se3 films on (100) $SrTiO_3$ grown by molecular beam epitaxy", Anil K. Debnath, R. Prasad, Ajay Singh, Soumen Samanta, **Ashwini Kumar**, Anil Bohra, Debarati Bhattacharya, Saibal Basu, Niraj Joshi, Dinesh K. Aswal and S. K. Gupta, *RSC Advances*, **2015**,*5*, 87897-87902.

Dedicated

to

my Parents

ACKNOWLEDGEMENTS

It is indeed a great opportunity for me to express my sincere gratitude towards many people whom I have been accompanied with during my Ph.D work at BARC Mumbai. To begin with, I would like to express my deepest gratitude to my guide, **Prof. D. K. Aswal** for his invaluable guidance, consistent encouragement, active support and limitless patience throughout the study. Amidst all his official assignments, he was attentive enough to spare his valuable time for me. It has been great pleasure and privilege working with him. I express my sincere gratitude to my co-guide, **Prof. Kallol Roy** for providing the right direction in choosing research topic at the time of joining this institute. I also thank him for his lectures on mathematico statistical methods.

I would like to express my words of thanks to former Head TPD, **Dr. S.K. Gupta**, and present Head, **Dr. S.C. Gadkari** for their administrative support and permitting me to pursue research in his division.

I would like to thank chairman of my Doctoral committee, **Prof. A. P. Tiwari** for conduction and evaluation of progress of my Ph.D work and for important suggestions during the research period.

I owe my thanks to **Dr. A.K. Debnath** for his guidance in the lab and carrying out XPS measurement and analyses. I am greatly indebted to my mentor **Dr. Ajay Singh** for his excellent guidance, encouragement and support in every stage of my work. He has always taken keen interest in analyzing the results and clearing my doubts. This thesis in present form would not have been possible without his enthusiastic support.

I must thank **Dr. Arvind** and **Shri R. Prasad** for extending their support during initial stages in carrying out the experimental work. I am especially thankful to **Dr. Soumen**

Samanta for always being available for scientific discussions and his numerous help on several occasions. I would like to extend my deepest appreciation to **Dr. Purushottam Jha** for helping me in fabricating and characterizing Organic transistors and many scientific discussions a number of times. I express my heartfelt gratitude to **Dr. Shovit Bhattacharya**, **Dr. Niranjan Ramgir** and **Dr. Niyanta Datta** for technical support and cordial encouragement.

I place on record, my sincere thanks to **Dr. K. P. Muthe** for his encouragement and support by accompanying me in the lab on holidays. I am thankful to **Dr. A.K. Chauhan**, **Dr. Manmeet Kaur**, **Dr. Vibha Saxena**, **Dr. S. P. Koiry**, **Dr. Veerender**, **Dr. Ranita Basu** ,**Dr. Ranu Bhatt**, **Mrs K. Ganpathi** and **Shri K. N. Meshram** for extending support and help at various stages of thesis work. Special thanks to Chauhan sir for carrying out Raman spectroscopic measurements. Heartiest thanks to my colleagues **Mr. Anil** and **Ms. Meetu** for backing me up when my morale was fading in the end.

It gives me immense pleasure to thank my friends and batchmates especially **Anshu**, **Abhay**, **Ankur**, **Naresh**, **Harshit**, **Nitin**, **Eshita** and **Archana** for their affection and good wishes. It’s a happy reminiscence of spending some of the most cheerful days with them.

The support of my parents under all circumstances and their unending patience perhaps has been one of the most important factors in the successful completion of thesis work. Their unconditional love and concern is what I am blessed with always.

Finally I would like to give my soul respect to almighty for giving me courage and patience enabling me to complete this work.

Table of Contents

SYNOPSIS

Chemical sensors play an increasingly important role in monitoring the environment we live in, providing information on industrial manufacturing processes and their emissions, quality control of foods and beverages, and a host of other applications. In order to monitor different harmful gases in the environment, varieties of gas sensors have been developed and, many of them are available commercially. Metal-oxides semiconductors *viz.*, ZnO, SnO_2, WO_3, In_2O_3 etc. are most commonly used as sensor materials. The mechanisms of gas response have essentially been explained based on trapping of electrons by adsorbed molecules and band bending induced by these charged molecules. For *n*-type metal oxides, the negative charge trapped in oxygen species causes an upward band bending and thus a reduced conductivity compared to the flat band situation. Reaction of these oxygen species with reducing gases or a competitive adsorption and replacement of the adsorbed oxygen by other molecules decreases and can reverse the band bending, resulting in an increased conductivity. Exactly opposite takes place for *p*-type metal oxides.

Recently organic semiconductors (*i.e.*, polymers and small molecule materials) have also been employed for gas sensing applications. Organic semiconductors can be divided into two categories: polymers and small molecule materials. Conducting Polymers can be prepared in solution form, and therefore their films can be prepared using spin coating, drop casting, screen printing etc. On the other hand, thin films of molecular semiconductor can be prepared by thermal evaporation.

Organic semiconductors offer many advantages in comparison to their inorganic counterparts, which make them particularly attractive for sensor applications. First, they can be deposited at or near room temperature on large area surfaces and are compatible with mechanically flexible supports such as paper and plastic. This enables their use in roll-to-roll fabrication techniques, which can dramatically decrease manufacturing costs: an important attribute for disposable sensors. Second, the properties of organic semiconductors can be reversibly tailored by interaction with various analytes. Therefore these materials have the potential for fabrication of gas sensors with high sensitivity and selectivity.

Although a number of papers on the gas sensing properties of organic semiconductors have been reported in literature, there are only a few studies on flexible organic sensors. Flexible sensors have enormous applications in food preservation, environmental monitoring, wearable medical devices, smart fabrics etc. The flexible sensors based on *p*-type Cobalt Phthalocyanine *i.e.* a stable organic molecule and Poly [N-9′-heptadecanyl-2,7-carbazole-alt-5,5-(4′,7′-di-2-thienyl-2′,1′,3′-benzothiadiazole)] (abbreviated as PCDTBT), a new conducting polymer, have been fabricated. In order to make CoPc based flexible sensor, first thin films deposition conditions (such as films thickness, deposition rate, substrate temperature) were optimized to get highly crystalline films. The optimized parameter for synthesis of crystalline CoPc was found as: thickness ~ 20 nm, deposition rate: 0.2-0.5 Å/s and substrate temperature ~ 100°C. The detailed structural and charge transport characteristics of CoPc films deposited on flexible bi-axially oriented polyethylene terephthalate (BOPET) substrates were investigated. Synthesized CoPc films exhibited a preferential (*200*) orientation with a high charge carrier mobility of 118 $cm^2 V^{-1} s^{-1}$ (at 300 K). These films exhibited a reversible electrical resistance changes upon bending them to different radius of curvature. Charge carrier mobility in these films systematically decreases upon bending, which implies that bending reduces π- π interactions among molecules. The detailed study suggested that charge transport in CoPc films is governed by a bias dependent crossover from ohmic (J–V) to trap-free space-charge limited conduction (J–V^2). Further chemiresistive gas sensing characteristics of these well characterized cobalt phthalocyanine films were thoroughly investigated. Chemiresitive gas sensors work on the principle of change in resistance on exposure to gas. At room temperature, these films exhibited a reversible change in resistance on exposure to ammonia and hydrogen sulfide gases in the 5–50 ppm range along with high response (%), high selectivity and fast response / recovery. The chemiresistive sensing properties were found to improve (from 15 % to 25 % for 20 ppm of NH_3) significantly under bend conditions owing to creation of more numbers of interaction sites. In order to improve the sensitivity and selectivity of CoPc film towards H_2S, the surface modification of CoPc films was done with a thin layer (~ 1nm) of gold (Au). The surface morphology of the gold modified films shows that gold forms nano-islands over the CoPc surface. The Au – CoPc films exhibited very high charge carrier density at the surface due to (i) formation of hole accumulation layer owing to the difference in work function of Au and CoPc and (ii) enhanced adsorbed oxygen on the CoPc surface owing to spillover effect. Both of these effects make the Au–CoPc films more oxidative to the H_2S in comparison to pure CoPc films. The response of the films on exposure to H_2S is attributed to the shrinkage of the hole accumulation layer of CoPc due to electron transfer from adsorbed electron donor H_2S. The gas sensing characteristics of the films were found to be stable for the bending radius >20 mm. Although modifying the CoPc with Au has improved the response percentage (by nearly 1.5 times for 10 ppm of H_2S) as well as selectivity for the H_2S gas but the response time and recovery time of these hybrid films was high. Therefore in order to achieve a goal of high response (%) along with fast response / recovery, the CoPc films of varying thickness were prepared on ZnO nanowires (*n*-type semiconductor) coated BOPET substrate. It has been found that increasing thickness of CoPc (> 15 nm), hybrid films exhibited a transition from *n* to *p*-type conduction due to uniform coating of CoPc on ZnO. Such ZnO nanowires coated with CoPc films enhance the surface area of active CoPc layer resulting in high response (%) due to large numbers of interaction sites and fast response / recovery due to easy accessibility of these interaction sites. The x-ray photoelectron spectroscopy and work function measurement reveals electron transfer from ZnO to CoPc and formation of *p-n* junction with barrier height of 0.4 eV and depletion layer width of ~ 8.9 nm. The formation of *p-n* junction between CoPc and ZnO gives rise to very high response (%) towards H_2S gas due to enlargement of the depletion width.

In the present thesis work in addition to the chemiresistive gas sensor, organic Field effect transistors (FETs) based on PCDTBT and CoPc as actives layers and PMMA as dielectric layer were fabricated for gas sensor applications. PCDTBT and PMMA layers were deposited using spin coating, while CoPc layer was deposited using thermal evaporation under ultra high vacuum. It has been found that PCDTBT based FETs were found to be selective towards ppm level of NO_2 gas. In FET geometry, we have the additional advantage of tailoring the sensor characteristics using the gate terminal. The response (%) of fabricated device towards NO_2 gas was studied as a function of gate voltage (V_{GS}) and it has been found that response (%) decreases with increasing V_{GS}, which is attributed to more influence of gate voltage in controlling FETs characteristics. As both PCDTBT and CoPc based FETs were made on flexible BOPET substrate, therefore their electromechanical properties were also investigated by fixing the edges of flexible device between the arms of a vernier calliper and the device was bent to different radii of curvatures by moving the arms of the vernier calliper. The mobilities of the both devices were of the order 10^{-5} $cm^2V^{-1}s^{-1}$ but it was found that the mobility do not degrade much under bent conditions, highlighting the important application of such devices in flexible gas sensors.

In summary, it has been demonstrated that the gas sensing characteristics such as response (%), selectivity, response / recovery times of a *p*-type organic semiconductor based gas sensor can be improved by enhancing the specific surface area of active organic layer and formation of junction with n-type material. The simplest approach to achieve this is the synthesis of a porous network of *n*-type materials that acts like a core and modification this *n*-type core with a thin layer of *p*-type organic semiconductor. In the present work it has also been shown that in organic chemical field effect transistor the gate voltage can also be used to tune the response (%) towards the target gas.

List of Figures

List of Tables

List of frequently used abbreviations

Abbreviation	**Meaning**
AFM	Atomic Force Microscope
BGTC	Bottom gate top contact
BOPET	Biaxially oriented polyethylene terephthalate
ChemFET	Chemical sensitive field effect transistor
CoPc	Cobalt Phthalocyanine
CPs	Conducting Polymers
CuPc	Copper Phthalocyanine
HOMO	Highest occupied molecular orbital
ITO	Indium tin oxide
LDL	Lowest detection limit
LTEL	Long term exposure limit
LUMO	Lowest unoccupied molecular orbital
MBE	Molecular beam epitaxy
MDL	Minimum detection limit
MPcs	Metal phthalocyanines
NWs	Nanowires
OFET	Organic field effect transistor
OSC	Organic semiconductor
OTFTs	Organic thin film transistors
PANI	Polyaniline
PCDTBT	Poly [N-9′ heptadecanyl-2, 7-carbazole-alt-5, 5-(4′7′-di-2-thienyl 2′, 1′, 3′ benzothiadiazole)]
PET	Polyethylene terephthalate
PL	Photoluminescence spectrum
PMMA	Poly (methyl methacrylate)
ppb	Parts per billion
ppm	parts per million
PPy	Polypyrrole
PTh	Polythiophene
QCM	Quartz crystal microbalance
SCLC	Space charge limited current
SEM	Scanning electron microscope
STEL	Short term exposure limit
TEM	Transmission electron microscope
TFTs	Thin film transistors
TGBC	Top gate bottom contact
TGTC	Top gate top contact
TWA	Time weighted average
UHV	Ultra high vacuum
UV/Vis	Ultra-violet visible spectrum
VOCs	Volatile organic compounds
XPS	X ray photoelectron spectroscopy
XRD	X ray diffraction

List of notations and variables

Notation	Meaning
C_{diel}	Gate dielectric capacitance per unit area
E_g	Energy gap
I_{DS}	Drain to source current
J	Current density
K	Dielectric constant
L	Gate length
λ	Wavelength
μ_{sat}	Mobility in saturation region
N_{it}	Interface trap density
r	Bending radius
ΔR	Change in resistance
R_0	Base resistance
R_a	Resistance in air
R_{air}	Resistance in air
R_g	Resistance in the presence of gas
R_{gas}	Resistance in the presence of gas
S	Sensor Response
S	Subthreshold slope
T	Temperature
V	Voltage
V_{DS}	Drain to source voltage
V_{GS}	Gate to source voltage
V_{so}	Switch on voltage
V_{Th}	Threshold Voltage
W	Depletion region width
W	Gate width

List of symbols / formulae

Symbol/formulae	Meaning
Au	Gold
Co	Cobalt
D_2O	Deuterium oxide (Heavy water)
H_2S	Hydrogen Sulfide
NH_3	Ammonia
NO	Nitric Oxide
NO_2	Nitrogen dioxide
ZnO	Zinc Oxide

CHAPTER 1

Introduction

1.1 Introduction

In the last two decades organic semiconductors have witnessed wide popularity in the scientific community. The various advantageous features of organic semiconductors such as ease of tailoring the functionality of organic semiconductors, easy processing, and tendency to be compatible with a variety of substrates including flexible plastic substrates has enabled the development of organic semiconductor based devices that can substitute the abundant inorganic devices in various applications. Various recent innovations in both syntheses of organic semiconductors and device development have resulted in remarkable improvements in both the performance and the environmental stability of organic semiconductor devices, which had initially hindered their commercial applications. The above said interesting properties of organic semiconductors can be harnessed for the development of gas sensors *i.e.* a device used to sense chemical or biological species in the environment, in the human body, in food and water, or elsewhere [1]. For example, chemical scientists envision diagnostic sensors that detect changes in biomarker levels (*e.g.*, changes in glucose levels in people with diabetes); environmental sensors that detect toxins in food or water; and national security sensors that detect trinitrotoluene (TNT) or other explosives. These sensors based on organic materials are chemically compatible with biological systems that inorganic material based devices are not.

Traditionally metal oxide semiconductor (*e.g.*, SnO_2, ZnO, CuO, TiO_2) based gas sensors have been used to fabricate chemiresistive type gas sensors. Most of the metal oxide based chemiresistive sensors operate at high temperature in the range 200°C-500°C [2]. These metal oxide based sensors, being rigid and unadaptable are poorly integrated into low-cost, battery operated flexible devices intended for the future applications in the internet of things. On the other hand organic semiconductors present materials which are stretchable, flexible and mechanically soft. Organic Semiconductors due to their room temperature gas sensing operation propose a solution to the problems imposed by inorganic ones. Therefore a growing attention has been paid to the use of organic materials and printing technologies allowing the preparation of thin organic sensitive layers or organic based electrolytes for printed chemiresistors, Chemical sensitive field effect transistors (ChemFET) or electrochemical sensors, respectively. Since these organic semiconductors based sensors usually work at room temperature, exhibit low power consumption and can be fabricated on flexible substrates by using cost effective printed techniques. This fact makes them attractive for logistic sector (cold chain, monitoring of perishable goods during transport) and multi-sensor devices and systems which monitor environmental air-pollution or protect humans from dangerous concentrations of hazardous and toxic gases.

1.2 Requirement for gas Sensors

The living standards of human race in the 21st century grew at a remarkable pace owing to the industrial revolution. Industrialization demands the specific gas detection and monitoring for the benefit of the society. These include hydrocarbons (for the exploration of oil fields), oxygen (for breathable atmospheres and combustion processes *e.g.* in boilers and internal combustion engines) and, other various gaseous chemicals (for medical applications, manufacturing of different chemicals etc.). However, the extensive industrialization has a negative aspect as well, that is, emission of gases that pollute environment and pose risk to the public health. Thus, there is a need of gas sensors to measure the pollution level in the atmosphere so that appropriate steps can be followed to control the pollution. Gas Sensors play an important role in various modern technological processes where control and analysis of evolved gases are necessary. Not only in industries, gas sensors may be used to detect toxic gases both outdoor and indoor including the work place. Even at very low concentration toxic gases are very dangerous to human health. The principal gases that cause air pollution from automobiles are nitrogen oxides, NO_x (NO and NO_2), and carbon monoxide (CO). In addition, NO_x gases and sulphur oxides (SO_x) emitted from coal- fired plants cause acid rain and global warming and produce ozone that leads to serious metropolitan smog from photochemical reactions; these must be detected and reduced. Sometimes in industry the uses of toxic gases are necessary to perform various processes and release of such gases also pollutes the atmosphere. For example in the heavy water production plants large amount of reducing gases such as H_2S and NH_3 is used for D_2O enrichment. H_2S is also released into the air as a product of decomposition of dead plant and animal material in limited supply of oxygen. Anthropogenic releases of H_2S into the air result primarily from the extraction and refining of oil and natural gas and from paper and pulp manufacturing. Ammonia, NH_3 which is used in pharmaceuticals at a large scale is another toxic gas which is respiratory tract irritant. In addition, a great amount of volatile organic compounds are also being produced by construction materials and households; in this context formaldehyde is the most dangerous among indoor pollutants as it harms all living organisms. Table 1.1 lists some of these toxic gases, their short term exposure limit (STEL) time weighted average (TWA) for 15 minutes duration; long term exposure limit (LTEL) time weighted average for 8 hour duration; their sources and health hazards.

Table 1.1: List of some toxic gases, their toxic limits and origin [2].

Sr. No.	Gas	Characteristic		LTEL (8-hour TWA)	STEL (15 minutes TWA)	Present in/exposure from/source	Health hazards / effected body parts
		Colour	Odour				
1	H_2S	colourless	Rotten egg smell	10	15	Sewer lines, manholes , underground lines, oil & natural gas refineries	tearing of the eyes, respiratory tract irritation
2	NO_2	Reddish brown	Irritating, sharp odor	3	5	Combustion processes	Irritates lungs, shortness of breath, pulmonary edema
3	NO	colourless gas or red-brown gas	odorless	25	-	Carbon arc, Oxyacetylene torch, Cellulose nitrate combustion, Diesel exhaust, lightning	Cough, shortness of breath, painful breathing, chest pains increased breathing rate, weakness, methemoglobinemia
4	NH_3	colourless	Strong, pungent odour	25	35	Fertilizers, synthetic fibres, refrigeration & air-conditioning equipment	Burning of nose, throat and respiratory tract, burns or open sores in eyes
5	Cl_2	Yellow-green	strong, distinctive odor	0.5	1	Manufacturing solvents, pesticides, synthetic rubber, refrigerants, paper industry	burning sensation in nose, throat and eyes, Pulmonary edema
6	CO	colourless	odourless	50	300	Incomplete combustion of natural gas, LPG, Coal, kerosene diesel, etc.	Impaired vision and coordination, unconsciousness, headache, dizziness, nausea & vomiting
7	HCOH	colourless	Pungent odour	0.75	2	Composite wood products, automobiles, Burning natural gas or kerosene,	Eye , nose and throat irritation, coughing and breathing difficulties
8	CH_3COCH_3	colourless	Distinctive fruity or mint-like odour	500	250	Forest fires, biomass burning,	Respiratory tract, eyes
9	C_2H_5OH	colourless	slight chemical odour	1000	-	Drugs and Pharmaceuticals , resins , lacquers industries	Nausea, vomiting, dizziness, respiratory paralysis
10	HCl	colourless	irritating pungent odour	1	5	coal-burning power plants, incineration of plastics such as PVC	Irritation of respiratory tract with burning, choking and coughing, eye irritation, severe burns
11	SO_2	colourless	irritating smell	2	5	Volcanic activity, Burning of fossil fuels	Nose, throat and lung irritation, with coughing, and severe shortness of breath (pulmonary edema)
12	PH_3	Colourless	garlic-like odour	-	0.3	reduction of phosphate in decaying organic matter, fumigation	headache, restlessness, dizziness, loss of feeling, hypotension, irregular heartbeat

1.3 Types of gas sensors

A gas sensor device typically consists of two main parts namely sensitive or active layer and the signal measurement / processing unit *i.e.* transducer. The active layer is the heart of sensor that physically or chemically interacts with the test gas molecule; this interaction is the binding of the gas molecules to the active layer. The transducer is the part of the sensor that converts this binding into a meaningful electrical output. Depending on the readout of transducers, gas sensors can be classified as follows:

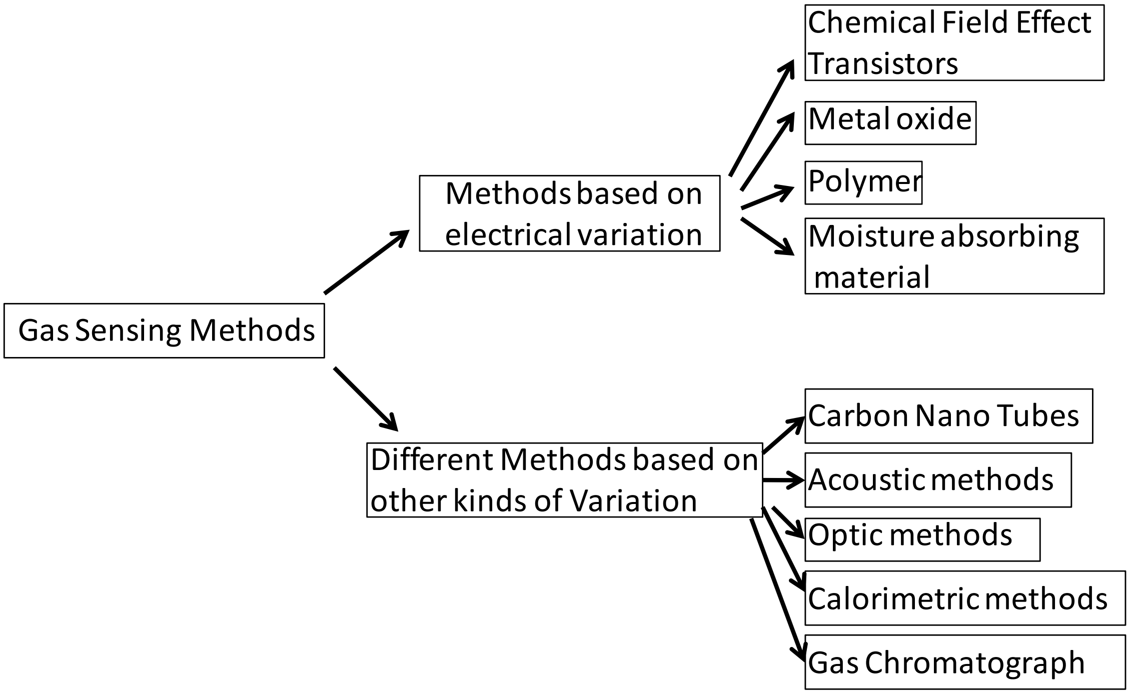

Figure 1.1: Schematic showing different way of detecting the gas molecules using a sensor.

Gas Sensors can be graded according to the approach we use for gas sensor design. According to this approach, gas detector comes in two main types: portable devices and fixed gas detectors. The first is used to monitor the atmosphere around personnel and is worn on clothing or on a belt/harness. The second, fixed, type may be used for detection of one or more gas types. Fixed type detectors are usually mounted near the process area of a plant or control room.

Table 1.2: Classification of Gas Sensors

Type of sensor	Gas Sensor	Detection Principle
Solid State Sensors	Chemiresistive	A change in conductivity of semiconductor is measured when it interacts with the analyzing gas.
	Chemical field effect transistors (ChemFET)	Current –Voltage (I-V) curves of a field effect transistor (FET) are sensitive to a gas when it interacts with gate.
	Calorimetric	The concentration of combustible gas is measured by detecting the temperature rise resulting from the oxidation process on a catalytic element.
	Potentiometric	The signal is measured as the potential difference (voltage) between the working electrode and the reference electrode. The working electrode's potential must depend on the concentration of the analyte in the gas phase.
	Amperometric	Diffusion limited current of an ionic conductor is proportional to the gas concentration.
Mass Sensitive Sensors	Acoustic	Change in frequency of surface-acoustic waves (SAW) excited on a quartz or piezoelectric substrate upon ad- or absorption of gas in a suitable sorption layer (*e.g.* metals, polymers).
	Microelectromechanical systems (MEMs) based sensors	Change in mechanical bending of micro- or nanocantilevers upon adsorption of gas.
Optical Sensors	Surface Plasmon Resonance (SPR)	Change in SPR signals is proportional to the refractive index close to the sensor surface and, is therefore, related to the amount of bound gas molecules.
	Optodes	The change of optical properties measured can base on absorbance, reflectance, luminescence, light polarization, Raman and others.

1.4 Basic Characteristics of a Chemiresistive Gas Sensors

The electrical resistance of a chemiresistive sensor changes drastically when exposed to the molecules of analyzing gas. Increase or decrease in resistance depends on the nature of the active layer material (*p*-type or *n*-type) and the kind of analyzing gas (oxidizing or reducing). For example a p-type semiconductor will exhibit the rise of resistance on exposing it to the reducing gas (such as H_2S, NH_3 etc) and resistance will drop if the gas is oxidising (Cl_2, NO_2 etc) in nature. The response curve of a sensor is characterized by the following parameters [2]:

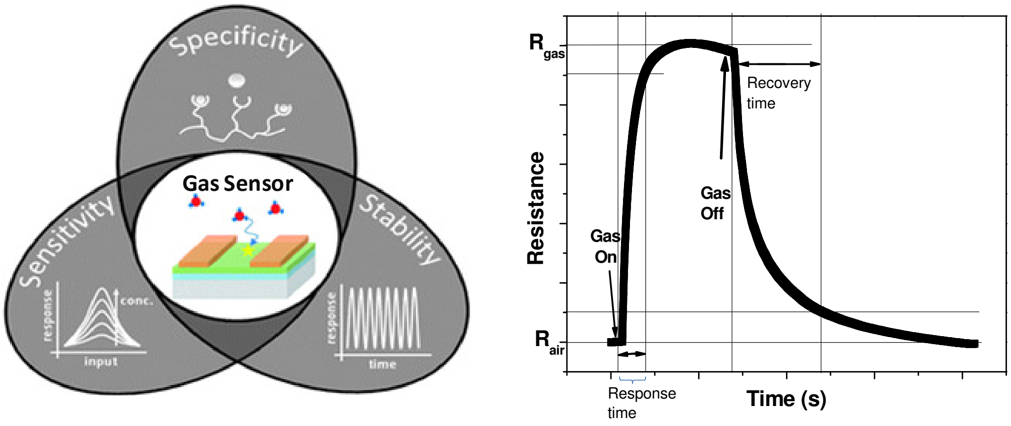

Figure 1.2: Key Requirements and Performance parameters of a chemiresistive gas sensor.

I. Sensitivity: The sensitivity (S) of a sensor can be defined in many ways. The often used definitions are the following:

   a. A ratio of resistance of active layer in air to that in gas *i.e.* $S = R_{air}/R_{gas}$. A high value of S indicates that the material is a very good sensor.

   b. $S\ (\%) = 100 \times (R_{air} - R_{gas})/R_{air}$. A positive value of S implies film resistance decreases on gas exposure and vice versa.

II. Selectivity: Usually most chemiresistive sensors exhibit significantly high value of sensitivity for many gases under similar operating conditions. Thus the selectivity or specifity of a sensor towards analyzing gas is expressed in terms of dimension that compares the concentration of the corresponding interfering gas that produces the same sensor signal. This factor is obtained by:

$$Selectvity = \frac{sensitivity\ of\ the\ sensor\ towards\ interfering\ gas}{sensitivity\ towards\ the\ desired\ gas}$$

III. Response time: The response time is the time interval over which resistance attains a fixed percentage (usually 90 %) of the final value when the sensor is exposed to full scale concentration of the gas. A small value of response time is indicative of a good sensor.

IV. Recovery time: This is the time interval over which sensor resistance reduces to 10 % of the saturation value when the sensor is exposed to full-scale concentration of the gas and then placed in the clean air.

V. Long term stability: This is the ability of the sensor to maintain its properties when operated continuously for long durations in hostile environment. The good sensors are operated to work for several years without showing a drift in any of the above four parameters.

1.5 Organic Semiconductors

Organic semiconductors are classified into two categories: (i) low molecular-weight or small organic molecules and (ii) conducting polymers [3]. From a chemical structure point of view there are big differences between these two kinds of materials and this is reflected also in technological aspects. Polymeric macro-molecules are constituted by the repetition of a fundamental unit, the monomer, and are soluble in organic solvents, so they can be processed solution wise. Small organic molecules and can be further divided into two sub-classes: pigments which are insoluble in organic solvents and dyes, which are soluble. As a result of their chemical properties, polymers can be solution processed, for example being spin-coated from a solution of appropriate organic solvents, while small molecular materials are usually sublimated and in some cases can be solution processed.

Semiconductor behaviour in organic materials is possible because carbon atom has the ability to form sp^2 hybridization where the sp^2 orbitals are formed within a plane and the p_z orbitals are in the plane perpendicular to it [4]. For organic molecules, a σ bond is formed between two carbon atoms by axial overlap of two sp^2 hybrid orbitals. This creates a large energy difference between the occupied bonding orbitals and the unoccupied antibonding orbitals. This large energy difference leads to insulating properties and thus longer chain of carbon atoms would have larger gap between the highest occupied molecular orbital (HOMO) and the lowest unoccupied molecular orbital (LUMO). However, in sp^2 hybridization, the unhybridized p_z orbitals form additional π bonds perpendicular to the plane of sigma bonds. These bonds have much smaller difference between the HOMO and LUMO energy levels leading to semiconducting properties.

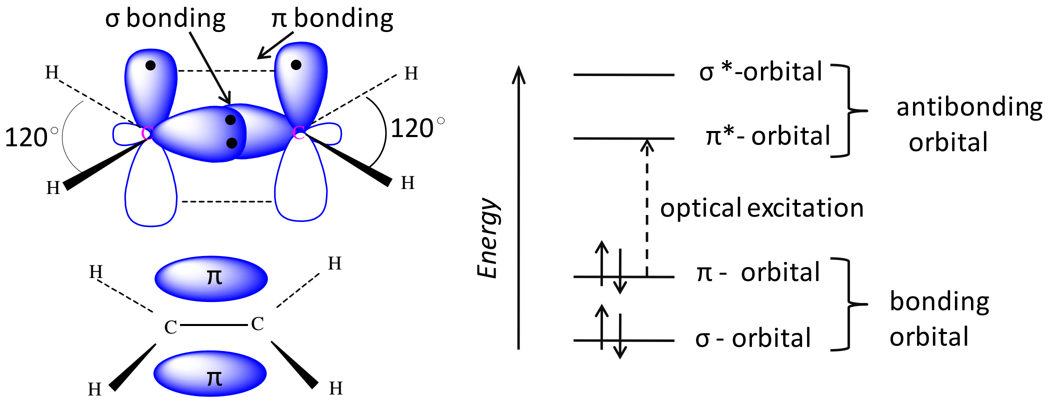

Figure 1.3: Illustration of formation of band gap formation using ethylene molecule

In organic semiconductors, this energetic difference of HOMO and LUMO levels constitutes the energy gap of the material. The size of this gap depends on the degree of delocalization of π electrons, which, in turn, depends on the conjugation of the molecule. As the conjugation of the molecule or polymer increases , the π electrons become more delocalized; the energetic difference between subsequent discrete energy states can be explained and visualized by an analogue of the particle in a box model of quantum physics by considering that this energetic difference scales with the extent of delocalization according to : $E \propto \frac{1}{L^2}$ where E is the energetic difference or the HOMO-LUMO energy gap and L is the size of the box in the typical model or can be thought as the length of delocalization in a 1-dimensional π system.

1.5.1 Basic Properties of Organic Semiconductors

- Both the classes of organic semiconductors have in common a system of π conjugated molecules. In a π conjugated system, there is a unhybridized *p* orbital present at a minimum of three consecutive carbon atoms in the molecular backbone. The overlap of *p* wavefunctions of each carbon atom with the one from the nearest neighbour is what allows to have electron delocalization along the molecular backbone. Both the polymers and molecular materials have in common extended delocalized π electron system which allows to transport charge carriers [5, 6].

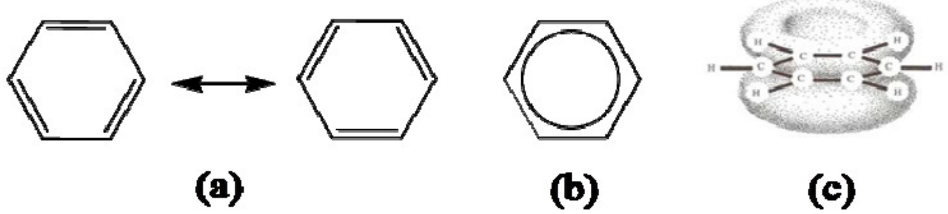

Figure 1.4: Illustrating charge delocalization in benzene

- In organic materials, defects that lead to states made up of non bonding orbitals usually end up being in the σ manifold rather than the π manifold of states. As a result, defect states typically occur in the energy gap of the σ manifold, as opposed to energy gap in the π manifold, which is the real gap of the material. Thus, organic semiconductors are relatively insensitive to defects [5].

- Organic Semiconductors have two important peculiarities as compared to their inorganic counterparts. One is the existence of well defined spin states (singlet and triplet) as in isolated molecules which has important consequence for photo- physics of these materials. A second important difference arises from the fact that optical excitations (exciton) are usually localized on one molecule and have considerable binding energy. In photovoltaic cells this amount of energy has to be overcome before a pair of independent positive and negative charge carriers is generated.

The charge transport carrier transport mechanism in organic semiconductors can fall between two extreme cases: band or hopping transport. Band transport is typically observed in highly purified molecular crystals at low temperatures. However, since electronic delocalization is weak the bandwidth is small in comparison to inorganic semiconductors (typically a few kT at room temperature). Therefore room temperature mobilities in molecular crystals reach only values in the range 1 to 10 cm^2/Vs. As a characteristic feature of band transport the temperature dependence of mobility follows a power law behaviour $\mu \propto T^{-n}$ with n =1...3 upon going to lower temperature. However, in the presence of traps significant deviations from such behaviour are observed.

In the other extreme case of an amorphous organic solid hopping transport prevails which leads to much lower mobility values (at best around 10^{-3} cm^2/V-s, in many cases however much less).Instead of a power law the dependence then shows an activated behaviour with activation energies *ΔE* between 0.4 and 0.5 eV and the mobility also depends on the applied electric field.

- In case of organic materials the current density is not linearly dependent on carrier density and electric field since both the carrier density and mobility depend on the electric field. The mobility strongly depends on the purity and growth conditions. It is nowadays approaching towards amorphous silicon but it is order of magnitude less than crystalline silicon. It is also to be noted that intrinsic carrier density in pure organic semiconductors is many orders of magnitude lower than Si. So in order to enhance the carrier density in organic semiconductor can be following routes are used:

  (i) (electro-) chemical doping,
  (ii) field-effect doping,
  (iii) carrier generation from contacts, and
  (iv) photo generation of carriers

1.5.2 Comparison between Organic and Inorganic Semiconductors

In inorganic semiconductors, such as Si or Ge, the strong covalent bonding among atoms leads to formation of allowed valence and conduction bands, which are separated by a forbidden energy gap. Also the long-range ordering leads to delocalization of the electronic states. By thermal activation or photoexcitation, free electrons are generated in the conduction band, leaving behind positively charged holes in the valence band. However, in the case of organic solids, while intramolecular interactions are mainly covalent, intermolecular interactions are rather weak because the molecule-molecule interactions are through Van der Waals forces. As a result, the transport bands in organic solids are much narrower than those in inorganic semiconductors. Also disorders present in the organic solid can easily disrupt the band structure. Thus in molecular solids, the concept of allowed energy bands have limited validity and excitations as well as interactions localized on individual molecules play a predominant role.

The covalent, periodic structure of inorganic semiconductor results in band energy *i.e.*, conduction band and valence band. In general, organic semiconductors don't have bands but discrete energy levels (HOMO, LUMO analogous to the edges of valence and conduction band). Another consequence is doping effect. In inorganic semiconductor, atomic doping normally just increases carrier density and does not interfere the band structure. On the other hand, molecular doping in (weak Van der Waals interaction) organic semiconductor affects the molecular packing and assembly, hence the morphology and electronic properties of the film such as mobility, density of state distribution etc.

It is noticed that the effective masses of charge carriers in organic materials are much greater than that of the inorganic materials probably because of the strong bonding inside the molecules and weak intermolecular bonding among the molecules so that the electrons are largely localised in the molecules. This is in contrary to inorganic materials where the interatomic forces are large causing strong overlapping of the atomic orbitals and strong electron delocalization.

An exciton can be categorised as Frenkel exciton if the electron – hole pair is located on the same molecular unit, or a Wannier- Mott exciton if the pair spans over a few adjacent molecular units, also known as transfer excitons. Unlike inorganic semiconductors, the excitons in organic semiconductors are mostly Frenkel exciton, which means that the exciton is localised on a single polymer unit or a small molecule.

Table 1.3: Comparison of inorganic semiconductors with organic semiconductors

Parameter	**Inorganic Semiconductors**	**Organic Semiconductors**
Bonding	Ionic, Covalent, Metallic (2-4 eV)	Ionic or covalent within molecule (intramolecular), but the solid is held together by weak Van-der Waal force (0.01eV). Therefore solid's behaviour to a larger extent governed by individual molecules (except increased vibrational modes)
Charge carrier	Electrons, holes, ions	Polarons, excitons (though neutral)
Effective mass	m_e or less	$(10^2 - 10^3)\ m_e$
Transport type	Band	Hopping
Mobility	$10^2 – 10^4$ cm^2/V-s	10^{-6}- 10^2 cm^2/V-s
Exciton	Wannier-Mott	Frenkel, Charge transfer
Luminescence	Band to band recombination at practical temperature	Exciton recombination

1.5.3 Applications of Organic Semiconductors

(a) Organic Display Technology

Organic light-emitting diodes (OLEDs) are built from one or more layers of organic and hybrid materials sandwiched between two electrodes (*e.g.*, indium tin oxide), all on a plastic or other substrate. Unlike other display technologies, which require a backlight in order for the display to show, OLEDs generate their own light via electroluminescence and therefore they do not require backlight. They require less power and are more energy-efficient than backlight- dependent display technology. TVs based on OLED technology are not only more spectacular than previous technologies in respect to crisper colours and sharper contrasts but also, lighter, thinner and more efficient.

(b) Organic Photovoltaics

Organic photovoltaics (OPVs), or organic solar cells, now a days are viewed as one of the most exciting near future applications of organic electronics, not necessarily as a replacement for silicon photovoltaics, rather because of the unique ways that OPVs can be used due to their flexibility, large-area coverage, and low cost.

(c) Organic Field Effect transistor Technology (OFET)

Transistors are the basic building block of electronic devices, either as an amplifier or as a switch. Although Organic field effect transistors cannot achieve mobility comparable to traditional semiconductors such as Si or GaAs, OFETs have several unique properties not shared by conventional transistors, most notably their flexibility. Because OFETs can be manufactured at or near room temperature, they enable the manufacture of integrated circuits on plastic or other flexible substrate that would otherwise not withstand the high temperature conditions of silicon- based device manufacture. OFETs are also highly sensitive to specific biological and chemical agents, making them excellent candidate for biomedical sensors and devices interfering with biological systems.

1.6 Molecular Semiconductors

The semiconducting properties of molecular materials can be explained from the covalent bonding between carbon atoms, σ bonds made from the sp^2 hybridisation of 3 valence atomic orbitals of the carbon atom : $2s$, $2p_x$ and $2p_y$. For such a hybridization state, the fourth orbital $2p_z$ lies perpendicular to the σ- bond plane. It is the lateral overlap of these out of plane $2p_z$ atomic orbitals, which gives the π bonds. Absorption spectra display the existence of strong absorption bands in the range of 400 and 800 nm caused by the π - π * transition of conjugated macro cycle of 18 π electrons. The common electronic feature of molecular semiconductors is the π- conjugated system, which is formed by the overlap of p_z-

orbitals. Due to the orbital overlap, the π-electrons are delocalized within the molecule and the energy gap between the highest occupied molecular orbital (HOMO) and the lowest unoccupied molecular orbital (LUMO) is small, *i.e.*, exhibiting transition frequencies within the visible range. Activation of free electrons by photo excitation or chemical doping can lead to a tremendous increase of the electric conductivity from about 10^{-12}Scm^{-1} to values in the range 10^2 Scm^{-1}, which indicates semiconducting character of the molecular solids.

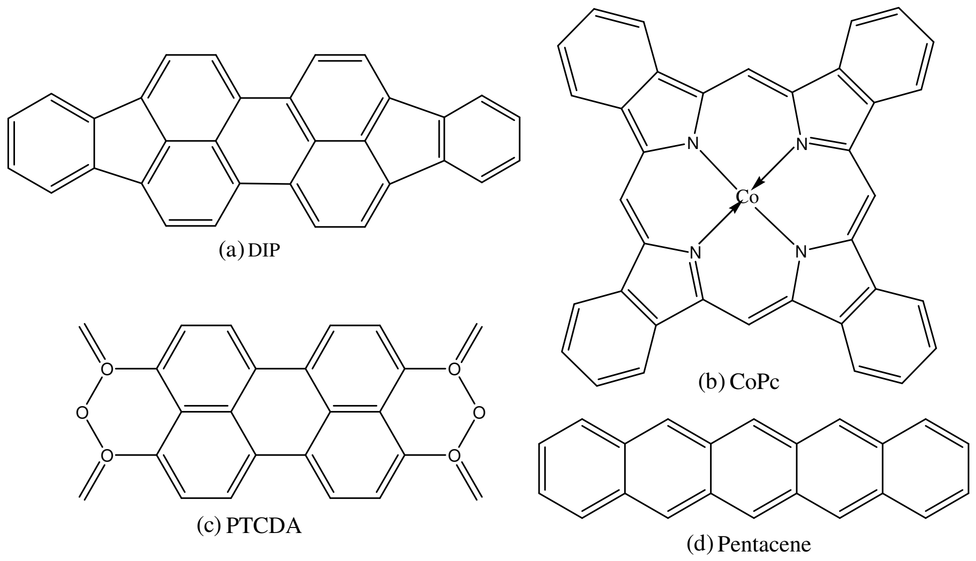

(a) DIP

(b) CoPc

(c) PTCDA

(d) Pentacene

Figure 1.5: Examples of some common molecular semiconductors

The structure of some of the prominent molecular semiconductors are shown in Fig.1.5. These molecular semiconductors are Diindenoperylene (DIP), Cobalt Phthalocyanine (CoPc), Perylenetetracarboxylic dianhydride (PTCDA), Pentacene. Among various molecular semiconductors mentioned above, metal phthalocyanines (MPcs) and metal-free derivative has been the subject of extensive study. MPcs have been synthesized with nearly every transition metal in the periodic table. MPcs have been used as dyes, catalysts, photovoltaics and gas sensors. MPcs chemical properties may be tuned through variation of the metal centre as well as functionalization of the macrocycle. In air, MPcs undergo no noticeable degradation up to several hundred centigrade and in vacuum do not decompose below 900°C.

MPcs are relatively economical as compared to other materials in the category of small organic molecules. Although Phthalocyanines have been synthesized with nearly every transition metal in the periodic table, the phthalocyanine ring itself has been modified by using differing template sizes, as well as organic functional groups. The standard phthalocyanine ring contains four diiminoisoindolenine units but subphthalocyanines with three such subunits have been prepared around small boron cations, and superphthalocyanines with five subunits have been templated around large uranium cations. The UV/Vis spectra of MPcs show absorption peaks at the Soret (B) band (λ = 300-350 nm) and the Q band (λ = 600-700 nm) [7]. In addition to that minor absorption peaks are present below λ = 300 nm, designated the N, L and C bands. The Q band is attributed to π- π^* transitions of the phthalocyanine ring [7, 8].

Standard MPcs are highly crystalline materials. MPcs are known to crystallize in herringbone-type structure, with the *z*-axis in the direction of the metal centre column. Standard MPcs consist of a central metal atom (*e.g.* Co, Cu, Fe etc.) having square-planar coordination with four pyrrolic nitrogen atoms. The most common MPcs (M = H_2, Fe, Co, Ni, Cu, Zn) exhibit two monoclinic crystalline phases, denoted as α and β phases. The stabilities

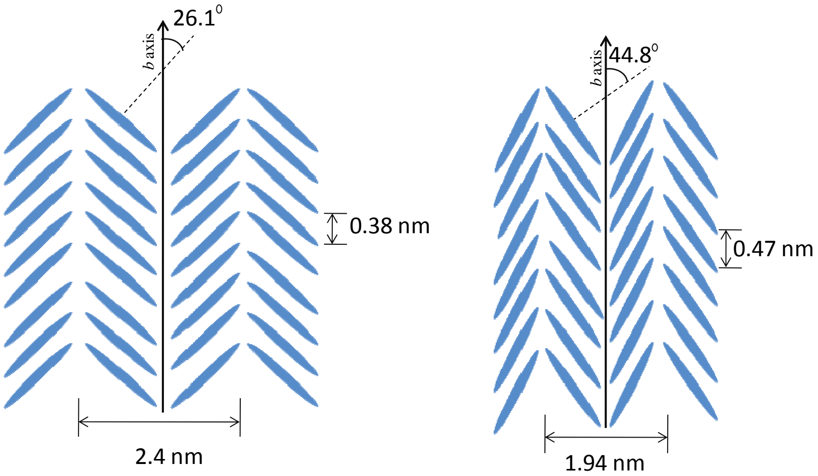

Figure 1.6: Schematics of molecular arrangement in FePc crystals in (a) α-FePc and (b) β-FePc.

of the two phases are temperature dependent, with α phase forming at lower temperatures (below 100°C) and β phase forming at higher temperature (above 100°C). These phases differ in the tilt angle of the molecular plane to the stack axis, the phase has a tilt angle of 26.5° and the β phase has a tilt angle of 46.8°.These crystal forms are adopted by the large number of unsubstituted MPcs that are essentially planar; however, phthalocyanines with large central metals (PbPc), axially coordinating ligands (TiOPc), or lanthanide bis (phthalocyanines) have unique crystal structures. Molecular arrangements in the direction of charge transport and morphology control are important for applications in molecular electronics and gas sensing technologies. For example, higher mobilities have been achieved in organic field effect transistor (OFET) of CuPc when the molecular stacking axis is oriented parallel to the electric field as opposed to perpendicular to the field or randomly oriented. Porous MPc films with larger grain structures are found to respond faster and more sensitively to analyte vapours, but these sensors exhibit larger current drifts and are less reproducible.

Thin films of MPcs for device applications can be prepared using a variety of methods. The thermal stability of MPcs makes sublimation the most popular method for film deposition, which is capable of producing a wide variety of physical structures. In particular, organic molecular beam epitaxy (OMBE) produces extremely well-controlled films ideal for gas sensing applications. Soluble functionalized phthalocyanines may be deposited by spin – coating, which is an inexpensive method for preparation of nanoscale films. Films may also be produced using Langmuir - Blodgett techniques. Structural control is important for thin film applications as it may affect the charge transport and gas sensing behaviour of MPcs based devices. MPcs films form agglomeration of small crystalline grains with grain diameter ranging from a few tens of nm to a few microns. MPc grain size is strongly affected by the deposition method, films-substrate interaction, substrate temperature during deposition, deposition rate and post deposition annealing.

The growth mechanisms of thin films in case of inorganic semiconductor are well known and classified into three modes depending on the relative surface energy of surface-to-film: layer-by-layer growth (Frank-van der Merwe mode), island growth (Volmer-Weber mode), mixed growth (Stranski - Krastanov mode). While these growth modes may be applicable to organic thin films, there are issues specific to organic molecules, which can lead altogether to different growth behaviour. The most fundamental difference between growth of inorganic and organic films is that the organic molecules are 'extended objects' and thus have internal degrees of freedom, that is, orientational and vibrational degrees of freedom. The orientational degrees of freedom allows molecules to adsorb at the surface of the substrate in 'lying-down' or 'standing up' configurations that may lead to altogether different growth mechanisms. Similarly, the vibrational degrees of freedom can influence the interaction of molecule with the surface and thermalization upon adsorption and subsequent diffusion. Other factors affecting growth mechanisms of organic films may include low symmetries of the molecular crystal structures polymorphism, kinetics barriers, and a delicate balance between the two types of non-covalent interactions at the interface, that is molecule-molecule and molecule-substrate. These issues are a function of different processing parameters such as substrate temperature, rate of deposition, annealing time and substrate material.

1.6.1 Electrical Conductivity of Metal Phthalocyanines

Majority of MPcs exhibit *p*-type conductivity and it has been observed that MPcs are highly resistive in dark, high vacuum environments. On exposure to air, their electrical conduction increases drastically [9]. The air induced conductivity in Phthalocyanine films has been attributed to different mechanisms. For polycrystalline films it is assumed that O_2 absorbs only at the air / MPc interface and at grain boundaries because the MPc structure is very tight and unaffected by exposure to air. It has been reported that the formation of charge transfer complexes by coordination of O_2 to MPc metal centres at the air / phthalocyanine interface leads to the formation of oxidized MPc $^+$ and O_2^- species and injection of hole charge carriers into the bulk solid [9].

$$MPc + O_2 \leftrightarrow (MPc + h^+) + O_2-$$

The presence of superoxide adduct of CoPc has been detected in several electron paramagnetic resonance (EPR) studies [10]. There is also evidence that weaker O_2 adsorption may occur on the four *meso* – nitrogens of free base H_2Pc, leading to conductivity increases that are not as large as those for the MPcs. The crystal structure of MPcs are generally unaffected by exposure to air, so it is assumed that this reaction occurs via adsorption of O_2 to surface MPc molecules. Gas effusion studies on ZnPc suggest a ratio of approximately one molecule for every phthalocyanines; correlation with capacitance-voltage plots suggests that only one superoxide adduct is present for every 10,000 O_2 molecules on the film.

1.6.2 Gas Sensing Mechanism in Metal Phthalocyanines

As discussed above in MPcs the electrical charge carriers are introduced by oxygen doping. As a surface dopant, oxygen occupies only a fraction of the binding sites on the MPc films; therefore interactions with analyte vapors in air could result in two different mechanisms of analyte binding (Fig. 1.7) [9].

Analytes could either bind to open surface metal coordination sites, or could compete with oxygen for occupied metal surface sites. There is additional possibility of weak binding (physisorption) to the organic region of the MPc molecule for non-coordinating analytes which may be governed by weak hydrophobic and possibly charge transfer interactions.

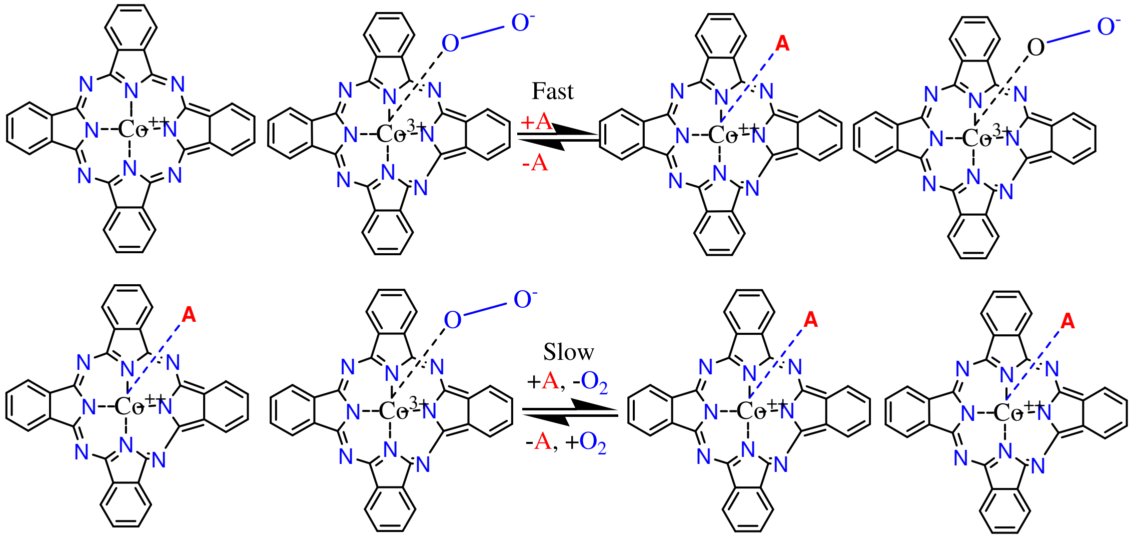

Figure 1.7: Chemisorption model of CoPc interaction with oxygen and coordinating analytes A.

When MPc films are exposed to oxidizing gases *viz.*; NO_x, charge transfer complexes, are formed and holes are injected which increase film currents. The interaction of Phthalocyanines with reducing gases, such as NH_3, has the opposite effect. Decreased current upon analyte binding to these films has been attributed to electron donation from reducing gas to trap charge carriers [11].

1.7 Conducting Polymers

Conducting (or conjugated) polymers (CPs) are promising materials for application in various sensors including chemical and biosensor owing to their light weight, easy processing, tuneable electronic and optic properties, large area fabrication and especially potential for fabricating flexible or wearable sensors [12, 13]. Intrinsic /doped as well as functionalized conducting polymers have been used as an active sensing element for fabricating sensors. In general, the fabrication of a sensor requires a good quality thick or thin film that is uniform and free of pin-holes. Several techniques such as dip coating, drop casting, layer- by- layer self assembly, Langmuir - Blodgett (LB) technique, spin coating, inkjet printing, gravure printing, slot die coating and screen printing were used to prepare high quality films of CPs for use in sensors. In addition, ultra-thin films of conducting polymers were also prepared using Langmuir–Blodgett or self-assembly technique. The interaction of analyte with the CPs is rather complex. Nevertheless, various models were suggested to understand the mechanism. These models are mainly described by adsorption isotherms that characterize the adsorption / desorption dynamic equilibrium of the system at a constant temperature. CPs are characterized by repeated units in which atomic valency is not satisfied by chemical bonds. The leftover valence electrons of adjacent carbon atoms overlap and form double bonds that give rise to *π*-bonds. *π*- electrons are delocalized over large segments of the polymer chain, which is responsible for the electronic properties of the conjugated polymers. Polymers can consist of ~ 10^4-10^6 monomers strung together to form a molecular chain. Typical conjugated polymers include straight chain units, five or six member rings, and all combination of these.

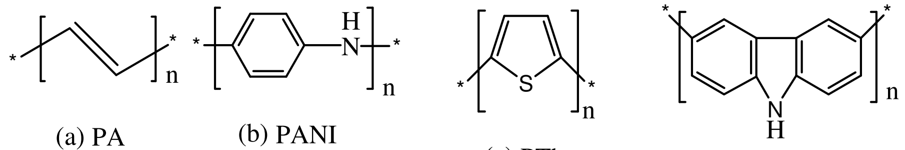

(a) PA (b) PANI (c) PTh (d) PCz

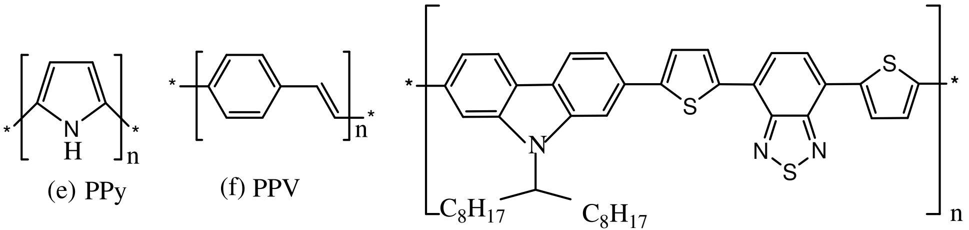

(e) PPy (f) PPV (g) PCDTBT

Figure 1.8: Examples of some common conducting polymers

Chemical structures of some of the commonly known CPs are shown in Fig. 1.8. These Conducting Polymers are Polyacetylene (PA), Polyaniline (PANI), Polythiophene (PTh), Polycarbazole (PCz), Polypyrrole (PPy), Poly (p-phenylene vinylene) (PPV), Poly [N-9′ heptadecanyl-2, 7-carbazole-alt-5, 5-(4′7′-di-2-thienyl 2′, 1′, 3′ benzothiadiazole)](PCDTBT).

The addition of heteroatom (atoms other than carbon and hydrogen) and side chains allow for an even larger variety in this class. Their electronic properties can be tailored by the synthesis, and their electrical conductivity can be varied from about 10^{-12}Scm^{-1} to values in excess of 10^5 Scm^{-1}. CPs are treated as quasi one-dimensional system, wherein the polymer chains are assumed to behave independently with one another, and their physical and chemical properties depend on interactions within the single chains. The π-bonding scheme of conjugated polymers decreases the gap between occupied HOMO and unoccupied LUMO states. The band gap of these polymers tends to lie between 1.5 and 3 eV, in the same range as that of inorganic semiconductors.

1.7.1 Electrical conductivity of Conducting Polymers

Conjugation is not just enough to get conductivity in the polymer. In order to achieve high conductivity in conducting polymers doping is necessary. Conducting polymers can be doped by redox reaction or by protonations. However when an electron is added to or withdrawn from a conducting polymer, a chain deformation takes place around the charge, which costs the elastic energy and puts the charge in lower electronic state. The competition between the elastic energy and electronic energy determines the size of the lattice deformation, which can be of the order of 20 polymer units long. The localized charged particle along with the chain deformation is known as polaron. The hopping of polaron governs the charge transport in conducting polymers. Sometimes the charge transport is described by bipolarons. Bipolarons are similar to polarons but having double charge. Instead of single charge that distorts the chain there are two charges, which are bound together by the same chain deformations. However due to coulomb repulsion these charges repel each other, but they remain bound due to common chain deformations.

1.7.2 Gas sensing mechanism of Conducting Polymers

The interaction of the analyte with the CPs can be understood using following mechanisms:

Sensors based on change in doping levels

The physical properties of Conducting Polymers strongly depend on their doping levels. In general, conducting polymers can be doped / dedoped (called *Primary doping*) by using either redox reaction or acid base reaction leading to transfer of electrons from / to the analyte and can be achieved chemically or electrochemically. Thus the doping levels of conducting polymers can be easily changed by chemical reactions with many analytes at room temperature, and this provides a simple technique to detect the analytes.

(i). Doping / dedoping by redox reactions

Most of the conducting polymers are doped / undoped by redox reactions; therefore, their doping level can be altered by transferring electrons from / to the analytes. Electron transferring can cause the changes in resistance and work function of the sensing material. The work function of a conducting polymer is defined as the minimal energy needed to remove an electron from bulk to vacuum energy level. This process occurred when PPy, PTh and in some case PANI films exposed in NH_3, NO_2, I_2, H_2S and other redox-active gases [14-22]. Electron acceptors, such as NO_2 and I_2, can remove electrons from the aromatic rings of conducting polymers. When this occurs at a *p*-type conducting polymer, the doping level as well as the electric conductance of the conducting polymer is enhanced. An opposite process will occur when detecting an electron donating gas. However, this mechanism has not been understood clearly. For example, NH_3 is an electron-donor; when PPy reacts with ammonia; its electric resistance dwindles down sharply. However, after exposing CP films with dry nitrogen or air, the resistance of the sensing layer can be totally or partly recovered. Following reactions are possibly involved in the ammonia sensing process [23, 24]:

$$PPy^{+} + \ddot{N}H_{3} \rightarrow PPy^{0} + NH_{3}{}^{+}\ Adsorption$$

$$PPy^{0} + \ddot{N}H_{3} \rightarrow PPy^{+} + \ddot{N}H_{3}\ Desorption$$

Based on this mechanism, all p-type conducting polymers are expected to dedope under ammonia atmosphere. In fact, some different phenomenon was observed in thin polycarbazole film sensor [25].

(ii).Doping / dedoping by acid / base reactions

As mentioned previously, doping can also be achieved by protonic (or acid) doping. Protonic acids are Brönsted acids, which can easily give the H^{+} ion while conjugated polymers with heteroatoms in the polymer chain may be treated as weak Brönsted base, which can take up proton. In contrast to doping / undoping involving redox reaction, the number of electrons associated with the polymer backbone remains unaltered in this process. However, the energy levels are rearranged so as to produce a polaron in CP backbone leading to a highly conducting form of the polymer [26]. Among several conjugated polymers available, PANI possesses a high *pKa* value (or basicity) because of which this polymer can be protonated very easily relative to other conjugated polymers. Additionally, reversible doping / dedoping, high conductivity and stability of PANI thin films have been found useful for sensing material for several gases such as NH_3, HCl, N_2H_4, [27, 28], humidity sensor [29], toxic chemicals.

PANI is a special conducting polymer since its doped state can be controlled by acid/ base reactions. This is widely used to detect acidic and basic gases. When exposed to ammonia gas, PANI undergoes dedoping by deprotonation:

The proton on –NH- groups was transferred to NH_3 molecules to from ammonium ions while PANI itself turned into its base form. This process is reversible, and in fact when ammonia atmosphere is removed, the ammonium ion can be decomposed to ammonia gas and proton.

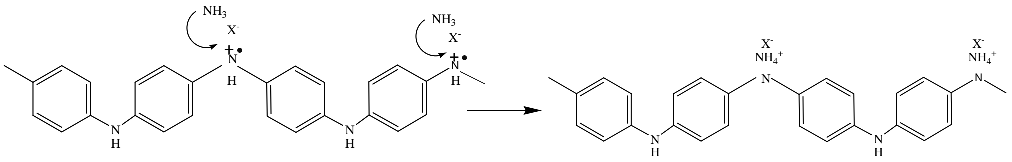

Figure 1.9: Protonation-Deprotonation mechanism of PANI to sense NH_3

Sensor based on Weak interactions:

CPs were widely investigated in sensors based on Lewis acids and bases detection method, however their interaction with neutral molecules, such as alcohols or other volatile organic compounds (VOCs) such as, benzene, toluene is not significant [30]. In addition to redox reactions, a partial charge transfer between the analyte and conducting polymer may result in formation of charge-transfer complex and therefore, leading to the change in electrical or optical signal [31]. The charge transfer is dependent on the electronegativity of the analyte and the work function of the conducting polymer [32]. Dipole-dipole interaction or hydrogen bonding may occur between analyte and the nitrogen atoms. The fabrication of sensors based on these mechanisms is discussed in following sections:

(i). Weak interactions involving absorbing or swelling:

CPs can absorb VOCs or solvents, thereby increasing its volume significantly causing swelling. The main sensing mechanism in detecting alcohols or VOCs is swelling owing to weak interaction such as polar (dipole / dipole or dipole / induced dipole) and dispersion (induced dipole / induced dipole) or polarizability involved between CP and the analyte. These weak interactions do not change the doping levels of the conjugated polymer, however they can weakly influence the electronic properties of CPs owing to the change in organic vapours resulting in large increase in the conductivity of PANI films and therefore, the organic vapours cause large increase in the conductivity of PANI films and therefore, can be utilized as potential sensors. Based on wide-angle XRD, the changes were attributed to crystallization of conducting polymers. Further experimental results demonstrated that ethanol and acetone both result in change in the crystallinity of conducting polymers. It was also observed that short chain alcohols such as methanol and ethanol interact more efficiently with CPs than longer chain alcohols and therefore show better sensitivity to methanol and ethanol. Camphor sulfonic acid (CSA) doped PANI was observed to respond to alcohol vapours [33]. Subsequently, PANI and its derivatives such as poly (o-toluidine), poly (o-anisidine), poly (N-methyl aniline), poly (N-ethyl aniline) and poly (diphenyl amine) were shown to have sensitivity to variety of vapours such as methanol, ethanol, propanol, butanol and heptanol vapours [34]. It was found that resistance decreases in the presence of small chain alcohols but an opposite trend is observed in the case of long chain alcohols. The increase in resistance due to adsorption of chloroform, acetone, ethanol, acetonitrile, toluene and hexane on PANI was attributed to swelling which leads to a higher distance between the PANI chains [35]. The swelling mechanism was also the basis of developing an electronic nose based on array of polymer composite sensors polypyrrole as conductive filler in insulating organic polymers matrix [36]. It is observed that the analyte can interact with both the insulating matrix and the conductive polymer matrix and therefore, the composites will swell to varying degrees depending on the polymer – odorant interactions. The swelling results a change in the conductivity of the polymer film.

(ii).Weak interactions involving Hydrogen Bonding

The interaction between analyte and CP may result in hydrogen bond formation between NH groups of CP and C=O group of the analyte. For example, in the case of PANI and PPy, methanol molecule forms two H-bonds as a bridge between PANI chain, twisting the chains and thereby localizing the polaron and cause decrease in conductivity [37] . Such a hydrogen bond has been confirmed using impedance spectroscopy. QCM gas sensor based on polyaniline was also fabricated to detect dibutyl phthalate (DBP) vapor. The sensor was extremely sensitive to DBP and could detect concentrations as low as 20 ppb, and could be easily recovered by N_2 purging. The interaction of PANI with DBP results from the strong tendency of DBP to form hydrogen bonding, which occurs between the PANI imine groups and the carboxyl groups of DBP. The process results in increase of mass of the film, and therefore, the frequency of QCM changes. Hydrogen bonding is destroyed when the film is purged with nitrogen gas. As a result DBP is desorbed, making the process reversible.

1.8 Theoretical models for charge conduction in organic semiconductors

In case of ohmic contact between metal and organic semiconductor, following bulk limited conduction mechanisms have been studied in this thesis. Although the equations explained below have initially been developed for insulators they are well valid for organic semiconductors [38].

1.8.1 Ohmic Conduction

Ohmic conduction is caused by the movement of mobile electrons in the conduction band and holes in valence bad. In this mechanism the current density is linearly dependent on the electric field.

$$J = \sigma E = nq\mu E \tag{1.1}$$

where σ is electrical conductivity, n is the number of electrons in the conduction band and μ is the electron mobility. Current due to ohmic conduction is observed at low voltages in the *I-V* characteristics when injected charge carriers are negligible as compared to thermally generated carriers in the bulk.

1.8.2 Space charge limited conduction

At higher bias, the free carrier injected from the electrodes exceeds the thermal equilibrium value and the space charge effect is said to occur. The injected carriers influence the space charge and the electric field profile. The resulting field drives the current, and this current also sets up the field. The current produced due to the presence of a space charge effect is called the space charge limited current (SCLC).

The general approach for deriving the SCLC current-voltage characteristics of organic semiconductors exploits the Poisson equation, and is thus independent of the microscopic transport mechanism. The Poisson equation describes the relationship between the electric field *E* and the local charge density,

$$\frac{dE}{dx} = \frac{q}{\varepsilon_0 \varepsilon_r} n\,(x) \tag{1.2}$$

where q is the elementary charge, ε_0 is the permittivity of free space, and ε_r is the dielectric constant of the material. The total density of carriers is given by $n(x) = n_c(x) + n_t(x)$, where $n_c(x)$ is the density of carriers in conductive states, and $n_t(x)$ is the density of carriers in trapped states.

The current density equation is given by the current flow equation for the drift current,

$$J = q\mu(E)E(x)n_c(x) \tag{1.3}$$

where μ (E) is the field dependent mobility.

Combining Eqns. (1.2) & (1.3) we get the following current voltage relation

$$\frac{dE(x)}{dx} = \frac{J}{\varepsilon_0\varepsilon_r\mu(E)E(x)} + \frac{q}{\varepsilon_0\varepsilon_r}n_t\,(x) \tag{1.4}$$

To obtain the current-voltage characteristics from above equation, the differential equation has to be solved according to the boundary condition $E\,(0) = 0$, *i.e.*, an ohmic contact. The voltage is given by $V = \int_0^d E(x)dx$, where *d* is the thickness of the semiconducting layer. In the limiting case the mobility is assumed not to be strongly field dependent, and trapping is ignored so that only the free charge carriers are considered, Eqn. (1.4) is written as:

$$J = \varepsilon_0\varepsilon_r\mu E(x)\frac{dE(x)}{dx} \tag{1.5}$$

Integrating Eqn. (1.5) from $x = 0$ to $x = d$ results in *Mott-Gurney law*

$$J = \frac{9}{8}\varepsilon_0\varepsilon_r\mu\frac{V^2}{d^3} \tag{1.6}$$

Equation (1.6) describes the *J-V* relationship in case of SCLC Conduction for the trap free case.

The influence of single–level traps and traps distributed in energy is described as follows.

In the case of a single energy level at energy E_t, the distribution can be written as

$h(E) = N_t\delta(E - E_t)$ where N_t is the trap density and δ is the Dirac delta function.

Consider single energy level shallow trap lying between Fermi level and valence band (considering conduction by holes). The concentration of traps (holes) is given by [38] :

$$n_t = \int_{E_l}^{E_u} N_t \delta(E - E_t) \frac{1}{\left\{1 + exp\left(\frac{E_F - E}{kT}\right)\right\}} dE \tag{1.7}$$

Energies E_l and E_u are the lower and upper limits of the trapping level. On integrating above equation, we get [38]

$$n_t = \frac{N_t}{1 + \frac{N_t \theta_t}{n_c(x)}} \tag{1.8}$$

where $\theta_t = \frac{N_v}{N_t} \exp\left(\frac{-E_t}{kT}\right)$ and N_v is the effective density of states in valence band. Using Eqn. (1.8) for n_t and applying boundary condition, the solution of Poisson equation gives

$$J = \frac{9}{8} \theta_t \varepsilon_0 \varepsilon_r \mu \frac{V^2}{d^3} \tag{1.9}$$

It can be easily shown that

$$\theta_t = \frac{n_c}{n_c + n_t} \tag{1.10}$$

Thus θ_t represents ratio of free to total (free plus trapped) charge carriers. In the absence of traps, *i.e.*, $n_t = 0$ implies $\theta_t = 1$ and Eqn. (1.9) reduces to Eqn. (1.6). If $n_t >> n_c$, under this condition θ_t becomes the ratio of free to trapped carriers.

The SCL current-voltage characteristics are typically illustrated in a log-log plot because the SCL current bears a power law relationship with the bias. At low voltage the SCLC is not observed, and Ohm's law dominates the current voltage characteristics due to more number of thermal equilibrium free carriers. When the voltage becomes large enough, the SCL current starts to be noticeable and shallow trapping field region is entered. The voltage at which this transition occurs is given by:

$$V_{tr} = \frac{8}{9}\frac{qn_0 d^2}{\varepsilon\theta} \tag{1.11}$$

where n_o is thermally generated free electron concentration.

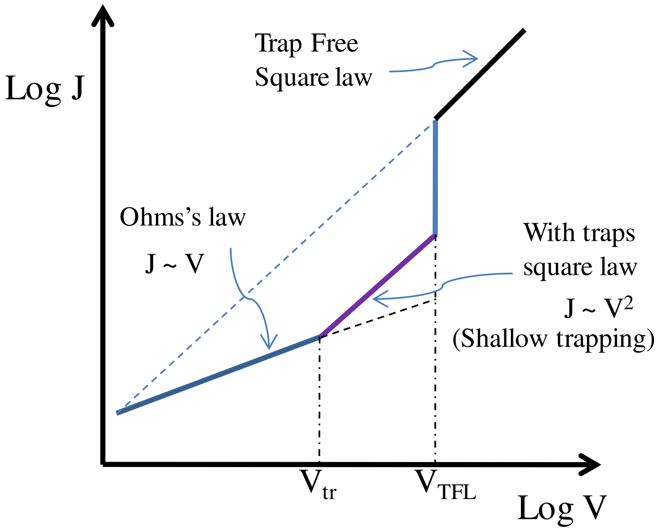

Figure 1.10: A typical log-log plot of current density-voltage characteristics for space charge limited injection into an organic semiconductor with a single trapping level. V_{tr} is transition voltage and V_{TFL} is trap-filled limit voltage.

As the voltage is further increased, more electrons are injected and eventually these injected electrons fill all the trapping sites in the material. At sufficient high voltage, known as trap-filled-limit voltage V_{TFL}, the entire population of the trap has been filled and the current rises nearly vertically [39].

$$V_{TFL} = \frac{qN_t d^2}{2\varepsilon} \tag{1.12}$$

Once trap-filled-limit voltage V_{TFL} is reached, very sharp increase in the current, *J-V* relationship is characterized by trap- free- square law (Eqn. 1.6).

Similarly in case of exponential distribution of traps $h(E) = \frac{N_t}{kT_c} exp\left(\frac{-E}{kT_c}\right)$, where N_t is the density of traps and T_c is the characteristic distribution constant.

The coupled Poisson and transport equation along with boundary condition can be solved to obtain the following analytical expression [40]:

$$J = \mu e^{1-l} N_v \left(\frac{\varepsilon_0 \varepsilon_r}{\alpha N_t}\right)^l \left(\frac{l}{l+1}\right)^l \left(\frac{2l+1}{l+1}\right)^{l+1} \frac{V^{(l+1)}}{d^{(2l+1)}} \tag{1.13}$$

where $\alpha = \frac{\pi/l}{\sin(\pi/l)}$ and $l = \frac{T_c}{T}$

Thus it can be seen that the presence of traps not only limits the magnitude of *J* but also distorts the V^2 behaviour.

In the case of Gaussian distribution of traps, the situation is more complex since exponent at the applied voltage (l+1) and thickness of the sample (2l+1) are not constant but they are functions of the applied voltage [41].

1.9 Survey on Gas Sensors reported using organic semiconductors on flexible substrate

In this section we present a review on gas sensors fabricated on different flexible substrates using organic semiconductor as a sensing material. The details of the survey are enlisted in the following table.

Table 1.4: Literature Survey on Gas Sensors reported using Organic Semiconductors on flexible substrate.

Sr. No.	**Substrate**	**Active layer**	**Deposition Method**	**Transducer type**	**Selective to**	**MDL (ppm)**	**Sensor Response**	**Temperature**	**Reference**
1	PET	Picene	Sublimation	ChemFET	O_2	10	-----------	RT	[42]
2	Polyimide	Reduced Graphene –CNT composite	Spin Coating, PECVD	Chemiresistive	NO_2	0.5	$(\Delta R / R_0)\%{\sim}2.5$	RT	[43]
3	PET	PPy	LBL Self assembly	Chemiresistive	NH_3	5	$\{(R_{gas} - R_{air})/R_{air}\} \sim 27$	RT	[44]
4	Kapton	Graphitized Carbon nanofibres	Spray Technique	Chemiresistive	NH_3	100	$\{(\Delta R / R_0)\text{x}100\}=0.38$	RT	[45]
5	Transparency Sheet	PANI-DBSA dispersion	Spin Coating	Chemiresistive	NH_3	2	$(\Delta R / R_0)\%=4.5$	RT	[46]
6	Polyimide	Titania Nanotube	RF Magnetron Sputtering, Electrochemical Oxidation	Chemiresistive	NH_3	50	$[\{(I_{gas}-I_0) / I_0\}\text{x}100]=30$	RT	[47]
7	Polyimide	Conductive Carbon Black Particles	Drop Casting	Chemiresistive	C_2H_5OH	60	$\{(\Delta R / R_0)\text{x}100\}$ 0.81 @ 100 ppm	RT	[48]
8	PET	MWCNTs-Pd	LBL in situ self-assembly Chemical functionalization	Chemiresistive	H_2	200	$(\Delta R / R_{air})=1.95$	RT	[49]

9	Metal foil	ZnO NRs-G/M	Hydrothermal, CVD, Thermal	Chemiresistive	C_2H_5OH	10	$R_{air} / R_g = 9$	300° C	[50]
10	Polyimide	Pt-PHEMA	Magnetron Sputtering, Inkjet Printing	Chemicapacitive	C_2H_5OH	200	$\Delta C / C = 2.0X10^{-15}$		[51]
11	PET	ZnO NSs	RF Magnetron Sputtering	Chemiresistive	H_2	200	$[\{(R_a - R_g) / R_a\}x100]=24.8$ %	RT	[52]
12	PDMS	PMMA/Pd/PMMA	Spin Coating, DC Magnetron Sputtering	Chemiresistive	H_2	600	------------------	RT	[53]
13	PET	RGO	Electrochemical	Chemiresistive	Rogor	0.0076	$(\Delta R / R_0)$% ~11	RT	[54]
14	Polyimide	PEUT &PDMS	Drop/Spray Coating	Chemicapacitive	C_2H_5OH	780		29° C	[55]
15	Polyimide	PANI-PVP	Electrospinning	Chemiresistive	NH_3	7	$(\Delta R / R_0)$%~20 @ 10ppm	RT	[56]
16	PET	PANI-$Cucl_2$	Inkjet Printing	Chemiresistive	H_2S	2.5	$(\Delta I / I)$ ~ 1	RT	[57]
17	PET	PPy coated SnO_2	Drop Casting	Chemiresistive	NO_2	0.5	$(\Delta R / R_0)$=0.6 %	RT	[58]
18	PEN	PSSA doped PANI	Vapor Deposition Polymerization, Spin Coating	Chemiresistive	NH_3	0.25	$\{(R_{max} - R_b)/ R_b\}x\ 100 =18$ %	RT	[59]
19	Polyimide	Graphene	CVD	ChemFET	NH_3	2600	$\{(\Delta R / R_0)x100\}$ ~ 200 %	RT	[60]
20	Paper (clean room)	Graphene	CVD	Chemiresistive	NO_2	200	$\{(R_{air} - R_{gas}) / R_{air}\}$ x100% =35	RT	[61]
21	PET	PANI/Graphene	Self Stabilized Dispersion Polymerization	Chemiresistive	H_2S	1		RT	[62]

22	PET	PANI	In situ Polymerization	Chemiresistive	NH_3	5	26 %@ 100 ppm	RT	[13]
23	PET	3D-Graphene foam	CVD	Chemiresistive	NO_2	200	ΔI ~ 0.42mA	RT	[63]
24	Polyimide	ZnO Nanorod	Hydrothermal	Chemiresistive	C_2H_5OH	10	R_a / R_g ~ 1.1	125° C	[64]
25	PET	PANI	In situ Chemical Oxidation Polymerization	Chemiresistive	NH_3	5	$\Delta R/R_0$ ~ 2	RT	[65]
26	BOPET	Au-Pcz	LB , Thermal Evaporation	Chemiresistive	H_2S	1	$[\{(R_g - R_a) / R_a\}x100] = 60$	RT	[66]
27	PET	Cu-SWCNTs	Spin Coating	Chemiresistive	H_2S	5	$\Delta R(\%)=11$ %	RT	[67]
28	PET	Graphite paste, Solid Polymer electrolyte		Electrochemical	NO_2	0.2		RT	[68]
29	BOPET	PANI-Ag APTMS	photopolymerization	Chemiresistive	H_2S	1	$[\{(I_g - I_a) / I_a\}x100] = 40$	RT	[69]
30	Transparency Sheet	Graphene-PEDOT:PSS	Inkjet Printing	Chemiresistive	NH_3	5	$[\{(R_{gas} - R_{air}) / R_{air}\}x100] = 1.2$	RT	[70]
31	PEN	P-29 DPP-SVS	Spin Coating	ChemFET	NH_3	28.9		RT	[71]

1.10 Scope of thesis

Flexible gas sensors are the key for futuristic technologies owing to low cost, low power consumption, integratibility with textile electronics, human body, food wraps and RFID tags etc. However as discussed in the previous section there is a very little work reported on the development of flexible gas sensors using organic semiconductor as active layer. Therefore this thesis aims at developing gas sensor using both small organic molecule as well as conducting polymer as active material. Amongst all the materials, we have chosen Cobalt Phthalocyanine (CoPc) and conducting polymer Poly [N-9′ heptadecanyl-2, 7-carbazole-alt-5, 5-(4′7′-di-2-thienyl 2′, 1′, 3′ benzothiadiazole)], (PCDTBT) (with a band gap of 3.4 eV and 1.8 eV respectively) for making chemiresistive and Organic field effect transistor gas sensors. **The main objectives of this thesis are:**

(i) Synthesis of flexible CoPc films with high charge carrier mobility as an active layer of the Chemiresistive sensors.

(ii) Investigation of charge transport and Chemiresistive gas sensing studies of flexible CoPc films.

(iii) Tailoring of the gas sensing properties of flexible CoPc films by sensitizers such as Au nanoparticles and ZnO nanowires.

(iv) Fabrication of flexible organic field effect transistor gas sensor conducting polymer Poly [N-9′ heptadecanyl-2, 7-carbazole-alt-5, 5-(4′7′-di-2-thienyl 2′, 1′, 3′ benzothiadiazole)], (PCDTBT) and investigation of its gas sensing properties.

The experiments, observations, results and their discussions are organized into following seven chapters:

Chapter one deals with the introduction of gas sensor, need for sensors, its classification, materials used for sensing layer. A brief description of organic semiconductors and their properties, advantages and how it is different from conventional inorganic semiconductors is given. It also presents a survey on gas sensors made using organic material on flexible substrate. It concludes with the gas sensing mechanism of organic semiconductor based chemiresistive and OFET sensor.

Chapter two deals with the different characterization techniques which have been used in the thesis work *viz.*, deposition techniques, structural and morphological characterization techniques, spectroscopy techniques etc. It also describes the experimental set ups which have been employed for gas sensing and charge transport studies.

Chapter three presents the charge transport characteristics of cobalt phthalocyanine films deposited on flexible bi-axially oriented polyethylene terephthalate substrate (BOPET). The films exhibit room temperature charge carrier mobility ~ 118 $cm^2V^{-1}s^{-1}$ in flat condition. It has been shown that the films are highly flexible and show the reversible resistance change on bending. CoPc films on BOPET were able to sense NH_3 gas. Further, it is demonstrated that in CoPc films on BOPET, bending stress enhances the sensor response due to decrease in π-π interactions.

Chapter four deals with enhancement in H_2S response of flexible CoPc film by its surface modifications using Au nanoparticles. As compared to pristine CoPc film the Au modified CoPc films were found to be more oxidative towards H_2S. The H_2S gas sensing characteristics of flexible Au modified CoPc flexible films were also studied in bent condition. The gas sensing characteristics of the films were found to be stable for the bending radius > 20 mm.

Chapter five deals with improvement in performance parameters of H_2S Sensor using random network of ZnO nanowires as the template for growth of CoPc. In this case the random network of *n*-type ZnO nanowires (ZnO NWs) films were grown on flexible BOPET sheet and later CoPc films of different thickness were grown on the ZnO nanowires network. With increasing thickness of CoPc (> 15 nm), heterojunction films exhibit a transition from *n* to *p*-type conduction due to uniform coating of CoPc on ZnO. The heterojunction films prepared with 25 nm thick CoPc layer exhibit highest response (268% at 10 ppm of H_2S) and fastest response (26 s) among all samples. The samples were characterized using different techniques such as TEM, Raman, XRD, PL and XPS. The detailed XPS analysis suggests that these heterojunction films with 25 nm thick CoPc exhibit the least content of chemisorbed oxygen, enabling the direct interaction of H_2S with the CoPc molecule, and therefore exhibit fastest response. The improved response is attributed to the high susceptibility of the *p–n* junctions to the H_2S gas, which manipulates the depletion layer width and control the charge transport.

Chapter six deals with the fabrication and characterization of Organic Field Effect Transistor (OFET) using CoPc and PCDTBT as active layer. The insulating layer used in each case is Poly (methyl methacrylate) (PMMA).It also presents application of PCDTBT based transistor for application as OFET Sensor.

Chapter seven gives the summary, conclusion and future scope of the thesis work.

CHAPTER 2

Experimental Techniques

2.1 Introduction

In this chapter, we describe the processes and equipments utilized for fabrication and characterization of chemiresistive and organic field effect transistor (OFET) gas sensors. In addition, we present the details of charge transport and gas sensing measurement setups.

2.2 Substrates and their preparation

For fabricating gas sensors we have used biaxially oriented polyethylene terephthalate (BOPET) substrate which is flexible in nature. BOPET is manufactured from molten PET which is biaxially oriented by drawing and subsequently followed by "heat set" under tension at temperature greater than 200° C. For measuring the work function, we have used ITO coated glass substrate.

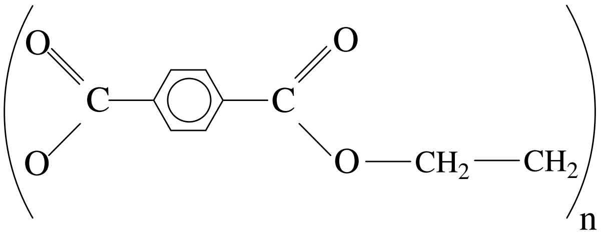

Figure 2.1: Chemical structure of flexible BOPET sheet.

The cleanliness of the substrates is of crucial importance for the subsequent growth of the films. Thus substrate preparation is very important step before growth studies. Therefore the substrates should be utmost clean before it is further processed for any application. For cleaning BOPET substrates, these were ultrasonicated for 5 min in methanol. Other solvents were observed to roughen the BOPET substrate. But for other substrates such as ITO coated glass, these were sonicated in three steps using trichloroethylene (TCE), acetone and methanol for 10 min each. TCE was used to remove grease, oil etc. from substrate. Acetone and methanol ultrasonication was done separately to remove polar and non-polar organic impurities and dust particles. To remove the solvent, the substrates were dried under the jet flow of dry high purity Ar gas.

2.3 Fabrication of Chemiresisitive type gas sensor on flexible substrate

In this section we discuss fabrication of active layer (*viz.*, CoPc, PCDTBT and composite of CoPc with Au and ZnO nanowires) for the gas sensor using various techniques employed in the present work.

2.3.1 Deposition of sensing layer using molecular beam epitaxy (MBE) technique

Molecular Beam Epitaxy (MBE) technologically is an improved version of the conventional thermal evaporation technique. The MBE technique is unique because it allows thickness of the layer to be controlled very precisely and atomically thin interfaces can be grown. Also, in-situ characterization of the growing film is possible using MBE.

The photograph of the MBE system (RIBER EVA 32 E) used for depositing thin film of Cobalt Phthalocyanine in the present thesis is shown in Fig. 2.2. It consists of three chambers *viz.*, Introduction Chamber, Analysis Chamber and Growth Chamber. All the three chambers are ultra high vacuum chambers and are made of stainless steel. All seals are made of OFHC copper gaskets. This construction allows high temperature baking (~200°C) of the entire MBE system to reduce outgassing from the walls. Analysis and Growth chambers are situated in a line, whereas, the Introduction Chamber is situated at 37° off the line joining Analysis and Growth Chambers. Introduction chamber is connected with Analysis chamber through gate valve and similarly Analysis chamber is connected with Growth chamber. There are two magnetically coupled sample transfer mechanisms. One is used to transfer the sample from Introduction to Analysis Chamber and the second is used to transfer sample from

Analysis to Growth Chamber. Therefore, substrate cleaning and characterization, film deposition and characterization are performed in-situ under UHV conditions.

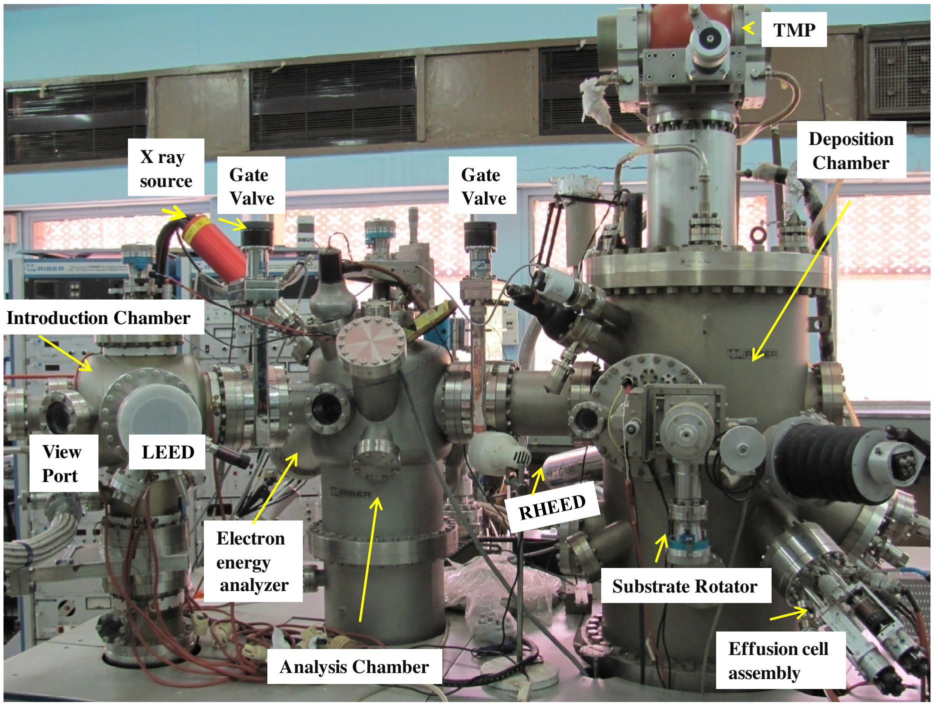

Figure 2.2: A photograph of MBE deposition system (RIBER EVA 32 E) used for the deposition of CoPc films.

For the deposition of MPc films, the pre-cleaned BOPET substrate was loaded into the introduction chamber. The chamber is pumped down to 10^{-7}torr and then the substrate was transferred to analysis chamber. The cleanliness of the substrate was confirmed by XPS studies. On finding the substrate free of impurities, it was transferred to the growth chamber for deposition where source material was preloaded. Before starting deposition, the source material was degassed for the removal of volatile impurities. During deposition the pressure of the growth chamber was maintained better than 10^{-9}torr. The deposition of the film was started when substrate had attained a temperature of 100 ºC and the substrate heater was controlled within ±1ºC accuracy of temperature. The deposition rate of the film was monitored by the flux gauge and the deposition rate was varied between 0.02 and 0.5 nm/s by controlling the effusion cell temperature. In order to achieve excellent uniformity in composition and thickness, the source-to-substrate distance was kept comparatively large (40 cm) and the substrate was rotated during the deposition. After the deposition, the film was transferred to the analysis chamber again and it was characterized by XPS. Finally the film was taken out through the introduction chamber for further ex-situ characterization and further studies.

2.3.2 Deposition of thin films using conventional Thermal Evaporation

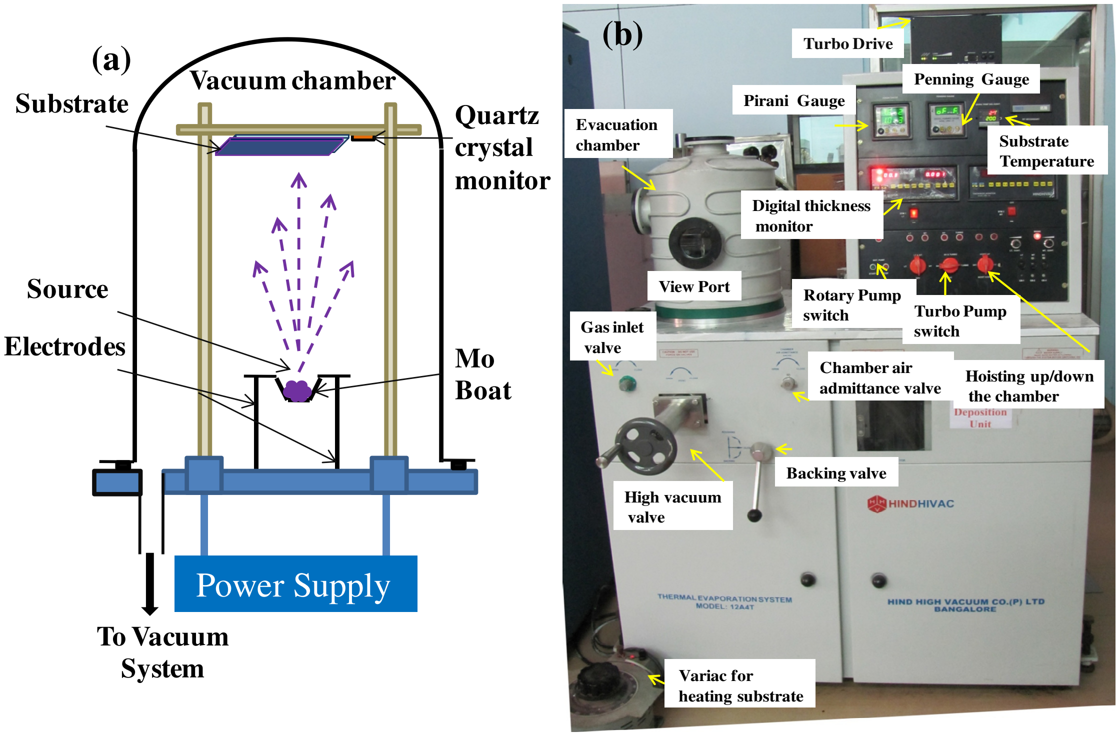

Figure 2.3: (a) Schematic of the thermal evaporation technique and (b) a photograph of the thermal evaporation system used for thin film deposition.

We have used Thermal Evaporation System from Hind High Vacuum Model 12A4T for depositing CoPc (for active layer of sensor) and Au (for contacts). The chamber is first evacuated by a double stage, direct driven, rotary vacuum pump, Model ED – 15 and after achieving a base pressure of ~ 5×10^{-3} mbar, a LEYBOARD molecular turbo pump (model

TURBOVAC361) was connected to the chamber and this turbo pump backed by rotary pump. The system comprised of a Pirani gauge (for measuring roughing and backing pressure from 0.5 m bar to 1 × 10^{-3} m bar) and Penning gauge (for measuring high vacuum in the chamber from 1×10^{-3} mbar to 1×10^{-7}m bar). The sufficient quantity of CoPc powder was kept in a Molybdenum Boat, and this boat was heated to sufficient temperature by passing high current. At high temperature CoPc powder sublimates and it gets deposited on the substrates. Before starting the deposition of CoPc on BOPET, source was first prepared by baking to remove moisture or volatile impurities if any. In a similar way, a thin layer of gold was deposited on CoPc films. Tungsten filaments were used for holding and evaporating gold wires.

2.3.3 Deposition using random network of ZnO nanowires on BOPET using hydrothermal technique

We have synthesized ZnO nanowires (NWs) for chemiresisitive sensor using hydrothermal method. In this method ZnO nanoparticles (NPs) were first prepared which acts as a seed. ZnO NPs were prepared by chemical process using zinc acetate dihydrate, $Zn(CH_3COO)_2(H2O)_2$,as a precursor. The KOH solution in methanol (5-15mM) was added dropwise to the solution of zinc acetate dihydrate in methanol (30-45mM) kept at a temperature 60°C-75°C.The volume ratio of the two solutions was maintained at 2:1. Growth at temperatures above 60°C ensures that precipitation of hydroxide does not take place [72]. Growth was carried out for a few hours under constant stirring.

A random network of ZnO-NWs was grown on BOPET by hydrothermal method using ZnO NPs as seed. The seed layer was prepared by spin casting the dispersed ZnO NPs onto the BOPET surface. The thickness of the seed layer was ~ 100 nm. The ZnO-NWs growth was carried out on the seed layer by suspending the wafer upside down in an open beaker filled with an aqueous equimolar (25mM) solution of zinc nitrate hexahydrate, $Zn(NO_3)_2.6H_2O$, and hexamethylenetetramine, $(CH_2)_6N_4$, at 90°C for 7 hours. After the growth of ZnO-NWs network, the substrate was rinsed under deionized water and dried under Ar flow.

2.4 Fabrication of flexible Organic Field Effect Transistor based Gas Sensor

Conducting Polymers and small molecules commonly employed in the fabrication of organic devices readily degrade (are doped) when exposed to atmospheric conditions. Hence, an inert Glove Box (MB 20G, M. BRAUN INERTGAS-SYSTEME GMBH) with oxygen and moisture levels <0.1ppm was used to fabricate organic transistors. The glove box is on slight positive pressure of Ar. The system works by the principle of gas circulation, where the working gas circulates between the glove box and the gas purifier. The gas purification system removes moisture and oxygen from the inert gas and a proprietary adsorbent to remove water, thus maintaining both H_2O and O_2 at < 0.1 ppm. A photograph of the glove box is shown in Fig. 2.4. The custom made glove box contains two boxes, Box I contains a spin coater (Delta6 BM/TT, *Suss Microtec Lithography GmbH*) for deposition of thin films and Box II contains a thermal evaporator (custom made by BOC Edwards Inc.) for metal contacts. The entire field-effect transition fabrication, as schematically represented in Fig. 2.5, can be carried out in this glove box, without exposing the samples to atmosphere. Briefly, a cleaned BOPET substrate was coated with thermally evaporated Al film (to be used as gate electrode) in Box- II. This sample was then transferred to Box- I for the deposition of PMMA dielectric (followed by annealing) and PCDTBT active layer depositions by spin coating. The samples was then transferred back to Box- I for deposition of the source-drain pairs of Au using thermal evaporation though a steel shadow mask. The detail of this process is presented in Chapter 6.

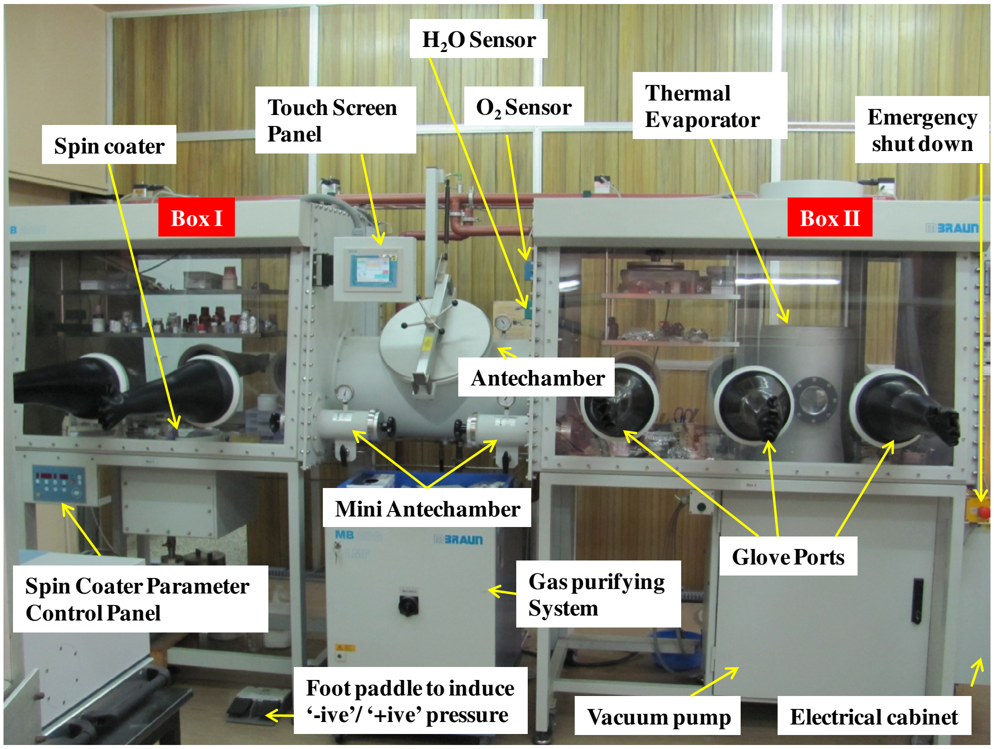

Figure 2.4: A photograph of the mbraun modular glove box system.

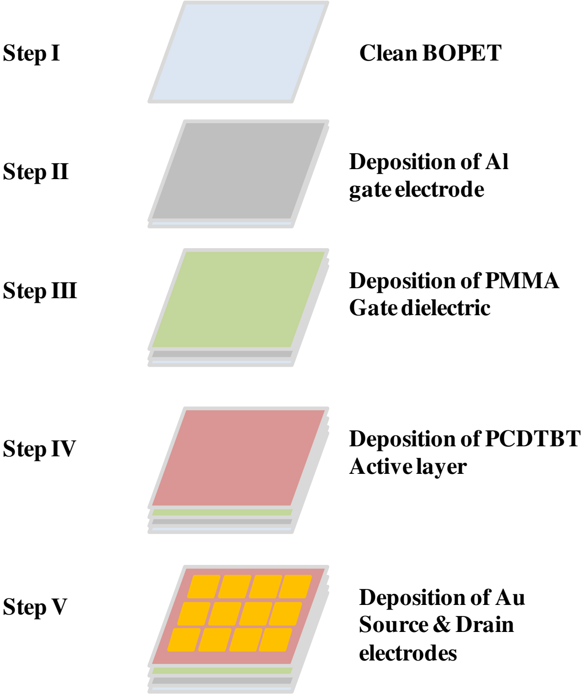

Figure 2.5: Sequence of depositing various layers in an organic field effect transistor gas sensor.

2.5 Characterization techniques

2.5.1 X-ray diffraction

The orientation and structure of the substrate as well as sensor films were determined using powder X-ray diffractometer (Seifert XRD 3003TT) in θ-2θ scan mode. Fig. 2.6(a) shows the schematic diagram of the diffractometer, which consists of an X-ray source, and a goniometer for mounting sample and X-ray detector. The X-ray source used was CuK_{α} having wavelength of 1.54056Å, which has been selected using a Graphite monochromator.

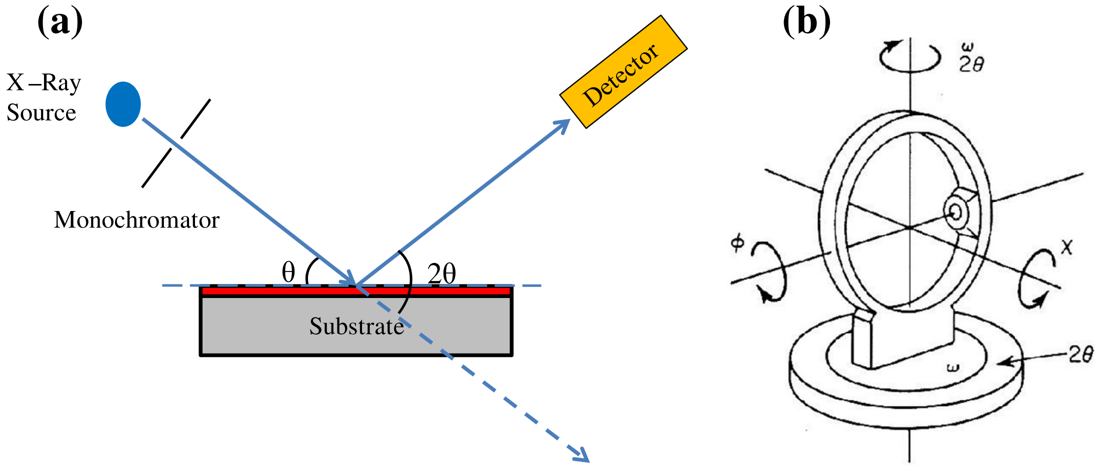

Figure 2.6: (a) Schematic diagram of powder X-Ray diffractometer and (b) Schematic representation of four circle diffractometer for texture measurements.

For mounting thin films, a specially designed Perspex holder (having a groove of dimension 10 mm×10 mm×1mm) was employed. The films were mounted on this groove using wax in such a way that X-rays fall on the film plane. Since the wavelength (λ) of X-rays coincides with the atomic spacing (d) in the solids, it diffracts in those orientations of 2θ, where the Bragg condition of diffraction *i.e.* $2d \sin\theta = n\lambda$ (θ being the angle which incident beam makes with the plane of sample) is satisfied [73]. While recording the diffraction pattern with detector, the sample is synchronously rotated along with the detector, such that the incident X-ray beam makes an angle θ with the plane of sample whereas detector is at angle 2θ with respect to incident beam. This is commonly known as θ-2θ scan of X-ray diffraction. The recorded diffraction pattern is compared with standard pattern to get information about the phase of the samples. The lattice parameters are obtained by fitting the recorded diffraction peaks using least-square fitting software.

X-ray diffraction measurements of thin films using conventional θ-2θ scanning methods generally produce a week signal from the film and an intense signal from the substrate. One of the ways to avoid intense signal from the substrate and get stronger signal from the film itself is to perform scan with a fixed grazing angle of incidence. This mode of scanning is popularly known as grazing incidence X-ray diffraction (GIXRD). The fixed angle is generally chosen to be above the critical angle for total internal reflection of the film material.

In this configuration, incident X-ray is fixed at a very small angle (*e.g.* 0.1°) with the sample surface and detector does 2θ scan. The sampling depth (D) is related with angle of incidence (Φ) by the formula,

$$D(\phi) = \frac{\lambda}{4\pi q} \tag{2.1}$$

where λ is the x-ray wave length (1.541Å), and

$$q = \left[\sqrt{\left(\phi^2 - \phi_c^2\right) + 4(\delta_i)^2} + \phi_c^2 - \phi^2\right]^{1/2} \left(\sqrt{2}\right)^{-1} \tag{2.2}$$

$$\delta_i = \lambda\left(\frac{\mu}{4\pi}\right) \tag{2.3}$$

Φ_c is the critical angle of incidence and μ is the linear absorption coefficient [74]. In the present studies, we have employed $\Phi = 0.1°$, which leads to a sampling depth of ~ 10 nm; and thus this technique becomes ideal for analyzing the structure of very thin films without having interference from the substrates.

Texture Analysis

The determination of the preferred orientation of the crystallites in polycrystalline aggregate is referred to as texture analysis, and the term texture is used as a broad synonym for preferred crystallographic orientation in the polycrystalline material, normally a single phase. The preferred orientation is usually described in terms of pole figures.

A pole figure is scanned by measuring the diffraction intensity of a given reflection (2θ is constant) at a large number of different angular orientations of the sample. A contour map of the intensity is then plotted as a function of angular orientation of the specimen. The most common representation of the pole figures are stereographic or equal area projections. The intensity of a given reflection (h,k,l) is proportional to the number of h,k,l planes in a reflecting condition (Bragg's law).Hence, the pole figure gives the probability of finding a given crystal-plane-normal as function of the specimen orientation. If the crystallites in the sample have a random orientation the recorded intensity will be uniform.

We can use the orientation of the unit cell to describe crystallite directions. The inverse pole figure gives the probability of finding a given specimen direction parallel to crystal (unit cell) directions. By collecting data for several reflections and combining several pole figures we can arrive at the complete orientation distribution function (ODF) of the crystallites within a single polycrystalline phase that makes up the material.

2.5.2 Atomic force microscopy

Atomic Force Microscope (AFM) is a microscope which uses a mechanical probe for studying the surface feature of a material down to atomic resolution. It measures the interatomic force between a sharp tip (a few microns long and often less than 100 Å in diameter) and sample surface. The tip is attached to the free end of a cantilever (100 to 200 μm long) or a tuning fork (typical length, thickness and width being 6.01, 0.35 and 0.61 mm respectively). Forces between the tip and the sample surface cause the cantilever to bend or deflect. A computer then generates the surface topography of the material by measuring the cantilever deflections.

AFM operates in three different modes: contact, non-contact and intermittent contact (or tapping) modes. In contact mode, the tip is brought into close contact with the sample surface (less than a few Å) and the dominant force is repulsive. In non-contact mode, the tip is separated in the order of tens to hundreds of Å from the sample surface and the interatomic force between the tip and sample is attractive (because of long-range van der Waals interactions). For studying the topography of organic material using contact mode, the problem is that sample surface may get scratched or damaged due to direct contact with the tip. This problem is overcome by intermittent contact mode.

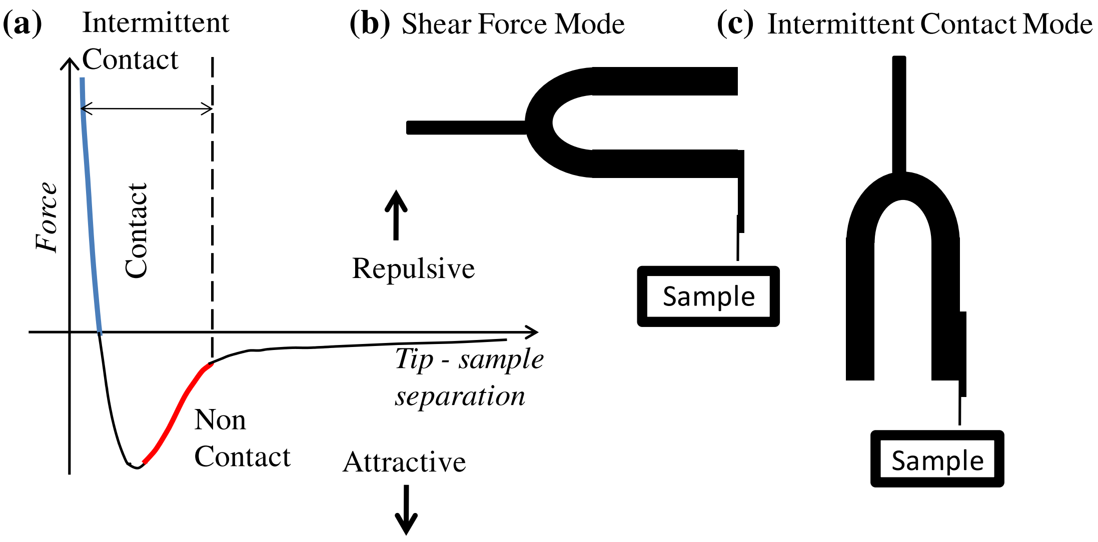

Figure 2.7: (a) Interatomic vs. Distance curve (tip-sample separation); Principle of two operation modes in tuning fork based AFM *viz.*, (b) shear force mode and (c) intermittent contact mode.

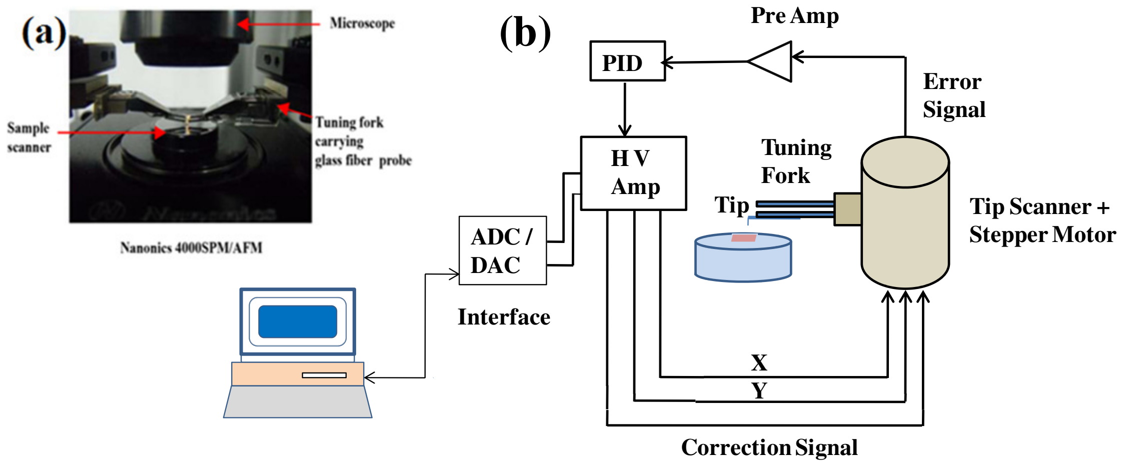

Figure 2.8: (a) A real snap of the AFM probe and sample stage (b) Block diagram of the used AFM system.

The atomic force microscope used in the present studies was Nanonics 4000SPM/AFM system, as shown in Fig. 2.8. In this system, the probe is made of the glass fibre tip (diameter 10nm) which is attached to tuning fork. The fork is attached with a piezocrystal. The image is recorded in tapping mode by oscillating the tip at resonance frequency. The probe was scanned in phase mode. During scan, phase changes due to tip surface interaction. The difference in signal called an error signal is sent to proportional, integrator and differentiator (PID) controller. PID sends the feedback via high voltage piezo driver to make constant phase by moving piezo driver in z direction at that x, y point. This way an image is generated. A schematic diagram of signal processing is shown in the Fig. 2.8 (b). The image so generated was processed (like smoothing, flattening etc) by NWS software [75]. This software was also used to study surface roughness by extracting line profile from the image.

Tuning Fork based AFMs basically operate in two modes: intermittent contact (tapping) mode and shear force (lateral) mode. In the case of intermittent contact mode, the tip is mounted perpendicular to the tuning fork prong as shown in Fig. 2.7 (b) so that the tip oscillates perpendicular to the sample surface. In the lateral force mode, the tip is mounted parallel to the tuning fork prong and oscillates nearly parallel to the surface of a sample as shown in Fig. 2.7 (c).

A constant sinusoidal voltage is applied to the one of the connectors of tuning fork to drive the sensor. The other connector of the tuning fork is connected to a reference signal generator of a lock-in amplifier. An I-V converter is used to convert the net current to a voltage. The current to voltage gain of the circuit is calibrated from dc to 100 kHz. Under the resonant condition, the tuning fork arm has the biggest displacement that corresponds to the maximum or peak voltage amplitude.

When the probe is approaching near the sample surface, the oscillation of the sensor is dampened due to probe - sample force interactions, resulting in a decrease in the output signal of the lock-in amplifier. The decreased signal is compared with a set –point of the feedback circuit and the resulting difference is fed back to the scanner via the high voltage amplifier in order to control the probe – sample distance during scanning. During the scan, the phase and amplitude of the quartz tunning fork oscillations are also recorded.

2.5.3 Scanning electron microscopy

A scanning electron microscope (SEM) consists of an electron gun, a lens system, scanning coils, an electron collector and a display.SEM provides information regarding morphology, topographical features, and phase distribution [76]. The schematic of a SEM is shown in Fig. 2.10. The scanned electron beam is produced in an electron microscope column. A vacuum of the order of 10^{-5} - 10^{-6} torr is required to be maintained in the space where sample is examined. The electron column is basically the illuminating system for the SEM, where electrons are generated and arranged through electric and magnetic fields in a proper direction to achieve the required incident beam at the specimen surface. The electron energy is typically 10-30 keV for most samples, but for insulating samples the energy can be as low as several hundred eV.

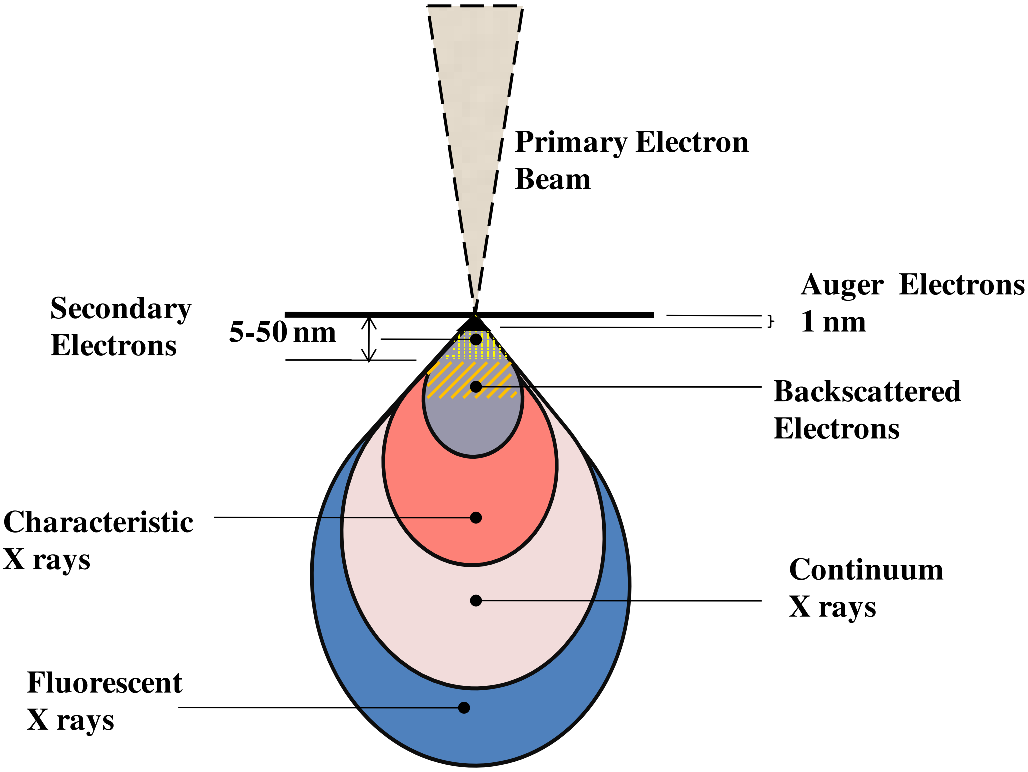

Figure 2.9: The tear-drop model of the electron interaction volume and the volume/depth from which the different signals originate.

As the highly energetic incident electrons are decelerated in the solid sample, a variety of signals is produced by electron-sample interactions. Two types of interactions occur between the electrons beam and the specimen: (i) elastic interactions and (ii) inelastic interactions. In elastic interactions, no energy is transferred from the electron to the specimen. There is, however, a deflection in path of electron due to coulomb interactions with the positive potential inside the electron cloud. In case of inelastic interactions, energy is transferred from incident electrons to the sample. The energy transferred to the specimen can cause different signals such as X-rays, Auger or secondary electrons, plasmons, phonons, UV quanta or cathodoluminescence.

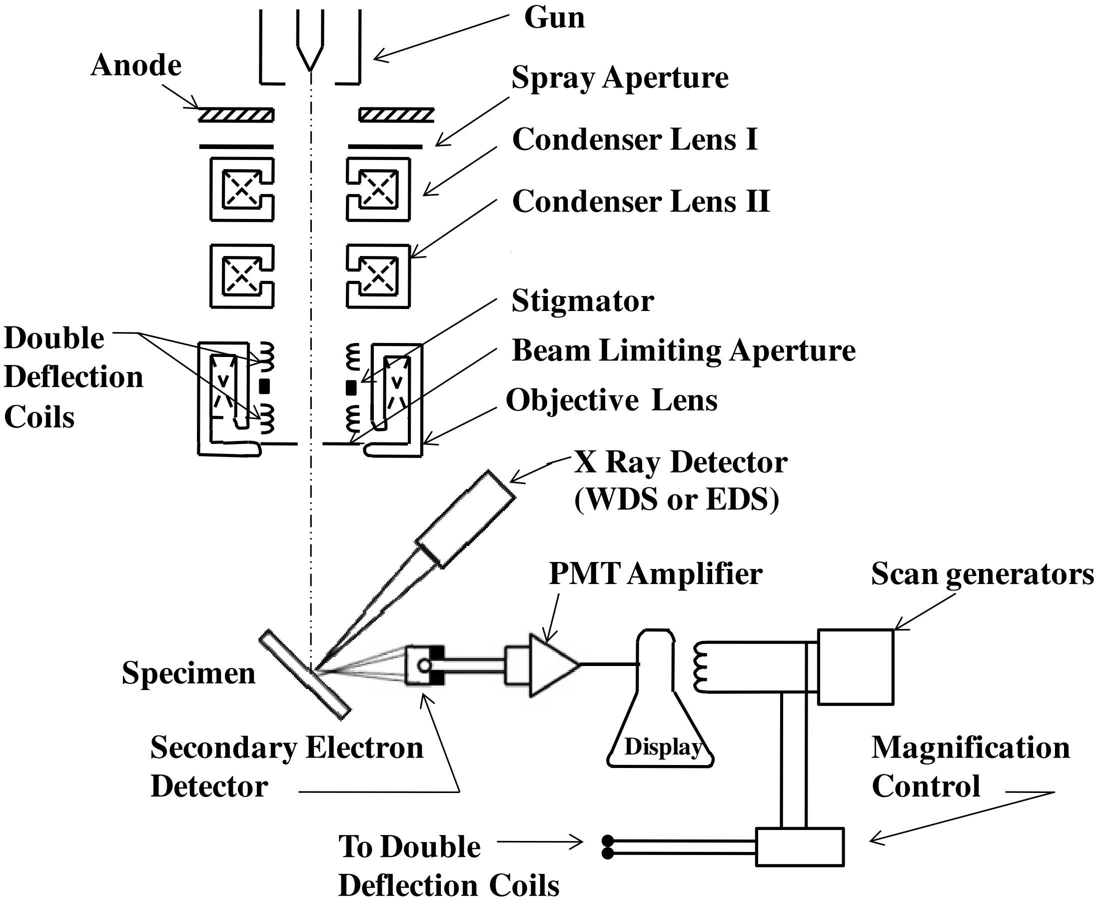

Figure 2.10: A typical sketch of a scanning electron microscope. Electron gun, specimen and various electrodes etc. need to be mounted in a chamber vacuum.

Secondary electrons and backscattered electrons are commonly used for imaging samples: secondary electrons are most valuable for showing morphology and topography of samples and backscattered electrons are most valuable for illustrating contrasts in composition in multiphase samples (*i.e.* for rapid phase discrimination). Due to interaction of focussed beam with solid, the backscattered electrons are somewhat defocussed resulting into lower resolution than one would expect. A majority of the secondary electrons come from a region very close to the sample surface (<50nm). Secondary electrons are characterized from other electrons by having energy less than 50 eV. Since the secondary electron intensity is a function of surface orientation with electron beam, they produce image of surface morphology. Secondary electrons are most commonly detected by Everhart-Thornley detector. The basic component of this detector is a scintillation material that emits light when struck by energetic electrons accelerated from the sample to the detector. The light from the scintillator is channelled through a light pipe or a photo multiplier, where light incident on a photo cathode produces electrons that are multiplied, creating a very high gain necessary to drive the display. SEM analysis is considered to be "non-destructive"; that is, x-rays generated by electron interactions do not lead to volume loss of the sample, so it is possible to analyze the same materials repeatedly.

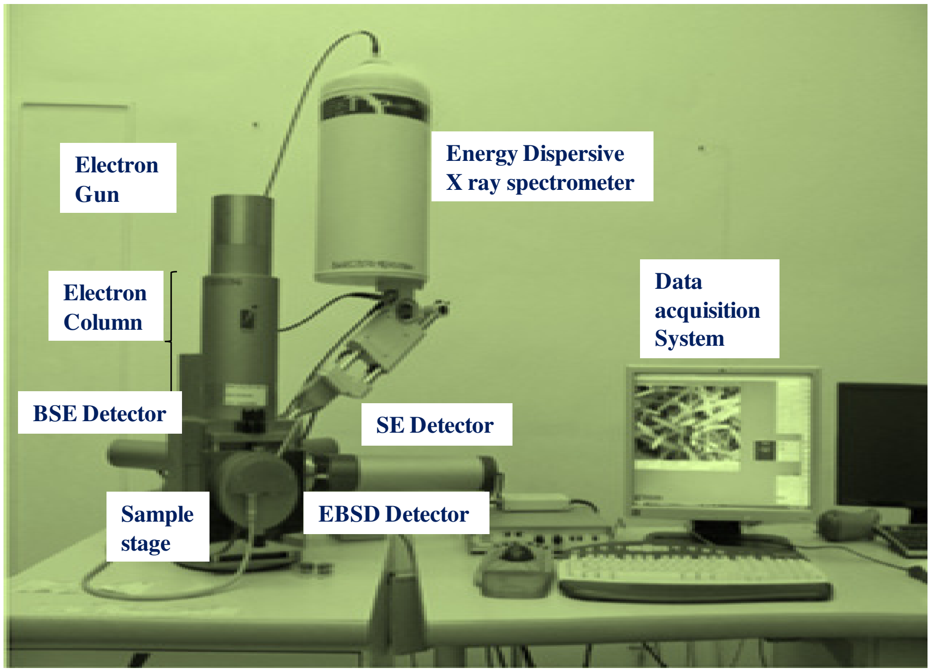

Figure 2.11: The photograph of the SEM used for imaging samples in this work.

2.5.4 Transmission Electron Microscope

Transmission electron microscope is ideal for investigating the nanomaterials, as very high resolution is possible (better than 0.5nm) using it. As the name suggests the electrons are transmitted through the specimen in this microscope. Electrons of very high energy (typically greater than 50 keV) are used which pass through a series of magnetic lenses. The basic components of TEM are electron source, condenser lens, intermediate lens, projector lens, objective lens and a fluorescent screen. The lenses are electromagnetic whose focal lengths are varied to obtain optimized images rather than moving the lenses themselves as is done in an optical microscope. Similar to SEM, the components and specimen of a TEM also have to be housed in a chamber having a high vacuum of the order 10^{-3}-10^{-4} Pa for its proper

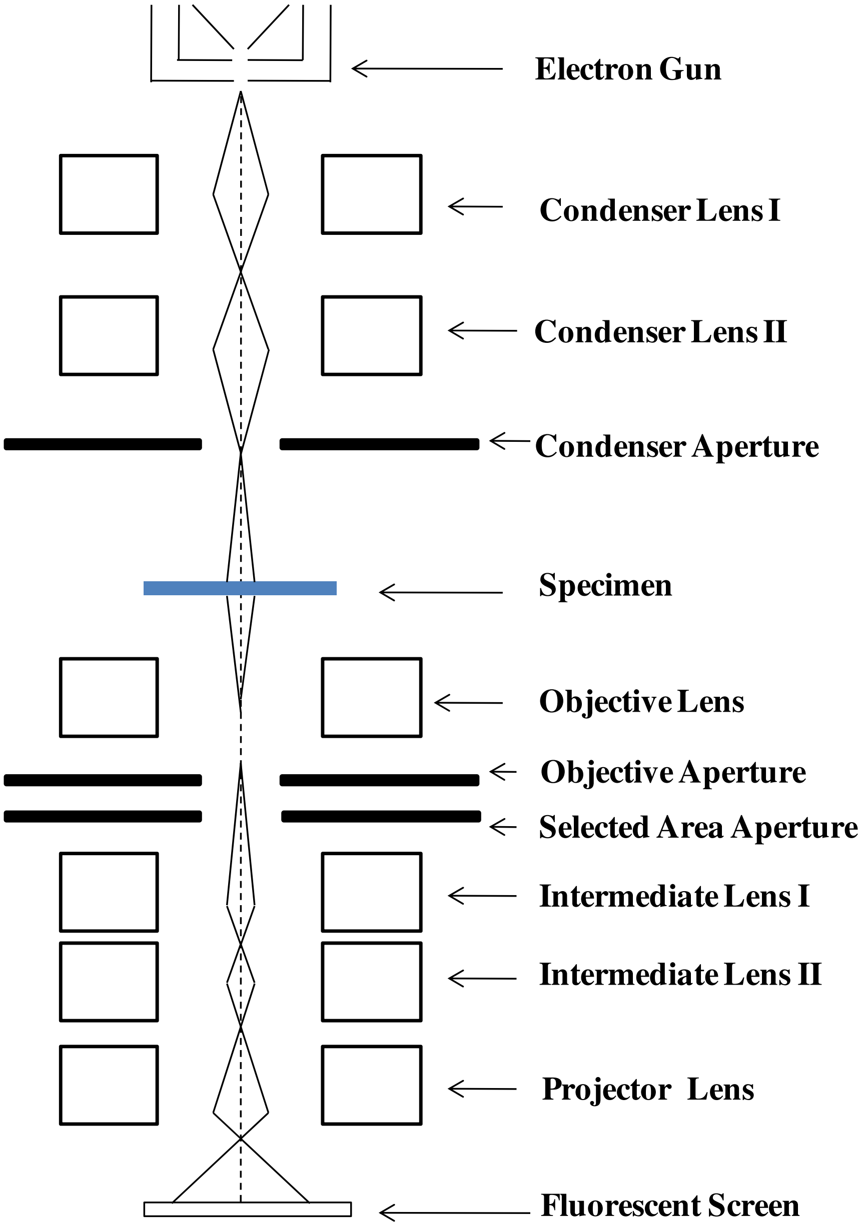

Figure 2.12: Schematic diagram of basic components in a TEM.

functioning. Using TEM, one can also obtain diffraction pattern which enables to understand the detailed crystal structure analysis of the sample. The machine which we have used for imaging is JEM-2100F (JEOL) and it was operated at 200 KV.

2.5.5 X-ray photoelectron spectroscopy

In XPS, the surface of sample is irradiated with photons of characteristic energy (usually MgK$_\alpha$ radiation).These photons directly interact with core electrons of the sample atoms. As a result, ionized states are created and a photoelectron is emitted with a kinetic energy given approximately by the difference between the photon energy and its binding energy. The measured photoelectron spectrum is therefore a direct indication of the binding energy of the different atomic electron levels and is often directly calibrated in eV of binding energy. The lower the kinetic energy, the higher the binding energy. Because usually the kinetic energy is plotted on the x-axis with increasing energy to the right, the binding energy increases from right to left. The inelastic mean free path of the photo electrons is determined by the probability to suffer an energy loss, and the attenuation length (taking into account inelastic and elastic scattering) is determined by the probability to be received by the electron energy analyzer. In both the cases, kinetic energy and matrix determine and limit the information depth to nanometre region. This fact makes XPS analysis surface specific.

In this work we have used XPS System (RIBER system model: FCX 700) consisting of Mg-K$_\alpha$ (1253.6eV) X ray sources and MAC-2 electron analyzer. The binding energy scale was calibrated with respect to Au-4f$_{7/2}$ line of 83.95eV.For charge referencing adventitious C-1s peak set at 285eV was used. Each data set was first corrected for the non-linear emission background. The data was then fitted with Gaussian function to find the peak positions.

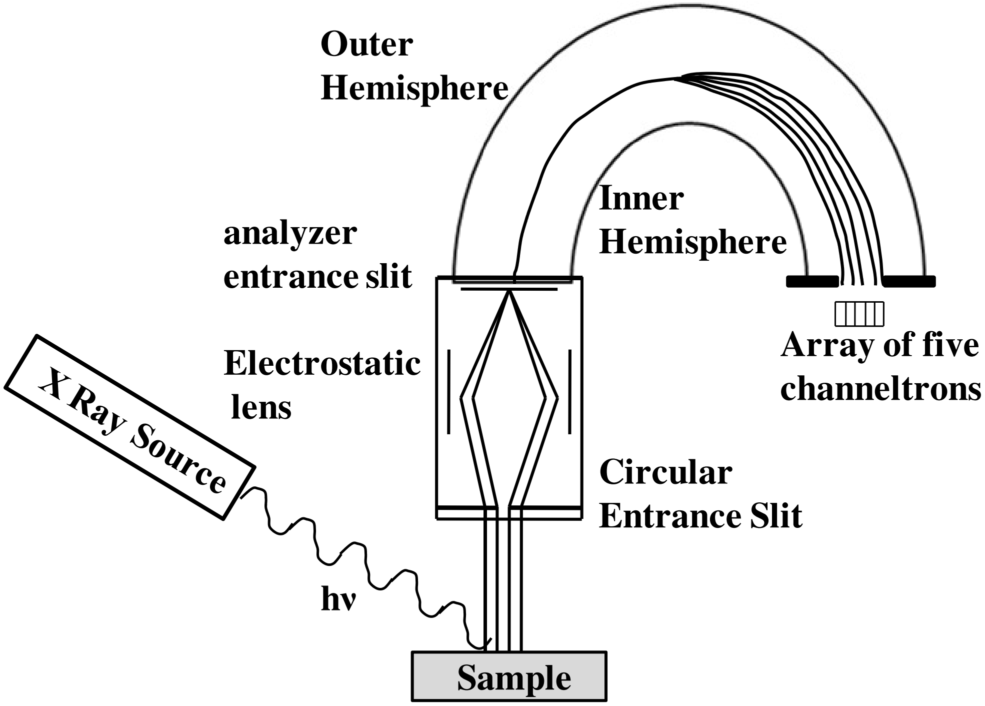

Figure 2.13: Schematic of the basic apparatus used in X-ray photoelectron spectroscopy. X rays are produced by the Al anode bombardment of electrons created at the filament. The X-rays impinge on a sample, producing photoelectrons that are detected after analysis in the electron energy analyzer.

2.5.6 UV- visible spectroscopy

UV-Visible Spectroscopy is a technique which measures the absorption of ultraviolet/visible radiation as a function of wavelength. When ultraviolet or visible light is absorbed by a molecule, there is electronic excitation among various energy levels within the molecule. Consequently, the wavelength of absorption peaks can be correlated with the type of bond present in the species. The absorption of UV or visible radiation corresponds to three types of electronic transitions: (i) transitions involving π, σ and n (non-bonding orbital) electrons, (ii) transitions involving charge free electrons, (iii) transitions involving d and f electrons [77]. The energy required for an electron in a bonding (σ) orbital to get excited to the corresponding antibonding (σ^*) orbital is large and thus not seen in typical UV-Vis spectrum. The energy required for an electron in a non-bonding orbital (n) to antibonding (σ^*) orbital is usually less than $\sigma \rightarrow \sigma^*$ transition. Light having wavelength in the range 150-

200 nm is absorbed for this transition. Most absorption spectroscopy of organic materials is based on transition of *n* or *π* electrons to *π** excited state and the absorption peaks for these transitions fall in the range 200-780nm. For $n \rightarrow \pi^*$ transitions the molar absorptivities are relatively low. Most UV/Visible spectroscopic studies are carried out between 180 -780 nm. The only molecular moieties that absorb light in the 200 - 800 nm region are *π* electron functions and hetero atoms having non bonding valence shell electron pairs. Chemical functionalities that are responsible for absorption are referred to as chromophore. Thus any species which is coloured absorbs visible light and any moiety with an extended system of alternating double and single bonds will absorb UV light. This makes UV-Visible spectroscopy applicable to a wide range of samples.

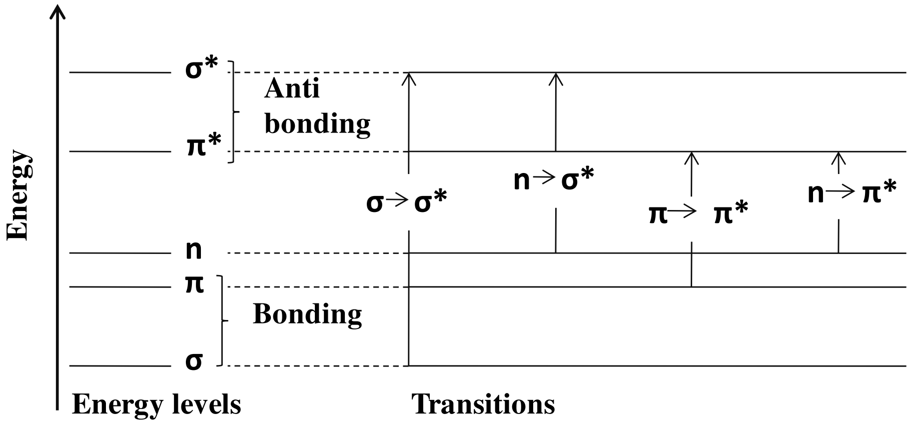

Figure 2.14: Electronic energy levels and possible electronic transitions of *π*, *σ* and *n* electrons

For our experiment we have used JASCO V-530 spectrophotometer. The schematic of the double beam single monochromator spectrometer is shown in Fig 2.15. In this spectrometer the intensity (I) of the beam passing through the sample is compared with a reference beam (I_0) and in output we get absorbance ($A = log_{10}I/I_0$) Vs. wavelength. Absorbance is directly proportional to the number of absorbing molecules (concentration) in the light path and path length as per Beer Lambert's law stated as $A = \epsilon lc$; where ϵ is molar absorption coefficient ,c is the concentration of absorbing species and l is the path length.

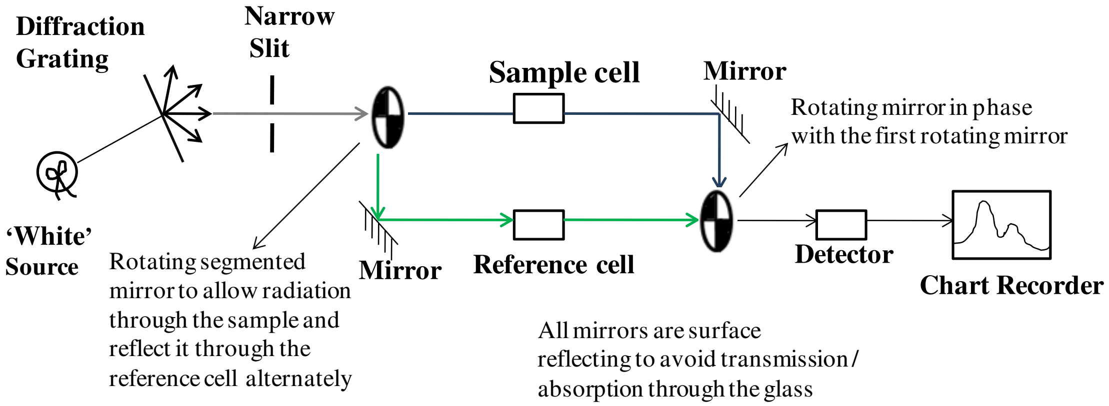

Figure 2.15: Block diagram of a typical double beam single monochromator UV-spectrometer.

2.5.7 Raman Spectroscopy

Raman spectra were recorded using LABRAM-1 micro/macro Raman spectrometer (Horiba Jobin Yvon, Bensheim, Germany). The 632.81 nm line of He-Ne LASER was used for excitation and the scattered Raman signals were analyzed in a back scattering geometry using a single Monochromator equipped with a Peltier Cooled CCD detector for multichannel detection.

Raman is a light scattering technique, in which molecular vibrations or collective excitations in solids (phonons) scatter incident light from a high intensity LASER light source. Most of the scattered light is at the same frequency as the LASER (elastic) and is called Rayleigh scattering (Figure 2.16 (a)). A small amount of light (typically 10^{-6} – 10^{-7} from the LASER intensity) is scattered at different frequencies (inelastic scattering), which depend on the chemical structure of the studied material – this is called Raman Scattering.

When the LASER light interacts with vibrations or phonons in the sample, the frequency of the LASER photons is shifted up or down. As compared to exciting radiation, the lines of longer wavelength are known as Stokes line and those having shorter wavelength are known as anti-stokes line (Figure 2.16 (a)). Raman shift defined by $\Delta\nu = \frac{1}{\lambda_0} - \frac{1}{\lambda_1}$ gives information about the phonon or vibrational modes in the material. Here λ_0 and λ_1 refer respectively to the excitation wavelength and Raman spectrum wavelength respectively. Thus a Raman spectrum features a number of peaks with shifted frequencies that exactly correspond to the frequencies of the molecular or phonon vibrations. These peaks can correspond to specific molecular bond vibrations, such as C-C, C=C, N-O, C-H, O-H etc, or / and groups of bonds such as benzene ring breathing mode, polymer chain vibrations, lattice modes etc.

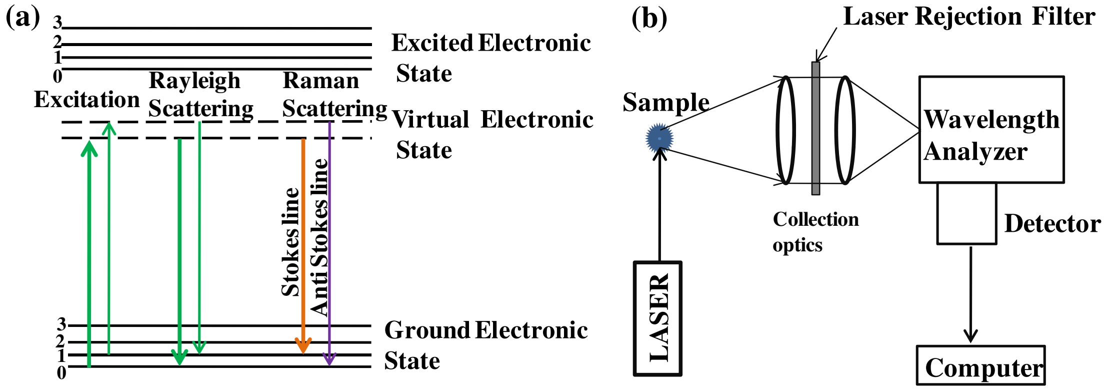

Figure 2.16: (a) Schematic of the energy levels involved in Raman spectroscopy. (b) Generic Raman spectrometer showing main components: LASER, collection optics, wavelength analyzer, detector, computer. Many variations of geometry and components are in common use. Laser filter is often called as a notch filter.

In a Raman micro spectrometer the sample is illuminated with a laser beam through an objective of the integrated research grade optical microscope. Light from the focal spot is collected in back reflected mode with the same high quality microscope objective and sent through a spectrograph. Frequencies close to the laser line, due to elastic Rayleigh scattering, are filtered out while the rest of the collected light is dispersed onto a two dimensional detector (spectroscopic quality CCD).

Raman spectroscopy is an advanced analytical technique based on the inelastic scattering (not absorption) of photons that interact with molecules in biological or chemical samples. The amount of photon energy shift indicates the type of bonds present in the sample molecules (C=O, CH_2, CH_3, CCl, etc). As a result, Raman spectroscopy is a very accurate technique that can identify with great specificity various molecular bonds and therefore produce a precise spectral fingerprint unique to the particular molecules and their structures.

2.5.8 Photoluminescence measurement by a Spectrofluorometer

Photoluminescence spectroscopy is a contactless, non-destructive method of probing the electronic structure of materials. Light is directed onto a sample, where it is absorbed and imparts excess energy into the material in a process called photo-excitation. One way this excess energy can be dissipated by the sample is through the emission of light, or luminescence. In the case of photo-excitation, this luminescence is called photoluminescence.

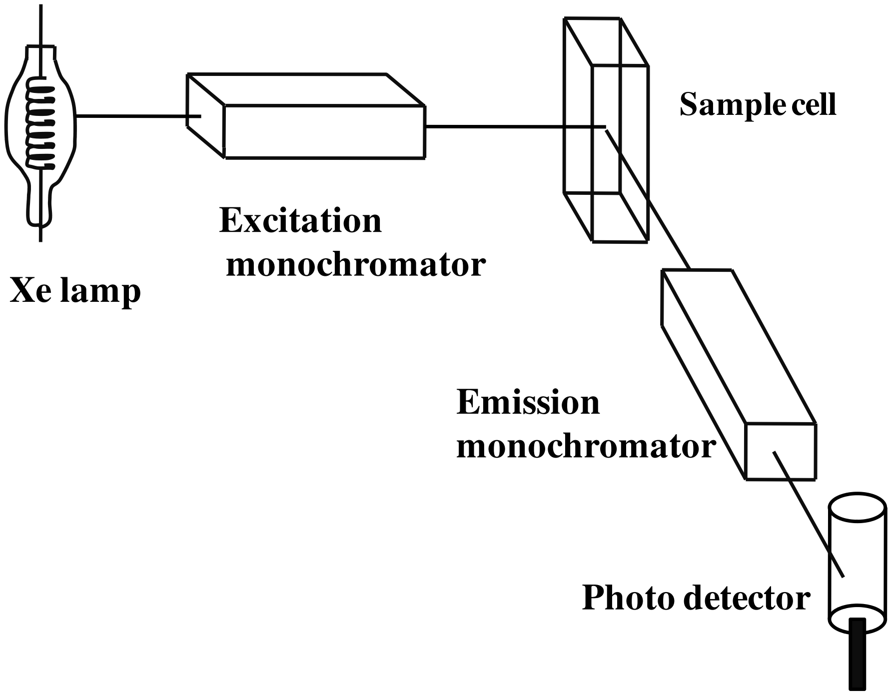

Figure 2.17: Schematic layout of a photoluminescence setup.

The intensity and spectral content of this photoluminescence is a direct measure of various important material properties. Photo-excitation causes electrons within the material to move into permissible excited states. When these electrons return to their equilibrium states, the excess energy is released and may include the emission of light (a radiative process) or may not (a nonradiative process). The energy of the emitted light (photoluminescence) relates to the difference in energy levels between the two electron states involved in the transition between the excited state and the equilibrium state. The quantity of the emitted light is related to the relative contribution of the radiative process.

A spectrofluorometer is an analytical instrument used to measure and record the fluorescence of a sample (Fig. 2.17). While recording the fluorescence, either the excitation, the emission, or both the wavelengths may be scanned. A continuous source of light shines onto an excitation monochromator, which selects a band of wavelengths. This monochromatic excitation light is directed onto a sample, which shows luminescence. The luminescent light is directed into a second emission monochromator, which selects a band of wavelengths, and shines them onto a detector. The signal from the detector is reported to a system controller and host computer, where the data can be manipulated and presented using special software.

Various light sources may be used as excitation sources; including lasers, photodiodes, and lamps; xenon arcs and mercury vapour lamps in particular. A laser only emits light of high irradiance at a very narrow wavelength interval, typically under 0.01 nm, which makes an excitation monochromator or filter unnecessary. The disadvantage of this method is that the wavelength of a laser cannot be changed by much. By contrast, a xenon arc has a continuous emission spectrum with nearly constant intensity in the range from 300-800 nm and a sufficient irradiance for measurements down to just above 200 nm. Filters and / or monochromators may be used in fluorimeters. A monochromator transmits light of an adjustable wavelength with an adjustable tolerance. The most common type of monochromator utilizes diffraction grating, that is, collimated light enters a grating and exits with a different angle depending on the wavelength.

The detector can either be single-channeled or multichannel. The single-channeled detector can only detect the intensity of one wavelength at a time, while the multichanneled one detects the intensity at all wavelengths simultaneously, making the emission monochromator or filter unnecessary.

2.5.9 Impedance Spectroscopy

The measurement of the electrical impedance of a sample as a function is often referred to as impedance spectroscopy. In this thesis work, Impedance Spectroscopy was employed to study the various electron transfer processes occurring at the interfaces of a sensor assembly and hence for the identification of different elements of a complex sensor device. Impedance spectroscopy studies in the frequency range of 1Hz to 1MHz were carried out using a frequency response analyzer (FRA) attached with a potentiostat (PG-STAT 20, Echo Chemie, The Netherlands).The peak to peak amplitude of ac signal and dc signal was maintained at 20mV and 500mV, respectively. The measured data were fitted using Zsimpwin software.

2.5.10 Kelvin Probe Technique

The Kelvin Probe is a non-contact, non-destructive vibrating capacitor device used to measure the work function of conducting materials or surface potential of semiconducting or insulating surfaces. The Kelvin Probe measures contact potential difference (V_{CPD}) between a conducting Au tip and a sample [78]:

$$V_{CPD} = \frac{\Delta\phi}{e} \tag{2.4}$$

where *e* is electronic charge and $\Delta\phi$ refers to difference in work function of the tip and the sample. This V_{CPD} is further used in calculation of the work function of the sample.

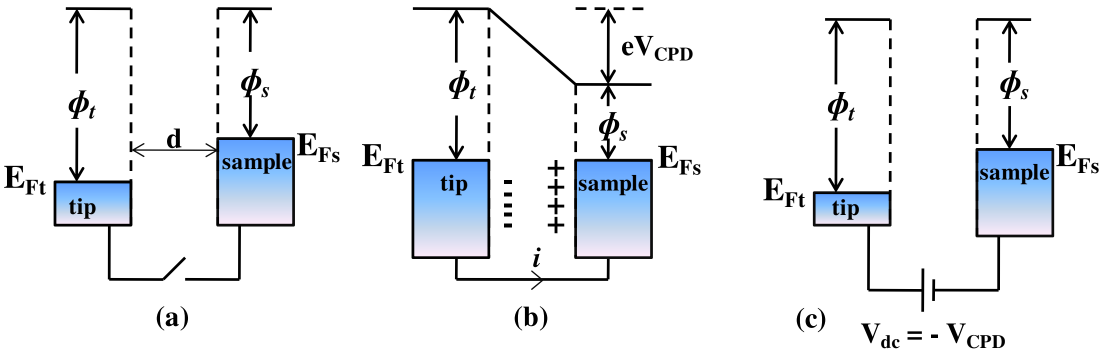

Figure 2.18: Block diagrams depicting Kelvin Probe processes. (a) Flat band condition. (b) band bending between metal and specimen after contact (c) Equilibrium condition after application of external voltage V_{dc}.

Figure 2.18 (a) shows tip and sample in close proximity, but without electrical contact between them. Their Fermi levels align at the vacuum level at energies corresponding to the respective work functions. As the tip and the sample are connected together by a wire as shown in Figure 2.18(b), electrons flow from the sample with the smaller work function to the tip with larger work function. This causes the sample with smaller work function to charge positively while the tip charges negatively. This creates a contact potential difference V_{CPD} between the tip and sample, shifting their electronic states relative to each other. An electrical force acts on the contact area due to V_{CPD}. As shown in Figure 2.18 (c), this force can be nullified. If an external bias V_{dc} that has the same magnitude as the V_{CPD} with opposite direction, the applied voltage eliminates the surface charge in the contact area. The amount of applied external bias that nullifies the electric force due to V_{CPD} is equal to the work function difference between the tip and the sample, therefore the work function of the sample can be calculated if the tip work function is known.

Work function is measured by applying an AC voltage, V_{ac} (ω) plus a DC voltage V_{dc} to the tip mounted just above the sample surface kept at a ground potential [79]. V_{ac} generates oscillating electrical forces between the Kelvin probe tip and sample surface. V_{dc} nullifies the oscillating electrical forces that originated from CPD between tip and sample surface. The electrostatic force between the tip and sample surface is given by [79, 80] :

$$F_{el} = -\frac{1}{2}\frac{\partial C}{\partial z}(V_{dc} - V_{CPD} + V_{ac}\sin\omega t)^2 \tag{2.5}$$

The above force can be divided into three components. The component which is used to measure the V_{CPD} is given by:

$$F_{\omega} = -\frac{\partial C}{\partial z}(V_{dc} - V_{CPD})V_{ac}\sin\omega t \tag{2.6}$$

When electrostatic forces are applied to the tip by V_{ac} with V_{dc}, additional oscillating components (due to the electrical force) will be superimposed to the mechanical oscillation of the tip. A lock-in amplifier is employed to measure the V_{CPD}, to extract the electrical force component with frequency ω (F_{ω}), as a function of V_{CPD} and V_{ac}. The output signal of the lock-in amplifier is directly proportional to the difference between V_{CPD} and V_{dc}. The V_{CPD} value can be measured by applying V_{dc} to the tip, such that the output signal of the lock-in amplifier gets nullified and F_{ω} equals zero. Subsequently, the value of V_{dc} is acquired for each point on the sample surface, composing a map of the work function or surface potential of the whole sample surface area.

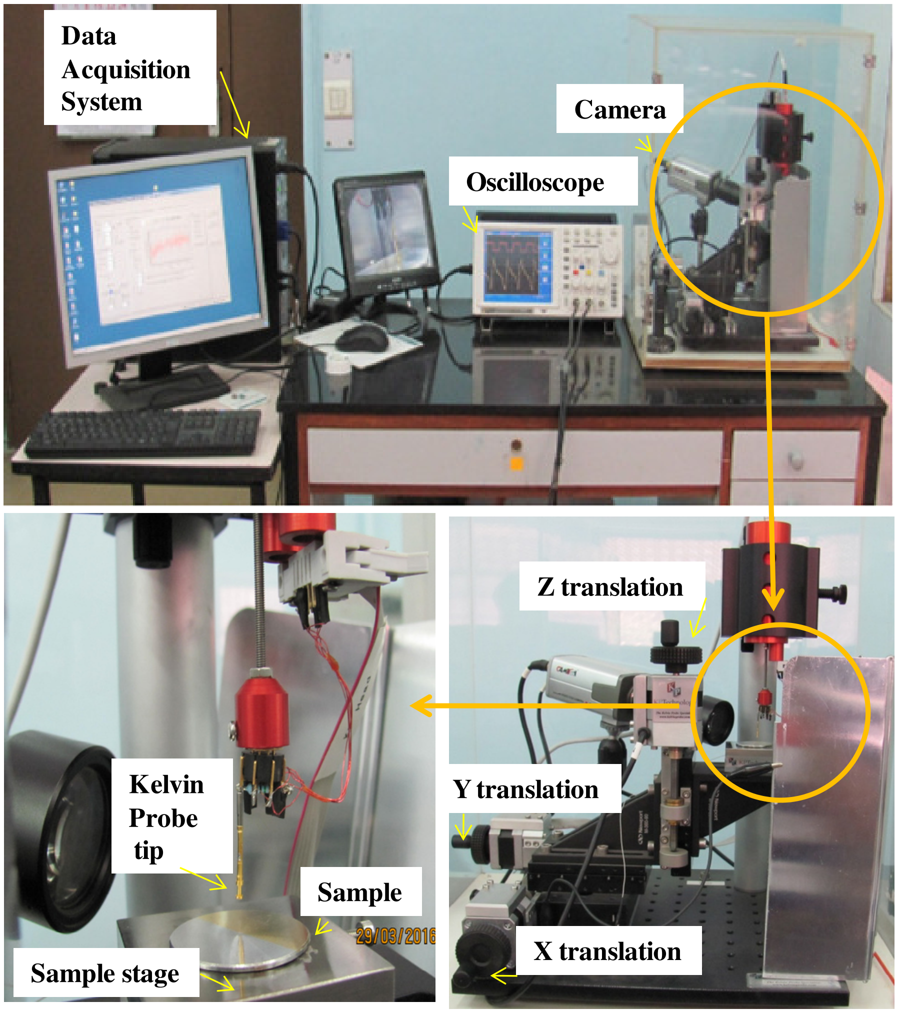

Figure 2.19: A photograph of Scanning Kelvin Probe system SKP5050 manufactured by KP technology.

2.6 Electrical measurement

The experimental procedure for electrode deposition and the charge transport measurements for sensor in configurations *viz.*, thin film and transistor are discussed in this section.

2.6.1 Metal electrodes deposition by thermal evaporation

To measure charge transport and gas sensing properties, gold electrodes were deposited using a thermal evaporation system, as schematically shown in Fig. 2.3(a). Gold pads (size: 2 mm ×3 mm) were deposited through a metal mask with different electrode spacing (12-100 μm). The films were loaded in vacuum chamber which is connected to a TMP based vacuum pumping system. To deposit gold electrodes, 99.99% pure gold wire is loaded on a tungsten filament, which was resistively heated by external power supply. To prevent diffusion of gold atoms into the Pc films, electrodes were deposited with very slow rate (0.5Å/s). The deposition rate and thickness of the deposited electrodes is monitored through a quartz crystal monitor. In OFET, for gate electrode aluminium was deposited with deposition rate of 0.5Å/s. However, for Source and Drain electrodes, Au was used.

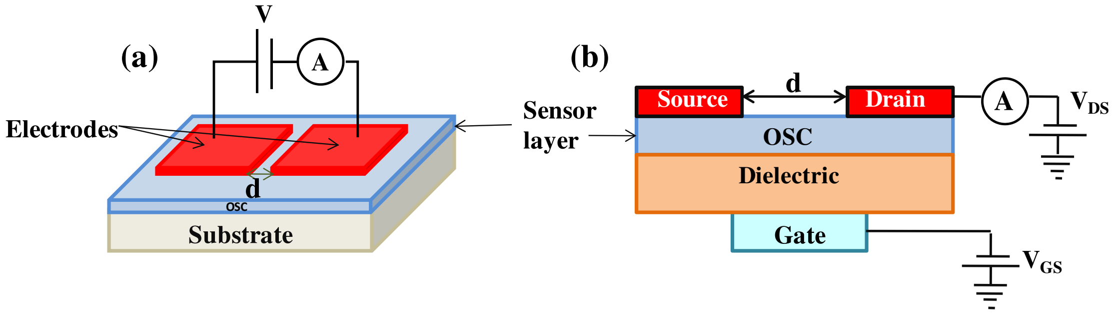

Figure 2.20: A schematic of (a) in plane charge transport measurement geometry in a thin film (b) charge transport in organic thin film transistor.

2.6.2 Conductivity measurement

In our studies, for chemiresistive type sensors *J-V* characteristics were measured using two-probe in-plane geometry. To measure *J-V* characteristics a silver wire was attached to the previously deposited electrode by conducting silver paint. Keithley 6487 picoammeter / voltage source and computer based data acquisition system were used to record the *J-V* characteristics. All measurements were carried out in dark to avoid the effect of photocurrent. In order to rule out the effect of film inhomogeneities, *J–V* characteristics were measured on at least three pairs of electrodes deposited on a film at different positions. In case of OFETs, *I-V* characteristics and capacitance were measured under ambient atmosphere using Keithley voltage source/current meter (model 6487) and Agilent 4980A LCR meter, respectively.

Micromanipulator tips were used to make contact from the electrode to source meter and LCR meter, the photograph is shown in Fig. 2.21.

For measuring the temperature dependence of the resistivity and temperature dependent *J–V* characteristics, the samples were mounted in a closed cycle cryostat. Conductivity measurements were carried out in a helium gas environment. The cryostat (CCR APD Cryogenics make) consists of a compressor, which compresses the Helium gas and expands it in the vicinity of the sample chamber. Because of Joule Thomson expansion of Helium gas, its temperature falls and it cools the region surrounding it. Platinum resistance sensors (Pt-100) are used to monitor the temperature. Lakeshore temperature controller (Lakeshore 330 auto tuning temperature controller) controls temperature of the sample chamber. A small manganin heater was used to heat the sample for measurements of transport properties at different temperatures.

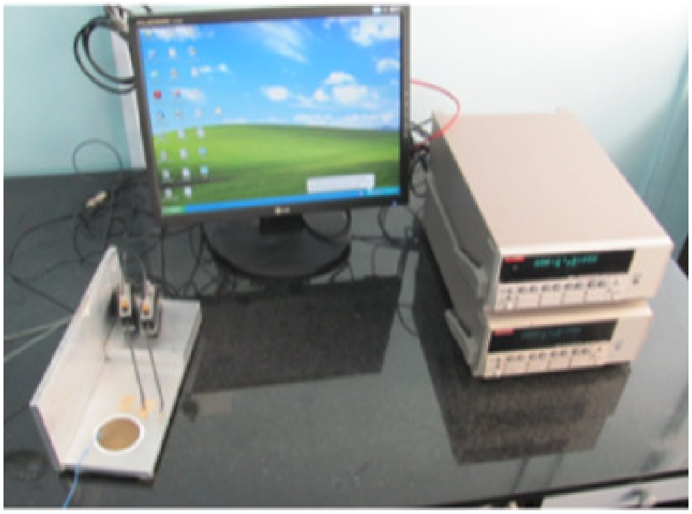

Figure 2.21: Experimental Set up for measuring transistor characteristics.

2.7 Gas sensing setup

The gas sensing studies of our devices were performed using a homemade gas sensitivity measurement set up. It consists of a cylindrical chamber made of stainless steel of

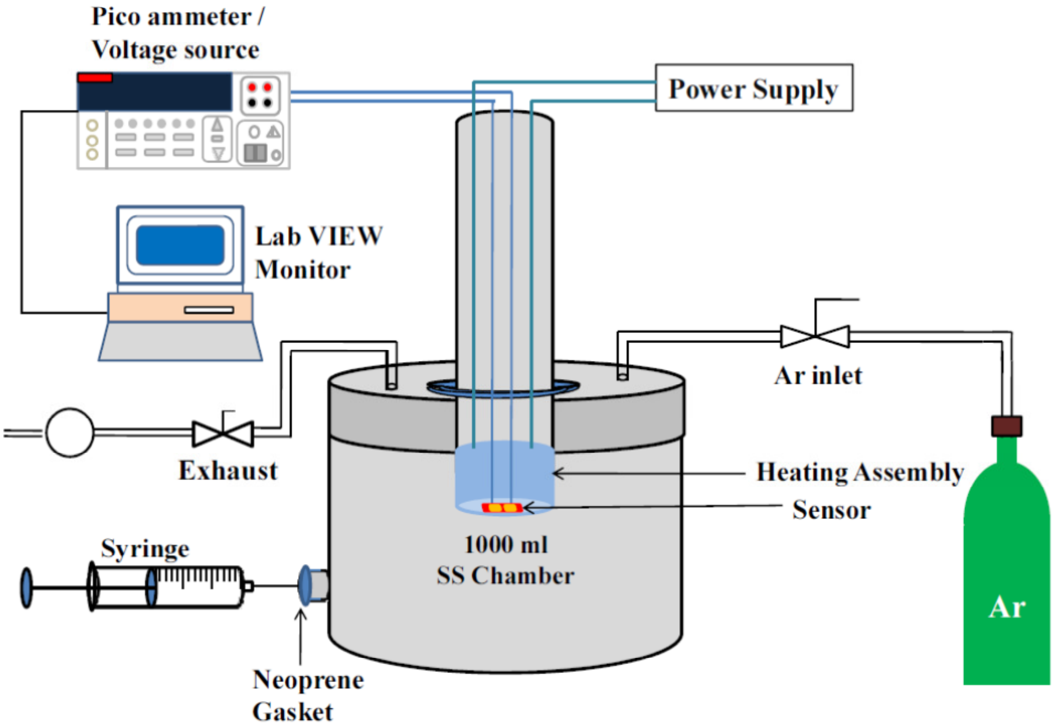

Figure 2.22: Schematic representation of gas sensing measurement setup.

volume 1000 cm^3.The chamber was made tight by rubber beading. The sensor was mounted on heater surface made of Stainless steel (grade 304). The temperature of the heater was controlled by an external power supply and temperature controller. A known amount of gas (to be sensed) was injected into the closed chamber using a micro-syringe. To measure the response of the sensor towards this gas, current at a particular bias as a function of time was measured by a picoammeter /voltage source and computer based data acquisition system using LabVIEW. For the recovery of the gas, sensor was exposed to ambient atmosphere by opening the chamber.

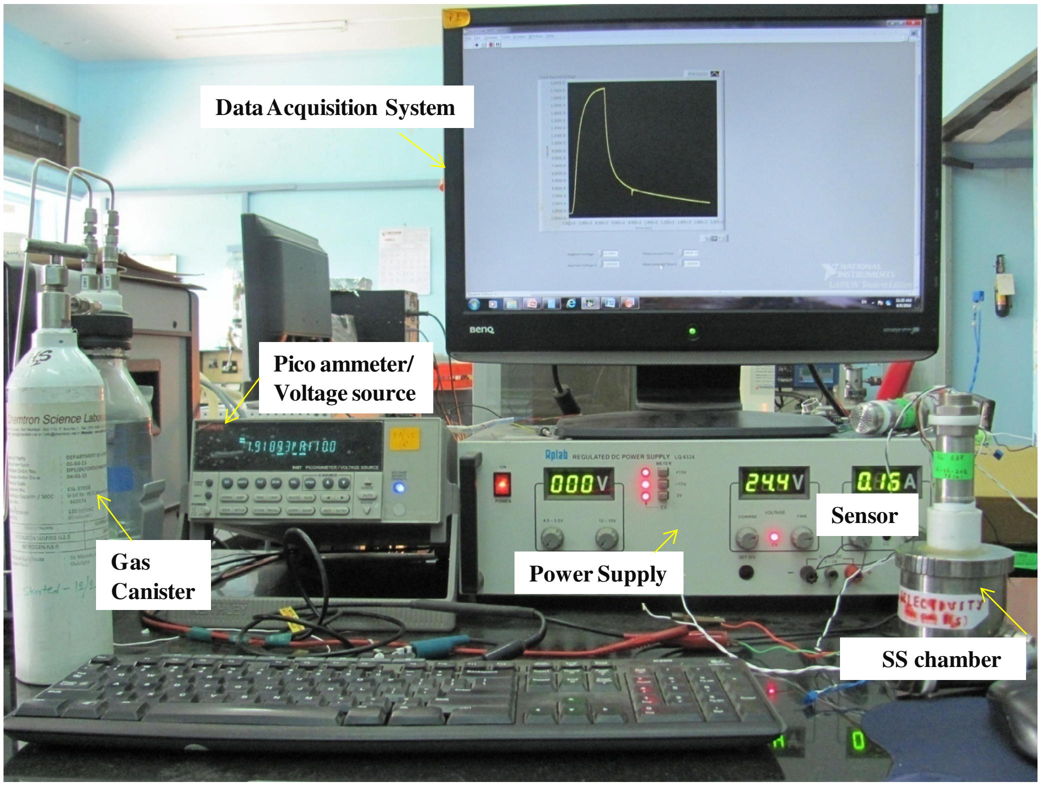

Figure 2.23: A photograph of gas sensing setup used in the present work.

CHAPTER 3

Growth of flexible Cobalt Phthalocyanine thin film with high charge carrier mobility and their application as NH_3 Sensor

3.1 Introduction

Plastic substrates have many attractive characteristics, such as, flexibility, light weight, shock resistance, softness and transparency apart from being low cost as compared to counterpart inorganic substrates. Development of high mobility organic semiconductor devices on flexible substrate (such as BOPET, PEN, POLYMIDE etc) is highly desired for the fast and low cost next generation technologies, such as paper-like flexible displays, optoelectronic applications (light-emitting or photo- voltaic diodes), thin-film transistors (TFTs), and integrated circuits (ICs) [81]. There are several challenges involved with the flexible electronics, which can be broadly classified into two categories: active layer related issues (*e.g.*, charge carrier mobility, electrode / active layer interface, etc.) and flexible substrate related issues (*i.e.*, mechanical flexibility, long term stability on repeated bending, etc.) [82]. In this context, patterned arrays of printed organic devices based on chemically stable organic semiconductors have been widely investigated. So far most of the work has been done for solution processed organic semiconductor thin films and reasonably high values of charge carrier mobility (~16 $cm^2 V^{-1} s^{-1}$) has been reported [83]. As seen from Table 1.4 of chapter 1, metal phthalocyanines, which have shown tremendous potential as a key component in organic photovoltaic and gas sensing devices [9, 84-86], have never been investigated for flexible gas sensor applications. Recently there has been an increasing number of reports on organic as well as inorganic films deposited on flexible substrates for their applications in chemical sensors [43, 87-90]. Studies of such functional devices fabricated on flexible substrates have become an important area of current research [81, 91-

94]. Commonly used methodologies to improve the gas sensing properties of organic / inorganic flexible films include: adding suitable doping, fabrication of nanostructures or hybrid structures and operating the sensor at high temperatures. One of the requirements of flexible sensors is that their sensing characteristics should not degrade upon bending conditions. However, most of the earlier studies shows that bending stress leads to the degradation of sensing characteristics of flexible sensors [43, 87, 95]. In this chapter we discuss the charge transport as well as room temperature chemiresistive gas sensing characteristics of CoPc thin films deposited on flexible BOPET substrate by MBE. The charge transport and gas sensing properties were studied in flat as well as in bend conditions and plausible mechanism for tailoring of these properties under flat and bend conditions are discussed in this chapter.

3.2 Experimental

3.2.1 Deposition of CoPc film on flexible BOPET sheet by MBE

Thin films of different thicknesses *i.e.* 5, 10, 20, 40, 70 and 100 nm were grown on pre-cleaned flexible BOPET substrates (size: 10mm × 10 mm) by molecular beam epitaxy (base vacuum ~ 10^{-8} mbar) [96]. BOPET substrates were procured from M/s DuPont. The growth temperature and deposition rate were respectively, 100°C and 2 Å/s. Substrate temperature higher than 100°C deforms the BOPET sheet. A few pairs of Au electrodes (3mm×2mm) separated by 12 μm were deposited using a metal mask for measuring in-plane current through these films. Subsequently, silver wires were attached to the gold electrodes using silver paint. Figure 3.1 (a) shows the thickness dependence of J (measured at 50 V) for CoPc films. It is evident that J attains a maximum value for the critical thickness of ~20 nm. For film thickness < 20 nm, low value of J is attributed to the incomplete coverage (mostly due to surface roughness ~ 6 nm). However for thickness >20 nm, the J gets suppressed due to enhanced molecular disorder (*i.e*. due to reduced effect of the interaction between substrate molecular chains and CoPc molecules). The higher molecular disorder in thicker film (70 nm) as compared to that of 20 nm thin film is evident from the XRD pattern shown in Fig. 3.1 (b). The thicker film (70 nm) shows a weak intensity of (200) peak along with a higher FWHM. As 20 nm thin CoPc film on BOPET is highly conductive and crystalline, in the following sections, we have made detailed studies on charge transport and gas sensing behavior apart from structural and morphological characterization of 20 nm CoPc film on BOPET.

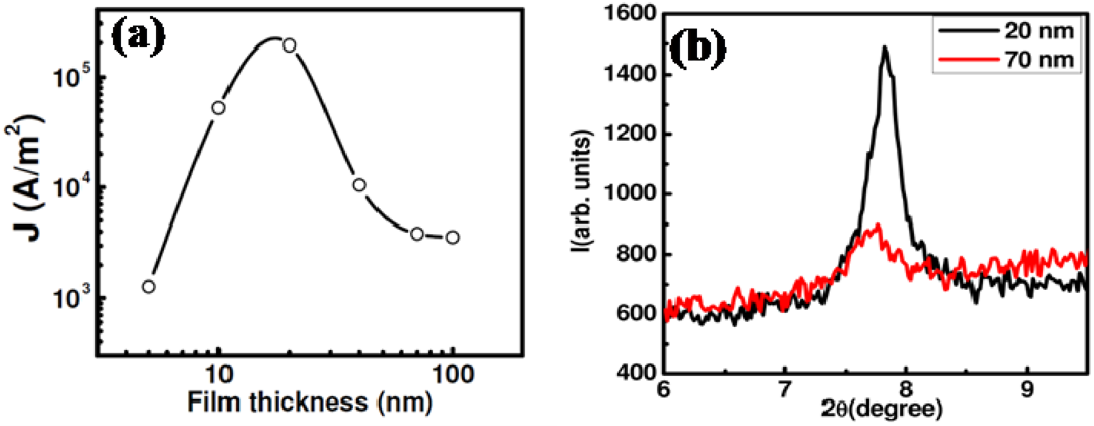

Figure 3.1: (a) Variation of *J* (measured at 50 V) for CoPc films of various thicknesses grown on BOPET substrate. (b) XRD data of 20 and 70 nm thick CoPc films grown on BOPET substrate.

3.2.2 Structural and morphological characterization

Structure of 20nm thick CoPc film grown on BOPET was determined by X-ray diffraction (XRD) using Co K_α (1.789A°) radiation. The surface morphology of the films was imaged by atomic force microscopy (AFM, Nanny's: MV4000) using tapping mode.

Figure 3.2 shows the morphological and structural properties of the BOPET substrate and the 20 nm thick CoPc films grown over it. The AFM image (Fig. 3. 2(a)) of a clean BOPET surface shows a granular morphology with a *rms* roughness of ~ 6 nm, whereas the XRD pattern (Fig. 3.2(b)) of the BOPET shows a broad diffraction peak at 29.9° with a full width

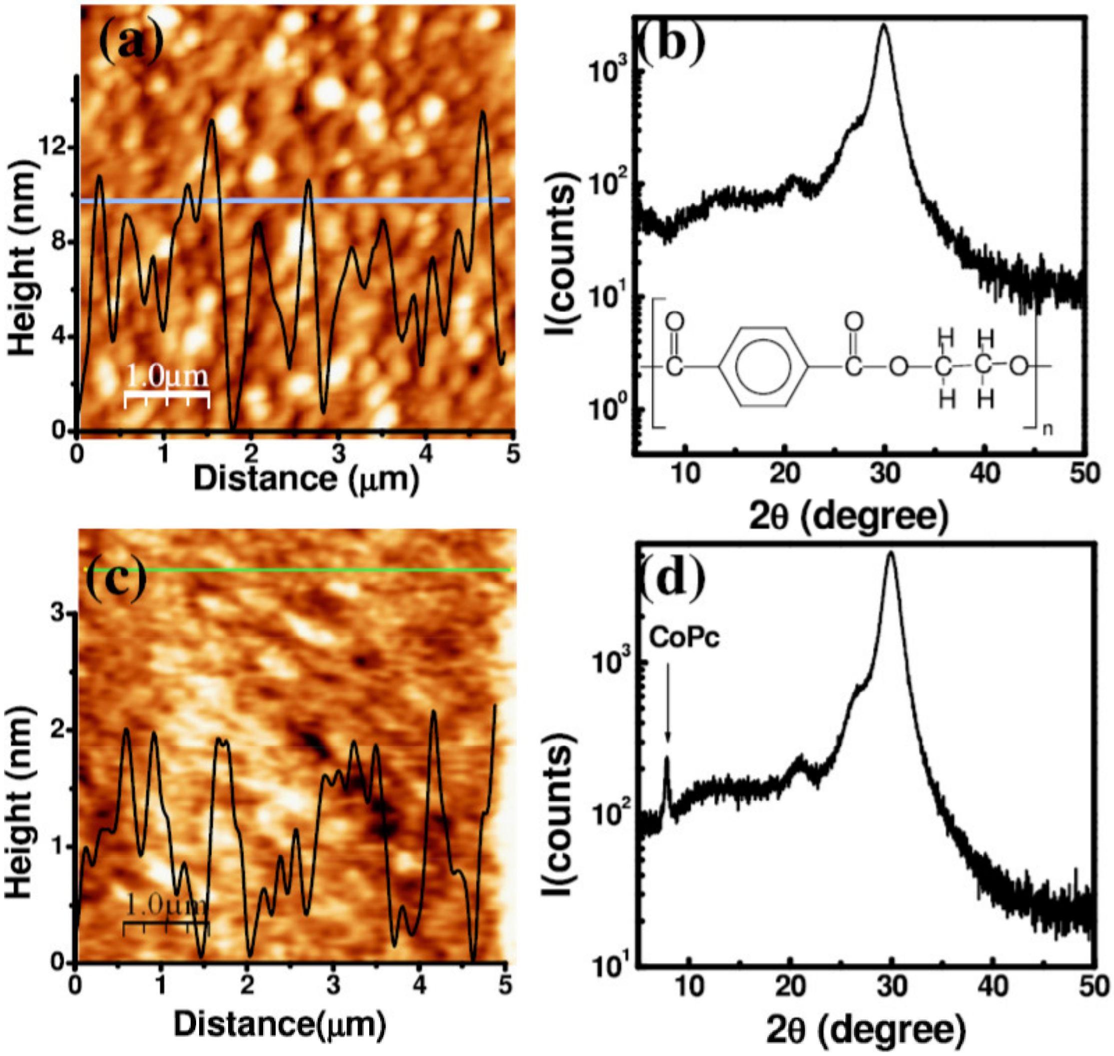

Figure 3.2: (a) AFM image of the bare BOPET substrate and the height profile across the line drawn in the image. (b) XRD pattern reordered for the BOPET substrate. The inset shows the molecular structure of PET. (c) AFM image of the 20nm thick CoPc film grown on BOPET substrate and the height profile across the line drawn in the image. (d) XRD pattern reordered for the CoPc films grown over BOPET substrate.

at half maximum (FWHM) of 1.59°, which clearly indicates the semi-crystalline nature of the substrate [97]. It may be noted that the manufacturing process of BOPET involves formation of a sheet from molten polyethylene terephthalate (PET), which is then biaxially oriented by drawing and, subsequently followed by "heat set" under tension at temperatures >200 ˚C [98]. The heat setting step prevents the sheet from shrinking back to its original un-stretched shape and locks-in the molecular orientation in the sheet plane. The molecular orientation also induces the formation of many crystal nuclei and from the XRD data we have estimated the PET crystallite size of ~ 6.35 nm. The AFM image of 20nm thick CoPc films grown on BOPET substrate (Fig. 3.2(c)) reveals that film consists of randomly distributed elongated grains with *rms* surface roughness of 1.1 nm.

The structural ordering of the CoPc film is evident from the XRD pattern shown in Fig. 3.2(d)). The presence of a Bragg peak at 7.8° corresponding to the (*200*) orientation of the α-CoPc phase, indicates that the film is crystalline with a-axis normal to the substrate plane [99]. The calculated value of a lattice parameter is found to be 26.2A°, which suggests that CoPc molecules are assembled in the "standing on" configuration. In the "standing on" configuration, π-π conjugation direction is parallel to the film plane, which is favorable for the in-plane charge transport and hence, for the chemiresistive gas sensing measurements.

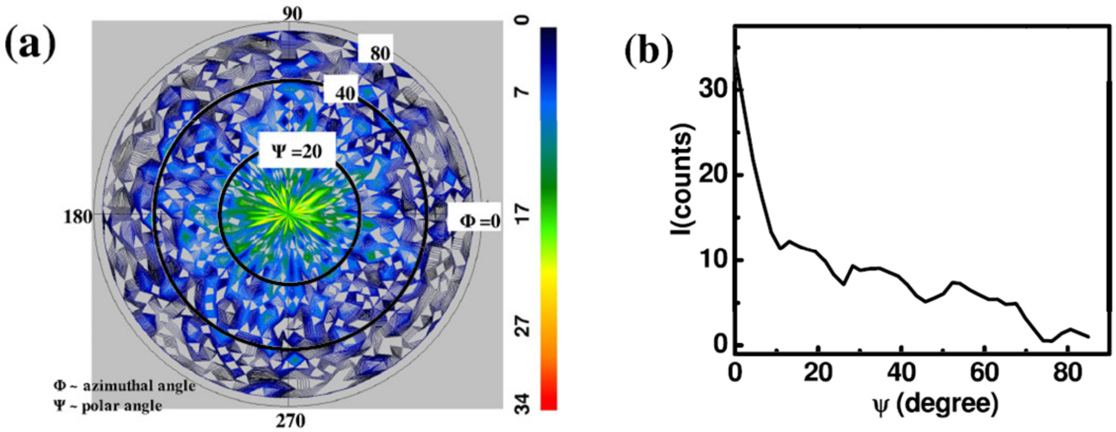

Figure 3.3: (a) X-ray pole figure contour recorded for the (*200*) Bragg peak of 20 nm thick CoPc films grown on BOPET substrate. (b) I-Ψ plot at Φ=171°derived from the pole figure data.

In order to further investigate the out-of-plane texturing of the CoPc molecules, X-ray pole figure measurements were carried out. X-ray pole figure measurement were performed using PANalytical instrument (model EMPYREAN) having Cu K_α (1.4418A°) radiation and 5-axis goniometer. For pole-figure measurements, the *h-h* goniometer is equipped with a texture-cradle with polar angle Ψ (*i.e.*, tilt angle from surface normal) range of 0° to 180° and azimuthal angle Φ (spindle axis rotation) of 0°-355°. X-ray lens and parallel plate collimator were used during the pole figure measurements. A typical 2-dimensional pole figure contour recorded for the *(200)* Bragg peak ($2\theta = 6.9°$) is shown in Fig. 3.3(a). From this figure following inferences are drawn: (i) the intensity (I) is maximum at the centre which monotonically decreases, indicating that there is no preferential texturing in the plane of the films. From the contour, a typically calculated I-Ψ plot at $\Phi = 171°$ is shown in Fig. 3.3(b). It is seen that the intensity falls sharply up to $\Psi = 10°$, but at higher Ψ values the drop is rather slow with several humps of low intensities. This suggests that the grown films have reasonably good out-of-plane texturing, considering the fact that the crystallization in molecular films predominantly takes place via weak van der Waals interactions. A good texturing of CoPc films on BOPET is attributed to (i) orientation of PET molecular chains in the substrate plane, leading to very smooth surface, and (ii) presence of polar groups, *i.e.*, C=O and O–C=O in the PET molecular chains, as shown in the inset of Fig. 3.2(b), that can electrostatically interact with CoPc molecules and a relatively stronger π-π interaction among CoPc molecules along the PET chains. Since PET crystallites are randomly distributed in the substrate plane and therefore this explains absence of in-plane texturing.

In order to investigate how the chemically non-interacting amorphous substrate influence the charge transport properties of CoPc films, 20 nm thick films were grown on glass and transparency sheet of the inkjet printer. The CoPc films prepared on glass substrate, exhibit hysteretic *J-V* characteristics, as shown in Fig. 3.4(a), which has been attributed to the presence of structural defects [100]. The films prepared on the transparency sheet of the inkjet printer shows non-hysteretic *J-V* characteristics, as shown in Fig. 3.4(b). However, the slope of *J-V* data at higher bias region is ~ 3.5, indicating the presence of exponential trap distribution in the films [101].

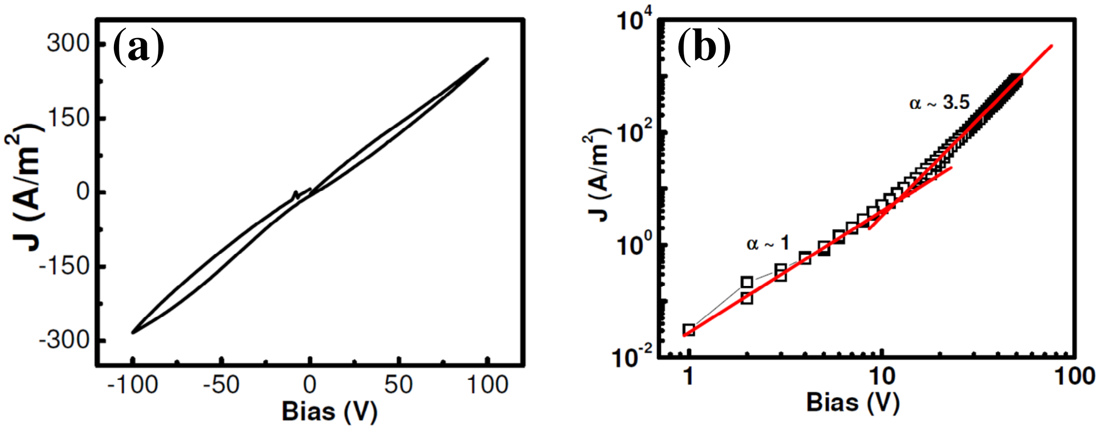

Figure 3.4: (a) *J-V* characteristics for CoPc films grown on glass substrate.(b) *J-V* characteristics of CoPc films grown on smooth side of plastic transparency sheet of the inkjet printer.

3.2.3 Current -voltage characteristics of the film

The temperature dependent current-voltage (*J-V*) measurements were carried out using Keithley 6487 voltage-source / picoammeter and computer based data acquisition system. The low temperature measurements were carried out using a closed cycle cryostat in dark ambient to avoid any possible contributions from photoconductivity. Figure 3.5 (a) shows the *J-V* characteristics of 20nm film on BOPET at different temperature. These curves are highly non-linear and symmetric under positive and negative bias. The *J-V* data plotted in log-log scale, as shown in the lower inset of Fig. 3.5(a), reveals two different power law behavior $(J \propto V^{\alpha})$ as a function of applied bias. At room temperature, for low bias, (<10V) α ~1 indicates ohmic conduction. For ohmic conduction the *J-V* characteristics can be described by $J = n_0 e\mu V/d$, where n_0 is the concentration of thermally generated holes, e is the electronic charge, μ is the hole mobility, and d is the electrode separation. For high bias (>10V), α ~ 2 indicates the shallow trap mediated space charge limited conduction (SCLC). SCLC occurs if the injected carrier density is higher than n_0 and *J* depends on applied bias through the relation: $J = \frac{9}{8}\theta\varepsilon\mu\frac{V^2}{d^3}$, where ε is permittivity (experimentally determined value of ε for our films is 2.45×10^{-11}F/m) and θ is the ratio of free to total (trapped plus free) charge carrier density [101].

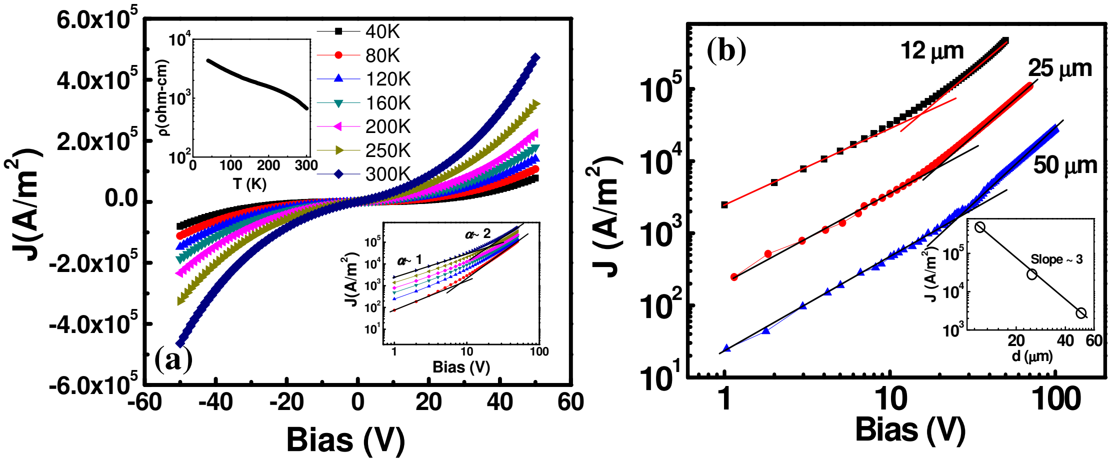

Figure 3.5: (a) Temperature dependent *J-V* characteristics of flexible CoPc films under flat condition. Lower inset shows the Log-log plots of *J-V* characteristics. Upper inset shows the variation of resistivity (ρ) in the temperature range 40 – 300K. (b) *J-V* characteristics of the 20 nm thin CoPc films grown on BOPET substrate recorded for different electrode separation of 12, 25 and 50 μm. Lower inset shows the Log-log plot of *J* versus d (electrode separation).

The crossover voltage between ohmic and SCLC decreases with the lowering of temperature due to reduction in thermally charge carriers. In order to test the validity of SCLC mechanism, *J-V* characteristics were recorded as a function of *d* as shown in Fig. 3.5(b). The variation of *J* (measured at 50 V) as a function of *d*, plotted in the inset of Fig. 3.5(b), reveals a linear fit with a slope of ~ -3, which confirms the SCLC mechanism. The temperature dependence of the resistivity, as shown in upper inset of Fig. 3.5 (a), indicates that at lowest temperature ~ 50 K resistivity increases by a factor of 6 as compared to the room temperature value, hence indicating low trap density if any. It may be noted that in case of disordered phthalocyanine films due to charge trapping by structural defects, the resistivity increases by four orders of magnitude on lowering the temperature [100].

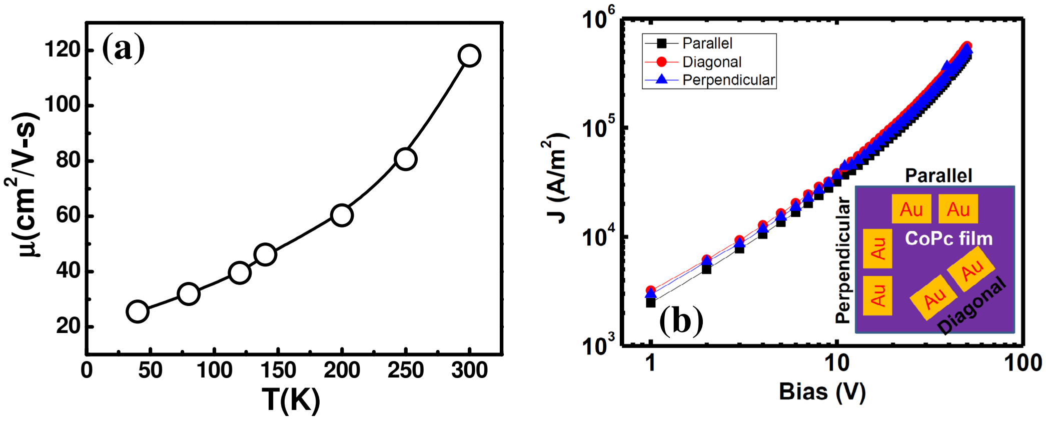

Figure 3.6: (a) Temperature dependence of the mobility (μ) obtained from the analysis of SCLC characteristics. (b) *J-V* characteristics of 20 nm thin CoPc films grown over BOPET substrate in three different electrode geometries shown in the inset.

The μ values at different temperatures were estimated from the slopes of J-V^2 plots assuming $\theta = 1$, *i.e.*, a trap free SCLC as the *J-V* characteristics did not indicate presence of trapping centres even at very low temperatures and the conductivity of these films is very high indicating low trap density, if any. The temperature dependence of μ is plotted in Fig.3.6 (a), which shows a monotonic decrease with temperature. The value of μ at 300K is found to be ~118cm^{2}V^{-1}s^{-1}, which is higher by three orders in magnitude as compared to that reported for disordered metal phthalocyanine films and of the same order that measured for highly ordered films grown along the 36.8° grain boundary of the $SrTiO_3$ bicrystal substrate [100]. This clearly indicates that the CoPc films on BOPET are intrinsically ordered in almost similar fashion as it was along the grain boundary of the $SrTiO_3$ bicrystal substrate. However, a major difference in the present case is that unlike $SrTiO_3$ bicrystal substrate the charge transport is isotropic in the film plane. The *J-V* characteristics measured using three different pair of electrodes fabricated at different angles in the plane of films were identical (Fig. 3.6(b)), which is in agreement with the pole figure measurements. Using the room temperature value of μ and equation for ohmic conduction for the low bias data, the estimated value of thermally generated hole concentration. (n_0) comes out to be 2.1×10^{13}(at 300 K), which is nearly two orders of magnitude higher as compared to the disordered metal phthalocyanine films [101].

3.3 Charge transport and chemiresistive gas sensing characteristics of CoPc film under bent condition

3.3.1 Effect of Bending CoPc film on film resistance

The bending measurements were performed by attaching the flexible samples to curved surfaces of different radii (*r*). The radius of bending was measured using vernier calliper.

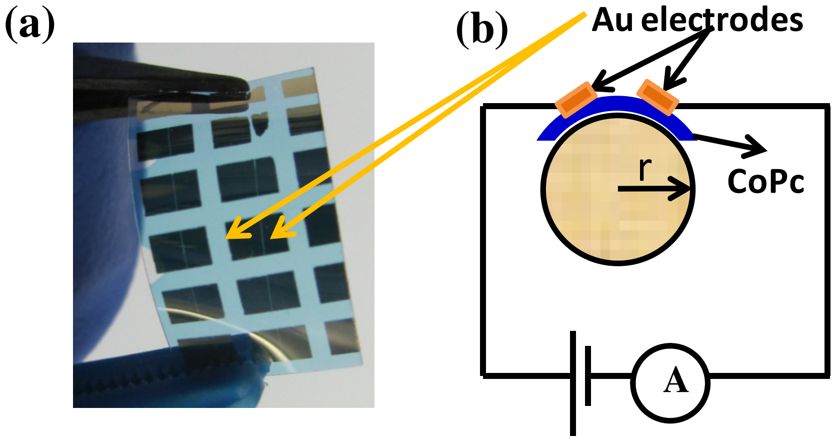

Figure 3.7: (a) Digital photograph of the 20 nm thick CoPc film on BOPET substrate along with patterned Au electrodes (b) Schematic of our bending set up along with charge transport measurement geometry.

The variation of room temperature resistance of the flexible CoPc films as a function of *r* is plotted in Fig. 3.8(a). It is seen that under flat condition (without bending, *i.e.*, $r\to\infty$) the films exhibit a resistance of 2.1±.2 M Ω. Decreasing the radius of the curved surface (*r*), a monotonous increase in the film resistance is observed. Under the bent condition, we have calculated the strain (ε) in the CoPc film by using the equation $\varepsilon=\left(\frac{d_F+d_S}{2r}\right)\frac{(1+2\eta+\chi\eta^2)}{(1+\eta)(1+\chi\eta)}$, where r is the radius of curvature, $\chi = (Y_F/Y_S)$, (Y_F and Y_S are the Young's modulus of the

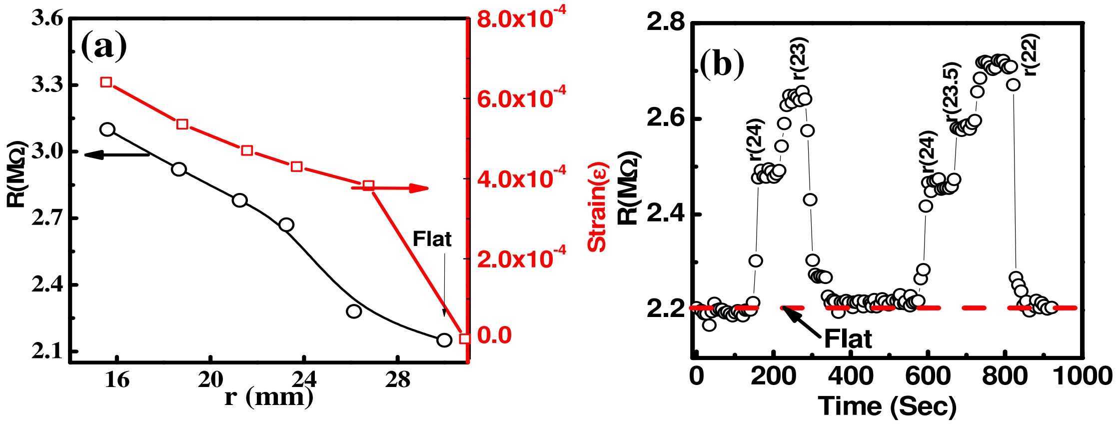

Figure 3.8: (a) Variation of CoPc film resistance and strain (ε) as a function of radius of curvature (r). (b) Change in CoPc film resistance with time upon subjecting to the bending at different r, which on releasing the bending reverts back to the flat position resistance (shown by red dotted line).

CoPc film and BOPET substrate, respectively), and $\eta = d_F/d_S$ (d_F and d_S are the thickness of CoPc film and BOPET substrate, respectively) [102]. The reported literature values of Y_F (CoPc) and Y_S (BOPET) are, respectively, 5.2 GPa and 2.7 GPa [103]. The experimentally measured values of d_F (CoPc) and d_S (BOPET) are, respectively, 20 nm and 120 μm. The calculated value of strain in CoPc film as a function of r is also plotted in Fig. 3.8(a). It is evident that the strain in film increases as r decreases. Therefore, the increase in resistance under bent conditions is not surprising as the strain in the film causes an increase in the intermolecular separation between CoPc molecules, which, in turn, reduces the π-π interaction responsible for the charge transport. To confirm if the strain induced increase in resistance revert back when the film resistance is brought to flat condition, a systematic study on the change in resistance with varying r was recorded as a function of time and the obtained results are shown in Fig. 3.8(b). The data clearly show that (i) within experimental errors the resistance of the films reverts back to the flat conditions, which is independent of both bending at different r and the number of bending times, and (ii) for a particular r

bending, the resistance does not change with time. Thus, a highly reversible resistance change with bending implies that these CoPc films are suitable for the flexible electronics applications.

3.3.2 Current-voltage characteristics of CoPc films under bent condition

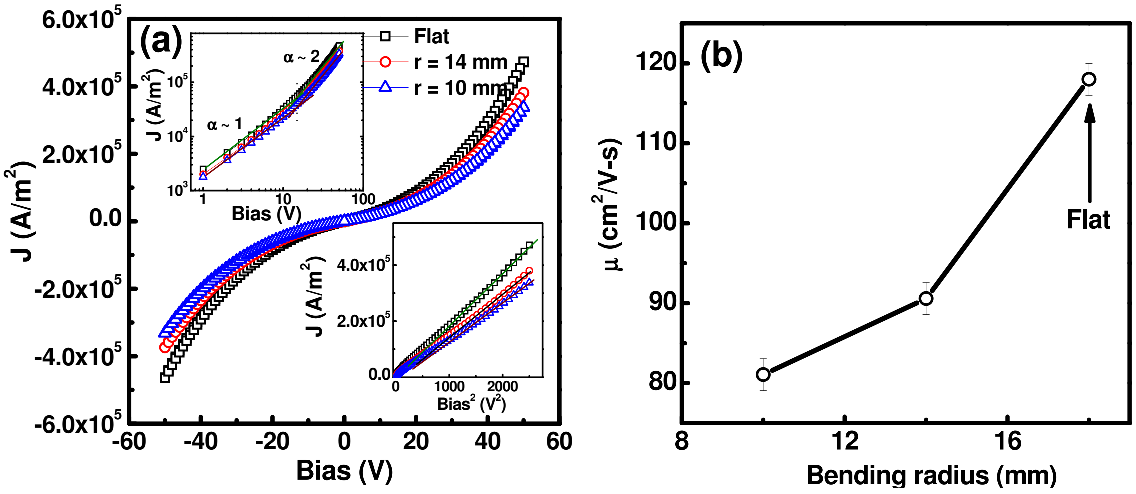

Figure 3.9: (a) Current-voltage (*J-V*) characteristics of CoPc films under flat condition and under different bending radius condition. Upper left inset show *J-V* plots in log-log scale. Lower right inset shows the plot of J-V^2 data. (b) Mobility (μ) versus bending radius of the CoPc films in the temperature range of 40-300 K.

Typical room temperature current – voltage (*J-V*) characteristics measured for CoPc films under flat (without bending *i.e.* $r \rightarrow \infty$) and for different r are shown in Fig. 3.9 (a). It can be seen that with increase in bending (*i.e.* decrease in r) the J decreases but the nature of the characteristic remains the same. It is interesting to note in Fig. 3.9(b) that with an increase in bending (*i.e.* decrease in r) the μ value (as calculated from space charge limited conduction) decreases, however the n_0 remain nearly same as 2.1×10^{11}cm^{-3}. It indicates that with a decrease in r the overlap of π-π electron cloud of CoPc molecules decreases, which obstruct the easy flow of charge between molecules, and hence, lowers the μ.

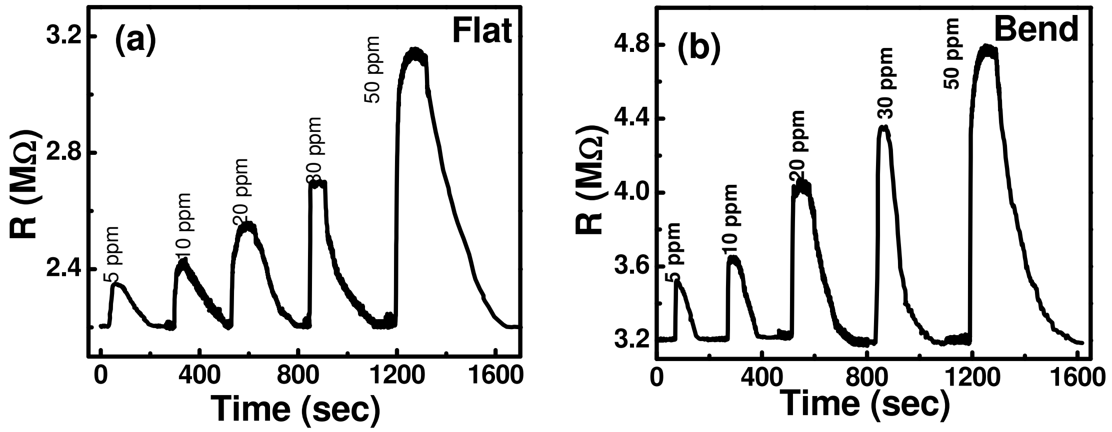

Figure 3.10: (a) Response (resistance versus time) plot for different concentrations of NH_3 under (a) flat condition and under (b) bent condition.

Figure 3.10 (a-b) shows the response / recovery curves (*i.e.* change in film resistance as a function of time on exposure to the different NH_3 concentrations and exposing to ambient conditions once saturation is achieved) of flexible CoPc films under flat and bend condition (r =10 mm) respectively. Films could not be bent for r <10 mm, as under high bent conditions the gold electrodes (pair of size 3 mm ×2mm separated by 12 μm) resulted in an unstable contact resistance.

Figure 3.11 (a) shows magnified and normalized response / recovery curves for 20 ppm NH_3 under flat and bend conditions. Several interesting inferences can be drawn from these data: (i) the resistance of films increases upon NH_3 exposure, indicating holes are the charge carrier; (ii) the base resistance under bend condition is higher than that under flat condition; (iii) the minimum detection limit (MDL) of the sensors is 5 ppm, which is well below the toxic limit (25 ppm) of NH_3; (iv) under flat condition the response time (*i.e.* time required to reach 90% of the saturation resistance upon NH_3 exposure) is ~25 s and recovery time is ~156 s, which under bend condition reduces significantly to ~2 s and 100 s, respectively; (v) the sensitivity (defined as: $S(\%) = \left|\frac{R_g - R_a}{R_a}\right| \times 100$, where R_a and R_g are the resistance values in the air and NH_3 , respectively) versus NH_3 concentration curves clearly show sensitivity is higher under the bend condition; (vi) the base resistance of the films does not drift with time, indicating their long term stability; and above results clearly show that under bend conditions high mobility flexible CoPc films exhibit enhanced sensitivity as well as fast response and recovery.

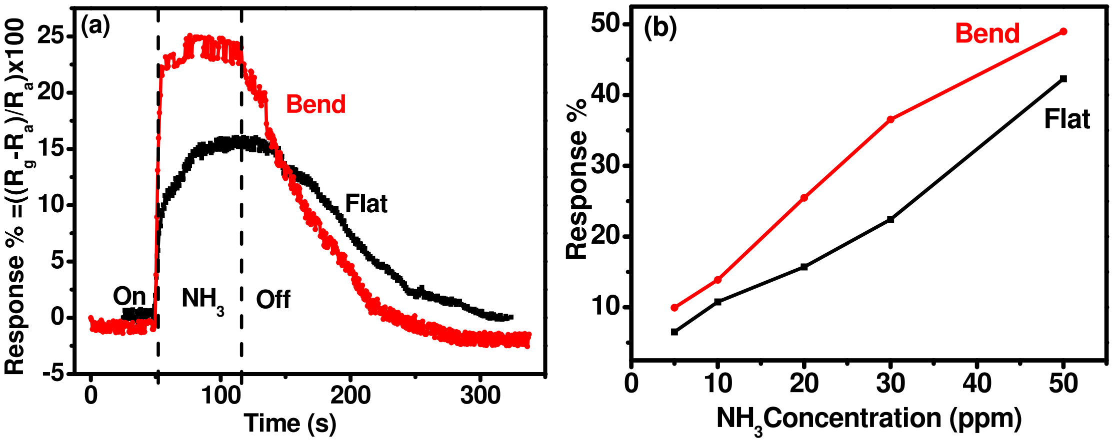

Figure 3.11: (a) Comparative response curve of CoPc films under flat condition and under extreme bend condition (bending radius: 10 mm) for 20 ppm of NH_3. (b) Response percentage versus NH_3 concentration for flat and bend condition.

3.4 Possible Mechanism of bending stress induced enhanced sensing

In order to explain this behaviour we schematically draw the arrangements of CoPc molecules on BOPET substrate under flat and bend conditions in Fig. 3.12. Metal phthalocyanines (MPc) are intrinsically insulators under high vacuum environment and turn semiconductors only when exposed to ambient conditions. This is because ambient oxygen gets chemisorbed at the surface, which in turn, induces hole carriers in the films via the process: $MPc+O_2 \leftrightarrow \left(MPc+h^+\right)+O_2^-$ [2, 84]. XPS results of our flexible CoPc films, clearly show the presence of chemisorbed oxygen at the surface [104]. MPc films acts as chemiresistive sensors because the analyte gases (both reducing and oxidizing) can interact with O_2^- as well as metal surface sites, which results in a change of electrical resistivity [9, 11, 105]. The interaction of oxidizing gases (*e.g.* Cl_2, NO_2 etc.) with MPc films generates holes in the films, and as a result, the resistivity of the film decreases. The interaction of MPc with the reducing gases (such as NH_3) has an opposite effect *i.e.* an increase in resistivity, which is attributed to the hole trapping within the films by the electrons donated from reducing gas [105]. The response of MPc for reducing gases increases significantly with their Lewis basicity [9].

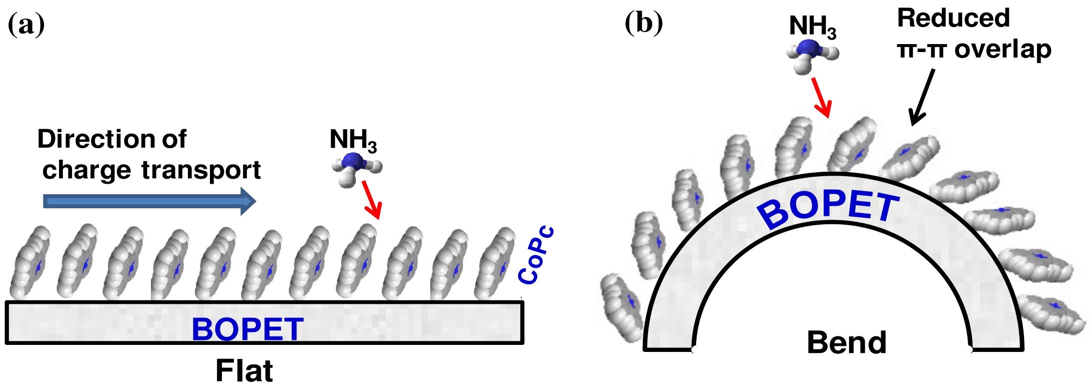

Figure 3.12: Schematic showing the charge transport in (a) flat as well as (b) bend condition.

Under flat condition, CoPc molecules are arranged in edge-on configuration, which results in improved π-π interaction, and hence, a high charge carrier mobility. In this case, NH_3 molecules can only interact with surface of the films as Co metal sites are unavailable owing to close packing. Under the bend condition, as shown in Fig. 3.12(b), the stress enhances the separation among CoPc molecules, which facilitates NH_3 molecules to interact with chemisorbed oxygen present on Co metal sites. An increase in the number of interaction sites under bend condition is responsible for high sensitivity as well as fast response / recovery. The resistance of films, irrespective of the number of bending cycles, fully restores back to the base value of the flat condition within experimental error limits, indicating the reversible nature of the interaction sites created on bending. NH_3 is a key component for the chemical industry, fertilizer factories and refrigeration industry. The toxicity limit of ammonia for human exposure is 25 ppm for 8 h [2]. Due to high toxicity of the gas, any leak in the system can results in life threatening situation. Traditional method of detection of presence of ammonia by chemical analysis is a time-consuming and complicated process. However the sensors based on metal oxides are sensitive to NH_3 but require high temperatures for operation [2, 106, 107]. In this respect, highly flexible CoPc films exhibiting high sensitivity and fast response / recovery under bend condition makes them an attractive candidate for ppm level of NH_3 sensing. In addition the advantage of room temperature operation, low cost of BOPET substrate and CoPc material shows the effectiveness of these flexi-sensors for commercial applications.

We would like to point out that structural ordering plays a significant role in the gas sensing properties of CoPc films. For example, CoPc films with poor structural order (exhibiting mobility ~9.4 $cm^2V^{-1}s^{-1}$) exhibits inferior gas sensing properties *viz.* high MDL of 20 ppm, low sensitivity, sluggish response / recovery and drift in the base resistance. The low mobility CoPc films are characterized by the presence of structural defects, which trap the charge carrier. Trapped carriers do not contribute to the current and therefore MDL is high and sensitivity is low for such CoPc films. Sluggish response / recovery of low mobility CoPc films are also due to the presence of grain boundaries and other structural defects along the charge transport direction. Our studies demonstrate that good structural ordering of CoPc films is essential for achieving stable and good sensing properties. These results are however in contrast to the state-of-the-art metal oxide semiconductor thin films based chemiresistive sensors, where granular and polycrystalline films yield better sensitivity. This is because in metal oxide films, the adsorbed oxygen content increases as the grain size decreases (owing to large surface area).

3.5 Conclusions

Finally we would like to point out that the high mobility in CoPc films on flexible BOPET is obtained for: (i) an optimum films thickness of 20 nm, and (ii) exclusively on BOPET structure. To prove the first point, the charge transport properties of the CoPc films with varying thickness deposited on BOPET substrates were investigated. It was found the *J* (measured at 50V) shows maxima at 20 nm. At thickness < 20 nm, the low value of *J* is attributed to the incomplete coverage (mostly due to high surface roughness of ~ 6 nm for BOPET). The maximum occurs at 20 nm, as the PET crystallites oriented in the substrate plane act as a template for the ordering of the CoPc molecules. At very high thickness (>>20 nm) of CoPc films, the influence of BOPET substrate is drastically reduced, which leads to the formation of disordered film (as also confirmed by XRD), which, in turn, is responsible for low values of *J*. In order to prove the second point, *i.e.*, the CoPc molecular ordering is exclusive to BOPET, CoPc films (thickness: 20 nm) were also prepared on other amorphous substrates, such as glass and plastic transparency sheet of the inkjet printer under identical experimental conditions. The films prepared on glass exhibited hysteretic *J-V* characteristics, which were attributed to the presence structural defects. The films prepared on the transparency sheet though exhibited non-hysteretic *J-V* characteristics, but the slope of *J-V* curve at higher bias region was ~3.5, indicating the presence of exponentially distributed traps in the films. The CoPc films (thickness ~ 20nm) deposited on transparent flexible BOPET substrates exhibit very high charge carrier mobility of ~ 118 $cm^2V^{-1}s^{-1}$ at 300 K. The high mobility in these flexible films is attributed to the strong molecular ordering of CoPc molecules in the “standing on” configuration on the BOPET surface that facilitates easy intermolecular transport of the charge carriers. The molecular ordering is caused by the electrostatic interaction between oriented PET chains (having C=O polar groups) and CoPc molecules as well as π-π interaction among CoPc molecules along the PET chains. These flexible films also exhibited a reversible change in the resistance under different bending conditions. The high charge carrier mobility along with the mechanical flexibility of the CoPc films grown on BOPET substrates suggests that they are a potential candidate for flexi-organic devices. In support of that, we have demonstrated the beneficial effect of bending stress on the chemiresistive gas sensing characteristics of high mobility CoPc films deposited on transparent flexible BOPET substrate. These flexible films show excellent response / recovery for ammonia in the concentration range of 5 to 50 ppm at room temperature. The low cost, room temperature operation, high sensitivity, fast response / recovery of CoPc flexible films makes them attractive candidates for flexi-gas sensor devices.

CHAPTER 4

Improved H_2S Chemiresistive Gas Sensing Properties of Cobalt Phthalocyanine Films modified by thin Discontinuous layer of Gold

4.1 Introduction

H_2S is one of the highly toxic gas with threshold limit ~ 10 parts per million (ppm) and hence detection of H_2S around this concentration is very crucial to protect human lives [108]. In the development history of H_2S sensor, metal oxide gas sensors have shown great potential with typical detection range in ppm levels with operating temperature ranging from room temperature upto few hundred degrees Celsius [109-112]. However the stiffness of these sensors associated with the use of rigid inorganic substrates as well has high power consumption have limited their application in various new areas that require flexible, lightweight, and mechanical shock-resistive sensing elements [91, 113]. In last few year metal phthalocyanines (MPcs) have been widely explored as promising candidate for gas sensors [9, 86, 114-117]. In MPcs charge carriers can be generated / depleted on interaction with analyte through the redox process. Their room temperature response towards analyte can be improved by: taking MPc with enhanced Lewis basicity [9], making composite with other MPc [114], ultrathin film to enhance the surface effects [86], and tuning of the surface potential by putting a top discontinuous layer of another MPcs on bottom MPc films [116]. In field of metal oxide based gas sensor sometimes their active layer is modified by the metal particle sensitizer to improve the selectivity towards a particular gas [111]. Taking advantage of this information we have modified the surface of flexible CoPc layer with the thin discontinuous layer of gold. Such a gold modified CoPc film exhibits highly improved chemiresistive gas sensing characteristics towards H_2S gas. So far the MPcs have been rarely explored for the H_2S detection [2, 117]. In this chapter, we demonstrate the highly improved

H_2S response (at room temperature) of flexible gold-cobalt phthalocyanine (Au-CoPc) heterojunction films as compared to the pure CoPc film. The lowest detection limit (LDL) of these sensors is 100 parts per billion (ppb), which is much lower in comparison to the recent and only report of H_2S detection using copper phthalocyanine films (LDL ~ 100 ppm) [117]. The effect of bending on gas sensing behavior is also discussed in this chapter.

4.2 Experimental details

CoPc films (thickness: 20 nm) were deposited on pre-cleaned bi-axially oriented flexible (BOPET) substrates (size: 10 mm × 10 mm × 100μm) by molecular beam epitaxy (base vacuum ~ 2×10^{-8} mbar) [118]. During the deposition process substrate temperature was kept fixed at 100˚C and deposition rate was ~ 0.1 Å/s. After deposition of the CoPc films, one of the portions of the films was masked in-situ and on other portion, a thin layer (~1 nm) of Au was deposited at room temperature. In the later part of this thesis the Au modified CoPc films will be termed as Au-CoPc. For electrical measurement few pairs of gold electrodes of size 3 mm × 2mm having separation of 12μm were deposited on both films using thermal evaporation. Silver wires were attached to these Au pads by silver paint. The electrical resistance of the films was measured by Keithley 6487 voltage source / picoammeter system. For gas sensing experiments the response curves (resistance versus time data) were recorded simultaneously for the CoPc and Au-CoPc films using a static gas testing setup. The schematic details of sample deposition, electrode fabrication and measurement set up are given in the Fig.4.1. Briefly, the films were mounted in a leak tight stainless steel chamber (net volume: 1000 cm^3). A desired concentration of the test gas in the chamber was achieved by injecting a known quantity of gas using a micro-syringe. The response data was acquired by a personal computer equipped with LabVIEW software. Once a steady state was achieved, recovery of films was recorded by exposing the sensors to air by slight opening of the lid of chamber. The response (%) of the sensors was calculated from the response curves using the relation [2]:

$$Response\ \% = \frac{|R_g - R_a|}{R_a} \times 100\ \% \qquad \text{- (4.1)}$$

where R_g and R_a are the resistance values of the sensor films in test gas and fresh air, respectively. Response and recovery times were defined as the times needed for 90% of total change in conductance upon exposure to test gas and fresh air, respectively. Gas sensing measurements were also carried out under bent condition of films. The bending experiments were carried out by mounting films on quartz tubes of different diameters.

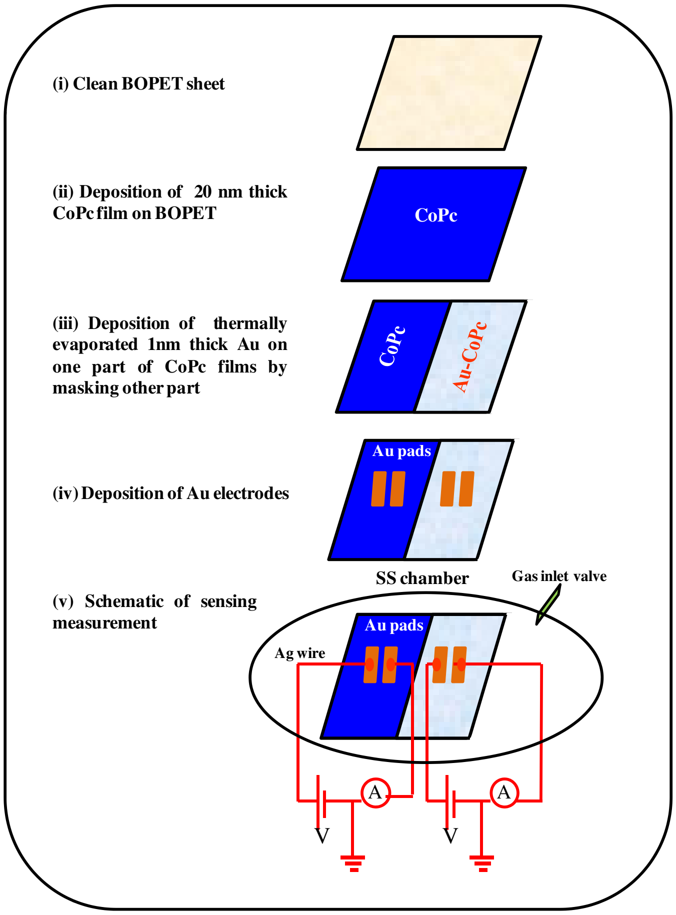

Figure 4.1: Schematic showing the steps of sample fabrication, Au electrode deposition, electrical characterization and sensing experiments.

4.3. Results and discussion

4.3.1 Morphology and structural characterization

Figure 4.2 shows the morphological and structural properties of CoPc and Au-CoPc films. The AFM image of CoPc films shown in Fig. 4.2(a) reveals that film consists of uniformly distributed elongated grains with average surface roughness of 7.8 nm. In the AFM image of Au-CoPc films (shown in Fig.4. 2(b)), in addition to the uniformly distributed CoPc grain the Au islands of 100-150 nm length scale can also be seen.

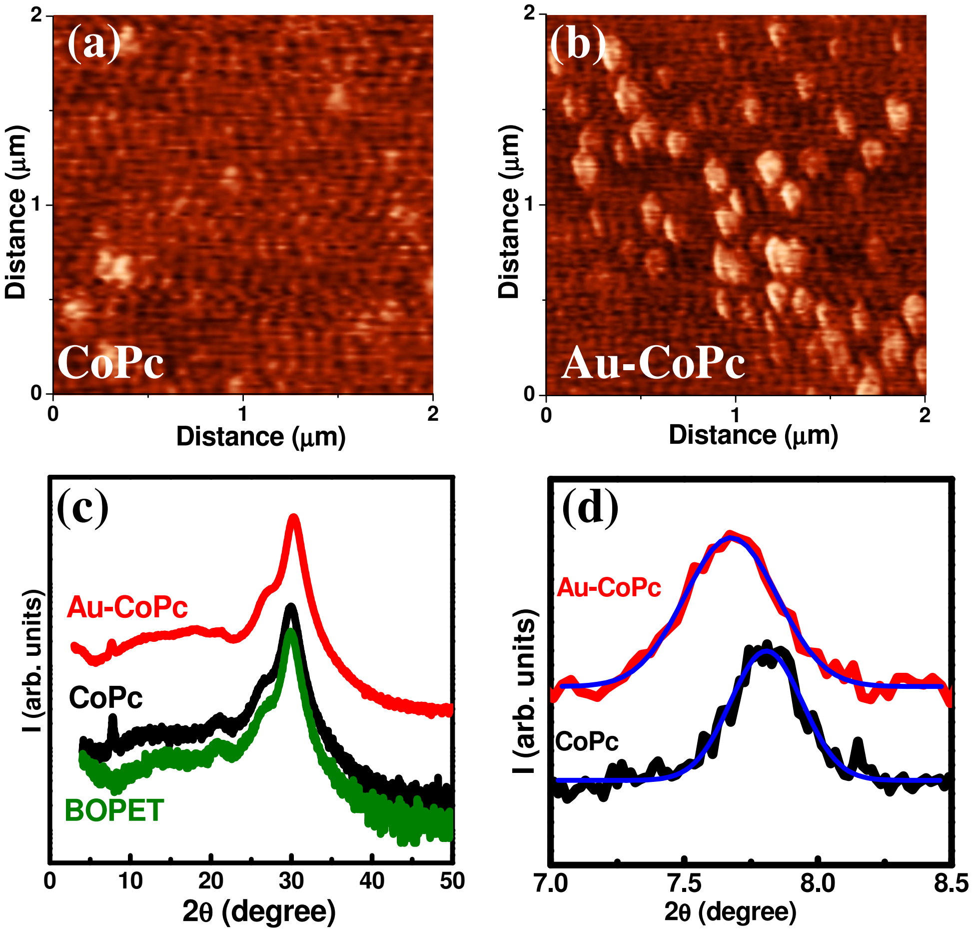

Figure 4.2: AFM images of (a) CoPc (b) Au-CoPc films. (c) XRD pattern recorded for CoPc, Au-CoPc films and BOPET samples. (d) Magnified view of the (*200*) diffraction peak corresponding to CoPc in pure CoPc and Au-CoPc films.

The average surface roughness of Au-CoPc films was found to be ~ 8.9 nm. X-ray diffraction (XRD) spectra for CoPc, Au-CoPc films and BOPET substrates are given in Fig.4.2(c). The magnified view of (*200*) diffraction peak corresponding to CoPc for both films is shown in Fig. 4.2(d). From these XRD diffractogram following inferences can be drawn: (i) Broad and intense diffraction peak observed at $2\theta = 29.9^{\circ}$ corresponding to the semi-crystalline BOPET substrate remains unaltered for both CoPc and Au-CoPc films. (ii) In the XRD data no diffraction peak corresponding to the Au nano-cluster was observed indicating their amorphous nature. (iii) Both films exhibited a diffraction peak at $2\theta = 7.8^{\circ}$ corresponding to the (*200*) orientation of the α-CoPc phase indicates that films are crystalline with a-axis normal to the substrate *i.e.* molecules are assembled in "standing on configuration" at the substrate plane [118]. (iv) For Au-CoPc films the (*200*) diffraction peak was slightly shifted to lower 2θ value and its full width at half maximum (FWHM) was higher (~ 0.25°) in comparison to pure CoPc films (~ 0.37°). From XRD data, the calculated value of a lattice parameter respectively for CoPc and Au-CoPc films was found to be 26.2 Å and 26.7 Å. The enhanced FWHM and a lattice parameter for Au-CoPc films were attributed to the disordered arrangement of CoPc molecules in films due to the incorporation of Au inside the CoPc films. The incorporation of Au inside the bulk of CoPc will disturb the long range periodicity as well as π-π interaction among CoPc molecules.

4.3.2 X-ray photoelectron spectroscopy

X-ray photoelectron spectroscopy (XPS) measurements were carried out to understand the interaction between Au and CoPc. The survey XPS spectra of the CoPc and Au-CoPc films are shown in Fig. 4.3(a) and it show the presence of common C1s, N1s, Co2p and O1s (due to the chemisorbed oxygen at surface) signals. The obtained high resolution XPS spectra shows that most significant changes were found for Au4f and Co2p$_{3/2}$ signals from Au-CoPc films. From Fig.4. 3(b) it can be seen that Au4f spectrum from Au-CoPc films shows a positive shift of 0.9 eV in binding energy with respect to the pure gold films [119].

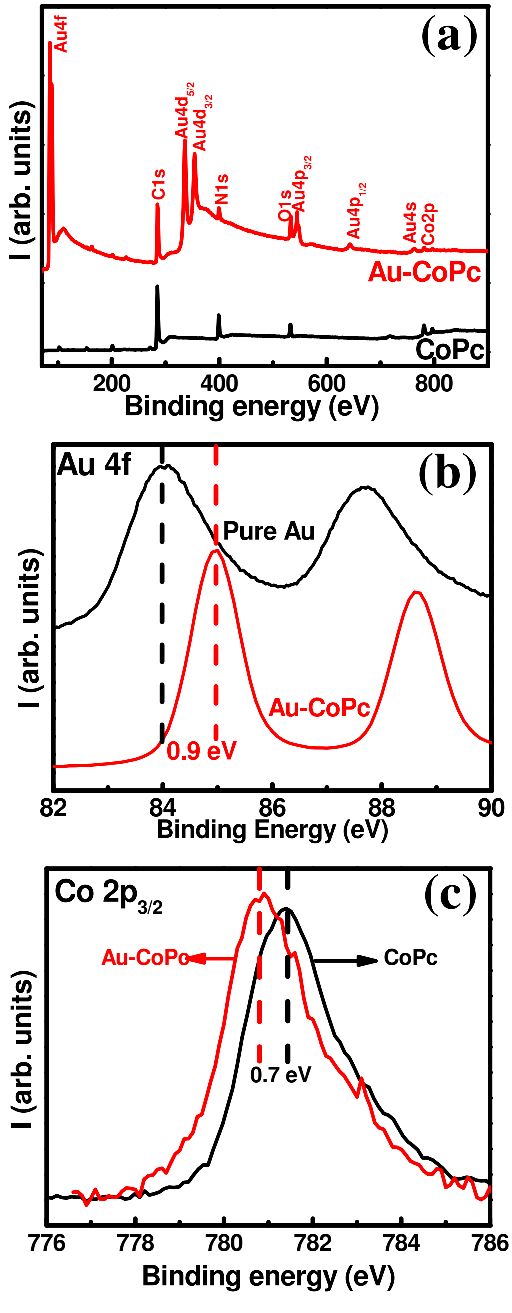

Figure 4.3: AFM images of (a) CoPc (b) Au-CoPc films. (c) XRD pattern recorded for CoPc, Au-CoPc films and BOPET samples. (d) Magnified view of the (*200*) diffraction peak corresponding to CoPc in pure CoPc and Au-CoPc films.

For Au (3nm)-CoPc films, the shift in binding energy was found to be ~ 0.3 eV and for Au (5 nm)-CoPc sample we did not observe any shift with respect to bulk Au4f signal. The lowering of binding energy shift (with respect to the bulk gold films) with increasing the thickness of Au layer suggests that Au atoms in the close proximity of CoPc surface are interacting with CoPc. Fig.4. 3(c) shows that $Co2p_{3/2}$ XPS spectra of both films, which reveals (i) more broadening toward high binding energy side for Au-CoPc films and (ii) an overall shift of the spectrum towards low binding energy in comparison to pure CoPc films. The enhanced inhomogeneous broadening of $Co2p_{3/2}$ spectrum for Au-CoPc films suggest the presence of two different environment of Co atoms, one which is in proximity to Au and other one similar to pure CoPc film. The shifting of $Co2p_{3/2}$ signal from Au-CoPc towards low binding energy suggests that there is a strong interaction between Au and CoPc at the interface, which is also supported by earlier reports [120, 121]. The quantification of the XPS data suggests that Au-CoPc films have more chemisorbed oxygen (atomic ratio of O/Co ~ 92%) as compared to the pure CoPc film (O/Co ~ 72%).

4.3.3 Raman spectroscopy

Raman spectroscopy measurements were carried out to obtain an insight of the interaction of Au with the CoPc molecule in films. Figure 4.4 (a) and 4.4 (b) respectively shows background corrected Raman spectra in the wave number region 450-1575 cm^{-1} of CoPc and Au-CoPc films. The Raman peaks arising from BOPET substrate have been identified and indicated with * mark. For pure CoPc films, the intense peak at ~ 684cm^{-1} is assigned to the totally symmetric breathing mode of the 16-membered macro-cyclic ring. The A_{1g} Raman mode at ~ 837 cm^{-1}, A_{2g} mode at ~ 490 cm^{-1}, B_{1g} mode at ~753 cm^{-1} and B_{2g} modes at ~592, 786 and 962 cm^{-1} have been attributed to the macro-cyclic deformation [22, 122-124]. The B_{2g} mode at ~786 cm^{-1} and A_{1g} mode at 837 cm^{-1} also involve concomitant stretching of the C-N bonds of the aza groups. The sharp intense peak at ~1539 cm^{-1} and ~1344 cm^{-1} are respectively assigned to the totally symmetric stretching vibration at the C_β-C_β and C_α-C_β bonds of the pyrrole rings while the peak at ~1139 cm^{-1} results from the breathing vibration of the pyrrole rings.

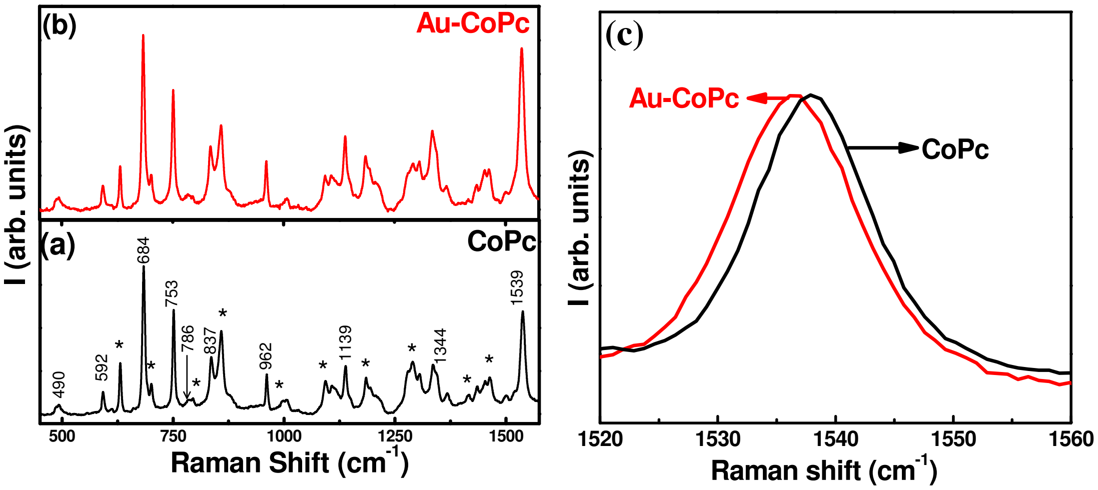

Figure 4.4: Raman spectra for (a) CoPc (b) Au-CoPc films. (c) Enlarged view of Raman band at 1538 cm^{-1} associated with vibration of pyrrole ring of CoPc molecule.

From Fig. 4.4(b) it can be seen that for Au-CoPc films Raman bands associated with the pyrrole rings exhibit higher intensity relative to the other peaks at low wave numbers. It is known from the literature that the Raman bands associated with the pyrrole rings are sensitive to the change in C-N-C bridging bond lengths and bond angles and also the steric and electronic factors governing the Co-N bonding in the complex [22, 122-124]. Since, few Raman bands have been selectively enhanced on Au modification, therefore it is proposed that interaction of the Au layer with the CoPc might have resulted in the non-planarity in the molecule. From Fig. 4.4(c) it is also seen that the highest intense bands associated with pyrrole rings are shifted to lower wave numbers than in the pure CoPc films. It is suggested that interaction of CoPc with the Au atoms softens the rigidity of the Co-N bonds that in turn decreases the vibrational frequencies at C_α and C_β of the pyrrole ring. It is interesting to note that the Raman bands at ~786 and 837cm^{-1}, which have significant contribution from the Co-N stretching vibration are also shifted to lower wave number but there is hardly any increase in intensities.

4.3.4 Charge transport measurement

Typical temperature dependence of electrical resistivity data for CoPc and Au-CoPc films are shown in Fig. 4.5(a). From data of Fig. 4.5(a) it can be seen that: (i) both samples exhibit semiconducting behavior, (ii) Au-CoPc films are more resistive in comparison to CoPc films and (iii) resistivity of Au-CoPc films increase very rapidly with the lowering of temperature indicating the presence of molecular disordering (also supported by the XRD data). Typical temperature dependent current – voltage (*J-V*) characteristics plotted in log-log scale for CoPc and Au-CoPc films are respectively shown in Fig. 4.5(b) and Fig. 4.5(c). For both the films *J-V* data has been taken in bias range of 0-50V. From Fig. 4.5(b), it is seen that for CoPc films *J-V* characteristics are non-linear, and exhibits two different power law behavior ($J \sim V^\alpha$) as a function of applied bias with varying α values. At room temperature, for low bias (<10 V) α ~1 indicates ohmic conduction [118]. For ohmic conduction the *J-V* characteristics can be described by $J = n_0 e \mu V/d$; where n_0 is the concentration of thermally generated holes, e is the electronic charge, μ is the hole mobility, and d is the electrode separation. For high bias (>10 V), α ~2 indicates the shallow trap mediated space charge limited conduction (SCLC) [118]. SCLC occurs if the injected carrier density is higher than n_0 and J depends on applied bias through the relation: $J = \frac{9}{8}\theta\varepsilon\mu\frac{V^2}{d^3}$, where ε is permittivity (experimentally determined value of ε for our films is 2.45×10^{-11}F/m) and θ is the ratio of free to total (trapped and free) charge carrier density [118]. The crossover voltage between ohmic and SCLC decreases with the lowering of temperature due to reduction in thermally charge carriers.

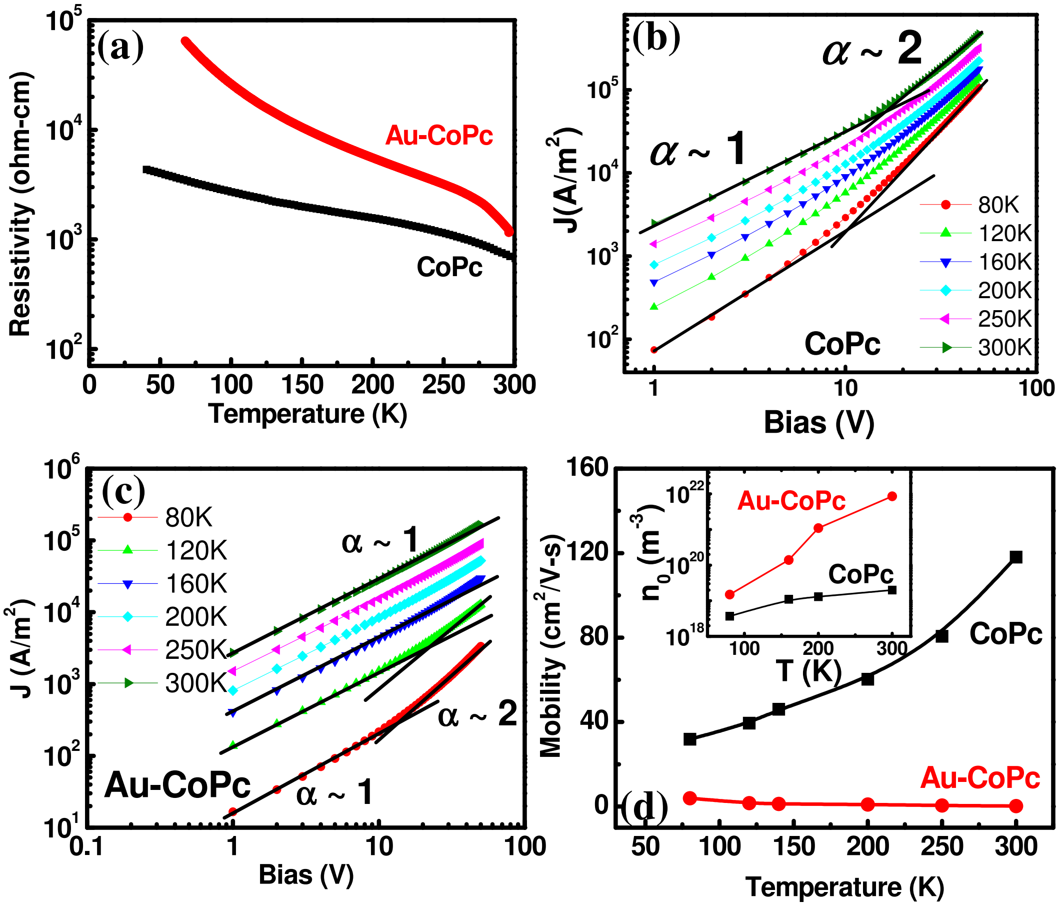

Figure 4.5: Temperature dependence of (a) resistivity (b) and (c) current-voltage characteristics (d) Mobility and carrier concentration for CoPc and Au-CoPc films.

From Fig. 4.5(c), it can be seen that for Au-CoPc films, *J-V* characteristics are linear up to 130 K in the bias range of 0-50V. For the same films, *J-V* data recorded in the bias range of 0-100V shows that around 70 V there is a transition from ohmic to SCLC. In addition, the *J-V* data (in the bias range 0-50V) recorded below 130 K also exhibits a transition from ohmic conduction to SCLC. A transition from ohmic conduction to the SCLC with increasing bias or with lowering of temperature rules out the possibility of formation of metallic conduction channel in the CoPc matrix by incorporation of Au. For both films, μ values at different temperatures were estimated from the slopes of the J-V^2 plots and the results obtained are shown in Fig. 4.5(d). In case of Au-CoPc films the estimation of μ was done using the data obtained in 0-100 V bias range. In the estimation of μ, we assumed $\theta = 1$ *i.e.* a trap free condition as the characteristics does not indicates the presence of trapping centres. The data analyses yielded the respective room temperature value of μ for the CoPc and Au-CoPc films as ~ 118 cm^2/V-s and 0.3 cm^2/V-s.

The origin of very high mobility for pure CoPc films on BOPET substrate is attributed to the better molecular periodicity of CoPc molecules. High structural ordering of CoPc molecules on BOPET substrate is attributed to (i) orientation of PET molecular chains in the substrate plane, leading to very smooth surface, and (ii) presence of polar groups, *i.e.*, C=O and O-C=O in the PET molecular chains, which can electrostatically interact with CoPc molecules and favours a relatively stronger π-π interaction among CoPc molecules along the PET chains. Using the value of μ and equation for ohmic conduction for low bias data, we have estimated the n_0. Respective room temperature value of n_0 for CoPc and Au-CoPc is estimated as 2.1×10^{13} cm^{-3} and 8.6×10^{15} cm^{-3}. Nearly three orders of magnitude higher n_0 for Au-CoPc films indicate that deposition of the Au layer on top of CoPc films generates extra charge carriers in the CoPc films due to heterojunction effect. The detailed Raman spectroscopy of the films suggests that the interaction of Au with CoPc affects the planarity of the CoPc molecules. The overall structural disorder among CoPc molecules created by the Au (as seen from XRD and Raman data's) may be responsible for the lowering of charge carrier mobility in Au-CoPc films.

4.3.5 Chemiresistive gas sensing properties

Fig. 4.6(a) and 4.6(b) respectively shows the response / recovery curves (*i.e.* change in the films resistance as a function of time on exposure of different H_2S concentration and ambient condition once the saturation is achieved) for the CoPc and Au-CoPc films. Fig.4.

6(c) shows the comparative normalized response / recovery data of both films for 10 ppm of H_2S exposure.

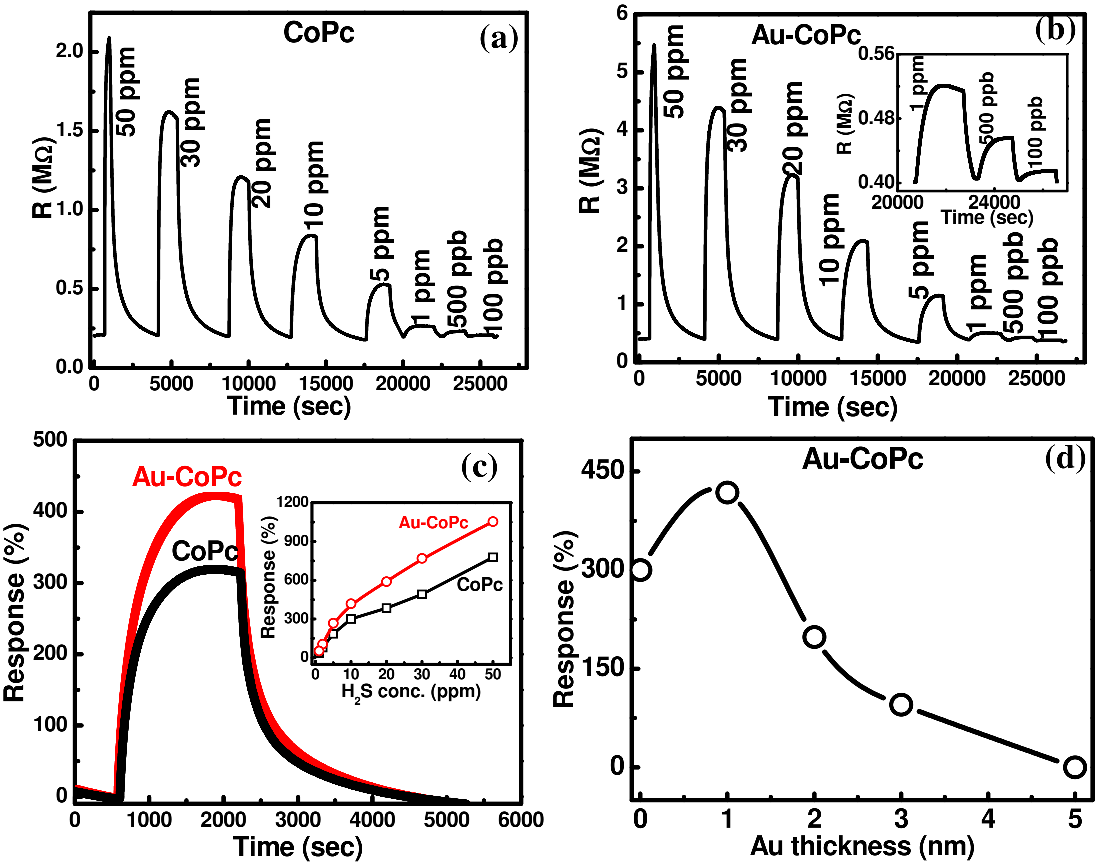

Figure 4.6: Chemiresistive gas sensing characteristics of CoPc and Au-CoPc films (a) and (b) shows the response curve for H_2S gas. Inset in Fig.4.6 (b) shows the expanded view response curve at low concentration of H_2S. (c) Comparative response at 10 ppm of H_2S. Inset shows the response (%) as a function of H_2S concentration (d) Response (at 10 ppm of H_2S) of Au -CoPc films having different thickness of Au.

Several interesting inferences can be drawn from these data: (i) resistance of both films increases on H_2S exposure indicating holes as majority charge carriers, (ii) the minimum detection limit (MDL) of these films is 100 ppb, which is well below the toxic limit (10 ppm) of H_2S, (iii) both the films show a response time (*i.e.* time required to reach 90% of the saturation resistance upon 10 ppm of H_2S exposure) of 10 min and recovery time of 16 min, (iv) the comparative response / recovery curves clearly shows higher response (%) for Au-CoPc films. The effect of Au layer thickness on the response (at 10 ppm of H_2S) of Au-CoPc films is shown in Fig. 4.6(d).

From Fig 4.6(d), it can be seen that Au-CoPc films exhibit highest response for Au thickness of ~ 1 nm and response systematically decreases with increasing thickness of Au. The lowering of response for Au-CoPc films with thicker (> 1 nm) gold layer can be due to the formation of bigger size Au islands on CoPc surface. These big Au islands will cover most of the CoPc surface (active zone for interaction with H_2S) and as a result these films will exhibit lower response towards H_2S. It may be noted that Au-CoPc films with 5 nm thick Au layer exhibit metallic conduction (with base resistance ~ 40 mΩ), possibly due to the formation of a continuous of Au layer over the CoPc surface. These films do not exhibit any response towards H_2S gas, which also suggest that H_2S interacts with CoPc only.

The Au-CoPc films with 1 nm thick Au layer were further studied for selectivity; repeatability of response (at 5 ppm of H_2S exposure), long term stability. The selectivity histogram for a host of gases at concentration of 10 ppm is shown in Fig. 4.7(a). From the selectivity data it can be seen that Au-CoPc films exhibit highest response towards H_2S gas. These films also exhibit smaller response towards other reducing (NH_3) and oxidizing gases (Cl_2 and NO_2). The response of Au-CoPc films towards NH_3, Cl_2, and NO_2 is ~ 12%, 25% and 16% respectively. It is important to mention that on exposure to Cl_2 gas, the resistance of films reduces but on removal of Cl_2 gas it never recovers back to the original base resistance at room temperature indicating a permanent reaction between the Cl_2 and films. On exposure to NO_2 gas the films exhibits a reversible change in resistance. From inset of Fig 4.7(a) it can be seen that response data are highly repeatable for 5 ppm of H_2S dose. The long term stability of base resistance and response (at 5 ppm of H2S) of the Au-

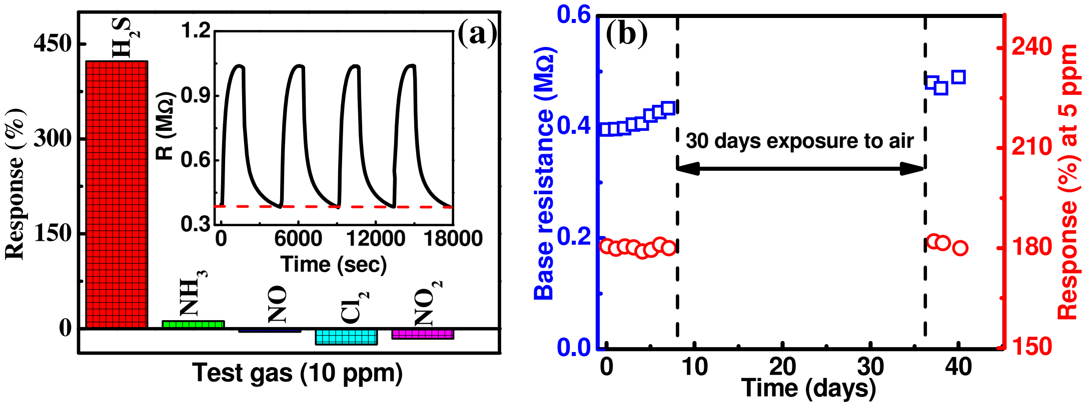

Figure 4.7: (a) Selectivity histogram of Au-CoPc films for host of gases (each 10 ppm). Inset shows the repeatability of the response (at 5ppm of H_2S dose) for Au-CoPc films. (b) Stability of response (at 5 ppm of H_2S dose) and base resistance of Au-CoPc films.

CoPc films were studied for 40 days and the results are shown in Fig. 4.7(b). To perform these tests, initially every day we have tested the base resistance and response for 7 days and after that sample were kept in air for 30 days. After 30 days we have again tested the sample, and from Fig. 4.7(b) it can be seen that the base resistance of the films slightly increases with time but no significant variation in response (at 5ppm) was observed for 40 days.

Table 4.1 Comparison of Au-CoPc heterojunction film based chemiresistor to other heterojunction / composite based H_2S gas sensors.

Chemiresistor sensor Films	LDL (ppm)	Response (%)	Res. time (s)	Ref.
Cobalt phthalocyanine-gold	0.1	424 / 10 ppm	540 (at 10 ppm)	This work
Polyaniline-silver nanocomposite	1	6 / 10 ppm	360 (at 10 ppm)	[69]
Polypyrrole-silver nanocomposite	5	98/10 ppm	6 sec (at 10 ppm)	[125]
Polycarbazole-gold	1	120/ 10 ppm	180 (at 10 ppm)	[66]
Polypyrrole-tungsten oxide	0.1	81/ 1ppm	360 (at 1 ppm)	[126]
Polypyrrole-tungsten oxide	200	150/ 200 ppm	200 (at at 200 ppm)	[127]
Polythiophene-tungsten oxide	5	100/5 ppm	3 (at 5 ppm)	[128]

Polypyrrole-tungsten oxide	1000	225/ 1000 ppm	250 (at 1000 ppm)	[129]
poly3-hexylthiophene-zinc oxide	4	5/ 4 ppm	300 (at 4 ppm)	[130]

A comparison of the H_2S sensing properties of Au-CoPc heterojunction films with other reported organic-inorganic heterojunction thin films is given in Table 4.1. From Table 4.1, it can be seen that Au-CoPc films reported in our work exhibit lowest detection ~ 100 ppb *i.e*. comparable to other report organic-inorganic heterojunction films. It can also be seen that the response (%) of Au-CoPc films is quite high in comparison to other heterojunction films.

4.3.6 Mechanism of H_2S sensing

In the light of above results, now we discuss the H_2S sensing results of CoPc and Au-CoPc films. In pure CoPc films, due to low coordinated structure of Co atoms in CoPc molecules, it is the most preferable sites for the chemisorptions of oxygen. CoPc films are intrinsically insulators and turn semiconductors only when they are exposed to atmosphere [2, 9]. For pure CoPc films the adsorbed oxygen results in the formation of a hole accumulation layer, which is shown by red colour in Fig.4.8 (a).

The interaction between H_2S and CoPc films can be understood by the following equation:

$$2H_2S_{(g)} + 3O_2^{-}{}_{(ads)} \rightarrow 2H_2O_{(g)} + 2SO_{2(g)} + 6e^{-} \qquad -(4.2)$$

The H_2S gas interacts with the adsorbed oxygen species of CoPc film and releases large number of electrons in the film. The released electrons captures the hole charge carriers of CoPc films and as a result the resistance of samples will rise on H_2S exposure. Once the sample chamber is open, the recovery of samples takes place by picking up oxygen from the atmosphere. The schematic of H_2S sensing by CoPc films is shown in Fig. 4.8(a), here the reduction in hole density on exposure to H_2S is shown by thinner accumulation layer. The enhanced response of Au-CoPc films in comparison to pure CoPc films is attributed to the

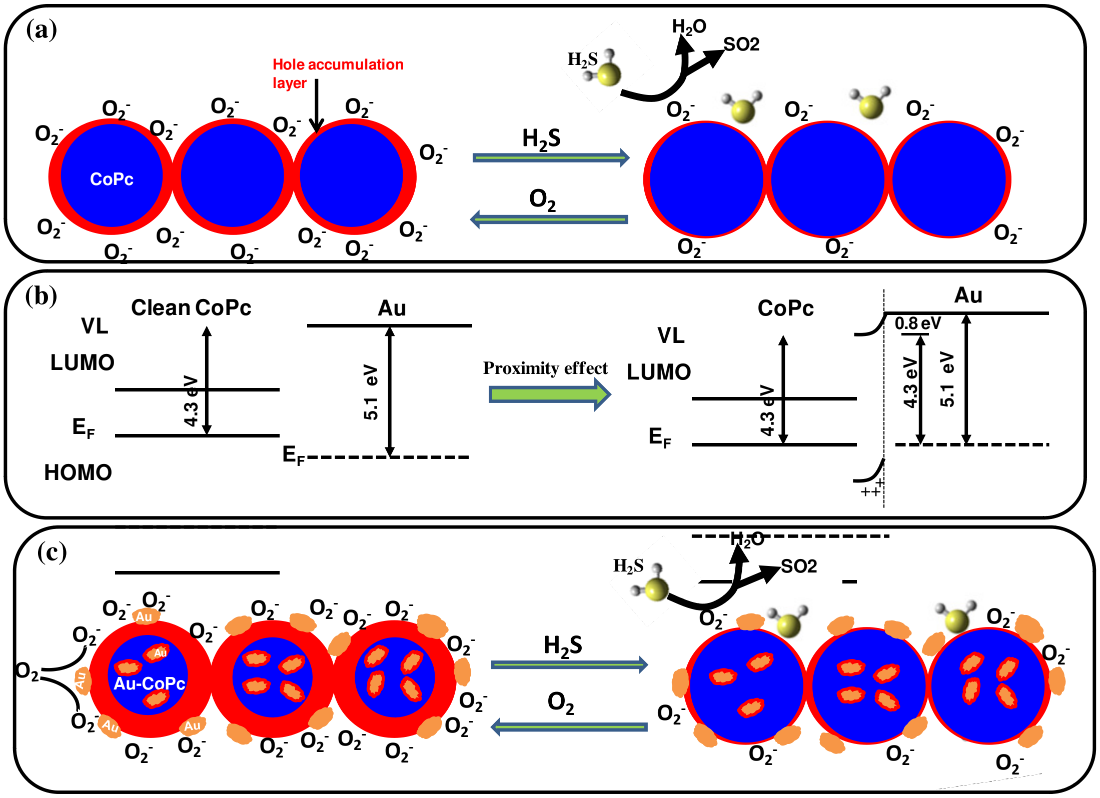

Figure 4.8: (a) Schematic diagram exhibiting the mechanism of H_2S sensing for pure CoPc film (b) Schematic of the energy band diagram for CoPc and Au as individual and in close proximity.(c) Schematic diagram exhibiting the mechanism of H_2S sensing for Au-CoPc film.

dual role played by Au *i.e.* difference in work functions of Au and CoPc leading to accumulation layer at the Au-CoPc interface (Fig. 4.8b), and catalytic effect of Au (Fig.4.8(c)). The work function (WF) values obtained from Kelvin probe system obtained for fresh CoPc and Au were respectively found to be 4.3 eV and 5.1 eV (shown in Fig. 4.8(b)). Due to the difference in WF values, when CoPc and Au come in close proximity there is an alignment of Fermi levels due to which there is a transfer of electrons from CoPc to the Au. This process results in band bending of ~ 0.8 eV at the Au-CoPc interface. The transfer electrons from CoPc to the Au results in a hole accumulation layer. Secondly Au acts as a sensitizer thereby catalyzing the dissociation of molecular oxygen species by spillover effect [111]. Au modification significantly increases the quantity of chemisorbed oxygen (also supported by XPS data) and creates additional active sites along with more hole carrier density in the Au-CoPc films. Both effects (*i.e.* alignment of Fermi level and more chemisorbed oxygen) results in high density of hole carriers in Au-CoPc films. Presence of large number of adsorbed oxygen species in Au-CoPc films in comparison to pure CoPc films implies more reactive sites for H_2S oxidation, and therefore, enhanced H_2S response. The impedance spectroscopy results suggest that for both films the predominant interaction between H_2S and CoPc molecules takes place at the grain boundaries region.

4.3.7 Impedance spectroscopy

In the present work, response of senor was studied by the measurement of dc resistance of films. Sample resistance measured using dc current has contributions from different regions of the sample such as intra-grain, grain boundaries and electrode–sample interface [131]. Impedance spectroscopy is an important technique that has widely been used for distinguishing between different contributions to sensor response. We have performed the impedance measurement on the CoPc and Au-CoPc films. The impedance measurements were carried out on fresh film (in air) and under exposure of 20 ppm of H_2S gas, obtained spectra is plotted in Fig. 4.9 (a-b) in the form of Nyquist plot. It can be seen that impedance spectra shows a single semicircle from low frequency to high frequency region, and it can be fitted into an equivalent circuit as shown in Fig. 4.9(c). In the equivalent circuit model frequency independent resistance (R_0) is attributed to the bulk and surface contributions. The resistance (R_i) and capacitance (C_i) are attributed to the intra-grain region, while the resistance (R_g) and capacitance (C_g) is attributed to the grain boundary region. The corresponding mathematical equation for this equivalent circuit can be described as:

$$Z = Z' + jZ'' \tag{4.3}$$

where

$$Z' = R_0 + \frac{R_i}{1 + (\omega R_i C_i)^2} + \frac{R_g}{1 + (\omega R_g C_g)^2} \text{ and } Z'' = \frac{\omega R_i^2 C_i}{1 + (\omega R_i C_i)^2} + \frac{\omega R_g^2 C_g}{1 + (\omega R_g C_g)^2}$$

Here $\omega = 2\pi f$, and f is the frequency of A.C. Signal. From Fig. 4.9(a-b) it can be seen that there is very good agreement between the simulated (shown by solid lines) pattern and experimental data and the values of fitted parameters are given in Table-4.2. From Table-4.2 it can be seen that the inter-grain resistance (R_i) of fresh Au-CoPc films is higher than pure CoPc films, which again support the disordering of CoPc molecules by incorporated Au atoms. It is also seen that for both films, the exposure to H_2S results in an increase in R_i and R_g but the increase in R_g is found to be much larger. The results of impedance study suggest that for both films, the interaction between CoPc and H_2S gas takes place at the grain boundary region.

Table 4.2: Impedance parameters obtained for CoPc and Au-CoPc films by fitting experimental data to the equivalent circuit

Sample	**R_0(Ω)**	**R_g (kΩ)**	**C_g (nF)**	**R_i (kΩ)**	**C_i (nF)**
CoPc films-Fresh	10	229	40.6	0.9	50
CoPc films-H_2S exposed	100	846	168	0.96	498
Au-CoPc films-Fresh	10	193	2.97	6	80.9
Au-CoPc films- H_2S exposed	100	860	0.16	8	62.9

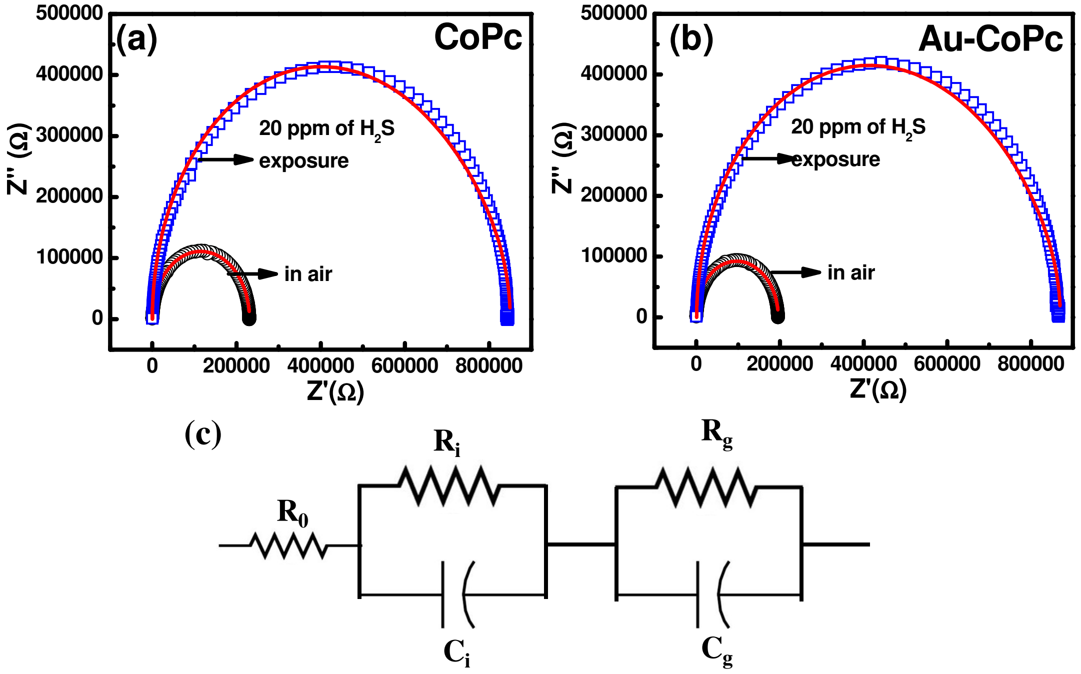

Figure 4.9: Impedance spectra of the fresh and H_2S exposed (a) CoPc films (b) Au-CoPc films. (c) Equivalent circuit used to fit the impedance data. Solid red line represents the fitting of the spectra using an equivalent circuit model.

4.3.8 Effect of bending on the gas sensing properties

Since both CoPc and Au-CoPc films were prepared on the flexible BOPET substrate therefore now we discuss the effect of bending on the chemiresistive gas sensing characteristics of the sensors. The results of sensing experiments (at 20 ppm of H_2S exposure) at bending radius (*r*) of 20 mm are shown in Fig. 4.10(a) and Fig. 4.10(b) respectively. From Fig. 4.10(c) it can be seen that under the bent condition, response of pure CoPc films exhibit slight improvement. In contrast the response of Au-CoPc films remains nearly same at high bending radius but reduces drastically (close enough to the response of CoPc films) at $r \leq 20$ mm. For Au-CoPc films, the lowering of the response under extreme bend condition might be due to the temporary weakening of the interaction between Au and CoPc, which destroys the charge accumulation layer on the CoPc side. In pure CoPc films, under flat condition, molecules are arranged in an ordered edge-on configuration, which resulted in an improved π -π interaction. In this case, H_2S molecules can only interact with surface of the films as Co metal sites are unavailable owing to close packing of molecules. Under the bend condition,

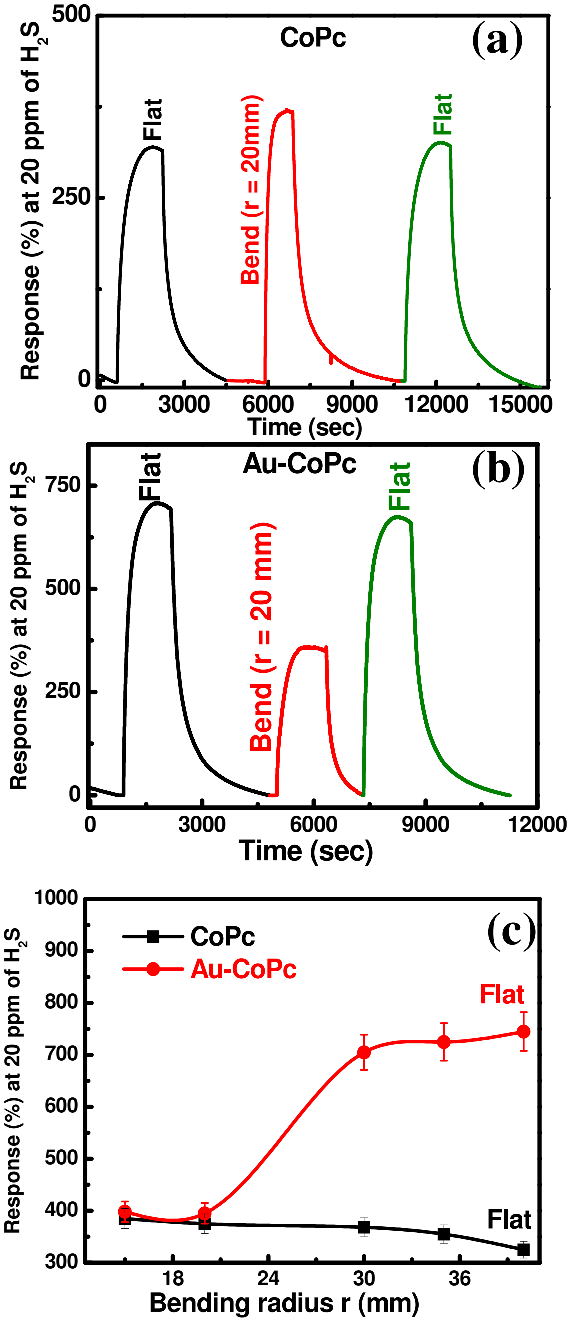

Figure 4.10: Chemiresistive response (at 20 ppm of H_2S) of (a) CoPc films and (b) Au-CoPc in the flat and bend conditions (c) response versus bending radius (*r*) plot.

stress enhances the separation among CoPc molecules, which facilitates H_2S molecules to easily interact with Co metal sites. An increase in the numbers of interaction sites under bend condition is responsible for high response of the CoPc films. From Fig. 4.10(a) and Fig. 4.10(b) it can be seen that the base resistance of films as well as the response characteristics of both the films - irrespective of the number of bending cycles - fully restores back to the original value of the flat condition within experimental error limits, indicating the reversible nature of the interaction sites created on bending.

4.4 Conclusions

In conclusion, we have demonstrated that modification of CoPc films by thin discontinuous layer of Au. Although Au introduces the structural disorder, but exhibits beneficial features for H_2S sensing. The optimized thickness of Au layer was ~ 1 nm for highest response towards the H_2S gas. The Au modified CoPc films exhibit improved response towards H_2S gas in comparison to the pure CoPc films. The main contributing factor for improved response of Au modified CoPc films is due to the high density of hole charge carrier, which makes these films more oxidative to the H_2S in comparison to pure CoPc films. The gas sensing characteristics of these heterojunction films are stable for bending radius > 20 mm. These hybrid films are promising candidate for incorporation into a portable, low-power, inexpensive, and easy-to-use light weight flexi-gas sensor devices for industrial control and personal healthcare.

CHAPTER 5

ZnO nanowires - cobalt Phthalocyanine heterojunction based chemiresistive gas sensor with highly improved gas sensing properties

5.1 Introduction

As discussed in the previous chapter, the sensitivity of cobalt phthalocyanine (CoPc) thin films based sensor towards H_2S gas can be enhanced by modifying its surface with a thin discontinuous layer of gold. However such a surface modification improves its sensitivity and selectivity for H_2S but the response and recovery times of such devices are large (~ few minutes). In order to lower the response / recovery times a highly porous-network with large surface is required. Previously to improve the sensitivity of a sensor, the hybrid materials comprising of organic-inorganic semiconductors has been employed [130, 132, 133]. In this chapter, we demonstrate a novel method of improving sensing performance by using a random network of *n*-type ZnO nanowires (NWs) as a template for growing CoPc films, terminating in a porous network of CoPc layer. On the other hand CoPc layer is depleted of charge due to formation of a *p-n* junction with ZnO. Such a specially fabricated inorganic-organic hybrid structure not only improves the sensitivity for H_2S but also lowers down the response time drastically.

5.2 Experimental Section

5.2.1 Growth of random network of ZnO nanowires on BOPET substrate

The random network of ZnO NWs was grown on biaxially oriented polyethylene terephthalate (BOPET) flexible substrate by hydrothermal method using ZnO nano particles (NPs) as seed [125]. Figure 5.1 schematically shows the different steps involved in the fabrication process. First ZnO NPs were prepared by dissolving Zinc acetate dihydrate

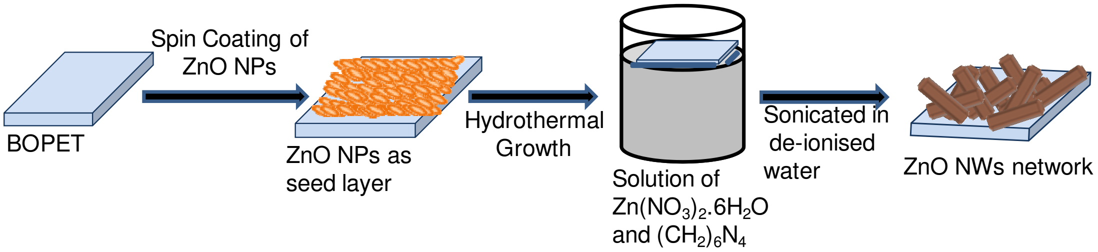

Figure 5.1: Steps involved in the synthesis of ZnO nanowires films on BOPET substrates.

(0.015M) in methanol (100ml) under strong stirring at 60°C. Later a 0.03M solution of sodium hydroxide in methanol (50ml) was added slowly at 60°C [134]. The volume ratio of two solutions was maintained as 2:1. The reaction mixture was stirred for 2 hours at 60°C. The resulting NPs in solution were having diameter between 5 and 10 nm and were stable for a period of around 2 weeks [134]. Coating of ZnO NPs on BOPET substrates was done by spin coating of as synthesized NP solution. The growth of ZnO NWs on these coated BOPET sheets was carried out by suspending these sheets over a solution containing aqueous equimolar (25 mM) concentration of Zinc nitrate and Hexamethylenetetramine (HMTA), $(CH_2)_6N_4$ at 90°C for approximately 7 h [134]. After growth the substrates were thoroughly rinsed in de-ionized water and dried under Ar flow. The growth of ZnO NWs on BOPET substrate was found to be very reproducible for the same condition of temperature and solution concentrations. In the present work, BOPET was chosen as substrate due to the presence of polar ester groups in the PET chains. Since ZnO also has polar surfaces therefore ZnO NWs grown on BOPET exhibit a good adhesion with the substrate due to dipolar attraction [135]. In addition the BOPET substrate has added advantage of flexibility, light weight and low cost.

5.2.2 Modification of ZnO NWs films by Cobalt Phthalocyanine

The network of ZnO NWs films deposited on BOPET sheet was modified with different thicknesses (*viz.*; 5 nm, 15 nm, 25 nm and 50 nm) of CoPc as shown schematically in Fig. 5.2. The CoPc thin films were deposited using thermal evaporation at high vacuum (~ 2×10^{-6} mbar) condition. During deposition of CoPc layer, ZnO NWs coated BOPET substrate was maintained at room temperature. The thickness of films was in-situ measured using quartz crystal monitor. Hereafter these samples will be referred as ZnO-CoPc (*d* nm), where *d* is the nominal thickness of the CoPc layer.

Figure 5.2: Schematic showing the modification of ZnO nanowires network by CoPc.

5.2.3 Current-voltage characteristics of ZnO-CoPc heterojunction films

Figure 5.3 shows the typical in-plane current-voltage characteristics of all samples in the bias range of ±100 V. One of the intriguing observations in the Figure 5.3 is that heterojunction films with increasing CoPc thickness up to 25 nm exhibit lowering of current

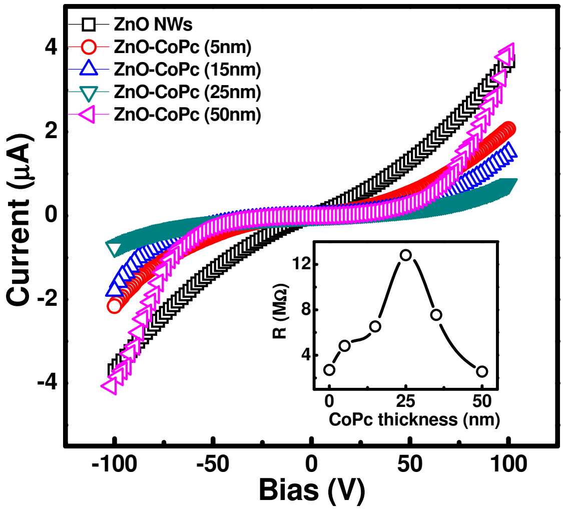

Figure 5.3: In-plane current-voltage characteristics of all samples. Inset shows the resistance

of the hybrid films as a function of CoPc thickness (at a fixed bias), while for higher CoPc thickness current enhances and reaches nearly close to the pure ZnO NWs films. To see this clearly, in the inset of Figure 5.3, the base resistance (measured at 100 V) of all sample is plotted. From inset of Figure 5.3 it can be seen that heterojunction films with CoPc thickness ~ 25 nm exhibit highest resistance among all samples and we later provide the explanation for this behavior. It is also interesting to note that ZnO NWs-CoPc (50 nm) sample exhibit a typical *I-V* characteristics which is similar to pure CoPc films, where with increasing bias (> 10V) an ohmic to space charge limited conduction takes place [136].

5.2.4 Studies using electron microscopy

The transmission microscope (TEM) images of the pure ZnO and ZnO-CoPc (25nm) heterojunction films are shown in Figure 5.4(a-b). As seen from Figure 5.4(a), the average

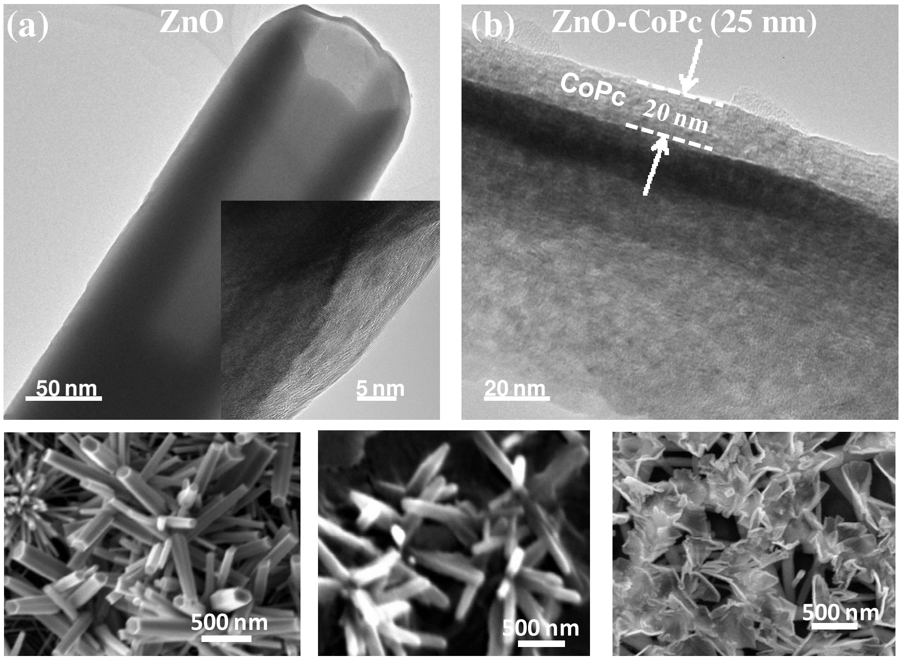

(c) ZnO NWs films **(d) ZnO-CoPc (15nm)** **(e) ZnO-CoPc (25nm)**

Figure 5.4: (a-b) TEM images of the (a) pure ZnO NW, inset shows the high resolution image of ZnO (b) ZnO-CoPc (25 nm) heterojunction film. (c-e) SEM images of the pure ZnO and hybrid films.

diameter of the pure ZnO nanowires is around ~ 110 nm. The high resolution TEM image shown in inset of Figure 5.4(a) reveals that these ZnO wires are polycrystalline in nature. From the TEM images shown in Figure 5.4(b) it can be seen that the estimated thickness of CoPc overlayer on ZnO nanowires in heterojunction films is close to the nominal thickness obtained from quartz crystal monitor. The TEM image shown in Figure 5.4(b) also reveals that CoPc layer grown on CoPc are not highly ordered.

5.2.5 X-ray photoelectron spectroscopy

The typical $Co2p_{3/2}$, and $Zn2p_{3/2}$ XPS spectra of all samples are shown respectively in Figure 5.5 (a) and 5.5(b). The respective binding energy value for $Co2p_{3/2}$ (in pure CoPc film) and $Zn2p_{3/2}$ (in pure ZnO NWs films) were found to be 781.8 eV and 1020.6 eV [84, 114, 119]. From Figure 5.5(a) it is evident that in comparison to pure CoPc films, the heterojunction films exhibits a shift of $Co2p_{3/2}$ peak towards lower binding energy with increasing CoPc thickness. On the other hand for heterojunction samples, with increasing CoPc thickness, $Zn2p_{3/2}$ peak exhibits a shift towards higher binding energy in comparison to the pure ZnO NWs films. Such a shift of XPS peaks indicates the electron transfers from ZnO NWs to CoPc. Since adsorbed oxygen plays a very important role in the gas sensing behaviour of ZnO and CoPc films therefore, for the heterojunction films we have measured the ratio of chemisorbed oxygen to the Co and result is plotted in Figure 5.5(c). It can be seen that ZnO-CoPc (25nm) sample exhibits the least content of chemisorbed oxygen. It may be noted that in heterojunction film, with increasing thickness of CoPc, the XPS signal from ZnO NWs become weak in intensity. From the XPS data, we have estimated the actual thickness of CoPc layer grown on ZnO NWs surface, which was determined from the attenuation of the intensities of characteristic $Zn2p_{3/2}$ and $Zn2p_{1/2}$ peaks [137].

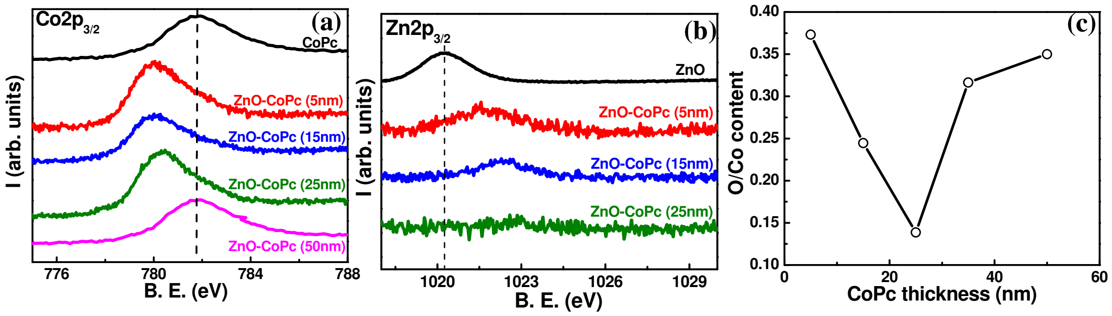

Figure 5.5: XPS spectra (a) Co-2p3/2 (b) Zn $2p_{3/2}$ for the ZnO NWs and heterojunction films. (c) O/Co content for ZnO-CoPc heterojunction films

According to Beer-Lambert law, the peak intensities (peak area) are expressed by [137]:

$$I_{2p_{3/2}} = I^0_{2P_{3/2}} e^{-d/\lambda_{2p_{3/2}} \sin\theta} \tag{5.1}$$

and

$$I_{2p_{1/2}} = I^0_{2P_{1/2}} e^{-d/\lambda_{2p_{1/2}} \sin\theta} \tag{5.2}$$

where I is the peak intensity of the core level electron $2p_{3/2}$ or $2p_{1/2}$ recorded for CoPc coated ZnO NWs, while I^0 corresponds to the peak intensity obtained from bare ZnO NWs. $Zn2p_{3/2}$ and $Zn2p_{1/2}$ intensity ratios can be calculated for bare and coated ZnO NWs:

$$R^0 = I^0_{2p_{3/2}} / I^0_{2p_{1/2}} \tag{5.3}$$

and

$$R = I_{2p_{3/2}} / I_{2p_{1/2}} \tag{5.4}$$

Combining equations (5.1)-(5.4) leads to the analytical expression for assessing the thickness:

$$d = \sin\theta / [(\lambda_{2p_{3/2}})^{-1} - (\lambda_{2p_{1/2}})^{-1}] \ln(R_0 / R) \tag{5.5}$$

The analyses were performed at an emission angle of 90°, so sin θ=1. The attenuation lengths were estimated using the Seah and Dench equation established for an organic coating:

$$\lambda = 0.11(E_k^{1/2}) \text{ in mg/m}^2 \tag{5.6}$$

where E_K is the kinetic energy of the core level electron Zn2$p_{3/2}$ (~232 eV) or Zn 2$p_{1/2}$ (~210 eV). It follows that for determining the thickness (in nm), one has to divide λ in mg/m² by the overlayer density in g/cm^3 which is taken as ~ 1.6 for CoPc layer. Equation (5.6) permits to estimate the attenuation length to 1.59 and 1.68 nm for Zn2$p_{3/2}$ and Zn 2$p_{1/2}$, respectively. Applying these values in Equation (5.5) yields a CoPc layer thickness of 22.2 nm which is quite close to the nominal CoPc thickness of ~ 25 nm.

5.2.6 Work function measurement

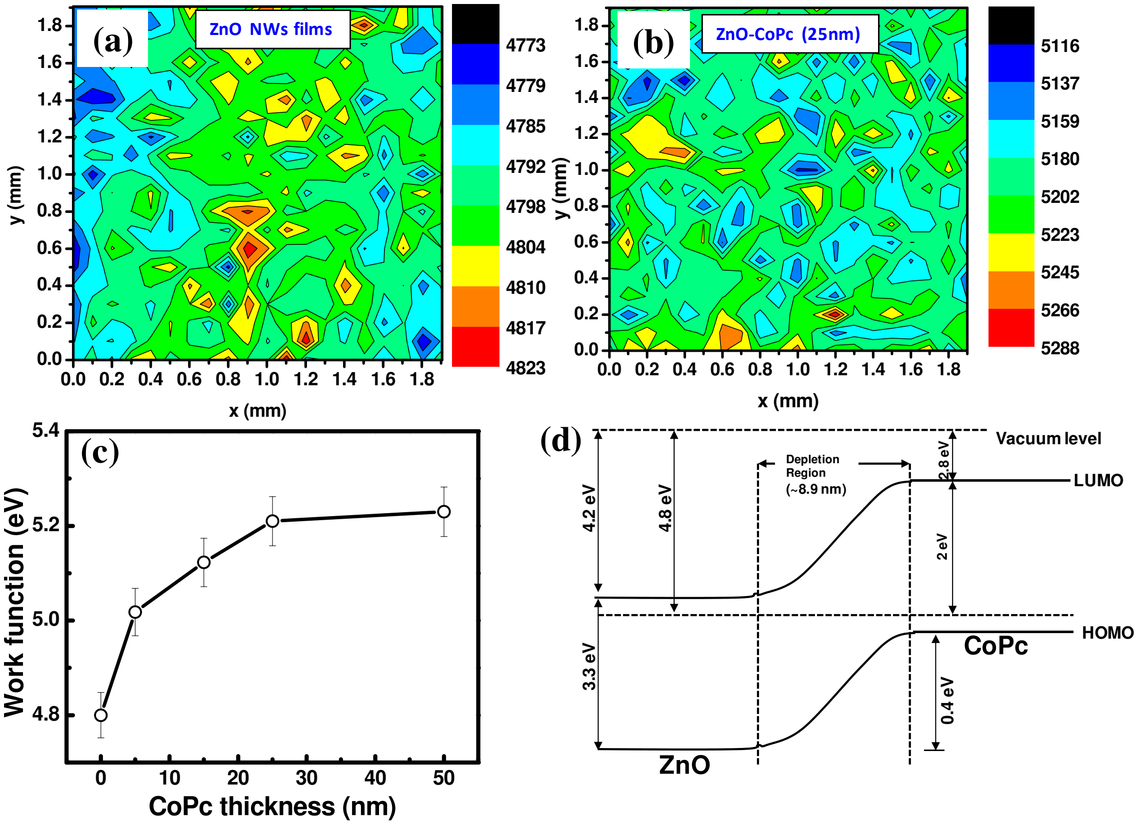

Figure 5.6: Work function mapping (scan area: 2 mm × 2mm) of (a) ZnO NWs (b) ZnO-CoPc (25nm) samples. (c) Plot showing work function of hybrid films as a function of CoPc thickness. (d) Schematic of the energy level alignment at ZnO-CoPc interface.

The possibility of charge transfer between ZnO and CoPc is further supported by the work function measurement. The typical work functions mapping results for ZnO NWs and ZnO-CoPc (25nm) films are shown in Figure 5.6(a) and 5.6(b) respectively. As seen from Figure 5.6(c), for pure ZnO NWs films the work function was found to be 4.8 eV and for heterojunction films it systematically increases with increasing CoPc thickness and attains a value 5.2 eV (*i.e.* comparable to the pure CoPc) at nominal thickness of 25 nm. The difference in work function of ZnO NWs and CoPc suggest that at the interface there is a transfer of charge from ZnO to CoPc resulting in the formation of a *p-n* junction with effective barrier height of 0.4 eV (shown schematically in Figure 5.6(d)).

5.2.7 X-ray diffraction

The XRD data for all samples are shown in Figure 5.7. In the x-ray diffraction data (shown in Figure 5.7(a)) obtained in the range of 30-70°, we observe diffraction peaks at $2\theta=$ 31.5°, 56.5° and 66.3°, which are attributed to diffraction from the (*100*), (*110*) and (*200*) atomic planes of hexagonal wurtzite phase of ZnO. The estimated lattice parameters of the ZnO was found to be a = 3.2480Å and c = 5.2068Å with c/a = 1.6031 and cell volume= 47.57Å^3. The obtained lattice parameters are consistent with the reported literature values [138]. Inset of Figure 5.7(a) shows the XRD patterns (enlarged view of only 31.5° diffraction peak corresponding to the (*100*) reflection of ZnO) of all samples. Large broadening of diffraction peak suggests the nanocrystalline nature of the ZnO. For heterojunction films with increasing thickness of CoPc layer, following two important points are noticed from XRD data shown in inset of Figure 5.7(a): (i) (*100*) diffraction peak of ZnO NWs systematically shifts to the lower 2θ values and (ii) (*100*) diffraction peak exhibit lowering of intensity as well as broadening. Both of these observations suggest that interaction between CoPc and ZnO NWs creates structural defects in the ZnO NWs close to the ZnO-CoPc interface.

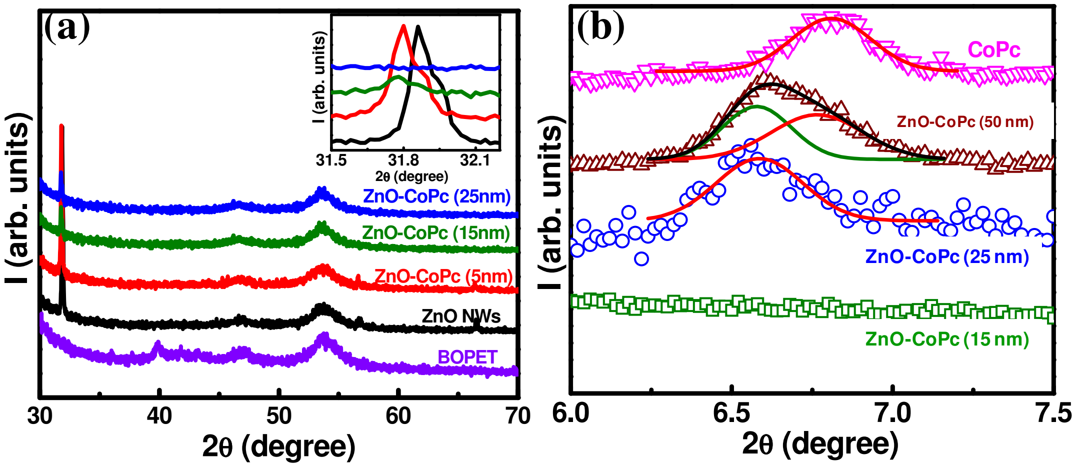

Figure 5.7: (a) XRD data and (b) GIXRD data for the pure ZnO NWs, pure CoPc and ZnO-CoPc heterojunction films

It is important to mention that CoPc diffraction peak is usually observed at low diffraction angles (< 10°) due to its large lattice parameters, therefore to obtain the information about the crystalline nature of CoPc in heterojunction films, the diffraction data was collected in the grazing incidence mode. In the grazing incidence x-ray diffraction data (GIXRD) shown in Figure 5.7 (b), the (*200*) diffraction peak corresponding to CoPc layer is observed at low angles. From Figure 5.7(b) it can be seen that in the heterojunction films with CoPc thickness ≤ 15 nm the CoPc does not exhibit crystalline nature (*i.e.* absence of diffraction peak). For ZnO-CoPc (25nm) sample the diffraction peak corresponding to CoPc is observed at ~ 6.52°. However for ZnO-CoPc (50 nm) sample the CoPc diffraction peak become asymmetric towards higher diffraction angle and it can be deconvoluted into two peaks, one at 6.52° corresponding to CoPc in immediate vicinity of ZnO NWs and other at 6.8° (*i.e.* exactly at same position for pure CoPc films) corresponding to the relaxed CoPc layer which is far from ZnO surface [99]. In summary, the XRD data suggests, CoPc layer in close proximity to ZnO -CoPc interface initially grows in a disordered way but later (*i.e.* around CoPc thickness of ~ 25 nm) at full coverage it attains a crystalline nature. The XRD data also suggest that the interaction of CoPc with ZnO NWs affects the molecular ordering of CoPc layer near the interface. As discussed earlier, there is a charge transfer from ZnO NWs to the CoPc molecules, which may affect the planarity of the CoPc molecule. As a result the inter-planar distance between the CoPc molecules increases and it shifts the diffraction peak of heterojunction films (with 25nm thick CoPc) to lower angles.

5.2.8 Photoluminescence study

Figure 5.8(a) shows the photoluminescence (PL) emission spectra of all samples. When pure ZnO NWs sample is excited with light of wavelength ~ 320 nm, it shows an emission line at ~380 nm, which is assigned to the near band edge (NBE) transition and an asymmetric band trailing at higher wavelength region (peak around 420 nm) due to defect originated from the oxygen vacancies [134]. From the PL emission spectra of heterojunction films, following inferences can be drawn: (i) The NBE peak exhibits a blue shift with increasing thickness of CoPc. For ZnO -CoPc (25 nm) sample the NBE peak is observed at ~ 355 nm. (ii) In addition to the defect related emission peak at ~ 420 nm, heterojunction films initially at low thicknesses of CoPc exhibit an additional peak at ~ 480 nm and it shifts to 510 nm for the ZnO -CoPc (25 nm) sample. By taking the area ratio of defect related emission (combining the contributions of 420 nm peak and other higher wavelength peak) to band edge emission, we could estimate the contribution of defect related emission as ~ 47% for pure ZnO NWs sample while for heterojunction films it increases with the thickness of CoPc layer. For ZnO - CoPc (25 nm) sample the contribution of defect related emission is found to be nearly 88%. The suppression of band edge emission in heterojunction films can be explained by the formation of *p-n* junction between *p*-type CoPc and *n*-type ZnO NWs. When a photon is incident on the films an exciton is formed. The *p-n* junction enhances the dissociation of exciton due to built in field. The electron which is released by dissociation of exciton is taken away by the ZnO layer and CoPc layer transports the holes. Hence the dissociation of excitons suppresses the electron-hole recombination which is necessary for PL band edge emission. The extent of interaction between ZnO NWs and CoPc is also manifested in the excitation profile of the samples (shown in Figure 5.8(b)). The excitation spectra of heterojunction films exhibit blue shift and broadening with respect to the pure ZnO NWs sample. For ZnO–CoPc (25 nm) sample the excitation spectra exhibits very large broadening, which extends from 220 nm to 360 nm and it suggest that in case the conduction band of ZnO is highly perturbed by the presence of CoPc layer.

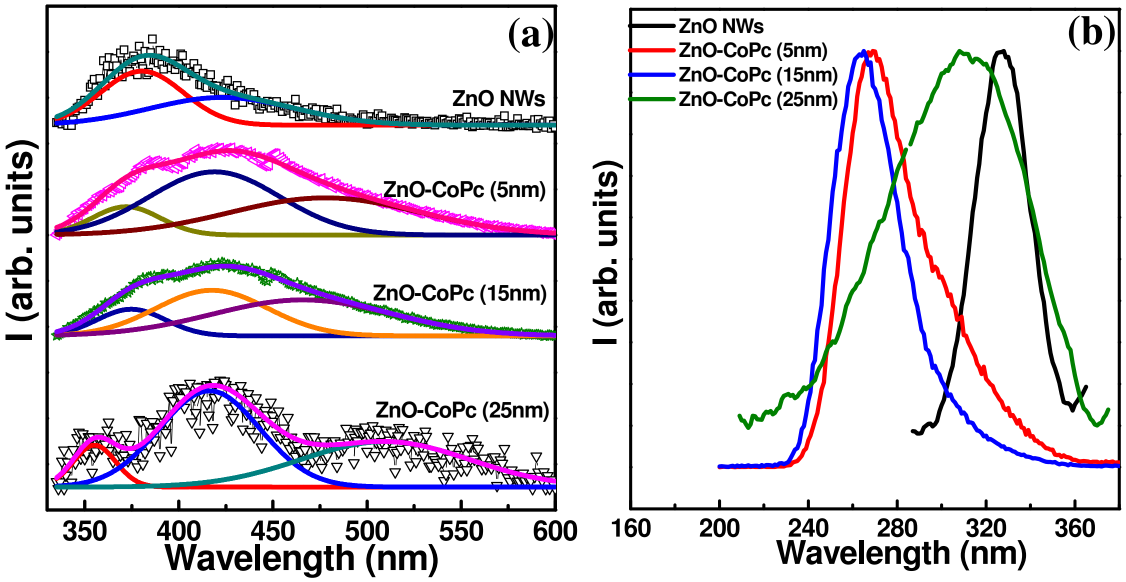

Figure 5.8: Photoluminescence (a) emission and (b) excitation spectra for all samples

5.2.9 UV-visible spectroscopic study

Figure 5.9(a) shows the electronic absorption spectra for pure ZnO NWs and heterojunction films. The estimated bang gap for pure ZnO NWs is found to be 3.6 eV [130, 139]. Some interesting features have been observed in the electronic absorption spectra of CoPc in the heterojunction films. For CoPc films the absorption in the visible region (close to 1.9 eV) is referred as Q band arising from the singlet *π*-*π** transition in the porphyrin ring (*i.e.*

intermolecular excitation) and has a doublet due to Davydov splitting [96]. The difference in the relative orientation of the molecules decides the extent of Davydov splitting. From Figure 5.9(a) it is evident that magnitude of Davydov splitting remains same at low thickness of CoPc but at higher thickness (~ 25 nm) of CoPc it enhances, which is consistent with the fact that at low thicknesses, CoPc grows randomly on ZnO but at higher thicknesses it attains a crystalline nature. For CoPc, the peak in absorption spectra in the near UV region is known as B- band or Sorret band. It is very important to note that for ZnO-CoPc (25nm) sample we observe a peak at 2.7 eV, the origin of which is attributed to the charge transfer (CT) excitation that is an intermolecular excitation [96]. The energy band gap has been obtained from the electronic absorption spectra using relation:

$$\alpha=\alpha_0(hv-E_g)^{1/2} \tag{5.7}$$

where α is the absorption coefficient, α_0 is a constant and hv is the photon energy.

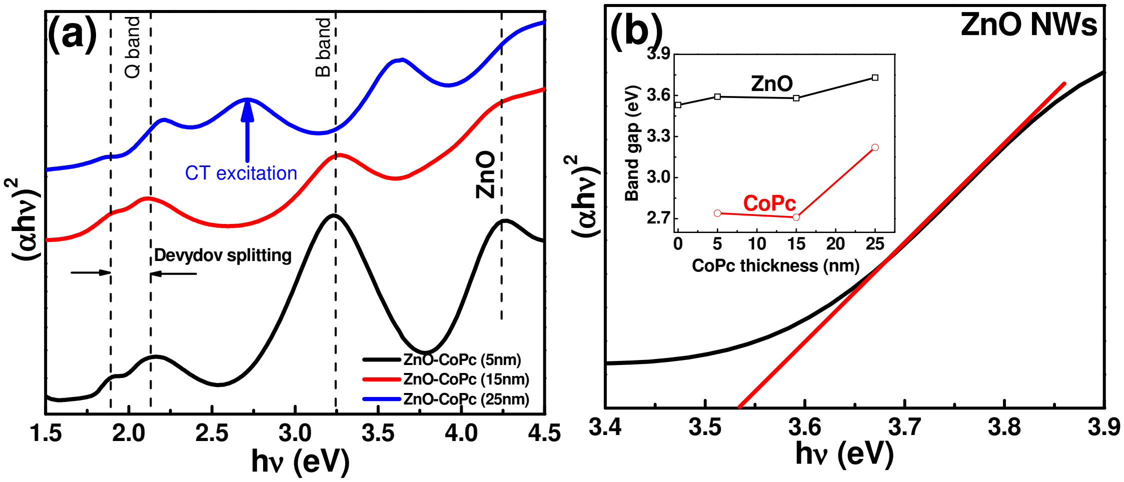

Figure 5.9: Electronic absorption spectra recorded for (a) pure ZnO NWs films and (b) for heterojunction films, here y-axis is plotted in log scale. Inset of Figure 5.9(a) shows the estimated band gap value for ZnO and CoPc in the heterojunction films.

As seen from Figure 5.9(b), the value of direct band gap E_g estimated for ZnO in pure films was found to be 3.5 eV and for heterojunction films it enhances with increasing CoPc thickness. The band gap of ZnO in the ZnO-CoPc (25 nm) is found to be 3.7 eV, such an enhancement of band gap is attributed to the electronic interaction between ZnO NWs and CoPc layers. For heterojunction film, the increase in E_g of ZnO with increasing CoPc thickness is also supported by the blue shift of NBE peak in the PL emission spectra. For CoPc layer the E_g value estimated from B band is found to be 2.7 eV (at low thickness of CoPc) and it increases to 3.2 eV when CoPc layer thickness is increased to 25 nm. The enhancement of E_g for both ZnO and CoPc layer in the heterojunction ZnO-CoPc (25 nm) films suggest strong electronic interaction between both.

5.2.10 Raman spectroscopy

Figure 5.10(a) and 5.10(b) respectively shows the Raman spectra in two different wave number regions of ZnO-CoPc heterojunction films. The ZnO lattice existing in Wurtzite structure has P63mc symmetry and contains two formula units in each primitive cell [140]. According to the group theoretical analysis, the irreducible representation for optical phonons is given by $A_1 + 2B_1 + E_1 + 2E_2$, of which the non-polar E_2 modes at ~100cm^{-1} and ~ 435cm^{-1} respectively due to the vibrational motion of the Zn sublattice and oxygen atoms form the two most prominent features in the Raman spectra of our samples [141]. As seen from Figure 5.10(b), up to 15 nm thickness of CoPc, no Raman peaks were observed that could be assigned to the CoPc layer. Interestingly, the E_2 modes of ZnO gradually increased in intensity with the increasing thickness of the CoPc layer till it completely covered the underlying ZnO layer. As discussed above, XPS data analysis of the heterojunction films suggests that ZnO which is inherently *n*-type semiconductor due to oxygen vacancies donates electron to the antibonding orbital of the CoPc layer and forms a charge transfer complex. Such electronic interaction complemented by the strain induced structural changes due to lattice mismatch result in the significant change of geometry of vibrational modes and hence the internal reorganization energy. Similar effects have been observed for photo-induced electron transfer in donor-acceptor (D-A) complexes [142]. Such geometric change in the D-A complex may even affect the Raman cross-section and hence the Raman intensities of a few selective bands, as observed in case of the ZnO-CoPc heterojunction films.

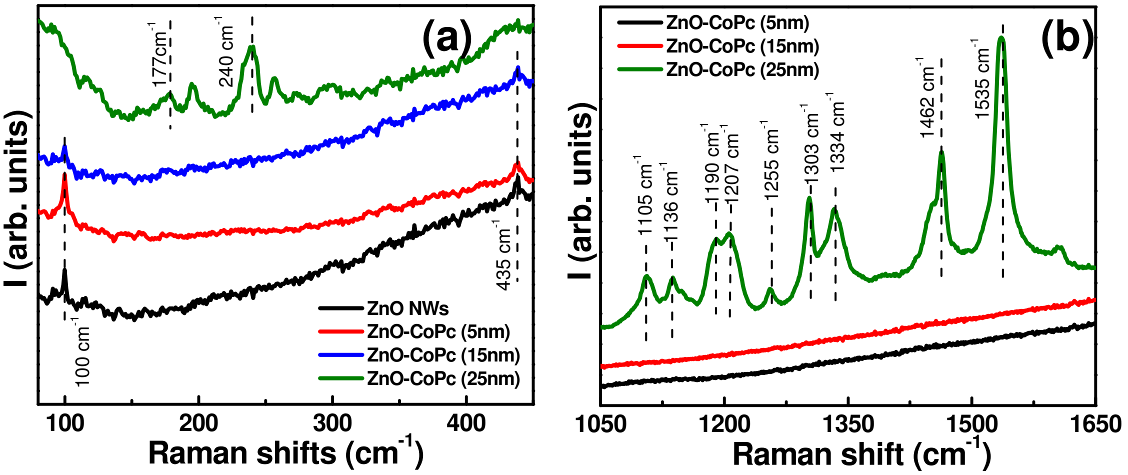

Figure 5.10: Raman spectra for pristine ZnO, pristine CoPc and their heterojunctions in (a) low wave number region 80-450 cm^{-1}. (b) high wave number region 1050-1650 cm^{-1}.

The intense peaks observed at higher wave number region (shown in Figure 5.10(b)) for ZnO-CoPc (25 nm) and ZnO-CoPc (50 nm) samples were assigned to the different modes of the CoPc molecule signifying the presence of the CoPc overlayer. For these hybrid films, the sharp intense peak at ~1539 cm^{-1} and ~1344 cm^{-1} were respectively assigned to the totally symmetric stretching vibration at the C_β-C_β and C_α-C_β bonds of the pyrrole rings whereas the peak at ~1139 cm^{-1} results from the breathing vibration of the pyrrole rings. These vibrations have been primarily assigned as isoindole ring stretches with large C-N contribution. The Co-N vibration is observed at 240 cm^{-1}. The vibration due to in-phase motion of isoindole group is observed at 177 cm^{-1} [141]. The other peaks assigned at Figure 5.10(b) matches very well with the reported values for Raman peak of CoPc [22, 123].

5.2.11 Summary of various characterization results

Based on charge transport, SEM, XRD, XPS, work function, Raman spectroscopy and PL results, we conclude that in heterojunction films there is a strong interaction between ZnO NWs and CoPc layer and sample with CoPc layer thickness ≥ 25 nm uniformly cover the ZnO NWs. The structure of ZnO NWs consists of tetrahedrally coordinated O^{2-} and Zn^{2+} ions planes which are placed alternately along the *c*-axis. It results in Zn^{2+}-terminated (*0001*) and O^{2-} terminated ($000\bar{1}$) end polar surfaces resulting in a normal dipole moment and spontaneous polarization along the *c*-axis of ZnO NWs [138].

In general on polar surfaces at low thickness, CoPc molecules can stack in a face on manner due to enhanced molecule – substrate interaction, however with increasing thickness molecule-molecule interaction dominates and as a result molecules prefers to stack in edge on manner. Such a competition of face on and edge in stacking pattern of CoPc molecules on polar ZnO surface may leads to the initial growth of CoPc in an amorphous way.

In ZnO-CoPc (25 nm) films in which ZnO NWs are uniformly coated with CoPc (thickness ~ 25 nm), transfer of electrons from ZnO NWs to CoPc will reduce the hole concentration in CoPc up to the depletion layer width. The depletion layer width (*W*) of the *p* - *n* junction formed at the ZnO-CoPc interface can be calculated using the following relation [143]:

$$W = \left[\frac{2\varepsilon_{CoPc}V_0}{eN_a} + \frac{2\varepsilon_{ZnO}V_0}{eN_d}\right]^{1/2} \tag{5.8}$$

Here ε_{CoPc} is the permittivity of the CoPc and it is taken as 3, ε_{ZnO} is the permittivity of the ZnO and it is taken as 8.7, V_0 is the energy barrier (0.4 eV) at ZnO-CoPc interface, *e* is the electronic charge and N_a is the acceptors concentration at CoPc (equivalent to the hole concentration ~ 3×10^{16} m^{-3}) and N_d is the donor concentration at ZnO (equivalent to the electron concentration ~ 1.3×10^{23} m^{-3}). The calculated value of W is ~ 8.9 nm and since $N_d >> N_a$ therefore depletion region is mostly extended in the CoPc region around the *p*-*n* interface. Since in the present case, the ZnO-CoPc (25 nm) sample exhibited least content of chemisorbed oxygen therefore such sample may have very low hole concentration and therefore actual W could be much larger than the estimated value. Since the depletion region obstructs the movement of charges therefore in such heterojunction films the conduction channel is quite narrow and hence these sample exhibited the highest resistance value (as discussed before in Figure 5.3) At present it is not clear why ZnO-CoPc (25 nm) exhibited the low content of chemisorbed oxygen, possibly it could be due to the presence of the built in field of the formed *p*-*n* junction (which is directed from ZnO NWs to the CoPc side) which may provide the extra barrier for the chemisorption of oxygen. In hybrid films with thicker CoPc layer (~ 50 nm) the role of depletion region in obstructing the charge transport will be negligible due to high hole concentration at the surface (due to more chemisorbed oxygen).

5.2.12 Chemiresistive gas sensing properties of ZnO-CoPc heterojunction films

Typical normalized response curves of pure ZnO NWs films and ZnO NWs - CoPc (having different thickness) films for 10 ppm of H_2S are shown in Figure 5.11(a). From Figure 5.11(a) following inferences can be drawn: (i) Pure ZnO NW films and heterojunction films with CoPc thickness $\leq$ 15 nm exhibit a decrease in resistance on H_2S exposure indicating the *n*-type conduction. (ii) Pure CoPc films of thickness ~ 25 nm exhibits an increase of resistance when exposed to H_2S, suggesting a *p*-type conduction. (iii) Heterojunction films with CoPc thickness of ~ 25 nm exhibits huge increase in the resistance on exposure to H_2S indicating that now CoPc starts playing a dominant role in conduction and hence a *p*-type behavior is observed. (iv) With further increase of CoPc thickness (> 25 nm) the response and recovery of heterojunction films becomes sluggish.

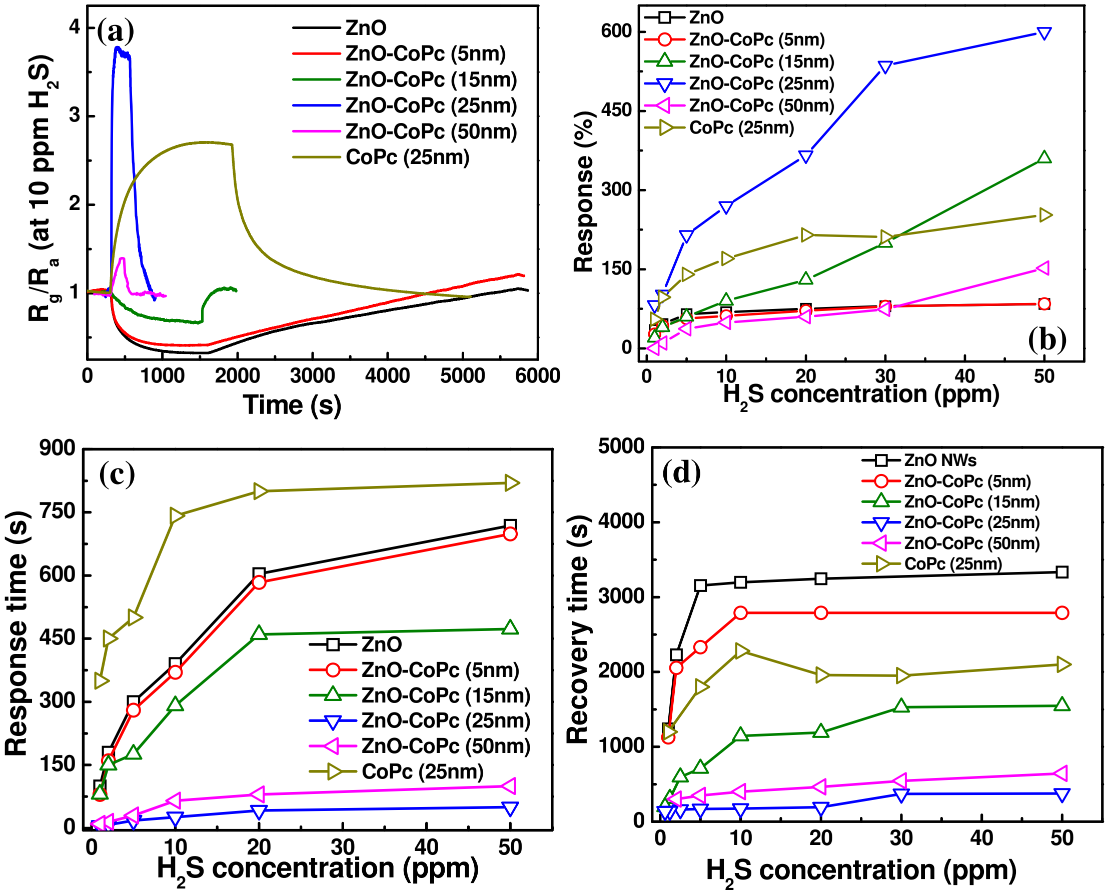

Figure 5.11: (a) Typical response curve (*i.e.* normalized resistance versus time) of all samples on 10 ppm exposure of H_2S gas. Here R_g and R_a stand for resistance in presence of gas and air respectively. (b) Response (%) as a function of H_2S concentration (c) Response time (d) Recovery time as a function of H_2S concentration.

The response (%) data for all samples is plotted in Figure 5.11(b). It can be seen that heterojunction films with CoPc thickness of ~ 25 nm exhibits highest response (%) in comparison to all other samples. The response time and recovery time data for all samples are shown respectively in Figure 5.11(c) and Figure 5.11(d).From Fig. 5.11 (c-d), it can be seen that ZnO-CoPc (25 nm) sample exhibits the fastest response and recovery (response time ~ 26 s and recovery time ~ 175 s at 10 ppm of H_2S) among all samples. It is also important to note that pure ZnO and pure CoPc films exhibit slow response kinetics.

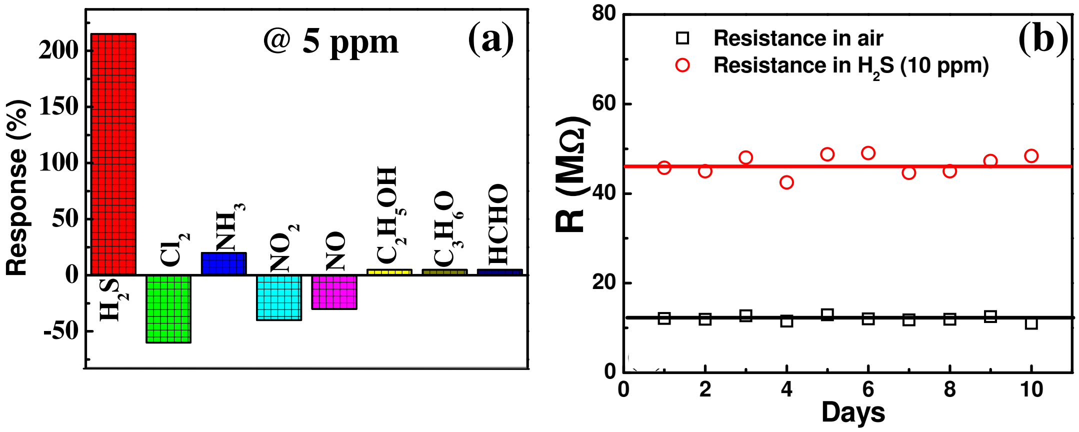

Figure 5.12: (a) Selectivity histogram (measured at 5 ppm) of ZnO-CoPc (25nm) samples for different gases. (b) Stability measurement of ZnO-CoPc (25nm) sample performed over a period of 10 upon repeated exposure to 10 ppm of H_2S.

Selectivity histogram for the ZnO-CoPc (25 nm) films is shown in Figure 5.12(a), which shows that these films are highly selective to the H_2S gas. Moreover, these heterojunction films were stable in atmospheric conditions for several months. Figure 5.12(b) shows the stability measurement of ZnO-CoPc (25 nm) films performed over a period of 10 days, the obtained result suggest that these films are quite stable (variation of about 10%) even after repeated exposure to 10 ppm of H_2S. The enhanced response (%), selectivity, fast response / recovery and stability at repeated exposure qualify these heterojunction films for rapid detection of H_2S in the range of 1-50 ppm at room temperature.

In the following part, we investigate among all samples why ZnO-CoPc (25 nm) films exhibited highest response (%) and fastest response for the H_2S gas. In Figure 5.4(a) we have shown the SEM images of samples. From Figure 5.4(c) it can be seen that pure ZnO NWs films makes a porous network of NWs and the typical diameter of these NWs is in the range of 50-110 nm and length in the range of 1-2 µm. The quasi-hexagonal ends of the ZnO NWs indicate that their main axis is preferentially oriented along [*0001*] direction, which is in accordance with the growth habit of wurtzite crystals. The surface morphology of the ZnO

NWs films did not change upon deposition of CoPc layer upto a nominal thickness of 5 nm and this is expected as at low thickness of CoPc, it tries to cover the surface of ZnO NWs. As seen from Figure 5.11(a), ZnO–CoPc (5 nm) films exhibit *n*-type behavior, which suggests that when thickness of CoPc is low, CoPc does not uniformly cover the surface of ZnO NWs and as a result *n*-type conduction of the ZnO NWs dominates the response. The morphology of the ZnO-CoPc (15nm) films exhibit slight increase in the diameter of the ZnO NWs (shown in Figure 5.4(d)) suggesting the increasing coverage of CoPc on ZnO-NWs surface. From SEM image shown in Figure 5.4(e), it can also be seen that the increase of CoPc thickness up to 25 nm, the ZnO NWs gets uniformly coated and in addition there is also a formation of thin lamellar sheets of CoPc interconnecting the CoPc coated ZnO NWs. The *p*-type conduction of ZnO NWs – CoPc (25 nm) sample also suggests that in these samples the ZnO NWs are uniformly coated with the CoPc.

5.3 Mechanism of the improved sensing behavior of ZnO-CoPc heterojunction films

Now we present plausible sensing mechanism of detection H_2S *i.e.* a highly reducing (electron-donor gas). (i) Since ZnO NWs exhibit *n*-type conduction and when it is exposed to atmosphere, oxygen molecules adsorb on the surface of the ZnO NWs and form O_2^- ions by capturing electrons. Thus ZnO NWs films show a high resistance state in air ambient. Its resistance falls down on exposure to a reductive H_2S because H_2S reacts with the surface O_2^- species, which results in an enhancement of electron concentration in the ZnO NWs. (ii) In pure CoPc films, due to low coordinated structure of Co atoms in CoPc molecules, it is the most preferable sites for the chemisorptions of oxygen. H_2S can interact with CoPc films by two processes, the first one can be the direct interaction with the Co sites free from adsorbed oxygen, this process leads to very fast response and second process is the competitive displacement of the chemisorbed oxygen, which is relatively a slow process [9]. The plausible mechanism of direct interaction of H_2S with the oxygen free Co sites can be understood by the dissociation of H_2S on the metal surface under ambient condition because it is a weak acid (acid dissociation constant *pKa* =7.05) [144]. The dissociation of H_2S results into H^+ and HS^- ions. The resulting HS^- anion mediates the reduction of CoPc (resulting in increase in the resistance) and it converts back to parent CoPc by exposing sample to the air [145] .

The second process, which is competitive displacement of the chemisorbed oxygen by H_2S from CoPc surface (responsible for response of the sensor) can be understood by the following equation [2, 134]:

$$H_2S + 3O^{2-} \rightarrow H_2O + SO_2 + 6e^- \tag{5.9}$$

The released electrons capture the hole charge carriers of CoPc films and as a result the resistance of samples rise on H_2S exposure. The recovery of the sample takes place by picking up the electron by atmospheric oxygen.

Based on these proposed mechanisms we now explain why ZnO-CoPc (25nm) sample exhibit fast response kinetics and highest response (%) among all samples. In ZnO-CoPc (< 25 nm) films, CoPc does not uniformly cover the ZnO nanowires, hence when such samples are exposed to H_2S they exhibit less response (%) and slow response kinetics due to superimposition of the response signals from CoPc (which shows the rise of resistance due to *p*-type conduction) and ZnO (which shows the lowering of resistance due to *n*-type conduction). In ZnO-CoPc (25nm) samples, ZnO nanowires are uniformly coated with CoPc layer and exhibit very low chemisorbed oxygen therefore direct interaction of H_2S with oxygen free Co sites is preferable and hence we observe a rapid response of the ZnO-CoPc (25nm) films. According to the morphology imaged by SEM for ZnO-CoPc (25 nm) sample the top surface of the CoPc coated ZnO NWs are interconnected with thin CoPc lamellar sheet and charge transport takes place via CoPc layer. Due to low density of holes in the CoPc layer (because of the less amount of chemisorbed oxygen) the depletion width extends more towards CoPc side from the ZnO-CoPc interface. When these heterojunction films are exposed to H_2S gas, the electrons donated by H_2S further extends the depletion region towards the CoPc layer and blocks hole conduction channel resulting in huge rise of resistance / response. The above proposed mechanism of H_2S sensing of heterojunction films is schematically shown in Figure 5.13. In ZnO-CoPc (50nm) samples, the ZnO nanowires network gets covered with thick CoPc layer and hence the diffusion of H_2S inside the bulk of films results in slow response.

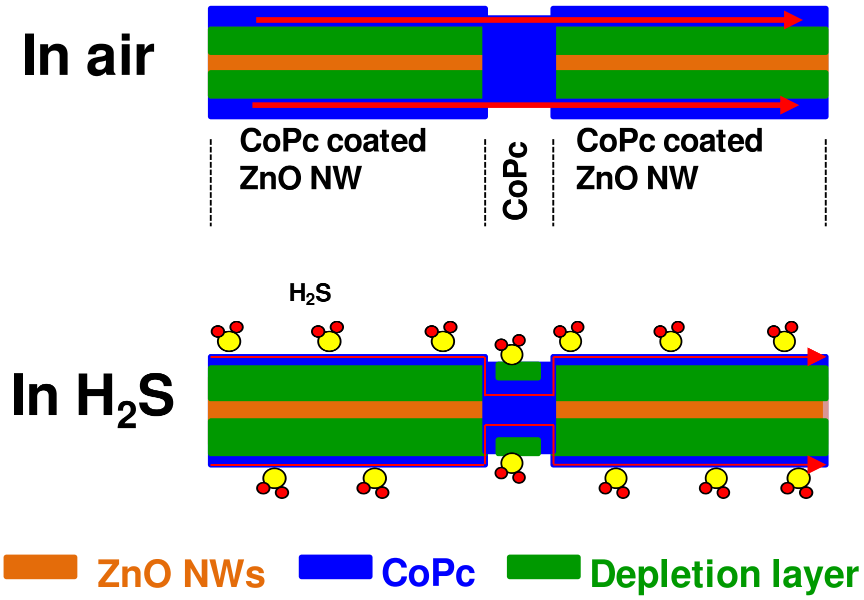

Figure 5.13: Schematic showing the H_2S sensing mechanism of ZnO - CoPc heterojunction films

5.4 Conclusions

A cobalt phthalocyanine modified ZnO nanowires network based H_2S sensor was fabricated in two steps. First the random network of ZnO nanowires was grown on light weight flexible BOPET sheets using hydrothermal method. In the second step these ZnO nanowires films were modified with different thickness of CoPc films. We have demonstrated that modification of *n*-type ZnO nanowires network by 25 nm thick *p*-type CoPc layer dramatically lowers the response / recovery times and improves the sensitivity for H_2S detection. The rapid response / recovery and high-sensitivity in these heterojunction films based sensor arises respectively due to direct interaction of H_2S with free Co sites and blocking of conduction channel by enlargement of the depletion layer width. Our results suggest that the ZnO-CoPc heterojunction films are attractive candidate for practical H_2S sensing applications, in view of its outstanding room-temperature sensitivity, excellent dynamic properties such as rapid response / recovery and high stability.

CHAPTER 6

OFETs using CoPc and PCDTBT as active layer

6.1 Introduction

Organic field effect transistors are metal-insulator–semiconductor (MIS) hybrid structure in which the active layer is an organic material. For more than a decade now, Organic Thin film transistors (OTFTs) based on conjugated polymers, oligomers, or other molecules have been envisioned as a viable alternative to the more traditional, mainstream thin-film transistors (TFTs) based on inorganic materials. Because of the relatively low mobility of the organic semiconductor layers, OTFTs cannot rival the performance of field effect transistors based on single crystalline inorganic semiconductors, such as Si or Ge, which have charge carrier mobilities about three orders of magnitudes higher. Consequently, OTFTs are not suited for use in applications requiring very high switching speeds. However, the processing characteristics and demonstrated performance of OTFTs suggest that they can be competitive for existing or novel thin-film-transistor applications requiring large-area coverage, structural flexibility, low temperature processing, and especially, low cost. Such applications include switching devices for active-matrix flat-panel displays (AMFPDs) based on either liquid crystal pixels (AMLCDs) [146] or organic light-emitting diodes (AMOLEDs) [147]. At present, hydrogenated amorphous silicon (a-Si:h) is the most commonly used active layer in TFT backplanes of AMLCDs [148]. The higher performance of polycrystalline silicon TFTs could change this requirement. OTFTs could also be used in active-matrix backplanes for “electronic paper” displays [149] based on pixels comprising either electrophoretic ink-containing cards [150]. Other applications of OFETs may be in smart cards and electronic identification tags.

Following are the four configurations of Organic Field Effect Transistors widely studied:

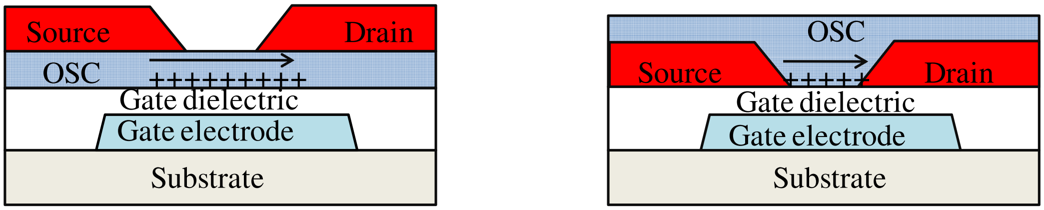

(a) Bottom Gate (inverted) staggered
(Bottom Gate Top contact)

(b) Bottom Gate (inverted) coplanar
(Bottom Gate Bottom Contact)

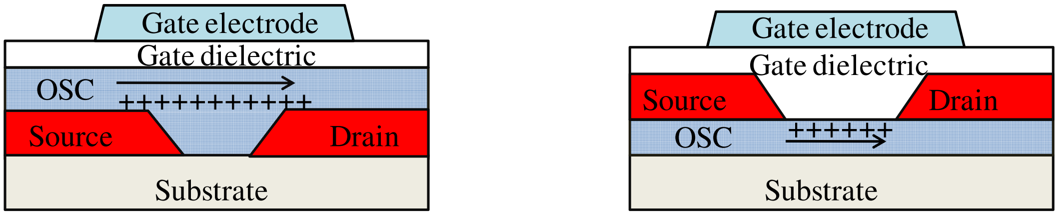

(c) Top Gate staggered
Top Gate Bottom Contact

(d) Top Gate coplanar
Top Gate Top Contact

Figure 6.1: Different configurations of Organic Field Effect Transistor.

Each of the four structures shown above has certain advantages and disadvantages. For example, the presence of an energy barrier at the interfaces between the organic semiconductor and source and drain contacts is expected to impede the charge carriers between the contacts and the semiconductor. Organic Thin Film Transistors (OTFTs) with a staggered structure in Fig. 6.1(a) and (c) have the advantage of being less affected by this energy barrier than OTFTs with a coplanar structure [151-155]. However, in the case of the bottom-gate coplanar structure (Fig. 6.1 (b)), the effect of the energy barrier on the carrier exchange efficiency can be substantially reduced by modifying the surface of the source and drain contacts with a thin organic monolayer carrying an appropriate dipole moment [155-159] or with a thin metal oxide [160-162].

An important advantage of bottom-gate coplanar structure (Fig. 6.1 (b)) is that the gate dielectric layer and the source and drain contacts are prepared before the organic semiconductor is deposited. The reason why this is important is that many high mobility organic semiconductors, especially vacuum-deposited small-molecule materials, but also many high-mobility polymers adopt a thin-film microstructure that is very sensitive to external perturbations. With the bottom-gate coplanar structure (Fig. 6.1 (b)), methods involving solvents and /or thermal treatments can be safely employed to prepare the gate dielectric and the contacts without harming the semiconductor layer.

The gate dielectric material and the processing conditions for the gate dielectric must be compatible with the substrate and in case of top-gate structures (Fig. 6.1 (c-d)), also with the previously deposited organic semiconductor layer.

An interesting approach for TFTs with the bottom-gate structure (Fig. 6.1(a-b)) is the use of a thin layer (SiO_2 or AlO_x) obtained by oxidation of the gate electrode surface in combination with a high-quality insulating organic self-assembled monolayer or multilayer [163].

6.2 Basic Operation of an Organic Field effect transistor

As in the case of conventional metal insulator semiconductor field effect transistors (MISFETs), an OFET operates as a voltage controlled current source. Unlike Si MISFETs, organic FETs usually do not operate in inversion mode, but in accumulation mode. Another point to be noted is that in Organic FETs, source and drain are usually implemented by directly contacting the organic semiconductor with a metal (*i.e.*, without doped contact regions).Depending on the choice of the materials for the semiconductor and the contacts, the charge transfer of one carrier type is usually more efficient than that of the other, and this determines whether the device operates as a *p*-channel FET or a *n*-channel FET.

Despite the fact that the transport physics in organic FETs is different from that of inorganic FETs, the current – voltage characteristics to a first order can be described with the same formalism [164]:

$$I_{DS} = \frac{\mu C_{diel} W}{L}\left\{(V_{GS} - V_{Th})V_{DS} - \frac{{V_{DS}}^2}{2}\right\} \qquad \text{for} \quad |V_{GS} - V_{Th}| > |V_{DS}| \qquad (6.1)$$

$$I_{DS} = \frac{\mu C_{diel} W}{L}\{(V_{GS} - V_{Th})^2\} \qquad \text{for} \quad |V_{DS}| > |V_{GS} - V_{Th}| > 0 \qquad (6.2)$$

where V_{Th}, for an OFET may be defined as the minimum gate-source voltage required to obtain appreciable drain current. I_{DS} is drain to source current. C_{diel} is the gate dielectric capacitance per unit area. μ is the charge carrier mobility. V_{GS} and V_{DS} refer respectively to gate-source and drain-source voltage respectively. L and W refer to channel length and width respectively.

Rearranging above equations, we get the following expressions for mobility in linear and saturation regions:

$$\mu_{lin} = \frac{L}{C_{diel} W V_{DS}} \frac{\partial I_D}{\partial V_{GS}} \qquad \text{for} \quad |V_{GS} - V_{Th}| > |V_{DS}| \qquad (6.3)$$

$$\mu_{sat} = \frac{2L}{W C_{diel}}\left(\frac{\partial \sqrt{I_D}}{\partial V_{GS}}\right)^2 \qquad \text{for} \quad |V_{DS}| > |V_{GS} - V_{Th}| > 0 \qquad (6.4)$$

Equations (6.1) and (6.2) describe the drain current for gate-source voltages above threshold voltage. Below the threshold voltage there is a region in which the drain current depends exponentially on the gate-source voltage. This is the subthreshold region. The subthreshold region exists between the switch on voltage and the threshold voltage. The switch-on voltage V_{so} marks the gate-source voltage at which the drain current reaches a minimum [165]. In the subthreshold region the drain current is due to carriers that have sufficient thermal energy to overcome the gate-voltage-controlled energy barrier near the source contact and mainly diffuse, rather than drift, through the semiconductor to the drain contact:

$$I_{DS} = I_0 exp.\left\{\frac{q|V_{GS} - V_{FB}|}{\eta kT}\right\} \text{ for } V_{Th} < V_{GS} < V_{so} \qquad (6.5)$$

The slope of the log (I_{DS}) versus V_{GS} curve in the subthreshold region is determined by the ideality factor η and the temperature T. It is usually quantified as the inverse subthreshold slope S (also called subthreshold swing):

$$S = \frac{\partial V_{GS}}{\partial(log_{10} I_{DS})} = \frac{\eta kT}{q} ln10 \tag{6.6}$$

The ideality factor η is determined by the density of trap states at the semiconductor / dielectric interface, N_{it}, and the gate dielectric capacitance, C_{diel} as:

$$\eta = 1 + \frac{qN_{it}}{C_{diel}} \tag{6.7}$$

$$S = \frac{kT}{q} ln10 \left(1 + \frac{qN_{it}}{C_{diel}}\right) \tag{6.8}$$

When $\frac{N_{it}}{C_{diel}}$ is small, the ideality factor η approaches unity. As compared to inorganic FETs, organic FETs, dielectric interface is typically of somewhat poor quality, mainly because the materials are deposited at much lower temperature, and thus the subthreshold swing is usually larger [164].

6.3 Organic field effect transistor gas sensors

A typical OFET sensor structure is shown in Fig. 6.2. It consists of a conductive film coated on a substrate covered by a thin dielectric film that is interfaced to the organic active layer. The organic active layer is generally a film of a few tens of nanometres of conducting polymers or oligomers. In the case of Organic FETs, the analyte detection is performed employing a bottom gate device structure where the active layer is directly exposed to the analyte and acts as both transistor channel material and sensing membrane.

Organic active layers usually are polycrystalline, with a granular morphology. Polycrystalline organic active layers are generally described as formed by contiguous grains having a crystalline core and amorphous grain boundary. Au source and drain electrodes are

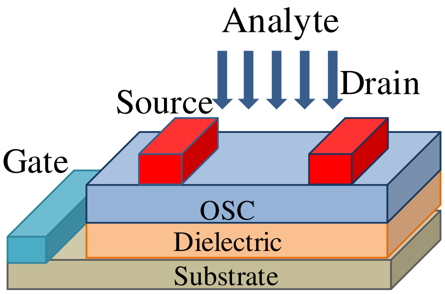

Figure 6.2: Structure of an OFET sensor. It is a typical bottom gate device where the polycrystalline organic thin film acts at the same time both as active layer and sensing membrane directly exposed to the analyte to be revealed.

defined by thermal evaporation through a shadow mask directly over the organic active layer, while a contact on the substrate is used to apply the gate bias. OFET sensors are operated in common source configuration *i.e.*, connecting the source contact to ground and biasing the gate and drain contacts against it. The operation of such a three terminal device is generally described in analogy to that of inorganic TFTs. In fact, OFETs show the source-drain current / voltage family of curves, I_{DS}-V_{DS} characteristics, very similar to those of inorganic FETs for each different gate bias, V_{GS} applied. The linear region takes place at a V_{DS} bias much lower than V_{GS}-V_{Th}.

Important points with regard to OFET sensors:

1. Gate bias variation can be used to improve the sensor performance [166]. This property drives directly from the fact that two distinct conductivity regimes can be established in an OFET: a bulk or three-dimensional transport regime, at no gate bias (“off” regime), and a two-dimensional transport regime occurring at V_{GS} beyond the threshold voltage V_{Th}. At no gate bias and at a fixed V_{DS} bias, OFET measures I_{DS} variation caused by the interaction and /or permeation of the analyte down to the gate dielectric will result in a three dimensional conductivity variation. In this case, the response acquired is exactly equivalent to that of a chemiresistor. Upon application of a gate bias, on the other hand, a

much higher two dimensional I_{DS}, confined near the gate dielectric/organic interface, is induced. In this regime the "on" I_{DS} change can be recorded and different device parameters, such as V_{Th} and μ, can also be simultaneously influenced during the exposure to the analyte.

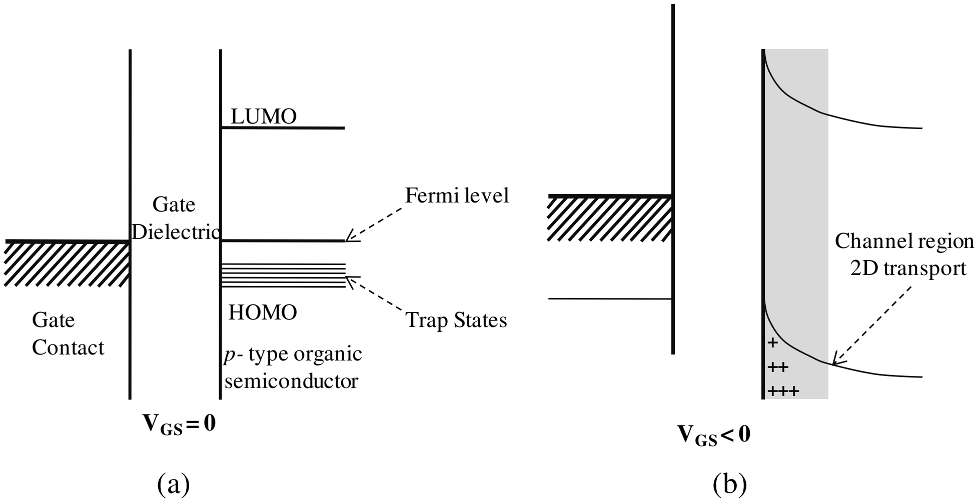

Figure 6.3: Schematic energy band diagram for a *p* –type OFET: (a) no gate bias; (b) gate voltage negatively biased with respect to the source.

2. The conduction mechanism plays a crucial role in determining the sensing mechanism of an OFET sensor. Several reactive species cause charge trapping – detrapping processes to occur, enhancing or lowering barrier between the grains. Therefore V_{Th} and μ can be greatly influenced by the interaction of the transistor active layer with a chemical species, which results in a change of the device drain – source on current and the two – dimensional conductivity. The active layer – analyte interaction has been modelled as the analyte molecules being adsorbed, or even trapped, at the surface of the grains. Threshold voltage and mobility depend on the volume density of trapped charges and on the potential barrier between contiguous grains, respectively [167].
3. One of the major advantages of OFET sensors is the ability to detect changes in V_{Th} by passing a negligible current through the conducting polymers. This makes OFET sensors

generally more stable than chemiresistors, especially in terms of signal to noise ratio.

4. The electrical behaviour of most CPs is not stable. In this respect, OFET sensors configuration can be very convenient, especially when operated in pulse mode. With an OFET sensor it is possible to obtain an almost complete recovery after analyte exposure by a strategic use of the gate potential applied to the gate electrode, allowing the device to operate at room temperature. It is important to note that the best results are obtained in the pulse mode because continuous biasing is not generally well tolerated by organic devices and small analyte response can be marked by current drifts. Thus the response of the OFET sensor can be modulated with the gate bias applied to the device, corroborating the multiparametric nature of the OFET sensor responses.
5. The strategy of using properly functionalized organic semiconductors can be exploited to obtain specific recognition [168]. The gate dielectric / organic semiconductor interface plays a crucial role in determining the transduction mechanism of an OFET sensor. In principle it is possible to tailor the recognition properties of an OFET sensor also by means of a proper choice of the dielectric / organic semiconductor interface. The ability to design selectivity properties of OFET sensors, in addition to the repeatability and gate bias enhancement of their response, will make OFET sensors a much more flexible option than existing portable sensor systems for a large number of sensing applications.

6.4 OFET using PCDTBT as active layer

In this section, we describe the detailed process steps for fabrication of OFET in BGTC geometry using PCDTBT as active layer and PMMA as dielectric layer.

6.4.1 Fabrication of PCDTBT based transistor in BGTC

We have fabricated OFET using PCDTBT as active layer in BGTC geometry keeping in mind its application as a gas sensor. In order to fabricate the bottom gate top contact

(BGTC) OFETs, first of all BOPET substrate (size ~ 4 cm × 3 cm) was ultrasonicated in methanol for 5 min. The clean BOPET substrate was taken inside glove box for deposition of gate electrodes by evaporating aluminium (thickness ~ 40 nm) layer onto BOPET substrates

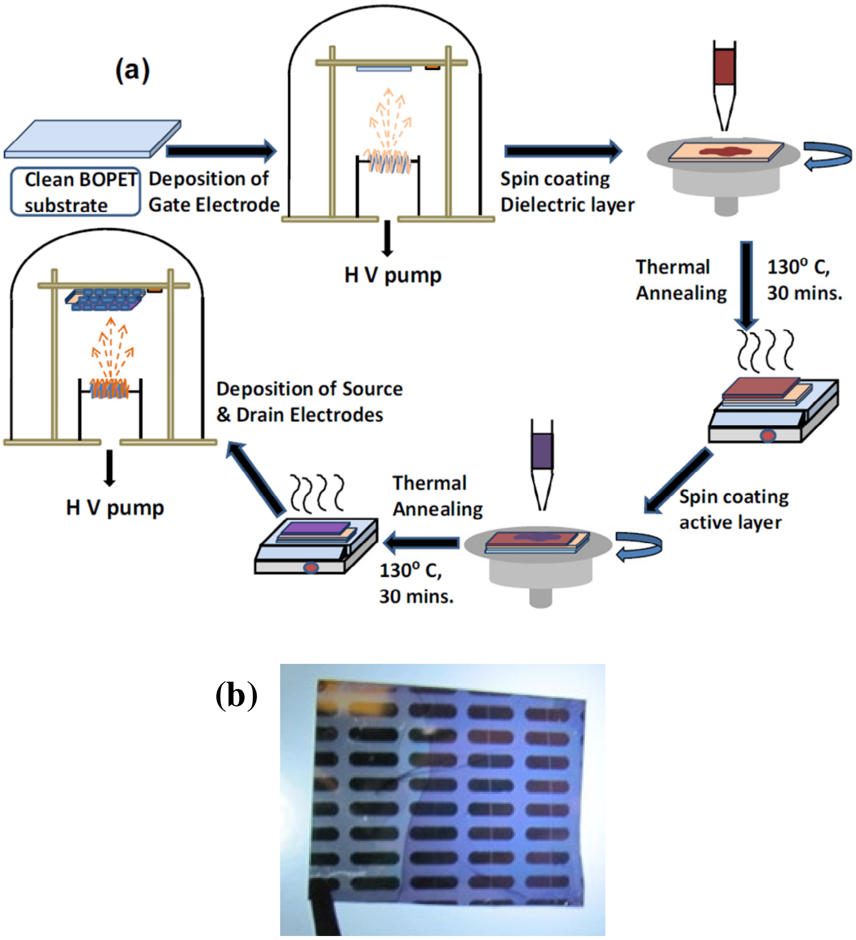

Figure 6.4: (a) Schematic of Process steps for fabricating BGTC transistor using PCDTBT as active material (b) Actual potograph of the fabricated device.

by thermal evaporation inside the glove box. The poly(methyl methacrylate) (PMMA) as a dielectric layer (thickness 400 nm) was then spin coated onto Al/BOPET using 80 mg/ml PMMA solution (prepared in PGMEA) at 1000 rpm for 80 s followed by an annealing at 130°C for 30 min. The PCDTBT active layer (thickness: ~ 40 nm) was spin-coated onto PMMA/Al/BOPET using a 10 mg/ml PCDTBT solution (prepared in 1, 2-dichlorobenzene and filtered using 0.45µm filters) at 4000 rpm for 60 s followed by annealing at 130°C for 30 min. The device structure was completed by thermally evaporating Au to act as source and drain electrodes through a 50 µm wire of a metal mask. The process steps in brief for fabricating PCDTBT based OFET is shown in Fig. 6.4.

6.4.2 Characterization of active layer using XPS

X ray phototelectron spectroscopic (XPS) studies of the active layer was carried out using a MgKα (1253.6 eV) source and MAC-2 electron analyzer under a base vacuum of 10^{-9} torr.The binding energy scale was calibrated to the Au $4f_{7/2}$ line of 84 eV. Typical N 1s, C 1s and S 2p spectra recorded for the PCDTBT active layer is shown in Fig. 6.5. The N1s spectrum could be resolved into two components at 399.3 and 400.2 eV, which are attributed

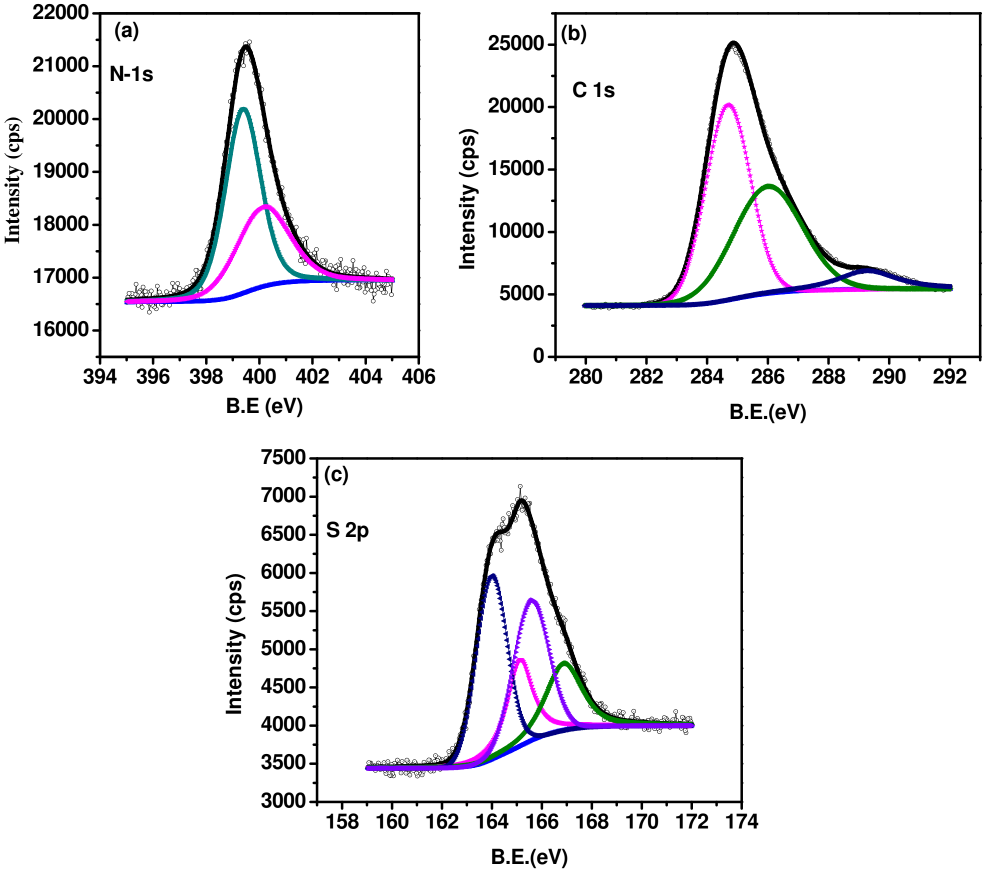

Figure 6.5: XPS Spectra of the active PCDTBT layer showing core level N1s, C 1s, S 2p peaks with resolved components.

due to the N in benzothiadiazole and carbazole units, respectively. The core level C 1s spectrum reveals presence of three peaks at 284.7, 286.1 and 289.2 eV, which can be assigned respectively to C-C bonds, C-N and /or C-S bonds /or C=O-OH bonds [169]. For S 2p spectrum, presence of four peaks is attributed to two different sulphur species: the first doublet *i.e.* 164.1 eV (S $2p_{3/2}$) and 165.6 eV (S $2p_{1/2}$) due to thiophene and the second doublet 165.2 eV (S $2p_{3/2}$) and 166.9 eV (S $2p_{1/2}$) due to benzothiadiazole [170]. These assignments are in fair agreement with the binding energies reported for S $2p_{3/2}$ in unbound thiophene (~164 eV) and benzothiadiazole (~ 166 eV) [170-172].

6.4.3 Characterization of PCDTBT based transistor

The illustration of the experimental set up along with an OFET device under test is shown in Fig. 6.6. To study the transfer and output characteristics of OFET, we have used two picoammeter / voltage sources. One picoammeter / voltage source is used for supplying voltage as well as measuring I_{DS}, while other is used just as a constant voltage source. The probe station consists of micromanipulators that can move the probe in three axes and a linear translation stage positioned on a table to lower the vibration. All measurements and data acquisition are automated using customized National Instruments LabVIEW codes running on a GPIB connected Windows based computer. Figure 6.7 shows typical output and transfer characteristics of the fabricated PCDTBT based FET having a channel length of 50 μm on a flexible BOPET substrate. The measurements were carried out under ambient conditions. The output characteristics *i.e.* drain-source current (I_{DS}) for the drain – source voltage (V_{DS}) ranging from 0 to −110V at different gate – source voltages (V_{GS}) (*i.e.* −50V, −60V, −70V) is shown in Fig. 6.7 (a).The output characteristics show a little hysteresis suggesting presence of traps in the channel. It has been observed that the chemisorbed oxygen in the organic semiconductor act as deep traps, which is reflected in hysteresis in the current-voltage characteristics.

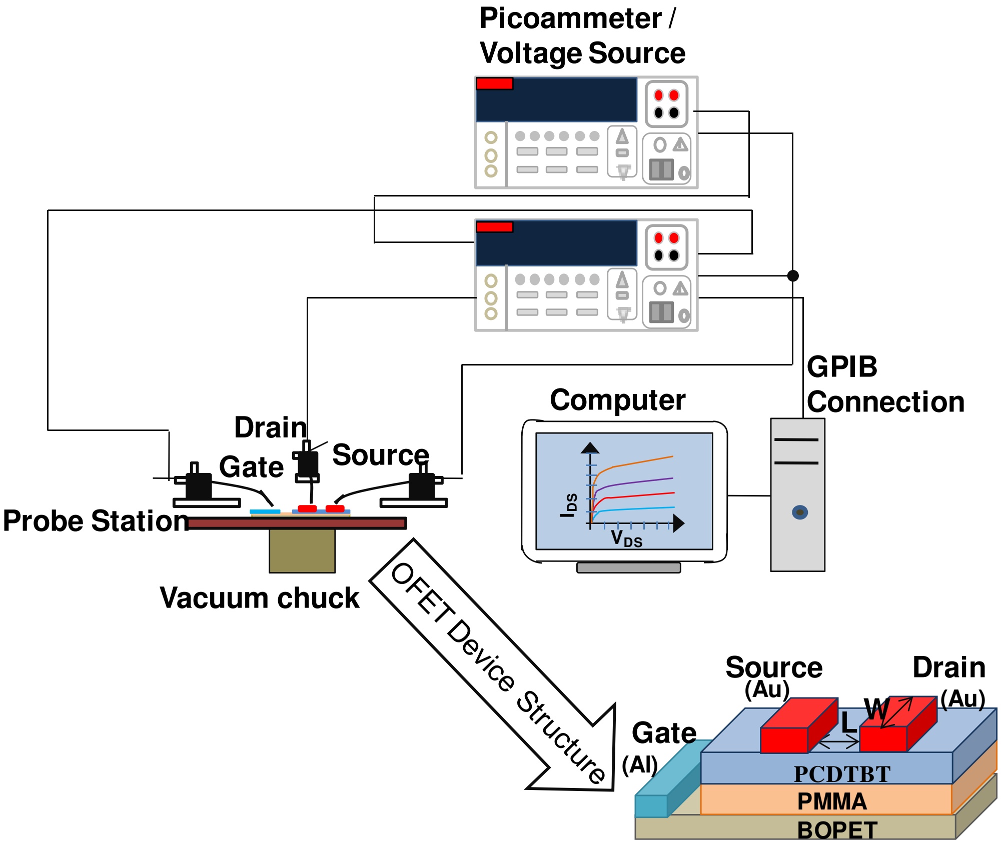

Figure 6.6: Schematic experimental set up and device structure under test.

The output characteristics correspond to a *p*-type behaviour *i.e.* accumulation of holes at the interface of active layer and dielectric on application of a negative gate-source voltage. Typical transfer characteristics measured for a FET with gate length of 50 μm is shown in Fig.6.7 (b), which was measured by varying the V_{GS} from 0 to -110V while keeping V_{DS} constant at –60V(*i.e.* in saturation region).

It is seen from the Fig.6.7 (a) that the drain current varies from 10^{-11}A to 10^{-7} A for $V_{DS} = -$ 60V. The on-off ratio- a ratio between the maximum drain current (on-state of the transistor) and the minimum drain current (off state) from this graph comes out to be ~2.57×10^{4}. It is to be noted that this value of on-off ratio is higher by two orders of magnitude as compared to those OFETs fabricated on ITO-coated PEN substrates [173]. The improved on-off ratio in the present case can be attributed to the use of Al as gate electrode and the low *rms* roughness of the BOPET substrate.

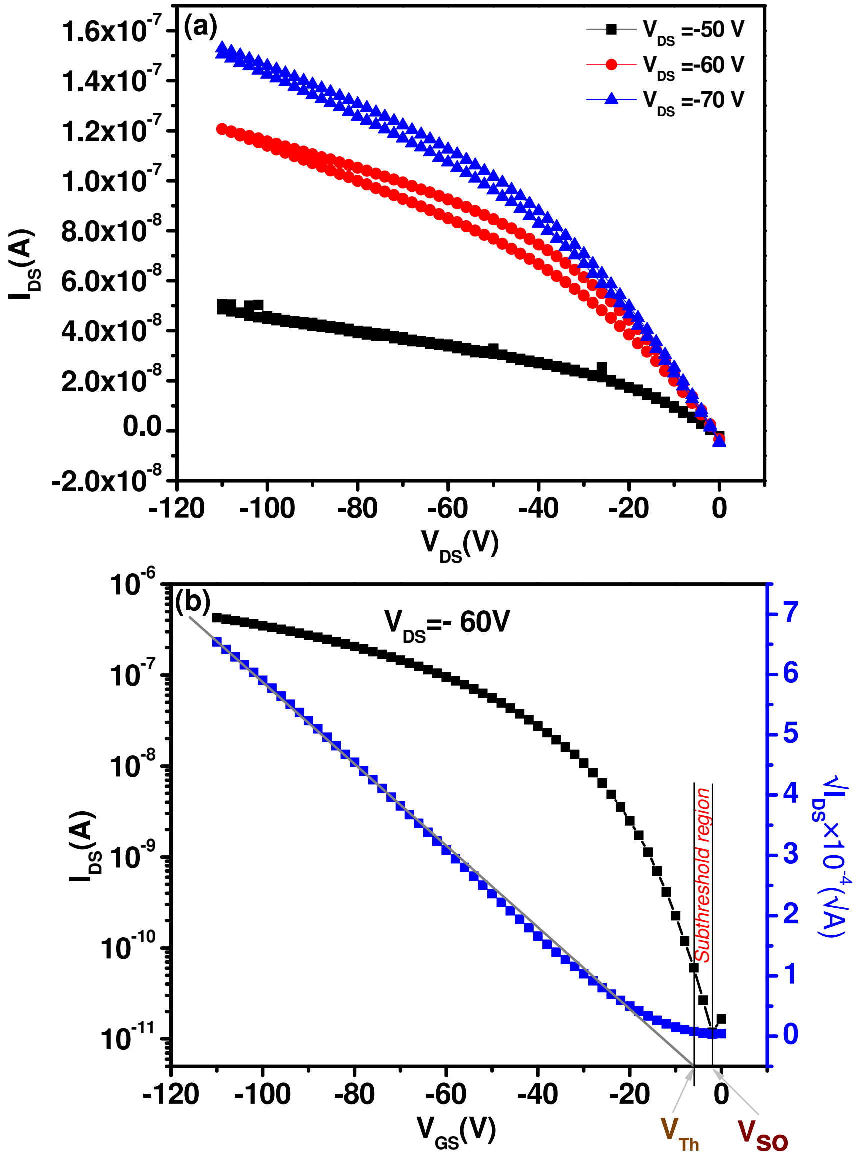

Figure 6.7: Device characteristics of a typical OFET with channel length of 50μm and channel width of 2mm. (a) Output characteristics *i.e*. variation of drain source current (I_{DS}) with the drain-source voltage (V_{DS}) ranging from 0 to -110V at different gate-source voltages (V_{GS}); (b) left scale: transfer characteristics in saturation region measured by varying the V_{GS} from 0 to -110V while keeping V_{DS} constant at -60V. Right scale: $\sqrt{|I_{DS}|}$ vs. $\mathrm{V_{GS}}$ plot. Area between red lines shows subthreshold region that lies between threshold voltage (V_{Th}) and switch-on voltage (V_{so}).

The field effect mobility μ in the saturation region, μ_{sat} was calculated from the slope of the square root of the drain-source current as a function of the gate-source voltage *i.e.* $\sqrt{|I_{DS}|}$ vs. V_{GS} plot, as shown in Fig. 6.7 (b), using the Eqtn. 6.4. In the present case, the value of C_{diel} for PMMA dielectric was measured to be ~ 8±1 nF/cm^2. The value of μ_{sat} for 50 µm gate length device came out to be ~ 6.21×10^{-4} cm^{2}V^{-1}s^{-1}. The low mobility obtained in our devices can be attributed to : (i) low molecular weight PCDTBT (36.5 kDa); (ii) amorphous and disordered nature of PCDTBT active layer, and therefore, the obtained μ value in our case is same as that typically reported for other amorphous conjugated polymers [164, 174].

Table 6.2: Summary of various OFET parameters *e.g.* mobility in saturation (μ_{sat}), on-off ratio, threshold voltage (V_{Th}), switch-on voltage (V_{so}), subthreshold swing (S) and trap density (N_{it}). The reported values are an average of 6-8devices.

L (µm)	On-Off ratio	μ_{sat} (cm^{2}V^{-1}s^{-1})	V_{Th} (V)	V_{so} (V)	S (V/decade)	N_{it} (cm^{-2} V^{-1})
50	$2.5\pm0.5\times10^4$	$6.21\pm1.1\times10^{-4}$	-8±1.2	-2±1	5.94±0.6	$4.95\pm0.6\times10^{12}$

As shown in Fig. 6.7 (b), the extrapolation to $I_{DS} = 0$ axis of the fitted straight line of $\sqrt{|I_{DS}|}$ vs. V_{GS} plot gives the threshold voltage (V_{Th}). The switch on voltage was determined from log I_{DS} vs. V_{GS} plot, where the I_{DS} attains a minimum. The values for V_{Th} and V_{so} as shown in Fig. 6.7(b) came out to be −8V and −2V respectively. These values are on higher side, which can be attributed to low dielectric constant of PMMA dielectric (k~3.5) [175].The region between V_{so} and V_{Th} is the subthresold region. In this region I_{DS} depends exponentially on V_{GS} as described by Eqtn (6.5) [164]. The slope of the log I_{DS} vs. V_{GS} plot is usually quantified as the inverse subthreshold slope (S) (known as subthreshold swing) and is expressed in Eqtn (6.6). The calculated value of S, extracted from the slope of the log I_{DS} vs.

V_{GS} plot (Eqtn. 6.6) is 5.94V/decade, and N_{it} calculated using (Eqtn. 6.8) is 4.95×10^{12} cm^{-2}V^{-1}. The obtained values of S and N_{it} are relatively; high which can be attributed to a poor quality of PMMA/PCDTBT interface as the device fabrication was done at room temperature. Various parameters derived from the transistor characteristics are summarized in Table 6.1.

6.5 OFET using CoPc as active layer

As we have obtained very high mobility (~ 118cm^{2}V^{-1}s^{-1}) CoPc films on BOPET, we were trying to replicate the same in transistor geometry. Here we describe the process details of fabricating OFET in both bottom gate and top gate geometries using CoPc as active layer.

6.5.1 Fabrication of CoPc based transistor

CoPc, which forms the active layer, was deposited using thermal evaporation at room temperature and at a slow rate (0.1 Å /s-0.3 Å /s) on a clean BOPET substrate. Au has been used as all the three electrodes *viz.*, source, drain and gate. For source and drain electrodes, we have deposited Au through a metal mask so that electrodes are spaced 50 μm apart. Insulating layer, as described in previous section, was prepared by dissolving 80 mg of PMMA in 1 ml of Propylene glycol monomethylether acetate. The insulating layer in OFETs was deposited by spin coating PMMA solution at 1000 rpm and subsequently the device was annealed at 130°C inside the glove box in every case. For making transistors in BGTC configuration, the deposition sequence is Au (gate), PMMA (dielectric), CoPc (50 nm thick) and Au (source and drain electrodes) respectively. The fabrication of top gate bottom contact (TGBC) configuration of transistors was performed by depositing Au (source and drain electrodes), CoPc (50nm thick), PMMA (dielectric), Au (gate) respectively. To fabricate transistors in top gate top contact (TGTC) configuration the deposition sequence of Au (Source and drain electrodes) and CoPc with respect to TGBC is reversed. The electrical characterization of the devices was carried out under ambient atmosphere using Keithley voltage source / current meter.

6.5.2 Characterization of CoPc based transistor

We have studied both the transfer and output characteristics of the transistor in every configuration except BGBC. Typical transfer characteristics in saturation region ($V_{DS} = -60$ V) of the devices in all the three configurations is shown in Fig. 6.8(a). From the transfer characteristics of the transistor, we have calculated the performance parameters of the device

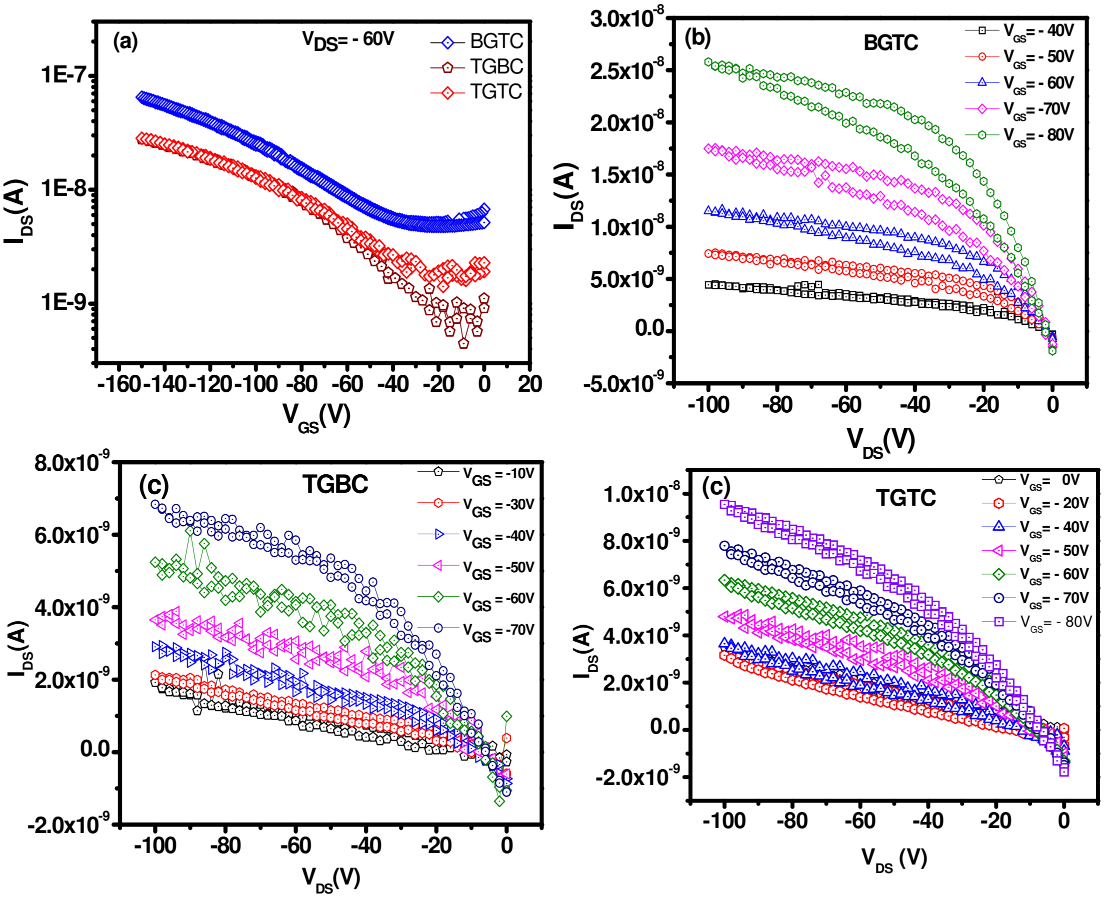

Figure 6.8: (a) Transfer characteristics of BGTC, TGBC and TGTC transistors in saturation region (V_{DS} = - 60V). Output characteristics of (b) BGTC, (c) TGBC, (d) TGTC transistors fabricated with CoPc as active material.

such as on-off ratio, threshold voltage and the mobility. As in PCDTBT based transistor here too the values of channel length L, width W and the gate dielectric capacitance per unit area C_{diel} are respectively 50 μm, 2 mm and 8.0×10^{-9}F/cm^2. Following table summarizes various parameters derived from the transistor characteristics.

Table 6.2: Comparison of different parameters of the OFET in three different configurations using CoPc as active layer.

Structure/Parameter	On Off Ratio	μ_{sat} (cm^2/V-s)	V_{Th} (V)
BGTC	12.73	1.86×10^{-5}	-39
TGBC	62.29	7.57×10^{-6}	-5
TGTC	19.98	6.91×10^{-6}	-18

Contrary to our expectation, the mobility of device using CoPc as active layer was found to be poorer as compared to that of PCDTBT based OFET.

6.6 PCDTBT based OFET sensor

The typical transfer and output characteristics of OFET sensor is shown in Fig. 6.9 (a) and (b) respectively. This device with a gate length of 50 μm has been fabricated in BGTC configuration for its application in gas sensing. The transfer characteristics with V_{DS} ranging from −40V to −80V are shown in Fig. 6.9(a). The output characteristics with the gate voltage V_{GS} ranging from 0 to −80 V at a step of −20V are shown in Fig. 6.9 (b).The drain source current increases linearly with the enhancement of the V_{DS} in the linear region, and saturates with the higher drain –source voltages owing to pinch off of the accumulation layer. The value of μ_{sat}, V_{Th} and on-off ratio of the device are calculated to be respectively 1.13×10^{-4}cm^{2}V^{-1}s^{-1},-3.6V and 566.

For gas sensing measurement, the device was transferred to airtight leak proof stainless steel chamber of volume 1000 cm^3. To measure the response of the sensor towards this gas, I_{DS} at V_{DS} = −50V, V_{GS} = −50V as a function of time was measured by a picoammeter / voltage source and computer based data acquisition system using LabVIEW.

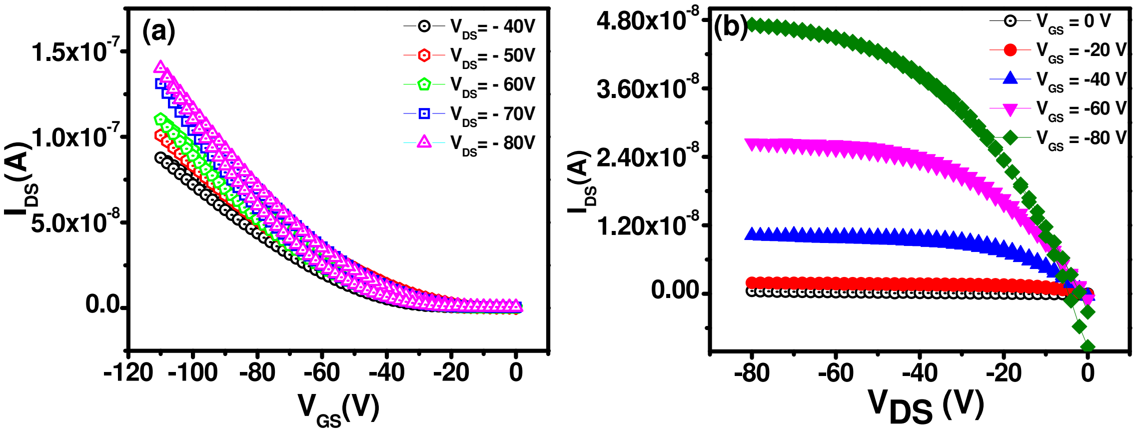

Figure 6.9:(a) Output (b) transfer characteristics of PCDTBT transistor.

Before exposing the sensor towards any gas, I_{DS} was left to stabilise for some time. To know the selectivity of PCDTBT based OFET, the device was exposed to a 10 ppm dose of different analytes *viz.*; H_2S, NH_3, NO_2, NO, C_2H_5OH. The selectivity histogram for different gases for 50 μm channel length PCDTBT based OFET at room temperature is shown in Fig. 6.10 (a). PCDTBT based OFET was found to be most selective towards NO_2 gas. As our sensor was found to be most selective towards $NO_{2,}$ we have performed a systematic study of sensor response towards varying doses of NO_2 at V_{DS}= – 50V, V_{GS} = – $50V_.$ Due to gate voltage bias stress effects, the time – resolved I_{DS} measurements were started when a stable I_{DS} current was reached under above bias conditions. The typical real time response curve of PCDTBT based OFET sensor at room temperature towards NO_2 gas for concentration varying in the range 1 ppm – 60 ppm is shown in Fig. 6.10 (b). From Fig. 6.10 (b), it can be seen that drain–source current increases in the presence of NO_2 gas, indicating holes are the charge carriers which further confirms that PCDTBT is a *p*-type polymer. The minimum detection limit (MDL) of the sensors is 1 ppm, which is well below the toxic limit (3 ppm) of NO_2.The typical value of response and recovery time for a dose of 10 ppm is ~ 6.5 minutes and 33 minutes respectively. As seen in inset of Fig. 6.10 (b) the response percentage increases almost exponentially with the concentration which is a common feature of all the gas sensors.

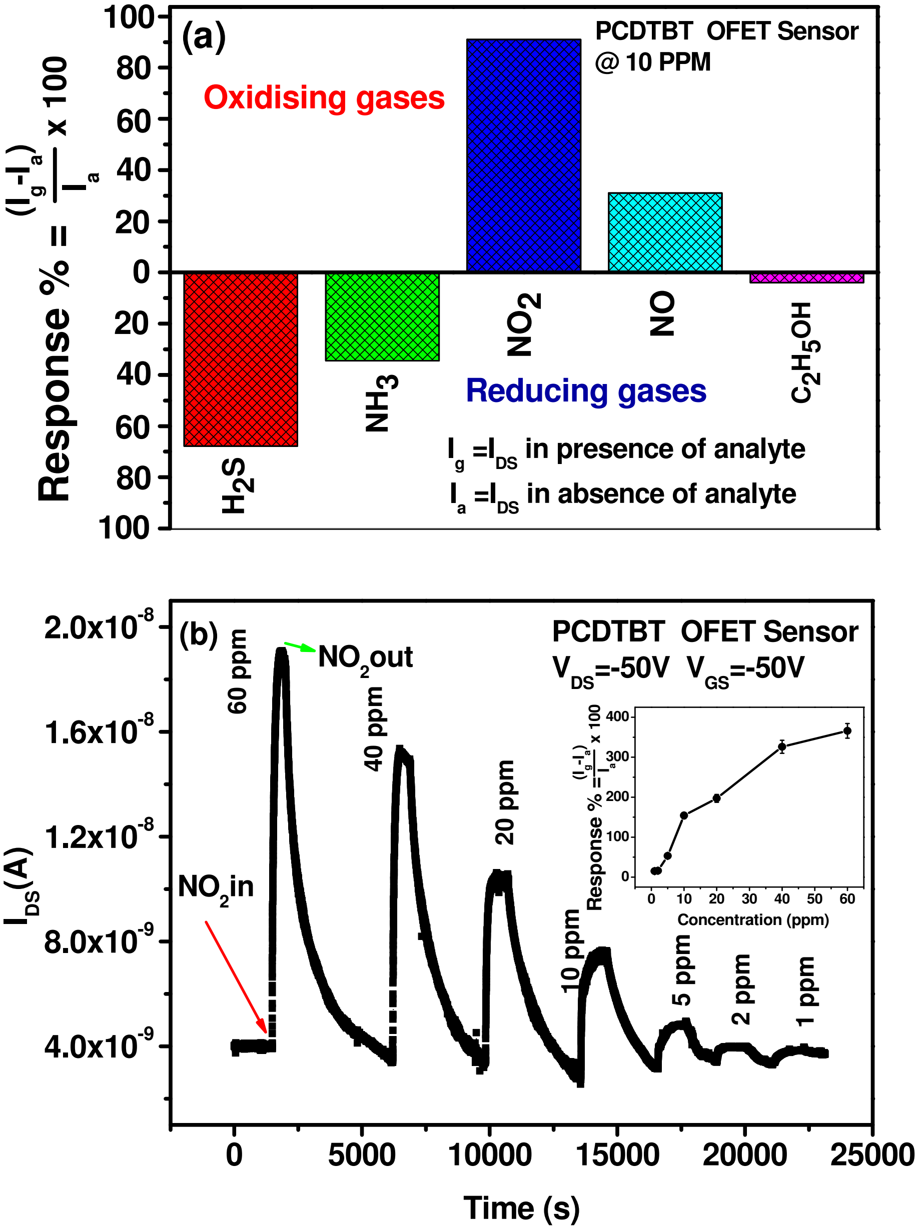

Figure 6.10: (a) Studies on Selectivity of PCDTBT base OFET sensor towards various analytes. (b) Drain- Source Current (I_{DS}) vs. time plot at different concentrations of NO_2 gas. Inset shows the response percentage vs. concentration plot for PCDTBT based OFET sensor.

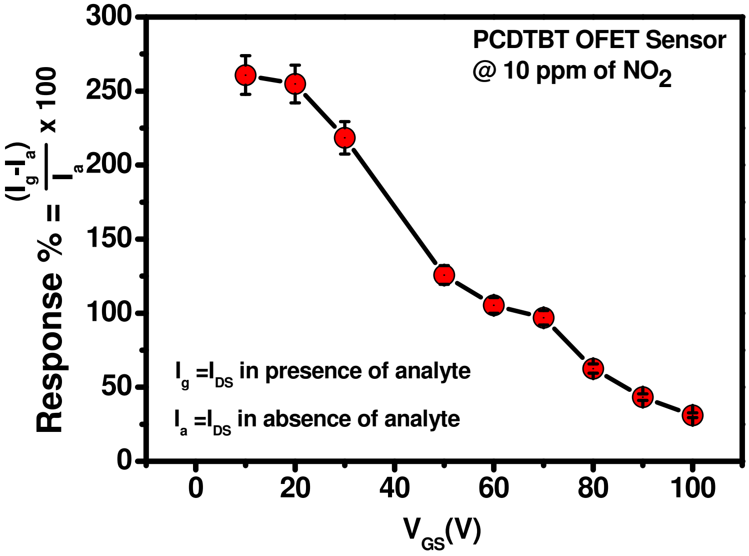

Figure 6.11: Effect of gate voltage on Response %

Fig. 6.11 shows the effect of gate voltage on sensor response. It can be seen that response towards NO_2 decreases with increasing V_{GS}. The decreasing response with increasing gate bias is attributed to more influence of gate voltage in controlling OFET characteristics.

6.7 Probable sensing mechanism using PCDTBT based OFET sensor

For detecting NO_2 using conducting polymer FET, doping effect and charge trapping are two kinds of mechanisms that has been proposed [176].The process of interaction of NO_2 with PCDTBT may be explained through the following mechanism (Fig. 6.12).

NO_2 is an oxidizing gas. So when PCDTBT based FET was exposed to NO_2 film, NO_2 was reduced to NO_2^- by removing electrons from the HOMO of PCDTBT and the cation radical formation takes place in PCDTBT chain as shown in Figure 6.12 (b). Next, an electron from the adjacent carbon atom pairs up with the free radical to form a new double bond and free radical moves to the next neighbouring carbon atom and this process continues because of conjugation as shown in Fig. 6.12 (b). In the next step, we have shown the movement of cation. The carbocation formed in previous step is attacked by electron from the left adjacent carbon atom Fig. 6.12(c) and the conductivity of the polymer enhances by the generation of new charge carriers (Fig. 6.12 (d)) in the polymer chain.

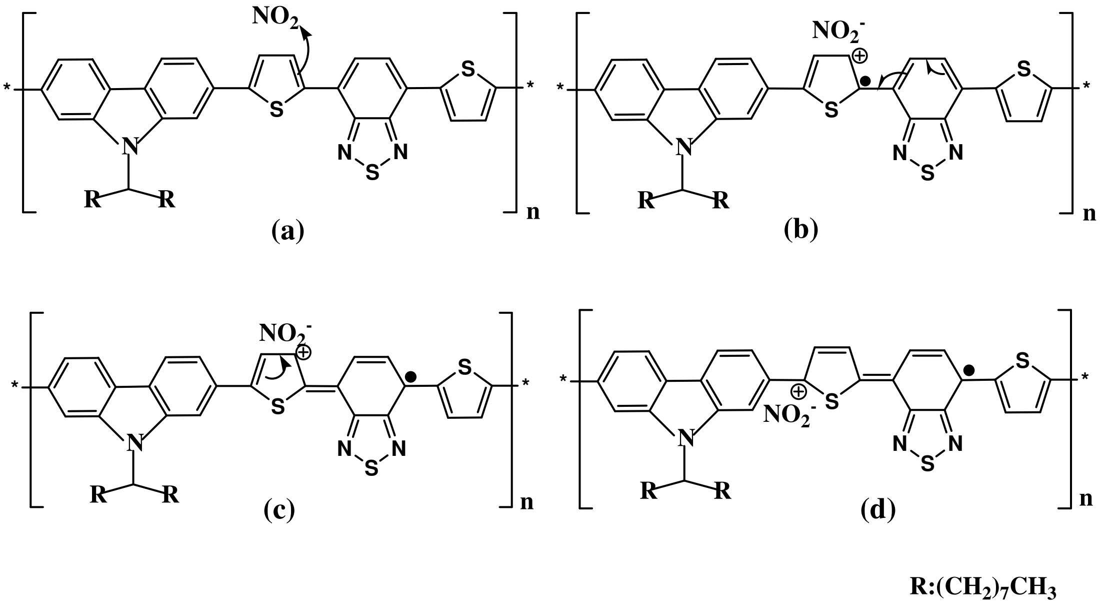

Figure 6.12: The process of interaction between the NO_2 molecules and PCDTBT: (a) removing electrons from PCDTBT to NO_2 molecules, (b) the formation of NO_2^- ions, cation radicals, (c) the establishment of new double bond, (d) the transfer procedure of holes created by the NO_2 molecule.

If another electron was further removed from an oxidized section of the polymer, two possibilities may occur. Either a second independent polaron may be created or, if it was the unpaired electron of the first polaron that was removed, a bipolaron was formed. As polarons and bipolarons mobile charges were formed across the backbone of the polymer, the creation of two energy levels was induced between the HOMO and the LUMO, which made the energy gap minimal. Hence, the conductivity of PCDTBT would increase. In this way, the interaction of oxidizing molecule like NO_2 with a *p* –type conducting polymer led to an increase of conductivity like a doping process. In case of PCDTBT based OFET sensor, I_{DS} would increase due to enhanced conductivity. Also, the dipole-dipole interaction between the analyte and polymer molecule can pull the polymer molecules more compact. Therefore, enhancing charge hopping transport by reducing the charge hopping distance can lead to an increase of I_{DS} as well [177].

Furthermore, the adsorbed oxidizing NO_2 molecules at the interface between the PCDTBT film and the dielectric layer could act as the electron taps, which in turn as the contributor to hole carriers, thus hole carrier density and *p*-type channel current increases.

6.8 Conclusions

We have demonstrated the fabrication of PCDTBT based OFET in BGTC geometry. From the transistor characteristics, we have calculated the different parameters of the transistor. Typical values of on-off ratio, mobility and threshold voltage of PCDTBT based transistor are respectively 2.5×10^{4}, $6.2\times10^{-4}cm^{2}V^{-1}s^{-1}$ and −8V. We also have fabricated and studied the transistor characteristics using Cobalt Phthalocyanine as active layer in BGTC, TGBC and TGTC configurations. The performance parameters of CoPc based devices were found to be poorer as compared to PCDTBT one.

Further we have studied the gas sensing properties of PCDTBT based OFET and they were found to be selective towards NO_2 with a minimum detection limit well below the toxic limit of NO_2 gas. The typical values of response percentage, response and recovery time for a dose of 2 ppm of NO_2 are 16, 234 s and 171 s respectively. We have proposed doping effect as the plausible mechanism for NO_2 sensing using OFET with PCDTBT as active layer.

CHAPTER 7

Summary and Conclusions

Flexible gas sensors based on organic semiconductors in chemiresistive and transistor configurations were fabricated. Organic semiconductors such as pure Cobalt Phthalocyanine (CoPc), its modification with inorganic nanostructures and Poly [N-9′ heptadecanyl-2, 7-carbazole-alt-5, 5-(4′7′-di-2-thienyl 2′, 1′, 3′ benzothiadiazole)] (PCDTBT) were used for fabricating devices owing to their thermal and chemical stability. For the development of sensor, CoPc and PCDTBT layer were deposited on flexible biaxially oriented polyethylene terephthalate (BOPET) substrates using MBE and spin coating processes respectively. All grown films were characterized by various techniques such as XPS, AFM, GIXRD, UV-Vis, FTIR, Kelvin probe and Raman Spectroscopy. The deposition parameters such as films thickness of ~ 20 nm, substrate temperature: 100°C and deposition rate of ~ 2Å/s were optimized to get high mobility CoPc films on BOPET sheet. The charge transport properties of CoPc films were investigated by measuring the temperature dependent *J-V* characteristics as well as resistivity in the temperature range 300-25 K. Stability of electrical properties as well as chemiresistive gas sensing properties of flexible CoPc film were investigated after bending them to different radii of curvature. For chemiresistive sensor, three type of sensing layers on flexible BOPET sheet were investigated namely (i) pure CoPc films (ii) CoPc films modified by thin layer (~ 1 nm) of Au, exhibiting enhanced sensor response towards parts per million (ppm) level of H_2S gas (ii) random network of ZnO nanowires (typical diameter ~ 100 nm and length~ 2μm) modified with varying thickness (from 5nm to 50 nm) of CoPc layer resulting in fast kinetics and enhanced response for H_2S gas.

In addition to the chemiresistive sensors, OFET based gas sensors were also fabricated. For fabricating OFET in bottom gate top contact geometry, PCDTBT as active layer and PMMA as insulating layer were used. Also, transistor devices were fabricated using CoPc thin film (high mobility films).

The main conclusions were mentioned at the end of every chapter. Here we present a summary of the important results:

(1) A high mobility of ~ 118 $cm^2 V^{-1} s^{-1}$ was achieved for an optimized 20nm thick CoPc film grown at 100°C on BOPET using MBE at a rate 2 Å /s. From XRD and pole figure measurement, the grown CoPc film was found to be highly crystalline with *a* axis - normal to the substrate plane. The high crystallinity and good texturing of CoPc films on BOPET was attributed to the interaction between CoPc molecules and polar groups (C=O) present in the oriented PET molecular. These flexible films exhibit reversible resistance change under bent condition. The increase in resistance under bent condition was because of reduced π-π molecular interaction under bent condition. Under the bent condition, these films exhibited high response and fast response / recovery (as compared to flat condition) towards NH_3 gas due to increase in number of interaction sites and their easily accessibility.

(2) Flexible CoPc films were modified by thin layer of Au. It was observed that addition of a thin layer of Au in pristine CoPc creates hole accumulation layer due to heterojunction effect. Moreover, Au also acts as a sensitizer thereby catalyzing the dissociation of molecular oxygen species due to spillover effect. As verified from XPS, Au modification significantly increases the quantity of chemisorbed oxygen and creates additional active sites along with more hole carrier density. Presence of large number of adsorbed oxygen species in Au-CoPc chemiresistor as compared to pristine CoPc implies more reactive sites for H_2S oxidation and therefore enhanced response.

In contrast to pure CoPc chemiresistor, in bent condition Au modified CoPc exhibited diminished response probably due to destruction of hole accumulation layer.

(3) A random network of ZnO nanowires (ZnO-NWs) was prepared on BOPET sheet using hydrothermal method and these nanowires were modified by CoPc layer of different thickness. It was demonstrated that among all the nanocomposite of ZnO with CoPc, ZnO nanowires modified with 25 nm thin CoPc exhibited best performance with a response (%) of 268, response time of 26 s and recovery time of 175 s for a dose of 10 ppm. From different techniques (XPS, Kelvin Probe, Raman, PL), it was confirmed that there was a formation of *p-n* junction between CoPc and ZnO nanowires and these heterojunction sample was found to have the least chemisorbed oxygen content and therefore the least hole concentration. When such hole depleted heterojunction films were exposed to H_2S, it further blocks the conduction channel and made the sample more resistive. These heterojunction based sensor exhibit fast kinetics due to least amount of chemisorbed oxygen content; which allows analyte to interact directly with Co metal sites.

(4) The best values of the ON/OFF ratio, mobility and threshold voltage obtained for PCDTBT based OFET fabricated on flexible BOPET substrate in BGTC configuration were found to be 2.6×10^4, 6.21×10^{-4} cm^2/V-s and -8V respectively. Comparatively, CoPc based OFETs were found to exhibit poor performance. PCDTBT based OFET device sensor was found to be selective towards NO_2 gas with a minimum detection limit of 1 ppm and a response time of 15s. The phenomenon of interaction of NO_2 with PCDTBT was explained using doping mechanism. Surprisingly, with increase in gate to source voltage, response percentage was found to reduce which was attributed to increase in drain to source current with increase in gate to source voltage.

In a nutshell, we have fabricated and studied flexible gas sensors on BOPET in both the geometries *viz.*, chemiresistive and OFET. A brief summary of the main results obtained in this work is presented in Fig. 7.1 and following inferences can be drawn from it:

- Chemiresistive sensor: Pristine CoPc and CoPc modified with inorganic nanostructures were used as sensing layers in this type of sensor. As compared to pure CoPc, Au modified CoPc sensor exhibited improved response percent for H_2S for a dose of 10 ppm but no significant improvement in response kinetics was observed. However, ZnO NWs – CoPc (25nm) heterojunction sensor shown modest response percent but very low response and recovery times.
- OFET sensor: PCDTBT was used as active layer in this category. PCDTBT based OFET was able to sense H_2S but once exposed, the sensor did not recover to the base current. However, it exhibited reproducible response time behaviour for NO_2 with a MDL of 1ppm.

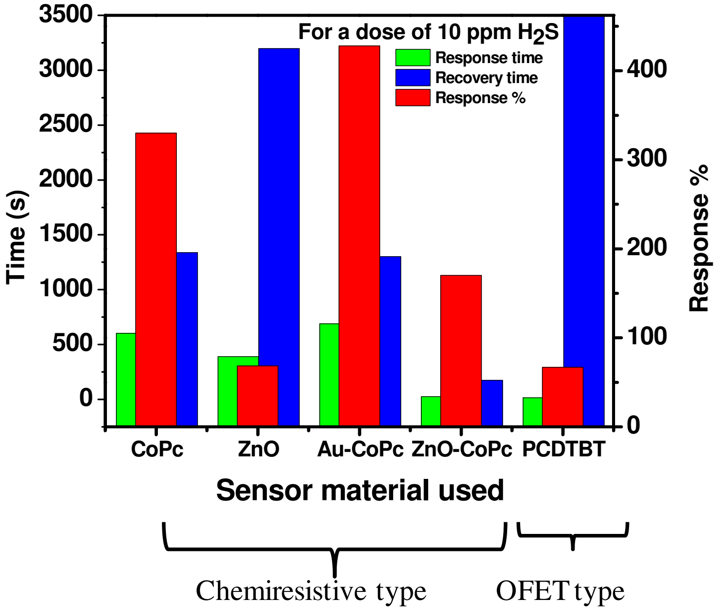

Figure 7.1: Typical values of H_2S Sensor parameters with different sensor materials.The optimized thickness of Au in Au-CoPc sensor is 1nm and that of CoPc in ZnO-CoPc sensor is 25nm.

A good sensor is the one which senses a particular analyte below its short term exposure limit with a reasonable response percent but fast response kinetics. So among all sensors which we have fabricated in class of chemiresistive type, ZnO NW-CoPc (25nm) sensor is the best sensor for H_2S. Further, PCDTBT based OFET sensor is suitable for NO_2 sensing.

Future Plan

This thesis opens up the following work for future:

- Modifying the surface of CoPc films with other metals such as Ag, Pt, Cu for improved selectivity towards many other gases such as NO, NO_2, Cl_2 etc.
- Heterojunction films of CoPc with other metal oxide nanostructure such as TiO_2, CuO, SnO_2 etc and investigating there gas sensing properties.
- Optimizing the parameters for achieving high mobility in CoPc based OFET and furthers their deployment as gas sensors.

References

1. A.Pray, L., in *Chemical Sciences and Society Summit*. September 2012: San Francisco, California, United States. p. 1-33.
2. Aswal, D.K. and S.K. Gupta, *Science and technology of chemiresistor gas sensors*. 2007: Nova Publishers.
3. Katz, H.E., Z. Bao, and S.L. Gilat, *Synthetic chemistry for ultrapure, processable, and high-mobility organic transistor semiconductors.* Accounts of Chemical Research, 2001. **34**(5): p. 359-369.
4. Schwoerer, M. and H.C. Wolf, *Introduction*, in *Organic Molecular Solids*. 2008, Wiley-VCH Verlag GmbH. p. 1-24.
5. Brütting, W., *Physics of organic semiconductors*. 2006: John Wiley & Sons.
6. Aswal, D.K. and J.V. Yakhmi, *Molecular and organic electronics devices*. 2010: Nova Science Publishers.
7. Edwards, L. and M. Gouterman, *Porphyrins: XV. Vapor absorption spectra and stability: Phthalocyanines.* Journal of Molecular Spectroscopy, 1970. **33**(2): p. 292-310.
8. Stillman, M.J. and A.J. Thomson, *Assignment of the charge-transfer bands in some metal phthalocyanines. Evidence for the S= 1 state of iron (II) phthalocyanine in solution.* Journal of the Chemical Society, Faraday Transactions 2: Molecular and Chemical Physics, 1974. **70**: p. 790-804.
9. Bohrer, F.I., et al., *Gas sensing mechanism in chemiresistive cobalt and metal-free phthalocyanine thin films.* Journal of the American Chemical Society, 2007. **129**(17): p. 5640-5646.
10. Zwart, J. and J. Van Wolput, *An ESR study of the reaction of cobalt phthalocyanines with ammonia and dioxygen.* Journal of Molecular Catalysis, 1979. **5**(1): p. 51-64.
11. Schöllhorn, B., et al., *Influence of peripheral electron-withdrawing substituents on the conductivity of zinc phthalocyanine in the presence of gases. Part 1: reducing gases.* Thin Solid Films, 1998. **326**(1): p. 245-250.
12. Seyedin, S., et al., *Knitted strain sensor textiles of highly conductive all-polymeric fibers.* ACS applied materials & interfaces, 2015. **7**(38): p. 21150-21158.
13. Bandgar, D.K., et al., *Simple and low-temperature polyaniline-based flexible ammonia sensor: a step towards laboratory synthesis to economical device design.* Journal of Materials Chemistry C, 2015. **3**(36): p. 9461-9468.
14. Nguyen, V. and K. Potje-Kamloth, *Electrical and chemical sensing properties of doped polypyrrole/gold Schottky barrier diodes.* Thin Solid Films, 1999. **338**(1): p. 142-148.
15. Van, C.N. and K. Potje-Kamloth, *Electrical and NO_x gas sensing properties of metallophthalocyanine-doped polypyrrole/silicon heterojunctions.* Thin Solid Films, 2001. **392**(1): p. 113-121.
16. Xie, D., et al., *Fabrication and characterization of polyaniline-based gas sensor by ultra-thin film technology.* Sensors and Actuators B: Chemical, 2002. **81**(2): p. 158-164.
17. Mello, S., et al., *Langmuir and Langmuir–Blodgett films from the N-hexyl-pyrrole-thiophene (AB) semi-amphiphilic copolymer.* Colloids and Surfaces A: Physicochemical and Engineering Aspects, 2002. **198**: p. 45-51.
18. Bhat, N., A. Gadre, and V. Bambole, *Investigation of electropolymerized polypyrrole composite film: characterization and application to gas sensors.* Journal of applied polymer science, 2003. **88**(1): p. 22-29.
19. An, K.H., et al., *Enhanced sensitivity of a gas sensor incorporating single-walled carbon nanotube–polypyrrole nanocomposites.* Advanced Materials, 2004. **16**(12): p. 1005-1009.
20. Li, G., et al., *Effect of thermal excitation on intermolecular charge transfer efficiency in conducting polyaniline.* Applied Physics Letters, 2004. **85**(7): p. 1187-1189.

21. Elizalde-Torres, J., H. Hu, and A. García-Valenzuela, *NO_2-induced optical absorbance changes in semiconductor polyaniline thin films.* Sensors and Actuators B: Chemical, 2004. **98**(2): p. 218-226.
22. Bartholomew, C., A. McConnell, and W. Smith, *Resonance Raman excitation profile of cobalt phthalocyanine at room temperature and 10 K.* Journal of Raman spectroscopy, 1989. **20**(9): p. 595-600.
23. Bhat, N., A. Gadre, and V. Bambole, *Structural, mechanical, and electrical properties of electropolymerized polypyrrole composite films.* Journal of applied polymer science, 2001. **80**(13): p. 2511-2517.
24. Yoon, H., M. Chang, and J. Jang, *Sensing behaviors of polypyrrole nanotubes prepared in reverse microemulsions: effects of transducer size and transduction mechanism.* The Journal of Physical Chemistry B, 2006. **110**(29): p. 14074-14077.
25. Saxena, V., et al., *Room temperature operated ammonia gas sensor using polycarbazole Langmuir–Blodgett film.* Sensors and Actuators B: Chemical, 2005. **107**(1): p. 277-282.
26. Hatchett, D.W., M. Josowicz, and J. Janata, *Acid doping of polyaniline: spectroscopic and electrochemical studies.* The Journal of Physical Chemistry B, 1999. **103**(50): p. 10992-10998.
27. Cao, Y., et al., *Electrical transport and chemical sensing properties of individual conducting polymer nanowires.* Nano letters, 2008. **8**(12): p. 4653-4658.
28. Nicolas-Debarnot, D. and F. Poncin-Epaillard, *Polyaniline as a new sensitive layer for gas sensors.* Analytica Chimica Acta, 2003. **475**(1): p. 1-15.
29. Vilkman, M., et al., *Poly (aniline) doped with 5-formyl-2-furansulfonic acid: A humidity memory.* Organic Electronics, 2010. **11**(3): p. 472-478.
30. Glidle, A., et al., *Determining compositional profiles within conducting polymer films following reaction with vapor phase reagents.* The Journal of Physical Chemistry B, 2007. **111**(16): p. 4043-4053.
31. Li, G., M. Josowicz, and J. Janata, *Electrochemical modulation of the electronic properties in conducting poly (phenylenesulfidephenyleneamine).* Synthetic metals, 2001. **125**(3): p. 273-278.
32. Blackwood, D. and M. Josowicz, *Work function and spectroscopic studies of interactions between conducting polymers and organic vapors.* The Journal of Physical Chemistry, 1991. **95**(1): p. 493-502.
33. Svetlicic, V., A.J. Schmidt, and L.L. Miller, *Conductometric sensors based on the hypersensitive response of plasticized polyaniline films to organic vapors.* Chemistry of materials, 1998. **10**(11): p. 3305-3307.
34. Athawale, A.A. and M.V. Kulkarni, *Polyaniline and its substituted derivatives as sensor for aliphatic alcohols.* Sensors and Actuators B: Chemical, 2000. **67**(1): p. 173-177.
35. Virji, S., et al., *Polyaniline nanofiber gas sensors: examination of response mechanisms.* Nano letters, 2004. **4**(3): p. 491-496.
36. Freund, M.S. and N.S. Lewis, *A chemically diverse conducting polymer-based" electronic nose".* Proceedings of the National Academy of Sciences, 1995. **92**(7): p. 2652-2656.
37. Tan, C. and D. Blackwood, *Interactions between polyaniline and methanol vapour.* Sensors and Actuators B: Chemical, 2000. **71**(3): p. 184-191.
38. Jain, S.C., M. Willander, and V. Kumar, *Conducting organic materials and devices*. Vol. 81. 2011: Newnes.
39. Lampert, M.A., *Simplified theory of space-charge-limited currents in an insulator with traps.* Physical Review, 1956. **103**(6): p. 1648.
40. Lampert, M.A. and P. Mark, *Current Injection in Solids (Academic, New York, 1970).* Chap, 1999. **10**: p. 215.
41. Nešpůrek, S. and P. Smejtek, *Space-charge limited currents in insulators with the Gaussian distribution of traps.* Czechoslovak Journal of Physics B, 1972. **22**(2): p. 160-175.
42. Kawasaki, N., et al., *Flexible picene thin film field-effect transistors with parylene gate dielectric and their physical properties.* Applied Physics Letters, 2010. **96**(11): p. 113305.

43. Jeong, H.Y., et al., *Flexible room-temperature NO_2 gas sensors based on carbon nanotubes/reduced graphene hybrid films.* Applied Physics Letters, 2010. **96**(21): p. 213105.
44. Su, P.-G., C.-T. Lee, and C.-Y. Chou, *Flexible NH_3 sensors fabricated by in situ self-assembly of polypyrrole.* Talanta, 2009. **80**(2): p. 763-769.
45. Monereo, O., et al., *Flexible sensor based on carbon nanofibers with multifunctional sensing features.* Talanta, 2013. **107**: p. 239-247.
46. Rizzo, G., et al., *Flexible, all-organic ammonia sensor based on dodecylbenzene sulfonic acid-doped polyaniline films.* Thin Solid Films, 2010. **518**(23): p. 7133-7137.
47. Jang, N.-S., et al., *Direct growth of titania nanotubes on plastic substrates and their application to flexible gas sensors.* Sensors and Actuators B: Chemical, 2014. **199**: p. 361-368.
48. Kim, Y.S., *Microheater-integrated single gas sensor array chip fabricated on flexible polyimide substrate.* Sensors and Actuators B: Chemical, 2006. **114**(1): p. 410-417.
49. Su, P.-G. and Y.-S. Chuang, *Flexible H_2 sensors fabricated by layer-by-layer self-assembly thin film of multi-walled carbon nanotubes and modified in situ with Pd nanoparticles.* Sensors and Actuators B: Chemical, 2010. **145**(1): p. 521-526.
50. Yi, J., J.M. Lee, and W.I. Park, *Vertically aligned ZnO nanorods and graphene hybrid architectures for high-sensitive flexible gas sensors.* Sensors and Actuators B: Chemical, 2011. **155**(1): p. 264-269.
51. Skotadis, E., et al., *Flexible polyimide chemical sensors using platinum nanoparticles.* Sensors and Actuators B: Chemical, 2013. **189**: p. 106-112.
52. Al-Salman, H.S. and M.J. Abdullah, *Hydrogen gas sensing based on ZnO nanostructure prepared by RF-sputtering on quartz and PET substrates.* Sensors and Actuators B: Chemical, 2013. **181**: p. 259-266.
53. Jang, B., et al., *Nanogap-based electrical hydrogen sensors fabricated from Pd-PMMA hybrid thin films.* Sensors and Actuators B: Chemical, 2014. **193**: p. 530-535.
54. Guo, Y., et al., *Electrical Assembly and Reduction of Graphene Oxide in a Single Solution Step for Use in Flexible Sensors.* Advanced Materials, 2011. **23**(40): p. 4626-4630.
55. Oprea, A., et al. *Integrated temperature, humidity and gas sensors on flexible substrates for low-power applications*. in *Sensors, 2007 IEEE*. 2007: IEEE.
56. Pecora, A., et al. *Chemoresistive nanofibrous sensor array and read-out electronics on flexible substrate*. in *Solid-State Sensors, Actuators and Microsystems Conference, 2009. TRANSDUCERS 2009. International*. 2009: IEEE.
57. Crowley, K., et al., *Fabrication of polyaniline-based gas sensors using piezoelectric inkjet and screen printing for the detection of hydrogen sulfide.* Sensors Journal, IEEE, 2010. **10**(9): p. 1419-1426.
58. Chen, X., et al. *Novel flexible room temperature NO_2 gas sensor based on polypyrrole coated SnO_2 nanoparticles*. in *Nano/Micro Engineered and Molecular Systems (NEMS), 2013 8th IEEE International Conference on*. 2013: IEEE.
59. Camara, M., et al. *Printed micro-hotplates on flexible substrates for gas sensing*. in *Solid-State Sensors, Actuators and Microsystems (TRANSDUCERS & EUROSENSORS XXVII), 2013 Transducers & Eurosensors XXVII: The 17th International Conference on*. 2013: IEEE.
60. Liu, Y., J. Chang, and L. Lin. *A flexible graphene FET gas sensor using polymer as gate dielectrics*. in *Micro Electro Mechanical Systems (MEMS), 2014 IEEE 27th International Conference on*. 2014: IEEE.
61. Yang, G., et al., *Flexible graphene-based chemical sensors on paper substrates.* Physical Chemistry Chemical Physics, 2013. **15**(6): p. 1798-1801.
62. Cho, S., et al., *Fabrication of water-dispersible and highly conductive PSS-doped PANI/graphene nanocomposites using a high-molecular weight PSS dopant and their application in H_2S detection.* Nanoscale, 2014. **6**(24): p. 15181-15195.
63. Lee, C., B.-J. Kim, and J. Kim, *(Invited) Flexible 3-Dimensional Graphene Foam-Based NO_2 Gas Sensors.* ECS Transactions, 2014. **61**(4): p. 79-83.
64. Ahn, H., et al., *Vertically aligned ZnO nanorod sensor on flexible substrate for ethanol gas monitoring.* Electrochemical and Solid-State Letters, 2010. **13**(11): p. J125-J128.

65. Bai, S., et al., *Transparent Conducting Films of Hierarchically Nanostructured Polyaniline Networks on Flexible Substrates for High-Performance Gas Sensors.* Small, 2015. **11**(3): p. 306-310.
66. Joshi, N., et al., *Flexible H_2S sensor based on gold modified polycarbazole films.* Sensors and Actuators B: Chemical, 2014. **200**: p. 227-234.
67. Asad, M., et al., *High sensitive and selective flexible H_2S gas sensors based on Cu nanoparticle decorated SWCNTs.* Sensors and Actuators B: Chemical, 2015. **210**: p. 1-8.
68. Kuberský, P., et al., *Towards a fully printed electrochemical NO_2 sensor on a flexible substrate using ionic liquid based polymer electrolyte.* Sensors and Actuators B: Chemical, 2015. **209**: p. 1084-1090.
69. Mekki, A., et al., *H_2S sensing using in situ photo-polymerized polyaniline–silver nanocomposite films on flexible substrates.* Organic Electronics, 2014. **15**(1): p. 71-81.
70. Seekaew, Y., et al., *Low-cost and flexible printed graphene–PEDOT:PSS gas sensor for ammonia detection.* Organic Electronics, 2014. **15**(11): p. 2971-2981.
71. Ryu, G.-S., et al., *High-performance diketopyrrolopyrrole-based organic field-effect transistors for flexible gas sensors.* Organic Electronics, 2015. **23**: p. 76-81.
72. Pacholski, C., A. Kornowski, and H. Weller, *Self-assembly of ZnO: from nanodots to nanorods.* Angewandte Chemie International Edition, 2002. **41**(7): p. 1188-1191.
73. Cullity, B.D., *Elements of X-ray Diffraction.* 2001.
74. Toney, M.F., et al., *X-ray depth profiling of iron oxide thin films.* Journal of Materials Research, 1988. **3**(02): p. 351-356.
75. Horcas, I., et al., *WSXM: a software for scanning probe microscopy and a tool for nanotechnology.* Review of Scientific Instruments, 2007. **78**(1): p. 013705.
76. Watt, I.M., *The principles and practice of electron microscopy.* 1997: Cambridge University Press.
77. Pavia, D.L., et al., *Introduction to spectroscopy.* 2008: Cengage Learning.
78. Melitz, W., et al., *Kelvin probe force microscopy and its application.* Surface Science Reports, 2011. **66**(1): p. 1-27.
79. Yasutake, M., D. Aoki, and M. Fujihira, *Surface potential measurements using the Kelvin probe force microscope.* Thin Solid Films, 1996. **273**(1): p. 279-283.
80. Sadewasser, S. and T. Glatzel, *Kelvin probe force microscopy: measuring and compensating electrostatic forces.* Vol. 48. 2011: Springer Science & Business Media.
81. Gelinck, G.H., et al., *Flexible active-matrix displays and shift registers based on solution-processed organic transistors.* Nature materials, 2004. **3**(2): p. 106-110.
82. Lewis, J., *Material challenge for flexible organic devices.* Materials today, 2006. **9**(4): p. 38-45.
83. Minemawari, H., et al., *Inkjet printing of single-crystal films.* Nature, 2011. **475**(7356): p. 364-367.
84. Debnath, A., et al., *Parts-per-billion level chlorine sensors with fast kinetics using ultrathin cobalt phthalocyanine films.* Chemical Physics Letters, 2009. **480**(4): p. 185-188.
85. Ng, T., et al., *Ambient effects on fullerene/copper phthalocyanine photovoltaic interface.* Appl Phys Lett, 2009. **94**(193304): p. 196.
86. Yang, R.D., et al., *Ultrathin organic transistors for chemical sensing.* Applied Physics Letters, 2007. **90**(26): p. 263506.
87. Kwon, O.S., et al., *Multidimensional conducting polymer nanotubes for ultrasensitive chemical nerve agent sensing.* Nano letters, 2012. **12**(6): p. 2797-2802.
88. Yin, J., et al., *Molecularly mediated thin film assembly of nanoparticles on flexible devices: electrical conductivity versus device strains in different gas/vapor environment.* ACS nano, 2011. **5**(8): p. 6516-6526.
89. Wang, L., et al., *Flexible chemiresistor sensors: thin film assemblies of nanoparticles on a polyethylene terephthalate substrate.* Journal of Materials Chemistry, 2010. **20**(5): p. 907-915.

90. Saran, N., et al., *Fabrication and Characterization of Thin Films of Single-Walled Carbon Nanotube Bundles on Flexible Plastic Substrates.* Journal of the American Chemical Society, 2004. **126**(14): p. 4462-4463.
91. Briand, D., et al., *Making environmental sensors on plastic foil.* Materials today, 2011. **14**(9): p. 416-423.
92. Forrest, S.R., *The path to ubiquitous and low-cost organic electronic appliances on plastic.* Nature, 2004. **428**(6986): p. 911-918.
93. Kaltenbrunner, M., et al., *Ultrathin and lightweight organic solar cells with high flexibility.* Nature communications, 2012. **3**: p. 770.
94. Wang, Z., et al., *Unlocking the full potential of organic light-emitting diodes on flexible plastic.* Nature Photonics, 2011. **5**(12): p. 753-757.
95. Tonezzer, M. and R. Lacerda, *Zinc oxide nanowires on carbon microfiber as flexible gas sensor.* Physica E: Low-dimensional Systems and Nanostructures, 2012. **44**(6): p. 1098-1102.
96. Debnath, A., et al., *Growth of iron phthalocyanine nanoweb and nanobrush using molecular beam epitaxy.* Physica E: Low-dimensional Systems and Nanostructures, 2008. **41**(1): p. 154-163.
97. Faraj, M., K. Ibrahim, and M. Ali, *PET as a plastic substrate for the flexible optoelectronic applications.* Optoelectronics and Advanced Materials, 2011. **5**(8): p. 879-882.
98. MacDonald, W.A., et al., *Latest advances in substrates for flexible electronics.* Journal of the Society for Information Display, 2007. **15**(12): p. 1075-1083.
99. Samanta, S., et al., *Bias and temperature dependent charge transport in high mobility cobalt-phthalocyanine thin films.* Applied Physics Letters, 2010. **96**(1): p. 013305.
100. Singh, A., et al., *Role of structural disorder in charge transport properties of cobalt phthalocyanine thin films grown by molecular-beam epitaxy.* Organic Electronics, 2010. **11**(11): p. 1835-1843.
101. Gould, R., *Structure and electrical conduction properties of phthalocyanine thin films.* Coordination Chemistry Reviews, 1996. **156**: p. 237-274.
102. Suo, Z., et al., *Mechanics of rollable and foldable film-on-foil electronics.* Applied Physics Letters, 1999. **74**(8): p. 1177-1179.
103. Kanari, M., et al., *Intermolecular elastic and plastic characteristics of organic phthalocyanine thin films evaluated by nanoindentation.* Applied Physics Letters, 2007. **90**(6): p. 061921.
104. Cai, J., et al., *Flexible thick-film electrochemical sensors: Impact of mechanical bending and stress on the electrochemical behavior.* Sensors and Actuators B: Chemical, 2009. **137**(1): p. 379-385.
105. Bohrer, F.I., et al., *Comparative Gas Sensing in Cobalt, Nickel, Copper, Zinc, and Metal-Free Phthalocyanine Chemiresistors.* Journal of the American Chemical Society, 2009. **131**(2): p. 478-485.
106. Timmer, B., W. Olthuis, and A. Van Den Berg, *Ammonia sensors and their applications—a review.* Sensors and Actuators B: Chemical, 2005. **107**(2): p. 666-677.
107. Zeng, Y., et al., *Enhanced ammonia sensing performances of Pd-sensitized flowerlike ZnO nanostructure.* Sensors and Actuators B: Chemical, 2011. **156**(1): p. 395-400.
108. Pandey, S.K., K.-H. Kim, and K.-T. Tang, *A review of sensor-based methods for monitoring hydrogen sulfide.* TrAC Trends in Analytical Chemistry, 2012. **32**: p. 87-99.
109. Mickelson, W., A. Sussman, and A. Zettl, *Low-power, fast, selective nanoparticle-based hydrogen sulfide gas sensor.* Applied Physics Letters, 2012. **100**(17): p. 173110.
110. Khanna, A., R. Kumar, and S. Bhatti, *CuO-doped SnO_2 thin films as hydrogen sulfide gas sensor.* Applied Physics Letters, 2003. **82**(24): p. 4388-4390.
111. Ramgir, N.S., et al., *Room temperature H_2S sensor based on Au modified ZnO nanowires.* Sensors and Actuators B: Chemical, 2013. **186**: p. 718-726.
112. Balouria, V., et al., *Nano-crystalline Fe_2O_3 thin films for ppm level detection of H_2S.* Sensors and Actuators B: Chemical, 2013. **181**: p. 471-478.
113. Bauer, S., *Flexible electronics: Sophisticated skin.* Nature materials, 2013. **12**(10): p. 871-872.

114. Kumar, A., et al., *Enhanced Cl_2 response of ultrathin bi-nuclear (cobalt–iron) phthalocyanine films.* Sensors and Actuators B: Chemical, 2012. **171**: p. 423-430.

115. Singh, A., et al., *Implication of molecular orientation on charge transport and gas sensing characteristics of cobalt–phthalocyanine thin films.* Organic Electronics, 2012. **13**(11): p. 2600-2604.

116. Wang, X., et al., *Highly sensitive gas sensor enhanced by tuning the surface potential.* Organic Electronics, 2011. **12**(12): p. 2230-2235.

117. Li, X., et al., *Copper phthalocyanine thin film transistors for hydrogen sulfide detection.* Sensors and Actuators B: Chemical, 2013. **176**: p. 1191-1196.

118. Singh, A., et al., *Flexible cobalt-phthalocyanine thin films with high charge carrier mobility.* Applied Physics Letters, 2012. **101**(22): p. 222102.

119. Moulder, J.F., J. Chastain, and R.C. King, *Handbook of X-ray photoelectron spectroscopy: a reference book of standard spectra for identification and interpretation of XPS data*. 1995: Physical Electronics Eden Prairie, MN.

120. Petraki, F., et al., *Interaction between cobalt phthalocyanine and gold studied by x-ray absorption and resonant photoemission spectroscopy.* The Journal of Physical Chemistry Letters, 2010. **1**(23): p. 3380-3384.

121. Petraki, F., et al., *CoPc and $CoPcF_{16}$ on gold: Site-specific charge-transfer processes.* Beilstein journal of nanotechnology, 2014. **5**(1): p. 524-531.

122. Szybowicz, M., et al., *High temperature study of FT-IR and Raman scattering spectra of vacuum deposited CuPc thin films.* Journal of molecular structure, 2004. **704**(1): p. 107-113.

123. Jennings, C., et al., *Raman spectra of solid films 3—Mg, Cu and Zn phthalocyanine complexes.* Journal of Raman spectroscopy, 1984. **15**(1): p. 34-37.

124. Tackley, D.R., G. Dent, and W.E. Smith, *Phthalocyanines: structure and vibrations.* Physical Chemistry Chemical Physics, 2001. **3**(8): p. 1419-1426.

125. Singh, A., et al., *Photo-induced synthesis of polypyrrole-silver nanocomposite films on N-(3-trimethoxysilylpropyl) pyrrole-modified biaxially oriented polyethylene terephthalate flexible substrates.* RSC Advances, 2013. **3**(16): p. 5506-5523.

126. Su, P.-G. and Y.-T. Peng, *Fabrication of a room-temperature H_2S gas sensor based on PPy/WO_3 nanocomposite films by in-situ photopolymerization.* Sensors and Actuators B: Chemical, 2014. **193**: p. 637-643.

127. Geng, L., *Gas sensitivity study of polypyrrole/WO_3 hybrid materials to H_2S.* Synthetic Metals, 2010. **160**(15): p. 1708-1711.

128. Bai, S., et al., *Polythiophene-WO_3 hybrid architectures for low-temperature H_2S detection.* Sensors and Actuators B: Chemical, 2014. **197**: p. 142-148.

129. Geng, L., et al., *H_2S sensitivity study of polypyrrole/WO_3 materials.* Solid-state electronics, 2006. **50**(5): p. 723-726.

130. Saxena, V., et al., *Enhanced NO_2 selectivity of hybrid poly (3-hexylthiophene): ZnO-nanowire thin films.* Applied Physics Letters, 2007. **90**(4): p. 3516.

131. Kaur, M., et al., *Detection of reducing gases by SnO_2 thin films: an impedance spectroscopy study.* Sensors and Actuators B: Chemical, 2005. **107**(1): p. 360-365.

132. Joshi, A., et al., *ZnO-nanowires modified polypyrrole films as highly selective and sensitive chlorine sensors.* Applied Physics Letters, 2009. **94**(10): p. 103115.

133. Li, M., et al., *Improved sensitivity of polychlorinated-biphenyl-orientated porous-ZnO surface photovoltage sensors from chemisorption-formed ZnO-CuPc composites.* Scientific reports, 2014. **4**.

134. Datta, N., et al., *Selective H_2S sensing characteristics of hydrothermally grown ZnO-nanowires network tailored by ultrathin CuO layers.* Sensors and Actuators B: Chemical, 2012. **166**: p. 394-401.

135. Padma, N., et al., *NO_2 sensors with room temperature operation and long term stability using copper phthalocyanine thin films.* Sensors and Actuators B: Chemical, 2009. **143**(1): p. 246-252.

136. Kumar, A., et al., *Room temperature ppb level Cl_2 sensing using sulphonated copper phthalocyanine films.* Talanta, 2010. **82**(4): p. 1485-1489.

137. Samanta, S., et al., *In Situ Diazonium-Modified Flexible ITO-Coated PEN Substrates for the Deposition of Adherent Silver–Polypyrrole Nanocomposite Films.* Langmuir, 2014. **30**(31): p. 9397-9406.
138. Wang, Z.L., et al., *Semiconducting and piezoelectric oxide nanostructures induced by polar surfaces.* Advanced Functional Materials, 2004. **14**(10): p. 943-956.
139. Park, S.H., et al., *The effect of ZnO surface conditions on the electronic structure of the ZnO/CuPc interface.* Applied Physics Letters, 2011. **98**(8): p. 082111.
140. Zhao, L.-L., et al., *Cobalt doping effects on photoluminescence, Raman scattering, crystal structure, and magnetic and piezoelectric properties in ZnO single crystals grown from molten hydrous LiOH and NaOH solutions.* Journal of Alloys and Compounds, 2015. **628**: p. 303-307.
141. Calizo, I., et al. *Micro-Raman spectroscopic characterization of ZnO quantum dots, nanocrystals and nanowires*. in *Integrated Optoelectronic Devices 2007*. 2007: International Society for Optics and Photonics.
142. Markel, F., et al., *Mode-specific vibrational reorganization energies accompanying photoinduced electron transfer in the hexamethylbenzene/tetracyanoethylene charge-transfer complex.* Journal of the American Chemical Society, 1992. **114**(15): p. 6208-6219.
143. Streetman, B.G. and S. Banerjee, *Solid state electronic devices*. 2010, Upper Saddle River, NJ: Pearson Prentice Hall.
144. Qin, C. and J.L. Whitten, *Interaction of S, SH and H_2S with Ag (100).* Surface science, 2005. **588**(1): p. 83-91.
145. Hartle, M.D., et al., *Chemically reversible reactions of hydrogen sulfide with metal phthalocyanines.* Inorganic chemistry, 2014. **53**(15): p. 7800-7802.
146. Schleupen, K., et al., *High-information-content color 16.3.* Desktop-AMLCD with. **15**: p. 187.
147. Riess, W., et al., *Influence of trapped and interfacial charges in organic multilayer light-emitting devices.* IBM Journal of Research and Development, 2001. **45**(1): p. 77-88.
148. Street, R.A., *Thin-Film Transistors.* Advanced Materials, 2009. **21**(20): p. 2007-2022.
149. Wisnieff, R., *Display technology: Printing screens.* Nature, 1998. **394**(6690): p. 225-227.
150. Comiskey, B., et al., *An electrophoretic ink for all-printed reflective electronic displays.* Nature, 1998. **394**(6690): p. 253-255.
151. Necliudov, P., et al., *Modeling of organic thin film transistors of different designs.* Journal of Applied Physics, 2000. **88**(11): p. 6594-6597.
152. Hill, I., *Numerical simulations of contact resistance in organic thin-film transistors.* Applied Physics Letters, 2005. **87**(16): p. 163505.
153. Gundlach, D., et al., *An experimental study of contact effects in organic thin film transistors.* Journal of Applied Physics, 2006. **100**(2): p. 024509.
154. Gupta, D., M. Katiyar, and D. Gupta, *An analysis of the difference in behavior of top and bottom contact organic thin film transistors using device simulation.* Organic Electronics, 2009. **10**(5): p. 775-784.
155. Payne, M.M., et al., *Organic Field-Effect Transistors from Solution-Deposited Functionalized Acenes with Mobilities as High as 1 cm^2/V. s.* Journal of the American Chemical Society, 2005. **127**(14): p. 4986-4987.
156. Gundlach, D.J., et al., *Contact-induced crystallinity for high-performance soluble acene-based transistors and circuits.* Nat Mater, 2008. **7**(3): p. 216-221.
157. Katz, H.E., et al., *Naphthalenetetracarboxylic diimide-based n-channel transistor semiconductors: structural variation and thiol-enhanced gold contacts.* Journal of the American Chemical Society, 2000. **122**(32): p. 7787-7792.
158. Gundlach, D.J., L.L. Jia, and T.N. Jackson, *Pentacene TFT with improved linear region characteristics using chemically modified source and drain electrodes.* IEEE Electron Device Letters, 2001. **22**(12): p. 571-573.
159. Cai, Q.J., et al., *Self-assembled monolayers mediated charge injection for high performance bottom-contact poly (3, 3'''-didodecylquaterthiophene) thin-film transistors.* Organic Electronics, 2008. **9**(6): p. 936-943.

160. Stadlober, B., et al., *Orders-of-Magnitude Reduction of the Contact Resistance in Short-Channel Hot Embossed Organic Thin Film Transistors by Oxidative Treatment of Au-Electrodes.* Advanced functional materials, 2007. **17**(15): p. 2687-2692.

161. Kumaki, D., T. Umeda, and S. Tokito, *Reducing the contact resistance of bottom-contact pentacene thin-film transistors by employing a* MoO_x *carrier injection layer.* Applied Physics Letters, 2008. **92**(1): p. 13301-13301.

162. Kano, M., T. Minari, and K. Tsukagoshi, *Improvement of subthreshold current transport by contact interface modification in p-type organic field-effect transistors.* Applied Physics Letters, 2009. **94**(14): p. 143304.

163. Majewski, L., et al., *High performance organic transistors on cheap, commercial substrates.* Journal of Physics D: Applied Physics, 2004. **37**(24): p. 3367.

164. Klauk, H., *Organic thin-film transistors.* Chemical Society Reviews, 2010. **39**(7): p. 2643-2666.

165. Meijer, E., et al., *Switch-on voltage in disordered organic field-effect transistors.* Applied Physics Letters, 2002. **80**(20): p. 3838-3840.

166. Torsi, L., et al., *Multi-parameter gas sensors based on organic thin-film-transistors.* Sensors and Actuators B: Chemical, 2000. **67**(3): p. 312-316.

167. Powell, M., *Analysis of field-effect-conductance measurements on amorphous semiconductors.* Philosophical Magazine B, 1981. **43**(1): p. 93-103.

168. Bissell, R.A., K.C. Persaud, and P. Travers, *The influence of non-specific molecular partitioning of analytes on the electrical responses of conducting organic polymer gas sensors.* Physical Chemistry Chemical Physics, 2002. **4**(14): p. 3482-3490.

169. Hauert, R., et al., *Influence of nitrogen doping on different properties of aC: H.* Thin Solid Films, 1995. **268**(1): p. 22-29.

170. Björström, C.M., et al., *Vertical phase separation in spin-coated films of a low bandgap polyfluorene/PCBM blend—effects of specific substrate interaction.* Applied Surface Science, 2007. **253**(8): p. 3906-3912.

171. Castner, D.G., K. Hinds, and D.W. Grainger, *X-ray photoelectron spectroscopy sulfur 2p study of organic thiol and disulfide binding interactions with gold surfaces.* Langmuir, 1996. **12**(21): p. 5083-5086.

172. Ishida, T., et al., *High Resolution X-ray Photoelectron Spectroscopy Measurements of Octadecanethiol Self-Assembled Monolayers on Au(111).* Langmuir, 1998. **14**(8): p. 2092-2096.

173. Jha, P., et al. *Poly (2, 7-carbazole) derivative based air stable and flexible organic field effect transistor*. in *AIP Conf. Proc*. 2013.

174. Wang, C., et al., *Semiconducting π-conjugated systems in field-effect transistors: a material odyssey of organic electronics.* Chemical Reviews, 2011. **112**(4): p. 2208-2267.

175. Yun, Y., C. Pearson, and M.C. Petty, *Pentacene thin film transistors with a poly (methyl methacrylate) gate dielectric: Optimization of device performance.* Journal of Applied Physics, 2009. **105**(3): p. 034508.

176. Andringa, A.-M., et al., NO_2 *detection and real-time sensing with field-effect transistors.* Chemistry of Materials, 2013. **26**(1): p. 773-785.

177. Li, B. and D.N. Lambeth, *Chemical sensing using nanostructured polythiophene transistors.* Nano letters, 2008. **8**(11): p. 3563-3567.